Hybrid dynamical system approaches for power converter systems and electric drives

Italian National Ph.D. Program in Autonomous Systems

ACADEMIC DISCIPLINE: SYSTEMS AND CONTROL ENGINEERING (IINF-04/A)

Final Dissertation

Hybrid Dynamical System Approaches For Power Converter Systems and Electric Drives

---

by

Silvia Di Girolamo

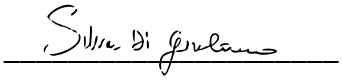

Administrative Headquarters:

Politecnico di Bari – Department of Electrical and Information Engineering

Hosting University:

University of Palermo – Department of Engineering

Referees:

Prof. Ronald Tetzlaff

Prof. Simon Fabri

Supervisors:

Prof. Filippo D'Ippolito

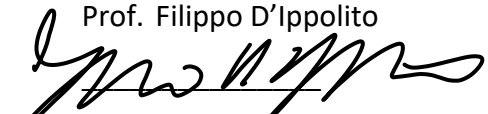

Prof. Antonino Sferlazza

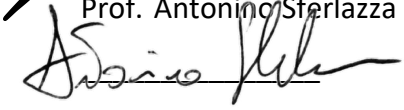

Coordinator of Ph.D Program

Prof. Mariagrazia Dotoli

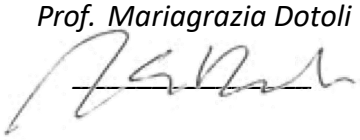

Course no. 38, 01/11/2022-31/10/2025

LIBERATORIA PER L'ARCHIVIAZIONE DELLA TESI DI DOTTORATO

Al Magnifico Rettore
del Politecnico di Bari

La sottoscritta Silvia Di Girolamo nata a Marsala il 29/12/1998
residente a Marsala in contrada Dara e-mail s.digirolamo@phd.poliba.it
iscritto al 3° anno di Corso di Dottorato di Ricerca in Autonomous Systems ciclo 38°
ed essendo stato ammesso a sostenere l'esame finale con la prevista discussione della tesi dal titolo:
Hybrid Dynamical System Approaches for Power Converter Systems and Electric Drives

DICHIARA

1) di essere consapevole che, ai sensi del D.P.R. n. 445 del 28.12.2000, le dichiarazioni mendaci, la falsità negli atti e l'uso di atti falsi sono puniti ai sensi del codice penale e delle Leggi speciali in materia, e che nel caso ricorressero dette ipotesi, decade fin dall'inizio e senza necessità di nessuna formalità dai benefici conseguenti al provvedimento emanato sulla base di tali dichiarazioni;
2) di essere iscritto al Corso di Dottorato di ricerca Autonomous Systems ciclo 38° corso attivato ai sensi del "*Regolamento dei Corsi di Dottorato di ricerca del Politecnico di Bari"*, emanato con D.R. n.286 del 01.07.2013;
3) di essere pienamente a conoscenza delle disposizioni contenute nel predetto Regolamento in merito alla procedura di deposito, pubblicazione e autoarchiviazione della tesi di dottorato nell'Archivio Istituzionale ad accesso aperto alla letteratura scientifica;
4) di essere consapevole che attraverso l'autoarchiviazione delle tesi nell'Archivio Istituzionale ad accesso aperto alla letteratura scientifica del Politecnico di Bari (IRIS-POLIBA), l'Ateneo archivierà e renderà consultabile in rete (nel rispetto della Policy di Ateneo di cui al D.R. 642 del 13.11.2015) il testo completo della tesi di dottorato, fatta salva la possibilità di sottoscrizione di apposite licenze per le relative condizioni di utilizzo (di cui al sito http://www.creativecommons.it/Licenze), e fatte salve, altresì, le eventuali esigenze di "embargo", legate a strette considerazioni sulla tutelabilità e sfruttamento industriale/commerciale dei contenuti della tesi, da rappresentarsi mediante compilazione e sottoscrizione del modulo in calce (Richiesta di embargo);
5) che la tesi da depositare in IRIS-POLIBA, in formato digitale (PDF/A) sarà del tutto identica a quelle **consegnate**/inviate/da inviarsi ai componenti della commissione per l'esame finale e a qualsiasi altra copia depositata presso gli Uffici del Politecnico di Bari in forma cartacea o digitale, ovvero a quella da discutere in sede di esame finale, a quella da depositare, a cura dell'Ateneo, presso le Biblioteche Nazionali Centrali di Roma e Firenze e presso tutti gli Uffici competenti per legge al momento del deposito stesso, e che di conseguenza va esclusa qualsiasi responsabilità del Politecnico di Bari per quanto riguarda eventuali errori, imprecisioni o omissioni nei contenuti della tesi;
6) che il contenuto e l'organizzazione della tesi è opera originale realizzata dal sottoscritto e non compromette in alcun modo i diritti di terzi, ivi compresi quelli relativi alla sicurezza dei dati personali; che pertanto il Politecnico di Bari ed i suoi funzionari sono in ogni caso esenti da responsabilità di qualsivoglia natura: civile, amministrativa e penale e saranno dal sottoscritto tenuti indenni da qualsiasi richiesta o rivendicazione da parte di terzi;
7) che il contenuto della tesi non infrange in alcun modo il diritto d'Autore né gli obblighi connessi alla salvaguardia di diritti morali od economici di altri autori o di altri aventi diritto, sia per testi, immagini, foto, tabelle, o altre parti di cui la tesi è composta.

Luogo e data Palermo, 15/01/2026 Firma Silvia Di Girolamo

Il/La sottoscritto, con l'autoarchiviazione della propria tesi di dottorato nell'Archivio Istituzionale ad accesso aperto del Politecnico di Bari (POLIBA-IRIS), pur mantenendo su di essa tutti i diritti d'autore, morali ed economici, ai sensi della normativa vigente (Legge 633/1941 e ss.mm.ii.),

CONCEDE

- al Politecnico di Bari il permesso di trasferire l'opera su qualsiasi supporto e di convertirla in qualsiasi formato al fine di una corretta conservazione nel tempo. Il Politecnico di Bari garantisce che non verrà effettuata alcuna modifica al contenuto e alla struttura dell'opera.
- al Politecnico di Bari la possibilità di riprodurre l'opera in più di una copia per fini di sicurezza, back-up e conservazione.

Luogo e data Palermo, 15/01/2026 Firma Silvia Di Girolamo

Silvia Di Girolamo

Hybrid Dynamical System Approaches for Power Converter Systems and Electric Drives

Thesis submitted for the degree of Philosophiae Doctor

Italian National Ph.D. Program in Autonomous Systems

Politecnico di Bari - Università degli Studi di Palermo

Tutors

Prof. Engr. *Filippo D'Ippolito*

Prof. Engr. *Antonino Sferlazza*

2025

The doctoral scholarship was funded by the European Union - Next Generation EU, Mission 4 Component 1 CUP D93C22000860005.

Dissertation submitted for the degree of *Philosophiae Doctor*
Italian National Ph.D. Program in Autonomous Systems

Cycle:
38th

Administrative Headquarters:
Politecnico di Bari

Hosting University:
Università degli Studi di Palermo

Title:
Hybrid Dynamical System Approaches for Power Converter Systems and Electric Drives

Ph.D Candidate:
Silvia Di Girolamo, Università degli Studi di Palermo (Palermo, Italy)

Tutors:
Prof. Engr. Filippo D'Ippolito, Università degli Studi di Palermo (Palermo, Italy)
Prof. Engr. Antonino Sferlazza, Università degli Studi di Palermo (Palermo, Italy)

Coordinator:
Prof. Engr. Mariagrazia Dotoli, Politecnico di Bari (Bari, Italy)

External Reviewers:
Prof. Engr. Simon Fabri, University of Malta (Msida, Matla)
Prof. Engr. Ronald Tetzlaff, Technische Universität Dresden (Dresden, Germany)

Last version:
December 22, 2025

Abstract

The modeling and control of dynamical systems are fundamental objectives in the field of control engineering. When approaching the problem of controlling physical or digital systems, dynamical models have historically been categorized into two types: continuous-time models, which are modeled by differential equations, and discrete-time models, which are modeled by difference equations. However, many real-world systems involve both continuous evolution and discrete events, requiring a more general framework. In recent years, a new class of models, known as hybrid dynamical systems, has gained significant attention in the control field thanks to its versatile modeling framework, which combines continuous-time dynamics with discrete-time evolution. This hybrid framework allows for the description of a broader class of systems and enables the development of more flexible and effective control strategies compared to traditional continuous-time approaches. This thesis explores both the theoretical foundations and practical implementations of hybrid control strategies, with a specific focus on power electronic and electrical drives. The thesis is organized into three main parts. The first part of the work develops the theoretical background and is divided into two sections. The first section introduces the modeling framework of hybrid dynamical systems, discussing solution concepts, stability analysis, and relevant applications. The second section focuses on switched systems, presenting their classification, stability properties, and interconnections with hybrid systems. Moreover, the concept of dynamic allocation is introduced as a flexible control principle that enables adaptive distribution of control inputs or energy resources among multiple subsystems, enhancing performance and robustness in hybrid architectures. In contrast to a static allocation scheme, where the control inputs or energy resources are distributed according to predefined rules, dynamic allocation represents an adaptive mechanism capable of continuously reallocating the control effort in response to variations in system states, external perturbations, and performance objectives. This mechanism enables the controller to leverage structural redundancies and inherent system flexibilities, enhancing system robustness, stability, and overall performance under time-varying operating conditions. Within the framework of hybrid dynamical systems, dynamic allocation can be interpreted as a hierarchical coordination mechanism that integrates continuous control actions with discrete switching events, ensuring a consistent interaction among interconnected subsystems. Its application to power electronic architectures, such as multi-input converters and multi-phase electrical drives, provides a rigorous framework for optimal energy management, loss minimization, and fault-tolerant operation, thus improving overall system efficiency and reliability.

The second part of the thesis is application-oriented, focusing on power electronic converters. This part is structured into three main sections, reflecting the energy flow in a typical power conversion system. The first section addresses the hybrid control of a DC-DC boost converter using a min-type strategy, aiming at efficient voltage regulation and robust dynamic performance. The second section focuses on multi-input converters and their role in microgrid integration, where a dynamic input allocation strategy is developed to manage multiple power sources while ensuring robust voltage control and decoupled current regulation without degrading overall system performance. The third section is dedicated to the DC/AC conversion stage, where an advanced nonlinear hybrid controller is designed for a differential boost inverter, integrating active disturbance compensation and a sliding mode component to enhance robustness and power quality. The third part of the thesis extends the proposed methodologies to electrical drives, highlighting their role as key end-users of power electronic conversion. This part is also structured into three main sections. The first section investigates robust nonlinear control for induction motors with adaptive disturbance compensation. The second section focuses on harmonic losses minimization in dual three-phase induction motors through dynamic input allocation. The third section presents sensorless control of a permanent magnet synchronous motor for energy recovery in automotive applications, comparing Kalman filters and MRAS observer approaches. The proposed control strategies are validated through rigorous mathematical analysis and robust Lyapunov-based stability proofs. The application problem is examined from a theoretical perspective, with the study concluding through numerical results obtained from simulations or experiments.

Contents

List of Figures

List of Tables

Preface

This thesis is submitted in partial fulfillment of the requirements for the degree of *Philosophiae Doctor* in Autonomous Systems. The full list of papers written by the author is reported hereafter.

List of Papers Written by the Author

With the exception of Chapter 1, which provides an introduction and a general overview of the thesis, Chapter 2, which presents an overview of hybrid dynamical systems, and Chapter 3, which presents an overview of switched systems, all other chapters in this thesis are associated with one publication. In particular, Chapter 4 is associated with the following publication:

- C. Albea-Sanchez, C. Alonso, G. García, L. Martínez-Salamero, and A. Sferlazza, "Min-type control strategy of a DC–DC synchronous boost converter". IEEE Transactions on Industrial Electronics.

Chapter 5 is associated with the following publication:

- S. Di Girolamo, F. D'Ippolito, M. Luna, M. Pucci, A. Sferlazza, and L. Zaccarian, "Control of a multi-input converter using dynamic input allocation". Singapore, 49$^{\text{th}}$ Annual Conference of the IEEE Industrial Electronics Society, Marina Bay Sands Expo and Convention Centre (IECON2023).

Chapter 6 is associated with the following publication:

- F. Alonge, S. Di Girolamo, F. D'Ippolito, G. Garraffa, V. Leonardi, I. Marchese, and A. Sferlazza, "Nonlinear robust control of a differential boost converter based on disturbance compensation and additional sliding-mode component". IEEE Access Journal.

Chapter 7 is associated with the following publication:

- A. Accetta, M. Cirrincione, S. Di Girolamo, F. D'Ippolito, M. Pucci, and A. Sferlazza, "Robust nonlinear control for induction motor drives based on adaptive disturbance compensation". IEEE Transactions on Industry Applications.
- A. Accetta, M. Cirrincione, S. Di Girolamo, F. D'Ippolito, M. Pucci, and A. Sferlazza, "Robust nonlinear control for high-performance induction motor drives based on adaptive disturbance compensation", Nashville, 15th Annual IEEE Energy Conversion Congress and Exposition (ECCE2023).

Chapter 8 is associated with the following publication:

- A. Accetta, S. Di Girolamo, F. D'Ippolito, M. Luna, M. Pucci, and A. Sferlazza, "Harmonic losses minimization of a dual-three phase induction motor by dynamic input allocation control". Tokyo, 4th International Conference on Power System and Electrical Technology (PSET2025).

Chapter 9 is associated with the following publication:

- S. Caltabellotta, M. Cirrincione, S. Di Girolamo, E. Pipitone, and A. Sferlazza, "Sensorless control of a permanent magnet synchronous motor for exhaust energy recovery of internal combustion engine: a comparison between Kalman filter and MRAS observer". System Science and Control Engineering.

International Journal Articles

[1] Goebel, R., Sanfelice, R. G., and Teel, A. R., "Hybrid dynamical systems," *IEEE control systems magazine*, vol. 29, no. 2, pp. 28–93, 2009.

[4] Lygeros, J., Johansson, K. H., Simic, S. N., Zhang, J., and Sastry, S. S., "Dynamical properties of hybrid automata," *IEEE Transactions on automatic control*, vol. 48, no. 1, pp. 2–17, 2003.

[5] Branicky, M. S., "Multiple lyapunov functions and other analysis tools for switched and hybrid systems," *IEEE Transactions on automatic control*, vol. 43, no. 4, pp. 475–482, 2002.

[8] Nešić, D. and Teel, A. R., "Input-to-state stability of networked control systems," *Automatica*, vol. 40, no. 12, pp. 2121–2128, 2004.

[11] Liberzon, D. and Morse, A. S., "Basic problems in stability and design of switched systems," *IEEE control systems magazine*, vol. 19, no. 5, pp. 59–70, 2002.

[13] Hespanha, J. P., "Uniform stability of switched linear systems: Extensions of lasalle's invariance principle," *IEEE transactions on Automatic Control*, vol. 49, no. 4, pp. 470–482, 2004.

[14] Filippov, A. F., "Differential equations with discontinuous right-hand side," *Matematicheskii sbornik*, vol. 93, no. 1, pp. 99–128, 1960.

[17] Shorten, R., Wirth, F., Mason, O., Wulff, K., and King, C., "Stability criteria for switched and hybrid systems," *SIAM review*, vol. 49, no. 4, pp. 545–592, 2007.

[19] Lan, Y.-H., Gu, H.-B., Chen, C.-X., Zhou, Y., and Luo, Y.-P., "An indirect lyapunov approach to the observer-based robust control for fractional-order complex dynamic networks," *Neurocomputing*, vol. 136, pp. 235–242, 2014.

[20] Sontag, E. D. and Wang, Y., "On characterizations of the input-to-state stability property," *Systems & Control Letters*, vol. 24, no. 5, pp. 351–359, 1995.

[22] DeCarlo, R. A., Branicky, M. S., Pettersson, S., and Lennartson, B., "Perspectives and results on the stability and stabilizability of hybrid systems," *Proceedings of the IEEE*, vol. 88, no. 7, pp. 1069–1082, 2002.

[26] Sferlazza, A., Albea-Sanchez, C., Martinez-Salamero, L., Garcia, G., and Alonso, C., "Min-type control strategy of a dc–dc synchronous boost converter," *IEEE Transactions on Industrial Electronics*, vol. 67, no. 4, pp. 3167–3179, 2019.

[28] Qiu, Y., Chen, X., and Liu, H., "Digital average current-mode control using current estimation and capacitor charge balance principle for dc–dc converters operating in dcm," *IEEE Transactions on Power Electronics*, vol. 25, no. 6, pp. 1537–1545, 2010.

[29] Vidal-Idiarte, E., Marcos-Pastor, A., Garcia, G., Cid-Pastor, A., and Martinez-Salamero, L., "Discrete-time sliding-mode-based digital pulse width modulation control of a boost converter," *IET Power Electronics*, vol. 8, no. 5, pp. 708–714, 2015.

[30] Deaecto, G. S., Geromel, J. C., Garcia, F. S., and Pomilio, J. A., "Switched affine systems control design with application to dc–dc converters," *IET control theory & applications*, vol. 4, no. 7, pp. 1201–1210, 2010.

[31] Theunisse, T. A., Chai, J., Sanfelice, R. G., and Heemels, W. M. H., "Robust global stabilization of the dc-dc boost converter via hybrid control," *IEEE Transactions on Circuits and Systems I: Regular Papers*, vol. 62, no. 4, pp. 1052–1061, 2017.

[32] Martínez-Salamero, L., García, G., Orellana, M., Lahore, C., and Estibals, B., "Start-up control and voltage regulation in a boost converter under sliding-mode operation," *IEEE Transactions on industrial electronics*, vol. 60, no. 10, pp. 4637–4649, 2012.

[33] Martinez-Salamero, L., Cid-Pastor, A., El Aroudi, A., Giral, R., Calvente, J., and Ruiz-Magaz, G., "Sliding-mode control of dc-dc switching converters," *IFAC Proceedings Volumes*, vol. 44, no. 1, pp. 1910–1916, 2011.

[34] Bosque-Moncusi, J. M., Valderrama-Blavi, H., Flores-Bahamonde, F., Vidal-Idiarte, E., and Martínez-Salamero, L., "Using low-cost microcontrollers to implement variable hysteresis-width comparators for switching power converters," *IET Power Electronics*, vol. 11, no. 5, pp. 787–795, 2018.

[36] Sanchez, C. A., Garcia, G., Hadjeras, S., Heemels, W. M. H., and Zaccarian, L., "Practical stabilization of switched affine systems with dwell-time guarantees," *IEEE Transactions on Automatic Control*, vol. 64, no. 11, pp. 4811–4817, 2019.

[38] Farhadi, M. and Mohammed, O., "Energy storage technologies for high-power applications," *IEEE Transactions on Industry Applications*, vol. 52, no. 3, pp. 1953–1961, 2015.

[39] Justo, J. J., Mwasilu, F., Lee, J., and Jung, J.-W., "Ac-microgrids versus dc-microgrids with distributed energy resources: A review," *Renewable and sustainable energy reviews*, vol. 24, pp. 387–405, 2013.

[40] Fontes, G., Turpin, C., Astier, S., and Meynard, T. A., "Interactions between fuel cells and power converters: Influence of current harmonics on a fuel cell stack," *IEEE Transactions on Power Electronics*, vol. 22, no. 2, pp. 670–678, 2007.

[41] Aman, S., Simmhan, Y., and Prasanna, V. K., "Energy management systems: State of the art and emerging trends," *IEEE communications Magazine*, vol. 51, no. 1, pp. 114–119, 2013.

[42] Chaouachi, A., Kamel, R. M., Andoulsi, R., and Nagasaka, K., "Multiobjective intelligent energy management for a microgrid," *IEEE transactions on Industrial Electronics*, vol. 60, no. 4, pp. 1688–1699, 2012.

[45] Chen, Y.-M., Liu, Y.-C., and Wu, F.-Y., "Multi-input dc/dc converter based on the multiwinding transformer for renewable energy applications," *IEEE transactions on industry applications*, vol. 38, no. 4, pp. 1096–1104, 2002.

[47] Zaccarian, L., "Dynamic allocation for input redundant control systems," *Automatica*, vol. 45, no. 6, pp. 1431–1438, 2009.

[50] Sanchis, P., Ursæa, A., Gubía, E., and Marroyo, L., "Boost dc-ac inverter: A new control strategy," *IEEE Transactions on power electronics*, vol. 20, no. 2, pp. 343–353, 2005.

[51] Jha, K., Mishra, S., and Joshi, A., "High-quality sine wave generation using a differential boost inverter at higher operating frequency," *IEEE Transactions on Industry Applications*, vol. 51, no. 1, pp. 373–384, 2014.

[52] Caceres, R. O. and Barbi, I., "A boost dc-ac converter: Analysis, design, and experimentation," *IEEE transactions on power electronics*, vol. 14, no. 1, pp. 134–141, 2002.

[53] Cortes, D., Vázquez, N., and Alvarez-Gallegos, J., "Dynamical sliding-mode control of the boost inverter," *IEEE Transactions on Industrial Electronics*, vol. 56, no. 9, pp. 3467–3476, 2008.

[54] Lopez-Caiza, D., Flores-Bahamonde, F., Kouro, S., Santana, V., Müller, N., and Chub, A., "Sliding mode based control of dual boost inverter for grid connection," *Energies*, vol. 12, no. 22, p. 4241, 2019.

[55] Qi, Q., Ghaderi, D., and Guerrero, J. M., "Sliding mode controller-based switched-capacitor-based high dc gain and low voltage stress dc-dc boost converter for photovoltaic applications," *International Journal of Electrical Power & Energy Systems*, vol. 125, p. 106 496, 2021.

[56] Deo, R. N., Shrivastava, A., and Chatterjee, K., "Implementation of sliding mode backstepping controller for boost converter in real-time for led application," *Expert Systems*, vol. 40, no. 6, e13095, 2023.

[57] Mohammadhassani, F. and Narm, H. G., "Dynamic sliding mode control of single-stage boost inverter with parametric uncertainties and delay," *IET Power Electronics*, vol. 14, no. 12, pp. 2127–2138, 2021.

[58] Musona, R. and Serban, I., "Differential single-phase inverters with active power decoupling: A survey," *IEEE Access*, vol. 11, pp. 53 654–53 670, 2023.

[59] Seo, S.-W. and Choi, H. H., "Digital implementation of fractional order pid-type controller for boost dc–dc converter," *IEEE Access*, vol. 7, pp. 142 652–142 662, 2019.

[60] Pereira, L. F. d. S., Batista, E., Brito, M. A. de, and Godoy, R. B., "A robustness analysis of a fuzzy fractional order pid controller based on genetic algorithm for a dc-dc boost converter," *Electronics*, vol. 11, no. 12, p. 1894, 2022.

[61] Caceres, R. O. and Barbi, I., "A boost dc-ac converter: Analysis, design, and experimentation," *IEEE transactions on power electronics*, vol. 14, no. 1, pp. 134–141, 1999.

[62] Cortes, D., Vázquez, N., and Alvarez-Gallegos, J., "Dynamical sliding-mode control of the boost inverter," *IEEE Transactions on Industrial Electronics*, vol. 56, no. 9, pp. 3467–3476, 2009.

[63] Flores-Bahamonde, F., Valderrama-Blavi, H., Bosque-Moncusi, J. M., García, G., and Martínez-Salamero, L., "Using the sliding-mode control approach for analysis and design of the boost inverter," *IET Power Electronics*, vol. 9, no. 8, pp. 1625–1634, 2016.

[64] Ahmad, S. and Ali, A., "Active disturbance rejection control of dc–dc boost converter: A review with modifications for improved performance," *IET Power Electronics*, vol. 12, no. 8, pp. 2095–2107, 2019.

[65] Zhuo, S., Gaillard, A., Guo, L., Xu, L., Paire, D., and Gao, F., "Active disturbance rejection voltage control of a floating interleaved dc–dc boost converter with switch fault consideration," *IEEE Transactions on Power Electronics*, vol. 34, no. 12, pp. 12 396–12 406, 2019.

[66] Zhou, X., Liu, Q., Ma, Y., and Xie, B., "Dc-link voltage research of photovoltaic grid-connected inverter using improved active disturbance rejection control," *IEEE Access*, vol. 9, pp. 9884–9894, 2021.

[67] Zhuo, S., Gaillard, A., Xu, L., Bai, H., Paire, D., and Gao, F., "Enhanced robust control of a dc–dc converter for fuel cell application based on high-order extended state observer," *IEEE Transactions on Transportation Electrification*, vol. 6, no. 1, pp. 278–287, 2020.

[69] Tan, S.-C., Lai, Y., and Tse, C. K., "Implementation of pulse-width-modulation based sliding mode controller for boost converters," *IEEE Power Electronics Letters*, vol. 3, no. 4, pp. 130–135, 2005.

[70] Gehan, O. et al., "A nonlinear state feedback for dc/dc boost converters," *Journal of Dynamic Systems, Measurement, and Control*, vol. 139, no. 1, 2017.

[71] Shtessel, Y. B., Zinober, A. S., and Shkolnikov, I. A., "Sliding mode control of boost and buck-boost power converters using method of stable system centre," *Automatica*, vol. 39, no. 6, pp. 1061–1067, 2003.

[76] Accetta, A., Cirrincione, M., Pucci, M., and Sferlazza, A., "Feedback linearization based nonlinear control of synrm drives accounting for self-and cross-saturation," *IEEE Transactions on Industry Applications*, vol. 58, no. 3, pp. 3637–3651, 2022.

[77] De Luca, A. and Ulivi, G., "Design of an exact nonlinear controller for induction motors," *Automatic Control, IEEE Transactions on*, vol. 34, no. 12, pp. 1304–1307, 1989.

[78] Kim, D.-I., HA, I.-J., and KO, M.-S., "Control of induction motors via feedback linearization with input-output decoupling," *International Journal of Control*, vol. 51, no. 4, pp. 863–883, 1990.

[79] Accetta, A. et al., "Robust control for high performance induction motor drives based on partial state-feedback linearization," *IEEE Transactions on Industry Applications*, vol. 55, no. 1, pp. 490–503, 2018.

[80] Accetta, A., Alonge, F., Cirrincione, M., Pucci, M., and Sferlazza, A., "Feedback linearizing control of induction motor considering magnetic saturation effects," *IEEE Transactions on Industry Applications*, vol. 52, no. 6, pp. 4843–4854, 2016.

[81] Alonge, F., Cirrincione, M., Pucci, M., and Sferlazza, A., "Input-output feedback linearization control with on-line MRAS based inductor resistance estimation of linear induction motors including the dynamic end-effects," *Industry Applications, IEEE Transactions on*, vol. 52, no. 1, pp. 254–266, 2016.

[82] Marino, R., Peresada, S., and Valigi, P., "Adaptive input-output linearizing control of induction motors," *Automatic Control, IEEE Transactions on*, vol. 38, no. 2, pp. 208–221, 1993.

[83] Alonge, F., Cirrincione, M., D'Ippolito, F., Pucci, M., and Sferlazza, A., "Adaptive feedback linearizing control of linear induction motor considering the end-effects," *Control Engineering Practice*, vol. 55, pp. 116–126, 2016.

[85] Han, J., "From PID to active disturbance rejection control," *Industrial Electronics, IEEE transactions on*, vol. 56, no. 3, pp. 900–906, 2009.

[86] Huang, Y. and Xue, W., "Active disturbance rejection control: Methodology and theoretical analysis," *ISA transactions*, vol. 53, no. 4, pp. 963–976, 2014.

[87] Guo, B.-Z. and Zhao, Z.-l., "On the convergence of an extended state observer for nonlinear systems with uncertainty," *Systems & Control Letters*, vol. 60, no. 6, pp. 420–430, 2011.

[89] Liu, C., Luo, G., Duan, X., Chen, Z., Zhang, Z., and Qiu, C., "Adaptive ladrc-based disturbance rejection method for electromechanical servo system," *IEEE Transactions on Industry Applications*, vol. 56, no. 1, pp. 876–889, 2019.

[90] Qu, L., Qiao, W., and Qu, L., "An enhanced linear active disturbance rejection rotor position sensorless control for permanent magnet synchronous motors," *IEEE Transactions on Power Electronics*, vol. 35, no. 6, pp. 6175–6184, 2019.

[91] Lin, P., Wu, Z., Liu, K.-Z., and Sun, X.-M., "A class of linear–nonlinear switching active disturbance rejection speed and current controllers for pmsm," *IEEE Transactions on Power Electronics*, vol. 36, no. 12, pp. 14 366–14 382, 2021.

[92] Tian, M., Wang, B., Yu, Y., Dong, Q., and Xu, D., "Discrete-time repetitive control-based adrc for current loop disturbances suppression of pmsm drives," *IEEE Transactions on Industrial Informatics*, vol. 18, no. 5, pp. 3138–3149, 2021.

[93] Zhang, Z., Chen, Y., Feng, X., Xie, S., and Zhao, C., "Linear active disturbance rejection speed control with variable gain load torque sliding mode observer for ipmsms," *Journal of Power Electronics*, vol. 22, no. 8, pp. 1290–1301, 2022.

[94] Alonge, F., Cirrincione, M., D'Ippolito, F., Pucci, M., and Sferlazza, A., "Robust active disturbance rejection control of induction motor systems based on additional sliding-mode component," *IEEE Transactions on Industrial Electronics*, vol. 64, no. 7, pp. 5608–5621, 2017.

[95] Marino, R., Peresada, S., and Valigi, P., "Adaptive input-output linearizing control of induction motors," *IEEE Transactions on Automatic control*, vol. 38, no. 2, pp. 208–221, 2002.

[96] De Luca, A. and Ulivi, G., "Design of an exact nonlinear controller for induction motors," *IEEE Transactions on Automatic Control*, vol. 34, no. 12, pp. 1304–1307, 2002.

[97] KIM, D.-I., HA, I.-J., and KO, M.-S., "Control of induction motors via feedback linearization with input-output decoupling," *International Journal of Control*, vol. 51, no. 4, pp. 863–883, 1990.

[98] Accetta, A., Di Piazza, M. C., Luna, M., and Pucci, M., "Electrical losses minimization of linear induction motors considering the dynamic end-effects," *IEEE Transactions on Industry Applications*, vol. 55, no. 2, pp. 1561–1573, 2018.

[100] Pant GK Singh, V., "Analysis of a multiphase induction machine under fault condition in a phase-redundant ac drive system," *Electric Machines &Power Systems*, vol. 28, no. 6, pp. 577–590, 2000.

[101] Jahns, T. M., "Improved reliability in solid-state ac drives by means of multiple independent phase drive units," *IEEE Transactions on Industry Applications*, no. 3, pp. 321–331, 1980.

[103] Bojoi, R., Farina, F., Profumo, F., and Tenconi, A., "Dual-three phase induction machine drives control—a survey," *IEEJ Transactions on Industry Applications*, vol. 126, no. 4, pp. 420–429, 2006.

[104] Fortescue, C. L., "Method of symmetrical co-ordinates applied to the solution of polyphase networks," *Transactions of the American Institute of Electrical Engineers*, vol. 37, no. 2, pp. 1027–1140, 1918.

[105] Nelson, R. and Krause, P., "Induction machine analysis for arbitrary displacement between multiple winding sets," *IEEE Transactions on Power Apparatus and Systems*, no. 3, pp. 841–848, 2007.

[107] Abbas, M. A., Christen, R., and Jahns, T. M., "Six-phase voltage source inverter driven induction motor," *IEEE Transactions on industry applications*, no. 5, pp. 1251–1259, 1984.

[109] Zhao, Y. and Lipo, T. A., "Space vector pwm control of dual three-phase induction machine using vector space decomposition," *IEEE Transactions on industry applications*, vol. 31, no. 5, pp. 1100–1109, 1995.

[110] Hu, Y., Zhu, Z.-Q., and Odavic, M., "Comparison of two-individual current control and vector space decomposition control for dual three-phase pmsm," *IEEE Transactions on Industry Applications*, vol. 53, no. 5, pp. 4483–4492, 2017.

[111] Pucci, M., "State-space space-vector model of the induction motor including magnetic saturation and iron losses," *IEEE Transactions on Industry Applications*, vol. 55, no. 4, pp. 3453–3468, 2019.

[112] Bojoi, R., Lazzari, M., Profumo, F., and Tenconi, A., "Digital field-oriented control for dual three-phase induction motor drives," *IEEE Transactions on Industry Applications*, vol. 39, no. 3, pp. 752–760, 2003.

[113] Bojoi, R., Farina, F., Griva, G., Profumo, F., and Tenconi, A., "Direct torque control for dual three-phase induction motor drives," *IEEE Transactions on Industry Applications*, vol. 41, no. 6, pp. 1627–1636, 2005.

[114] Levi, E., Bojoi, R., Profumo, F., Toliyat, H., and Williamson, S., "Multiphase induction motor drives–a technology status review," *IET Electric Power Applications*, vol. 1, no. 4, pp. 489–516, 2007.

[116] Aghaali, H. and Ångström, H.-E., "A review of turbocompounding as a waste heat recovery system for internal combustion engines," *Renewable and sustainable energy reviews*, vol. 49, pp. 813–824, 2015.

[117] Alshammari, M., Alshammari, F., and Pesyridis, A., "Electric boosting and energy recovery systems for engine downsizing," *Energies*, vol. 12, no. 24, p. 4636, 2019.

[118] Pasini, G. et al., "Evaluation of an electric turbo compound system for si engines: A numerical approach," *Applied Energy*, vol. 162, pp. 527–540, 2016.

[119] Arsie, I., Cricchio, A., Pianese, C., Ricciardi, V., and De Cesare, M., "Evaluation of co2 reduction in si engines with electric turbo-compound by dynamic powertrain modelling," *IFAC-PapersOnLine*, vol. 48, no. 15, pp. 93–100, 2015.

[123] Kant, M., Romagnoli, A., Mamat, A. M., and Martinez-Botas, R. F., "Heavy-duty engine electric turbocompounding," *Proceedings of the Institution of Mechanical Engineers, Part D: Journal of Automobile Engineering*, vol. 229, no. 4, pp. 457–472, 2015.

[124] Cipollone, R., Di Battista, D., and Gualtieri, A., "Turbo compound systems to recover energy in ice," *Int. J. Eng. Innov. Technol*, vol. 3, no. 6, 2013.

[126] Pipitone, E., Caltabellotta, S., Sferlazza, A., and Cirrincione, M., "Hybrid propulsion efficiency increment through exhaust energy recovery - part 1: Radial turbine modelling and design," *Energies*, vol. 16, no. 3, p. 1030, 2023.

[127] Pipitone, E., Caltabellotta, S., Sferlazza, A., and Cirrincione, M., "Hybrid propulsion efficiency increment through exhaust energy recovery - part 2: Numerical simulation results," *Energies*, vol. 16, no. 5, p. 2232, 2023.

[128] Gerada, D., Huang, X., Zhang, C., Zhang, H., Zhang, X., and Gerada, C., "Electrical machines for automotive electrically assisted turbocharging," *IEEE Trans. on Mechatronics*, vol. 23, no. 5, pp. 2054–2065, 2018.

[129] Consoli, A., Scarcella, G., and Testa, A., "Slip-frequency detection for indirect field-oriented control drives," *IEEE Trans. on Industry Applications*, vol. 40, no. 1, pp. 194–201, 2004.

[130] Qian, W., Panda, S. K., and Xu, J.-X., "Torque ripple minimization in pm synchronous motors using iterative learning control," *IEEE Trans. on power electronics*, vol. 19, no. 2, pp. 272–279, 2004.

[131] Wang, B., Chen, X., Yu, Y., Wang, G., and Xu, D., "Robust predictive current control with online disturbance estimation for induction machine drives," *IEEE Trans. on Power Electronics*, vol. 32, no. 6, pp. 4663–4674, 2016.

[132] Kulkarni, S. and Thosar, A., "Mathematical modeling and simulation of permanent magnet synchronous machine," *International Journal of Electronics and Electrical Engineering*, vol. 1, no. 2, pp. 66–71, 2013.

[134] Liang, D., Li, J., Qu, R., and Kong, W., "Adaptive second-order sliding-mode observer for pmsm sensorless control considering vsi nonlinearity," *IEEE Trans. on Power Electronics*, vol. 33, no. 10, pp. 8994–9004, 2017.

[135] Qiao, Z., Shi, T., Wang, Y., Yan, Y., Xia, C., and He, X., "New sliding-mode observer for position sensorless control of permanent-magnet synchronous motor," *IEEE Trans. on Industrial electronics*, vol. 60, no. 2, pp. 710–719, 2012.

[136] Wang, Z., Lu, K., and Blaabjerg, F., "A simple startup strategy based on current regulation for back-emf-based sensorless control of pmsm," *IEEE Trans. on Power Electronics*, vol. 27, no. 8, pp. 3817–3825, 2012.

[137] Alonge, F., Cirrincione, M., Pucci, M., and Sferlazza, A., "Input–output feedback linearization control with on-line mras-based inductor resistance estimation of linear induction motors including the dynamic end effects," *IEEE Trans. on Industry Applications*, vol. 52, no. 1, pp. 254–266, 2015.

[140] Kivanc, O. C. and Ozturk, S. B., "Sensorless pmsm drive based on stator feedforward voltage estimation improved with mras multiparameter estimation," *IEEE Trans. on Mechatronics*, vol. 23, no. 3, pp. 1326–1337, 2018.

[142] Rasvan, V., "Popov theories and qualitative behavior of dynamic and control systems," *European journal of control*, vol. 8, no. 3, pp. 190–199, 2002.

Italian Journal Articles

[3] Goebel, R., Sanfelice, R., and Teel, A., *Hybrid dynamical systems: Modeling, stability, and robustness. 41 william street*, 2012.

International Conference Proceedings

[18] Hespanha, J. P. and Morse, A. S., "Stability of switched systems with average dwell-time," in *Proceedings of the 38th IEEE conference on decision and control (Cat. No. 99CH36304)*, IEEE, vol. 3, 1999, pp. 2655–2660.

[21] Morse, A., "Supervisory control of families of linear set-point controllers," in *Proceedings of 32nd IEEE Conference on Decision and Control*, IEEE, 1993, pp. 1055–1060.

[27] Redl, R. and Sokal, N. O., "Current-mode control, five different types, used with the three basic classes of power converters: Small-signal ac and large-signal dc characterization, stability requirements, and implementation of practical circuits," in *1985 IEEE Power Electronics Specialists Conference*, IEEE, 1985, pp. 771–785.

[35] Albea, C., Garcia, G., and Zaccarian, L., "Hybrid dynamic modeling and control of switched affine systems: Application to dc-dc converters," in *2015 54th IEEE Conference on Decision and Control (CDC)*, IEEE, 2015, pp. 2264–2269.

[37] Sortomme, E. and El-Sharkawi, M., "Optimal power flow for a system of microgrids with controllable loads and battery storage," in *2009 IEEE/PES Power Systems Conference and Exposition*, IEEE, 2009, pp. 1–5.

[43] Li, Z., Onar, O., Khaligh, A., and Schaltz, E., "Design and control of a multiple input dc/dc converter for battery/ultra-capacitor based electric vehicle power system," in *2009 Twenty-Fourth Annual IEEE Applied Power Electronics Conference and Exposition*, IEEE, 2009, pp. 591–596.

[44] Di Napoli, A., Crescimbini, F., Capponi, F. G., and Solero, L., "Control strategy for multiple input dc-dc power converters devoted to hybrid vehicle propulsion systems," in *Industrial electronics, 2002. isie 2002. proceedings of the 2002 ieee international symposium on*, IEEE, vol. 3, 2002, pp. 1036–1041.

[46] Zaccarian, L., "On dynamic control allocation for input-redundant control systems," in *2007 46th IEEE Conference on Decision and Control*, IEEE, 2007, pp. 1192–1197.

[48] Sira-Ramirez, H., "Flatness and trajectory tracking in sliding mode based regulation of dc-to-ac conversion schemes," in *Proceedings of the 38th IEEE Conference on Decision and Control (Cat. No. 99CH36304)*, IEEE, vol. 5, 1999, pp. 4268–4273.

[49] Caceres, R. and Barbi, I., "A boost dc-ac converter: Operation, analysis, control and experimentation," in *Proceedings of IECON'95-21st Annual Conference on IEEE Industrial Electronics*, IEEE, vol. 1, 1995, pp. 546–551.

[68] Middlebrook, R. D. and Cuk, S., "A general unified approach to modelling switching-converter power stages," in *1976 IEEE power electronics specialists conference*, IEEE, 1976, pp. 18–34.

[84] Gao, Z., Huang, Y., and Han, J., "An alternative paradigm for control system design," in *Decision and Control, 2001. Proceedings of the 40th IEEE Conference on*, IEEE, vol. 5, 2001, pp. 4578–4585.

[88] Zhou, X., Cui, H., Ma, Y., and Gao, Z., "The research on energy conservation controller for asynchronous motor based on adrc," in *2017 29th Chinese Control And Decision Conference (CCDC)*, IEEE, 2017, pp. 4010–4014.

[99] Bojoi, R., Caponet, M. C., Grieco, G., Lazzari, M., Tenconi, A., and Profumo, F., "Computation and measurements of the dc link current in six-phase voltage source pwm inverters for ac motor drives," in *Proceedings of the Power Conversion Conference-Osaka 2002 (Cat. No. 02TH8579)*, IEEE, vol. 3, 2002, pp. 953–958.

[102] Ferraris, P. and Lazzari, M., "Phase numbers and their related effects on the characteristics of inverter fed induction motor, drives," in *1983 Annual Meeting Industry Applications Society*, IEEE, 1983, pp. 494–502.

[106] Ward, E. and Härer, H., "Preliminary investigation of an invertor-fed 5-phase induction motor," in *Proceedings of the Institution of Electrical Engineers*, IET, vol. 116, 1969, pp. 980–984.

[108] Lipo, T., "A dq model for six phase induction machines," in *Conf. Rec. ICEM'80*, 1980.

[122] Mohd Noor, A., Che Puteh, R., Rajoo, S., Basheer, U. M., Md Sah, M. H., and Shaikh Salleh, S. H., "Simulation study on electric turbo-compound (etc) for thermal energy recovery in turbocharged internal combustion engine," in *Applied Mechanics and Materials*, vol. 799, 2015, pp. 895–901.

[133] Morimoto, S., Kawamoto, K., Sanada, M., and Takeda, Y., "Sensorless control strategy for salient-pole pmsm based on extended emf in rotating reference frame," in *IEEE Industry Applications Conference*, IEEE, vol. 4, 2001, pp. 2637–2644.

[138] Cirrincione, M., Pucci, M., Sferlazza, A., and Vitale, G., "Neural based mras sensorless techniques for high performance linear induction motor drives," in *IECON - Annual Conference on IEEE Industrial Electronics Society*, IEEE, 2010, pp. 918–926.

[139] Kojabadi, H. M. and Ghribi, M., "Mras-based adaptive speed estimator in pmsm drives," in *IEEE International Workshop on Advanced Motion Control*, IEEE, 2006, pp. 569–572.

[141] Kim, Y. S., Kim, S. K., and Kwon, Y. A., "Mras based sensorless control of permanent magnet synchronous motor," in *SICE - Annual Conference*, IEEE, vol. 2, 2003, pp. 1632–1637.

Introduction

Chapter 1

Introduction

1.1 Motivation

Dynamical systems represent a fundamental tool for modeling and analyzing a wide variety of physical and engineering phenomena. Traditionally, such systems are classified as either continuous-time, when describing the evolution of physical variables, or discrete-time, when dealing with digital processes. However, in many modern applications, relying on only one of these modeling frameworks does not fully capture the complexity of the considered systems. This is the case, for example, for digitally controlled physical systems, or continuous-time systems that are subject to abrupt changes in some of their states, like systems subject to impact, which introduce instantaneous changes in their velocity. The most effective tool for characterizing the dynamics of such systems is the hybrid dynamical systems framework, where differential and difference equations, referred to as flows and jumps, respectively, are combined in the same dynamics, allowing for both continuous-time and discrete-time evolution of the state. Closely related to this framework is the class of switched systems, where the evolution of the state is determined by the interaction of multiple subsystems and the switching signal that selects them. Unlike hybrid systems, which explicitly combine flows and jumps, switched systems emphasize the role of switching among different continuous-time dynamics, which may lead to rich and complex behaviors. Both frameworks are essential for the analysis and control of modern engineering systems, particularly in the context of power electronics and electrical drives, where continuous physical dynamics interact with discrete technologies such as switches, logic circuits, and digital controllers. They enable improved performance, robustness, and flexibility compared to classical continuous-time control. The study of these classes of systems has attracted growing attention over the years, both for their theoretical significance, concerning modeling, stability, and solution concepts, and for their practical relevance in automatic control and power electronics (see, e.g., [1] for hybrid systems and [2] for switched systems). In [1], the authors introduce rigorous definitions of the modeling framework and the concept of solution to a nonlinear hybrid dynamical system, providing numerous Lyapunov-based results to assess its stability properties. In [2], the author provides a comprehensive treatment of switched systems, presenting their classification, fundamental solution concepts, and stability analysis tools, with particular emphasis on Lyapunov methods and dwell-time conditions. The theoretical investigation of hybrid and switched systems has been largely motivated by their relevance in real applications. Indeed, these frameworks are particularly suitable for describing engineering

systems where continuous-time physical dynamics interact with man-made technologies such as switches, logic variables, or digital controllers such as timers, sample-and-hold, or memory elements. Moreover, hybrid and switched frameworks naturally support dynamic allocation strategies, in which control effort or energy resources are adaptively distributed among multiple actuators or inputs to enhance system performance, robustness, and efficiency. From a theoretical standpoint, dynamic allocation represents a fundamental advancement toward achieving adaptive and optimal control, where system inputs are not statically assigned but continuously reallocated based on operating conditions and performance objectives. This approach integrates hybrid control theory with optimization and resource management, enabling the development of controllers capable of real-time adaptation in multi-source or multi-actuator systems. This is especially true in power electronics, where discontinuities, multiple operating modes, and digital control strategies naturally arise. In such systems, dynamic allocation of inputs or power sources provides a systematic approach to coordinate multiple operating modes and control channels, ensuring robust voltage and current regulation while adapting to varying loads or source conditions. Within this context, dynamic allocation can be interpreted as a hierarchical coordination mechanism that continuously analyzes system states, external disturbances, and performance objectives to optimally adjust the contribution of each actuator or power source. This approach enables the control system to leverage structural redundancies and inherent system flexibilities, maintaining stability and ensuring high performance under dynamic operating conditions. Within hybrid and switched frameworks, dynamic allocation coordinates both continuous control actions and discrete switching events, ensuring consistent interactions among subsystems. In power electronics applications, such as multi-input converters and multi-phase drives, this methodology provides a rigorous, adaptive approach for energy management, loss minimization, and fault-tolerant operation, enhancing efficiency, robustness, and reliability. In this context, hybrid and switched control architectures can overcome the limitations of classical continuous-time controllers and provide improved performance, robustness, and flexibility.

1.2 Thesis overview

This thesis investigates the modeling and control of hybrid and switched dynamical systems, with a particular focus on applications in power electronics and electrical drives. The aim is to demonstrate how hybrid and switched system tools can improve both the modeling accuracy and the performance of control strategies for complex engineering systems. The thesis is organized into three main parts: theoretical foundations, power electronic applications, and electrical drive applications.

- **Part I: Theoretical Foundations of Hybrid and Switched Systems**
  The first part provides a comprehensive theoretical background on hybrid and switched dynamical systems and is divided into two chapters:

  - **Chapter 2 - Hybrid dynamical systems**: This chapter introduces the modeling framework of hybrid systems, where continuous-time and discrete-time dynamics are combined through flows and jumps. Key concepts such as the notion of solution, stability properties, and illustrative examples are discussed. The chapter concludes with remarks on the significance of hybrid systems for modern engineering applications.
  - **Chapter 3 - Switched systems**: This chapter focuses on switched systems, in which the system's evolution is determined by switching among multiple continuous-time subsystems. The chapter covers classification, solution concepts, stability analysis, and the interconnection between switched and hybrid systems. A summary of practical motivations for applications concludes the chapter.

- **Part II: Applications in Power Electronics**
  The second part focuses on practical applications of hybrid control strategies in power electronic systems. This part is structured around three case studies:

  - **Chapter 4 - Min-type hybrid control strategy of DC-DC boost converters**: A min-type hybrid control approach is presented for synchronous DC-DC boost converters. This chapter includes dynamic modeling, the design of the min-type hybrid control law, hysteresis-based control, stability analysis, and performance considerations. Experimental setup and results illustrate the advantages of the proposed strategy in terms of robustness and dynamic performance.
  - **Chapter 5 - Hybrid control strategy of multi-input converters using dynamic input allocation**: This chapter addresses the control of a multi-input converter with overactuation. A dynamic input allocation strategy is proposed to achieve decoupled current regulation and enhanced stability. The chapter includes a detailed description of the converter circuit, dynamic modeling, equilibrium characterization, and simulation results demonstrating the effectiveness of the proposed hybrid control approach.
  - **Chapter 6 - Advanced nonlinear robust control of a DC/AC differential boost inverter with active disturbance compensation and sliding mode component**: A hybrid control approach is applied to a DC/AC differential boost inverter, integrating active disturbance compensation and a sliding-mode component. The chapter covers the dynamic modeling of the inverter, control problem formulation, design of the control algorithm, and both simulation and experimental validation. Performance evaluation demonstrates improved robustness and control accuracy compared to state-of-the-art strategies.

- **Part III: Applications in Electric Drives**
  The third part applies hybrid and switched system techniques to electrical drives,

highlighting their applicability beyond power converters. This part is organized around three case studies:

- **Chapter 7 - Adaptive robust nonlinear control strategies for high-performance induction motor drives**: This chapter presents a nonlinear robust control strategy for induction motors, including adaptive disturbance compensation to enhance robustness under parameter variations and external disturbances.
- **Chapter 8 - Dual-three-phase induction motor control for harmonic losses reduction using dynamic input allocation**: A dynamic input allocation approach is proposed to reduce harmonic losses in dual-three-phase induction motors, achieving decoupled control of multiple phases while maintaining overall system stability and performance.
- **Chapter 9 - Sensorless control strategies for high-speed permanent magnet synchronous motor in exhaust energy recovery**: This chapter investigates sensorless control techniques for permanent magnet synchronous motors, comparing Kalman filter and MRAS observer approaches in the context of energy recovery applications.

These three applications illustrate the practical relevance and flexibility of hybrid and switched system frameworks for modern power electronics, showing how theoretical tools can be effectively applied to improve performance, robustness, and control flexibility.

Part I
Theoretical Foundations of Hybrid Systems and Switched Systems

Chapter 2

Hybrid dynamical systems

Abstract

Dynamic systems are traditionally classified as either continuous-time or discrete-time dynamical systems, depending on whether their evolution is governed by differential or difference equations. These two classes of systems have been extensively studied in the literature, though as separate and distinct domains. However, many real-world systems inherently involve both continuous and discrete dynamics. Examples include digitally controlled mechanical devices, cyber-physical systems, and electronic circuits integrating analog and digital components. In such a case, modeling the system using purely differential or purely difference equations proves insufficient. Scenarios involving impacts, mode switching, logic-based control, or event-triggered updates require a formalism capable of capturing both types of behavior within a unified framework. Hybrid dynamical systems provide such a framework by combining continuous flows with discrete jumps, allowing for the accurate modeling and analysis of systems with interacting physical and logical components.

Contents

2.1 Introduction

Many dynamical systems combine behaviors that are typical of continuous-time dynamical systems with behaviors that are typical of discrete-time dynamical systems [3], [4]. For example, in a switched electrical circuit, voltages and currents that change continuously according to classical electrical network laws also change discontinuously due to switches opening or closing [2]. Some biological systems behave similarly, with continuous change during normal operation and discontinuous change due to an impulsive stimulus [5]. Similarly, velocities in a multibody system change continuously according to Newton's second law but undergo instantaneous changes in velocity and momentum due to collisions [6]. Embedded systems and, more generally, systems involving both digital and analog components form another class of examples [7]. Modern control algorithms often lead to both kinds of behavior, due to either digital components used in implementation or logic and decision-making encoded in the control algorithm [8]. These examples belong to the class of hybrid dynamical systems, or simply hybrid systems [9]. Hybrid dynamical systems represent a powerful tool in the context of systems analysis because of their capability to model a broad class of systems. The interaction of continuous and discrete time dynamics in a hybrid system leads to rich dynamical behavior and phenomena not encountered in purely continuous-time systems [3], [10]. Consequently, several challenges are encountered on the path to a stability theory for hybrid systems and to a methodology for robust hybrid control design [11]. Beyond these behavioral aspects, modeling hybrid systems also presents important challenges. Dynamical systems are beyond the descriptive power of common modeling tools for continuous-time dynamical systems, such as differential equations, and common modeling tools for discrete-time dynamical systems, such as difference equations. For example, standard differential equations cannot describe changes in a logical variable that can only take on the values of 0 and 1. Hence, differential equations on their own are not able to model a continuous-time system controlled by an algorithm involving logic. However, such a closed-loop system may be modeled through a combination of differential and difference equations. Another opportunity for combining the modeling tools for continuous-time and discrete-time dynamical systems comes in describing changes in a dynamical system that occur at different rates. For example, in a mechanical system with impacts, the evolution of velocities during a collision can be modeled as instantaneous changes. Difference equations can model such discrete events, and differential equations can describe the behavior between collisions [1]. While some concepts of generalized differential equations, involving time scales or measures that are not continuous, may treat such situations, a control theorist may find advantages in using the more familiar combination of difference and differential equations. In this thesis, the theoretical framework of hybrid dynamical systems is applied to the study and control of practical engineering problems, with a particular focus on power converters. These case studies demonstrate how hybrid system models facilitate the analysis and design of

systems where continuous and discrete dynamics interact in complex ways. The following sections present the mathematical modeling approach, solution concept, and sufficient conditions for the stability of hybrid dynamical systems.

2.2 Modeling framework of hybrid systems

The model of a hybrid dynamical system can be represented in the following form:

$$\mathcal{H} \quad \begin{cases} x \in \mathcal{C} & \dot{x} \in F(x) \\ x \in \mathcal{D} & x^+ \in G(x). \end{cases} \tag{2.1}$$

This modeling framework follows the approach introduced in [3]. Another common representation involves equations instead of set-valued mappings and differential or difference inclusions:

$$\mathcal{H} \quad \begin{cases} x \in \mathcal{C} & \dot{x} = f(x) \\ x \in \mathcal{D} & x^+ = g(x). \end{cases} \tag{2.2}$$

This representation suggests that the state of the hybrid system, represented by x, can change according to a differential inclusion $\dot{x} \in F(x)$ or a differential equation $\dot{x} = f(x)$ while in the set $\mathcal{C}$. It can change according to a difference inclusion $x^+ \in G(x)$ or difference equation $x^+ = g(x)$ while in the set $\mathcal{D}$. The notation $\dot{x}$ represents the velocity of the state x, while x^+ represents the value of the state after an instantaneous change. To simplify the terminology, the behavior of a dynamical system that a differential equation or inclusion can describe is referred to as flow. The behavior of a dynamical system that a difference equation or inclusion can describe is referred to as a jump. This leads to the following names for the four objects involved in (2.1) or (2.2):

- $\mathcal{C}$ is the flow set (where solutions are allowed to evolve continuously);
- f (or F) is the flow map (how the state changes along a flowing solution);
- $\mathcal{D}$ is the jump set (where solutions are allowed to evolve discretely);
- g (or G) is the jump map (how the state changes across jumping solutions).

As a model in (2.1) or (2.2) suggests, the flow set, the flow map, the jump set, and the jump map can be specialized to capture the dynamics of purely continuous-time or discrete-time systems on $\mathbb{R}^n$. The control of a continuous-time system with state feedback often faces both practical and theoretical challenges. For example, precise information about the state may not be available at all times due to sensor delay, quantization, or communication constraints. Moreover, system performance may be very sensitive to errors in the state measurements, or satisfactory performance of the closed-loop system may not be achievable by using just one state-feedback controller. These issues motivate the use of hybrid control strategies that combine continuous and discrete dynamics to improve robustness and flexibility.

2.3 Examples and application

This section presents concrete examples that demonstrate how the hybrid systems modeling framework can be applied across different contexts. The examples include real-world applications in science and engineering, specific control system scenarios, and systems characterized by explicit discrete or logical states. These cases highlight the interaction between continuous and discrete dynamics and illustrate the flexibility and practical applicability of hybrid system models.

2.3.1 Hybrid systems in science and engineering

Many mechanical systems naturally exhibit impacts, where instantaneous changes in velocity or momentum occur [6]. Examples include walking robots, colliding billiard balls, Newton's cradle, and even a simple bouncing ball. Between impacts, these systems evolve according to continuous dynamics. However, each impact can be approximated as instantaneous and hence leads to jumps in the state of the system. Consequently, systems with impacts can be viewed as hybrid systems. A classic example is the bouncing ball, which will be analyzed in the following.

Example 2.3.1 (*Bouncing ball*)

Consider a point mass bouncing vertically on a horizontal surface. Between impacts, the point mass evolves continuously under the acceleration of gravity. At impact, when the point mass hits the surface, the velocity changes instantaneously, reversing direction and possibly decreasing in magnitude due to energy dissipation. This effect can be easily represented using the hybrid framework 2.1, where the state of the point mass is described by:

$$x = \begin{bmatrix} x_1 \\ x_2 \end{bmatrix} \in \mathbb{R}^2,$$

where x_1 represents the height above the surface, and x_2 the vertical velocity. The flow condition is possible when the point mass is above the surface, or when it is on the surface with non-negative velocity. Hence, the flow set is:

$$\mathcal{C} = \{x \in \mathbb{R}^2 : x_1 > 0 \text{ or } x_1 = 0,\ x_2 \geq 0\}.$$

The flow map is naturally defined as:

$$f(x) = \begin{bmatrix} x_2 \\ -\gamma \end{bmatrix} \quad \text{when } x_1 > 0 \text{ or } x_1 = 0,\ x_2 > 0,$$

where $-\gamma$ is the acceleration due to gravity. At point $x = 0$, it is natural to set $f(0) = 0$. The resulting flow map f is not continuous at 0. Impacts happen when the point mass is on the surface with negative velocity. Hence, the jump set is:

$$\mathcal{D} = \{x \in \mathbb{R}^2 :\ x_1 = 0,\ x_2 < 0\}.$$

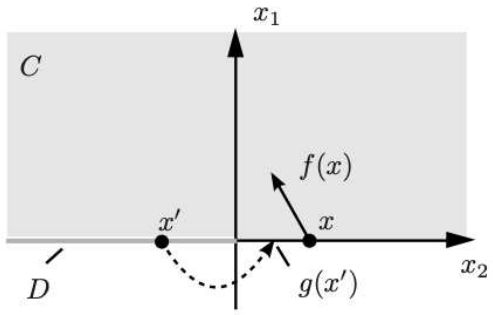

Figure 2.1: Flow and jump sets for the bouncing ball system.

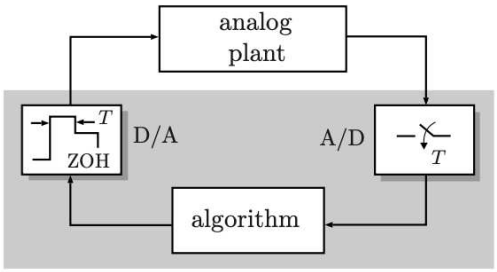

Figure 2.2: Digital control of a continuous-time nonlinear system with sample-and-hold devices.

The jump map, for some $\lambda \in (0, 1)$, is:

$$g(x) = \begin{bmatrix} 0 \\ -\lambda x_2 \end{bmatrix}.$$

A suitable extension is $g = -\lambda x$, which coincides with the jump map on the set $\mathcal{D}$. □

Fig. 2.1 illustrates the flow and jump sets defined for the bouncing ball system. Continuous flows follow each jump; consecutive jumps do not occur. This example illustrates how hybrid systems capture the interaction between continuous dynamics, driven by gravity, and discrete jumps, which represent instantaneous changes in velocity at impacts.

2.3.2 Control system examples

The control of a continuous-time system with state feedback presents both practical and theoretical challenges [12]. Precise state information may not always be available continuously, even when frequent measurements of the state are available. Moreover, the closed-loop system's performance can be highly sensitive to measurement errors, and achieving satisfactory control using a single state-feedback controller may not always be possible. These difficulties motivate the use of hybrid control strategies that combine continuous dynamics with discrete events such as sampling and control updates.

Example 2.3.2 (*Sample-and-hold control*)

Consider a continuous-time control system regulated by a state-feedback controller, which associates a control input to each system state. A common implementation of this controller in digital hardware uses a sample-and-hold strategy, described as

follows:

- *Sample: measure the current state of the system and compute the control input using the feedback controller based on the measurements;*
- *Hold: apply the computed control input as a constant value over a fixed time interval.*

This procedure is repeated indefinitely at regular sampling times. The processing of sampling and computing the control can be modeled as an instantaneous event. This leads to a continuous behavior of the closed-loop system between sampling times, according to the continuous-time dynamics of the control system and the constant value of the control, and an instantaneous change at every sampling time, when the control value is instantly updated. A schematic example of a sample-and-hold control system, where a digital device controls an analog plant, is shown in Fig. 2.2. The analog plant output is sampled by an analog-to-digital (A/D) converter; the digital controller computes the control action, which is then converted to an analog signal via a digital-to-analog (D/A) converter. For periodic sampling and zero-order hold (ZOH) implementation, sampling and control update events occur at a fixed sampling period T. To model this sample-and-hold closed-loop system within the hybrid system framework, consider its continuous-time dynamics:

$$\dot{z} = \bar{f}(z, u), \tag{2.3}$$

where $z \in \mathbb{R}^{n_p}$ in the state of the system, $u \in \mathbb{R}^{n_c}$ is the control variable, and $\bar{f} : \mathbb{R}^{n_p} \times \mathbb{R}^{n_c} \to \mathbb{R}^{n_p}$ is a function. Let the state-feedback controller be given by $u = k(z)$. The standard closed-loop, without a sample-and-hold strategy, leads to a continuous-time closed-loop system:

$$\dot{z} = \bar{f}(z, k(z)).$$

In the sample-and-hold implementation, the control input is updated only at discrete sampling times and maintained constant in between. Define the hybrid state as:

$$x = \begin{bmatrix} z \\ u \\ \tau \end{bmatrix} \in \mathbb{R}^{n_p+n_c+1},$$

where τ is a timer variable tracking the elapsed time since the last sampling instant. Suppose that the sampling period is T.

- *Flow occurs when the timer variable τ evolves continuously over the intervals $[0, T)$. During flow, the variable u remains constant, τ keeps track of elapsed time, and the state of the plant z evolves according to the dynamics in (2.3). Thus, the flow set and the flow map are:*

$$\mathcal{C} = \mathbb{R}^{n_p} \times \mathbb{R}^{n_c} \times [0, T), \quad f(x) = \begin{bmatrix} \bar{f}(x, u) \\ 0 \\ 1 \end{bmatrix}.$$

- *Jumps occur when the timer variable reaches T. At jumps, the variable u is updated to $k(z)$, the timer is reset to 0, and the state of the plant does not change. Hence, the jump set and the jump map are:*

$$\mathcal{D} = \mathbb{R}^{n_p} \times \mathbb{R}^{n_c} \times T, \quad g(x) = \begin{bmatrix} z \\ k(z) \\ 0 \end{bmatrix}.$$

This hybrid formulation captures the interaction between continuous-time plant dynamics and discrete-time control updates, enabling rigorous analysis of stability and robustness properties of sampled-data control systems. □

2.3.3 Modeling systems with explicit discrete state or logical modes

The state in many hybrid systems can be decomposed into a continuous and a discrete state. The discrete state takes values in a discrete, often finite, set and represents the mode in which the system, or part of it, operates (e.g., on/off, gear selection, or active controller). The discrete state, by its nature, can change only via a jump. The continuous state can change via flow and, sometimes, via a jump too. It may represent position, velocity, and other continuous-valued variables. For example, in a temperature control system, a discrete state can indicate whether a thermostat is on or off, while a continuous state can indicate the temperature. In such a case, the continuous state may not change via a jump. Suppose the discrete state represents whether a connection in an electrical circuit is open or closed, and the continuous variable represents the current in some part of the circuit. In that case, it may be natural to allow for instantaneous changes in the continuous variable that are simultaneous with changes in the discrete variable. A system with continuous and discrete states usually can be represented by a set $\mathcal{Q} = \{1, 2, ..., q_{max}\}$, and for each $q \in \mathcal{Q}$, a flow set $\mathcal{C}_q \subset \mathbb{R}^n$, a flow map $F_q : \mathbb{R}^n \rightrightarrows \mathbb{R}^n$, a jump set $\mathcal{D}_q \subset \mathbb{R}^n$, and a jump map $G_q : \mathbb{R}^n \rightrightarrows \mathcal{Q} \times \mathbb{R}^n$ [3], [7]. Such a system can be represented, analogously to (2.1), as follows:

$$\begin{cases} z \in \mathcal{C}_q & \dot{z} \in F_q(z) \\ z \in \mathcal{D}_q & (q, z)^+ \in G_q(z). \end{cases} \tag{2.4}$$

When $q = q^* \in \mathcal{Q}$ and $z \in \mathcal{C}_{q^*}$ flow occurs according to $\dot{z} \in F_{q^*}(z)$, with q constant. The condition $\dot{q} = 0$ is not explicitly mentioned in (2.4). When the discrete variable has the value $q^* \in \mathcal{Q}$ and the continuous variable z is in the jump set $\mathcal{D}_{q^*}$, a jump is possible, with both q and z changing values according to G_{q^*}. For a system where the continuous variable does not change via jumps, the inclusion $(q, z)^+ \in G_q(z)$ can be replaced by the simpler $q^+ \in G_q(z)$, in which case the equation $z^+ = z$ is usually not mentioned explicitly.

System (2.4) can be formulated in the form (2.1) by taking $x = \begin{bmatrix} q & z \end{bmatrix}^\top \in \mathbb{R}^{n+1}$, and

$$\mathcal{C} = \bigcup_{q \in \mathcal{Q}} (\{q\}) \times \mathcal{C}_q \quad F(x) = (0, F_q(z)),$$
$$\mathcal{D} = \bigcup_{q \in \mathcal{Q}} (\{q\}) \times \mathcal{D}_q \quad G(x) = G_q(z). \tag{2.5}$$

The general framework described above can be illustrated by the classic thermostat

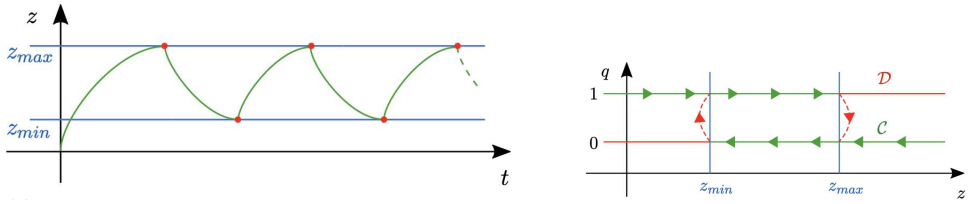

(a) (b)

Figure 2.3: (a) Temperature evolution as a function of continuous time t. (b) State-space representation.

control problem, where the temperature evolves continuously while the heater switches on and off discretely according to hysteresis logic.

Example 2.3.3 (*Thermostat control*)

Consider a thermostat regulating room temperature via a heater controlled by a discrete logic variable $q \in \{0, 1\}$. The system naturally forms a hybrid dynamical system since the continuous temperature evolves under differential dynamics depending on whether the heater is on or off, while discrete jumps in q occur when temperature thresholds are crossed, switching the heater state accordingly. This mechanism turns the heater on ($q^+ = 1$) when the temperature $z \in \mathbb{R}$ is smaller than a given z_{min}, and turns it off ($q^+ = 0$) when the temperature z exceeds an upper threshold z_{max}. The state of the system is given by $x = (z, q) \in \mathbb{R} \times \{0, 1\}$, and the state space can be represented by two lines, as shown in Fig. 2.3. The temperature evolves continuously, and its dynamics can be modeled as a differential equation $\dot{z} = \bar{f}(z, q)$. Under the assumption that the heater is well dimensioned, this function satisfies the following properties:

- *$\bar{f}(z, 1) > 0$ for $z \leq z_{max}$, meaning that the temperature increase when the heater is on;*
- *$\bar{f}(z, 0) < 0$ for $z \geq z_{min}$, indicating that the temperature decreases when the heater is off due to natural cooling.*

Instead, the heater state q changes instantaneously according to the hysteresis logic described above. These transitions occur only at discrete jump events. This leads to a hybrid system formulation, with continuous evolution for the temperature and discrete transitions for the heater state:

$$\dot{x} = \begin{bmatrix} \dot{z} \\ \dot{q} \end{bmatrix} = f(x) := \begin{bmatrix} \bar{f}(z, q) \\ 0 \end{bmatrix},$$

$$
\begin{aligned}
x \in \mathcal{C} &:= \{(z,q) : q = 0, z \geq z_{min}\} \cup \{(z,q) : q = 1, z \leq z_{max}\}, \\
x^+ = \begin{bmatrix} z^+ \\ q^+ \end{bmatrix} &= g(x) := \begin{bmatrix} z \\ 1-q \end{bmatrix}, \\
x \in \mathcal{D} &:= \{(z,q) : q = 0, z \leq z_{min}\} \cup \{(z,q) : q = 1, z \geq z_{max}\}. \qquad (2.6)
\end{aligned}
$$

Fig. 2.3 illustrates a typical solution trajectory of the described hybrid system. Initially, the temperature satisfies $z < z_{min}$ and the heater is active ($q = 1$). In this configuration, the system evolves continuously (flows) with the heater on, causing the temperature to increase until it reaches the upper threshold z_{max}. Once z reaches z_{max}, the solution cannot flow anymore, as the condition for flowing is no longer satisfied. However, since this point lies within the jump set, a discrete transition occurs: the heater is switched off ($q^+ = 0$) and the system starts cooling down. Through this alternating mechanism of heating and cooling, the temperature z remains confined within the desired bounds $[z_{min},\ z_{max}]$, a closed and bounded interval, namely a compact set. The resulting behavior forms a hybrid limit cycle, i.e., a periodic solution trajectory that other trajectories converge either asymptotically or, as in this case, in finite time. □

2.4 Concept of solution for hybrid systems

After introducing the model and its fundamental properties, it is essential to formally define the concept of a solution for a hybrid system. While the previous sections referred to solutions informally, a formal definition is now introduced to unify continuous-time and discrete-time dynamics under a common framework. This unified notion is crucial for analyzing and simulating hybrid systems, where both flows (governed by differential equations) and jumps (governed by difference equations) coexist. To this end, the data specifying a hybrid system are defined, and a generalized concept of time is introduced, capturing both continuous evolution and discrete transitions. Solutions to a hybrid system are then defined, and basic properties of solutions, such as existence and uniqueness, are addressed.

- A solution ϕ to the discrete-time system $x^+ = g(x),\ x \in \mathbb{R}^n$ is a sequence, $j \to \phi(j) \in \mathbb{R}^n$, defined for all $j \in \mathbb{N} = \{0, 1, 2, ...\}$, such that $\phi(j+1) = g(\phi(j))$ for all $j \in \text{dom } \phi$.
- A solution ϕ to the continuous-time system $\dot{x} = f(x),\ x \in \mathbb{R}^n$ is an absolutely continuous function of $t \to \phi(t) \in \mathbb{R}^n$, defined for all $t \in \text{dom } \phi = [0, T)$, such that $\frac{d\phi(t)}{dt} = f(\phi(t))$ for almost all $t \in \text{dom } \phi$.

The concept of solution for a discrete-time system is simpler, as for any initial condition $\phi(0) \in \mathbb{R}^n$, the solution can be indefinitely extended by iteratively applying the continuous

function g. For continuous-time systems, the solution must be continuous so that, according to Lebesgue integrability theory, the function coincides with the integral of its derivative. Note that a continuous function $t \mapsto \phi(t)$ is not necessarily differentiable, but it is differentiable almost everywhere, that is, loosely speaking, its derivative $\frac{d}{dt}\phi(t)$ is well defined for all times t in its domain, except for several isolated points. For this reason, the definition of continuous-time solution only requires that $\frac{d\phi(t)}{dt} = f(\phi(t))$ for almost all t. As a final remark, the continuous-time solutions are not always defined for all positive times since they may exhibit finite escape time, where solutions diverge to infinity in finite time. As discussed in Section 2.2, hybrid systems combine continuous and discrete dynamics. Consequently, a solution to a hybrid system must exhibit both types of behaviours. Since solutions may evolve in both continuous and discrete time, their domain must capture both aspects. For this purpose, the so-called hybrid time domain is defined.

2.4.1 Hybrid time domains

To rigorously analyze hybrid systems, it is crucial to define the concept of the hybrid time domain, which captures the combined continuous and discrete evolution of the system.

Definition 2.4.1 (*Compact hybrid time domain*)

A compact hybrid time domain $\mathbb{E}$ is a subset of $\mathbb{R}_{\geq 0} \times \mathbb{N}$ such that:

$$\mathbb{E} = \bigcup_{j=0}^{J-1} (\underbrace{[t_j, t_{j+1}]}_{I^j} \times \{j\})$$

for a given finite sequence of times $0 = t_0 \leq t_1 \leq t_2 \leq ... \leq t_J$, where $t_1,\ t_2, ..., t_J$ are called jump times. □

This definition applies to solutions evolving over a bounded (hybrid) time interval. It can be naturally extended to characterize the hybrid time domain of a solution evolving forever, that is, a complete solution.

Definition 2.4.2 (*Hybrid time domain*)

A hybrid time domain $\mathbb{E}$ is a subset of $\mathbb{R}_{\geq 0} \times \mathbb{N}$ such that any truncation is a compact hybrid time domain. Specifically, for any $[T, J] \in \mathbb{E}$, the set $\mathbb{E} \cap ([0, T] \times 0, 1, ..., J)$ is a compact hybrid time domain. □

A set $\mathbb{E}$ is a compact hybrid time domain if it is a union of a finite sequence of intervals of the form $[t_j, t_{j+1}] \times \{j\}$, whereas $\mathbb{E}$ is a hybrid time domain if it is a union of a finite or infinite sequence of such intervals, where the last interval (if it exists) may be of the form $[t_j, T)$, whit T finite or $T = \infty$. Fig. 2.4 illustrates an example of a hybrid time domain $\mathbb{E}$ given by the sequence of times $0 = t_0 < t_1 < t_2 = t_3 < t_4$. Note that for every $(T, J) \in \mathbb{E}$, the set $\mathbb{E} \cap ([0, T] \times \{0, 1, ..., J\})$ is a compact hybrid domain. Hybrid time domains enjoy some interesting ordering properties. Since they are ordered collections of time intervals I^j wherein the last point of a previous interval coincides with the starting point of the

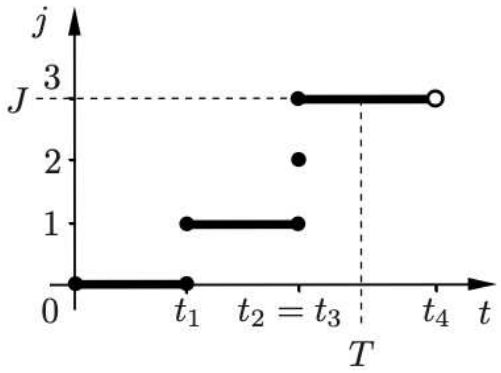

Figure 2.4: A hybrid time domain E.

next one, it always holds that for any $(t_1, j_1) \in \mathbb{E}$ and $(t_2, j_2) \in \mathbb{E}$ the following identities are true:

$$(t_2 > t_1) \Rightarrow j_2 \geq j_1, \quad (j_2 > j_1) \Rightarrow t_2 \geq t_1.$$

As a consequence, given any hybrid time domain $\mathbb{E} = \text{dom } \phi$ it is natural to associate with each $(t, j) \in \mathbb{E}$ the one-dimensional variable $t + j$, which is strictly increasing along any (continuous or discrete) evolution of $\phi(t, j)$. In the following, before providing the rigorous definition of a solution, it is useful to recall the data of the hybrid system.

2.4.2 Data of a hybrid system

A hybrid system is characterized by a mathematical model that defines how the system evolves through both continuous flows and discrete jumps. These two modes of evolution are governed by a structured set of elements, collectively referred to as the data of the hybrid system. This subsection introduces the formal definition of such data. Before defining the data of a hybrid system, the notion of a set-valued mapping is presented. A set-valued mapping from $\mathbb{R}^m$, or a subset S of $\mathbb{R}^m$, associates, with every point $x \in \mathbb{R}^m$, or every point $x \in S$, a subset of $\mathbb{R}^n$. This type of mapping is denoted using a double arrow, e.g., $M : \mathbb{R}^m \rightrightarrows \mathbb{R}^n$ or $M : S \rightrightarrows \mathbb{R}^n$, to distinguish it from standard single-valued functions.

Definition 2.4.3 (*Domain of a set-valued mapping*)

Given a set-valued mapping $M : \mathbb{R}^m \rightrightarrows \mathbb{R}^n$, the domain of M is the set

$$\text{dom } M = \{x \in \mathbb{R}^m : M(x) \neq \emptyset\}.$$

□

Definition 2.4.4 (*Data of a hybrid system*)

A hybrid system in $\mathbb{R}^n$ is described by the following four components:

- *a flow set $\mathcal{C} \subset \mathbb{R}^n$, which contains the state where continuous evolution (flow) is allowed;*

- *a set-valued mapping* $F : \mathbb{R}^n \rightrightarrows \mathbb{R}^n$ *with* $\mathcal{C} \subset \text{dom } F$*, called the flow map, which defines the possible directions of continuous evolution;*
- *a jump set* $\mathcal{D} \subset \mathbb{R}^n$*, which contains the state where a discrete transition (jump) may occur;*
- *a set-valued mapping* $G : \mathbb{R}^n \rightrightarrows \mathbb{R}^n$ *with* $\mathcal{D} \subset \text{dom } G$*, called the jump map, which determines the possible state after a jump.*

□

A hybrid system with the data as above will be represented by the notation $\mathcal{H} = (\mathcal{C}, F, \mathcal{D}, G)$ or, briefly, by $\mathcal{H}$. Based on the concept of hybrid time domain and the data of a hybrid system, the so-called hybrid arcs can be defined in the next subsection.

2.4.3 Hybrid arcs and trajectories

After introducing the data of a hybrid system, it is crucial to formalize the notion of solutions evolving along both continuous flows and discrete jumps. This is achieved through the concept of a hybrid arc, which generalizes trajectories by accounting for hybrid time domains.

Definition 2.4.5 (*Hybrid arc*)

A function $\phi : \mathbb{E} \to \mathbb{R}^n$ *is a hybrid arc if* $\mathbb{E}$ *is a hybrid time domain and if for each* $j \in \mathbb{N}$*, the function* $t \mapsto \phi(t, j)$ *is locally absolutely continuous on the interval* $I^j = \{t : (t, j) \in \mathbb{E}\}$. □

For a given hybrid arc ϕ, the notation dom ϕ represents its domain, which is a hybrid time domain. This notation aligns with the following set-valued interpretation of a hybrid arc. A hybrid arc ϕ can be defined as a set-valued mapping $\phi : \mathbb{R}^2 \rightrightarrows \mathbb{R}^n$ that is single-valued on its domain dom ϕ, i.e., the set of (t, j) where $\phi(t, j)$ is defined, which forms a hybrid time domain on which $t \mapsto \phi(t, j)$ is locally absolutely continuous for each fixed $j \in \mathbb{N}$. This interpretation is particularly important for solutions to hybrid systems, where it is generally inappropriate to prescribe an arbitrary hybrid time domain $\mathbb{E}$ and then determine a solution defined on it. Instead, one must find a solution ϕ and recognize that its domain is given by dom ϕ. Moreover, this approach facilitates the transfer of notions such as convergence and closeness from the set-valued analysis to the study of hybrid arcs and solutions of hybrid systems. Different classes of hybrid arcs are distinguished by the structure of their domains and the regularity of the associated trajectories. A hybrid arc ϕ is said to be:

- nontrivial if dom ϕ contains at least two points,
- complete if dom ϕ is unbounded, i.e., if length$(\mathbb{E}) = \infty$,
- Zeno if it is complete and $\sup_t \text{dom } \phi < \infty$,

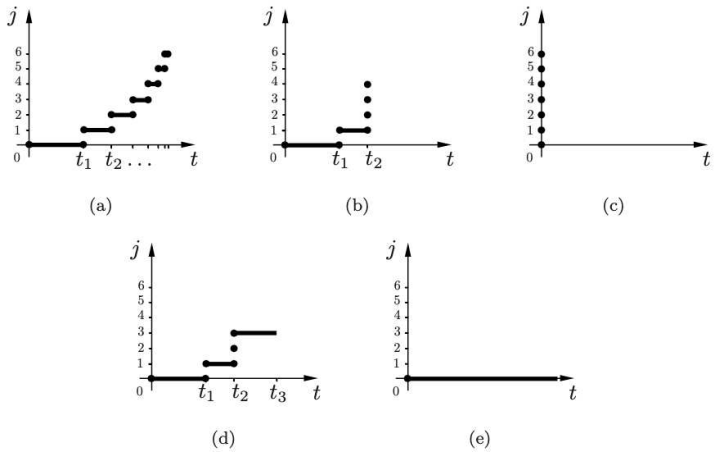

Figure 2.5: Hybrid time domains associated with various arc types: (a) Zeno, (b) eventually discrete, (c) discrete, (d) eventually continuous, and (e) continuous hybrid arcs.

- eventually discrete if $T = \sup_t \text{dom } \phi < \infty$ and dom $\phi \cap (\{T\} \times \mathbb{N})$ contains at least two points,
- discrete if nontrivial and dom $\phi \subset \{0\} \times \mathbb{N}$,
- eventually continuous if $J = \sup_j \text{dom}\phi < \infty$ and dom $\phi \cap (\mathbb{R}_{\geq 0} \times \{J\})$ contains at least two points,
- continuous if nontrivial and dom $\phi \subset \mathbb{R}_{\geq 0} \times \{0\}$,
- compact if dom ϕ is compact.

The hybrid time domains associated with some of the classes are illustrated in Figure 2.5. The definition of a hybrid arc is the last step before rigorously characterizing solutions to hybrid dynamical systems.

2.4.4 Definition of solution for a hybrid system

Consider a hybrid system $\mathcal{H} = (\mathcal{C}, F, \mathcal{D}, G)$. A solution is defined as a hybrid arc ϕ satisfying certain conditions determined by the hybrid time domain dom ϕ and the data of the hybrid system.

Definition 2.4.6 (*Solution to a hybrid system*)

A hybrid arc ϕ is a solution to the hybrid system $\mathcal{H} = (\mathcal{C}, F, \mathcal{D}, G)$ if $\phi(0,0) \in \overline{\mathcal{C}} \cup \mathcal{D}$, where $\overline{\mathcal{C}}$ denotes the closure of $\mathcal{C}$, i.e., the set $\mathcal{C}$ together with its boundary. The solution ϕ must satisfy:

- *for all $j \in \mathbb{N}$ such that $I^j := \{t : (t, j) \in \text{dom } \phi\}$ has nonempty interior*

$$\phi(t,j) \in \mathcal{C} \quad \text{for all} \quad t \in \text{int} I^j,$$
$$\dot{\phi}(t,j) \in F(\phi(t,j)) \quad \text{for almost all} \quad t \in I^j,$$

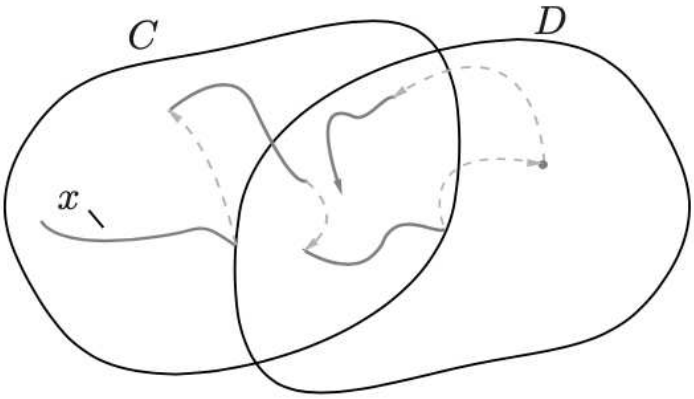

Figure 2.6: Evolution of a hybrid system solution.

- *for all* $(t, j) \in \text{dom } \phi$ *such that* $(t, j+1) \in \text{dom } \phi$,

$$\phi(t, j) \in \mathcal{D},$$
$$\phi(t, j+1) \in G(\phi(t, j)).$$

□

The solution to a hybrid dynamical system is formalized as a hybrid arc that is consistent with the system data. Definition 2.4.6 allows a broad range of behaviors: $\phi(t, j)$ is not required to remain in $\mathcal{C}$ at the boundaries of each interval I^j, nor it excluded that $\phi(t, j)$ may belong to the jump set $\mathcal{D}$ at interior points of I^j. As illustrated in Fig. 2.6, flow segments (solid curve) occur within $\mathcal{C}$, while jumps (dashed arcs) originate from $\mathcal{D}$. This solution concept captures both continuous-time and discrete-time dynamics. In particular, absolute continuity of the flow is only required for t within the flowing interval I^j. For compactness of notation, it is stated that $\phi(t, j) \in \mathcal{C}$ for almost all $t \in [t_1, t_2]$; when $\mathcal{C}$ is closed, this condition implies that $\phi(t, j) \in \mathcal{C}$ holds for all $t \in [t_1, t_2]$. When $\mathcal{C}$ is not closed, a solution may exit $\mathcal{C}$ at isolated points, which complicates the well-posedness of jumps and other properties. To avoid such issues, standard assumptions require $\mathcal{C}$ and $\mathcal{D}$ to be closed and the maps f and g to be continuous, ensuring robustness of the definitions. Moreover, since $\mathcal{C}$ and $\mathcal{D}$ may overlap, uniqueness of solutions is not guaranteed in general, although it can be established in simple cases (e.g., the bouncing ball). This motivates the use of Lyapunov-based analysis, which provides guarantees valid for all possible solutions. Furthermore, the state space defined by $\mathcal{C} \cup \mathcal{D}$ does not necessarily coincide with the entire $\mathbb{R}^n$, so some solutions may not evolve indefinitely once they leave this set. To formalize this situation, the notions of maximal and complete solutions are introduced.

Definition 2.4.7 (*Maximal and complete solutions*)

- *A solution* ϕ *to a hybrid system* $\mathcal{H}$ *is maximal if there exists no other solution* ψ *to* $\mathcal{H}$ *such that* dom ϕ *is a proper subset of* dom ψ *and* $\phi(t, j) = \psi(t, j)$ *for all*

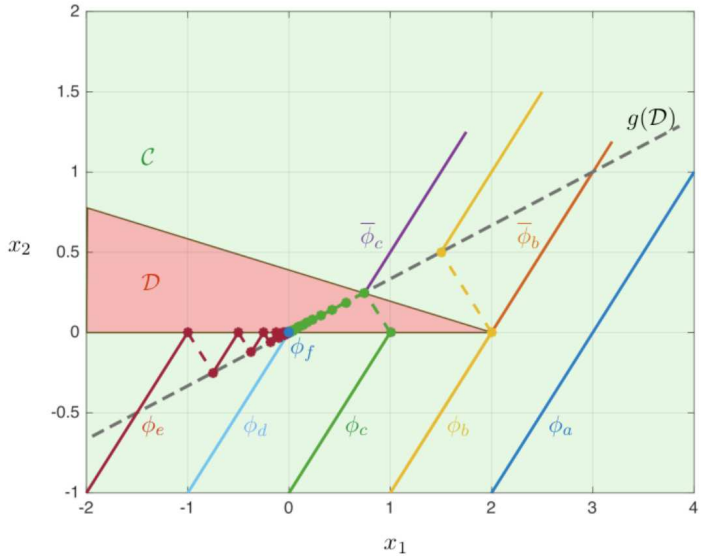

Figure 2.7: Solutions of Example 2.4.1 from different initial conditions in the phase plane. The red region represents the jump set $\mathcal{D}$, while the green one is the flow set $\mathcal{C}$. The dashed gray line is the set $g(\mathcal{D})$.

$(t, j) \in \text{dom } \phi$.

- *A hybrid time domain $\mathbb{E}$ is complete if it is unbounded, i.e., it evolves forever in continuous or discrete time, or both.*

□

Solutions to hybrid systems are not necessarily defined for all time; in other words, their domain may be bounded. The following example presents a hybrid system whose solutions are all complete, meaning they evolve indefinitely over an unbounded domain. Despite its simple structure, the system admits maximal solutions exhibiting a variety of behaviors. These include continuous evolution, eventually continuous but not fully continuous evolution, eventually discrete but not fully discrete evolution, and Zeno-type evolution that is neither purely continuous nor purely discrete.

Example 2.4.1

Consider a hybrid system in $\mathbb{R}^2$ given by:

$$\dot{x} = f(x) := \begin{bmatrix} 1 \\ 1 \end{bmatrix}, \; x \in \mathcal{C} := \mathbb{R}^2 \backslash \mathcal{D}, \tag{2.5a}$$

$$x^+ = g(x) := \begin{bmatrix} \frac{3}{4}x_1 \\ \frac{1}{4}x_1 \end{bmatrix}, \; x \in \mathcal{D} := \{x \in \mathbb{R}^2 : 0 \leq 5x_2 \leq 2 - x_1\}, \tag{2.5b}$$

where both sets $\mathcal{C}$ and $\mathcal{D}$ are closed and $\mathcal{C}$ is the closure of the complement of $\mathcal{D}$, so that $\mathcal{C} \cup \mathcal{D} = \mathbb{R}^2$.

- *The maximal solution from $\phi_a(0,0) = (2, -1)$, has the domain* dom ϕ_a =

$\mathbb{R}_{\geq 0} \times \{0\}$ *and is given by:*

$$\phi_a(t,0) = \begin{bmatrix} t+2 \\ t-1 \end{bmatrix}.$$

Its domain, $\operatorname{dom} \phi_a = \mathbb{R}_{\geq 0}$*, is called the continuous time domain.*

- *The maximal solution from* $\phi_b(0,0) = (1,-1)$ *has the domain* $\operatorname{dom} \phi_b = [0,1] \times \{0\} \cup [1,\infty) \times \{1\}$*, and the two solutions are defined as follows:*

$$\phi_b(t,j) = \begin{bmatrix} t+1 \\ t-1 \end{bmatrix},$$
$$\phi_b(t,1) = \begin{bmatrix} \frac{3}{2} \\ \frac{1}{2} \end{bmatrix} + \begin{bmatrix} t-1 \\ t-1 \end{bmatrix}.$$

  ϕ_b *flows from the initial point for one unit of time, reaches* $(2,0)$ *and jumps to* $(\frac{3}{2}, \frac{1}{2})$ *from there, and flows afterwards.*

- *The maximal solution from* $\phi_c(0,0) = (0,-1)$ *behaves similarly to* ϕ_b *and is given by:*

$$\phi_c(t,0) = \begin{bmatrix} 0 \\ -1 \end{bmatrix} + \begin{bmatrix} t \\ t \end{bmatrix},$$
$$\phi_c(t,1) = \begin{bmatrix} \frac{3}{4} \\ \frac{1}{4} \end{bmatrix} + \begin{bmatrix} t-1 \\ t-1 \end{bmatrix}.$$

- *The maximal solution from* $\phi_d(0,0) = (0,-1)$ *has the domain* $\operatorname{dom} \phi_d = ([0,1] \times \{0\}) \cup (\{1\} \times \mathbb{N})$ *and is given by:*

$$\phi_d(t,0) = \begin{bmatrix} 0 \\ -1 \end{bmatrix} + \begin{bmatrix} t \\ t \end{bmatrix},$$
$$\phi_d(1,j) = \begin{bmatrix} \frac{3}{4}^j \\ \frac{1}{4}^j \end{bmatrix}.$$

  ϕ_d *flows from the initial point for one unit of time, reaches* $(1,0)$ *and jumps to* $(\frac{3}{4}, \frac{1}{4})$ *from there, and then keeps on jumping infinitely many times.*

- *The maximal solution from* $\phi_e(0,0) = (0,0)$ *has the domain* $\operatorname{dom} \phi_e = \{0\} \times \mathbb{N}$ *and is given by:*

$$\phi_e(0,j) = \begin{bmatrix} 0 \\ 0 \end{bmatrix}.$$

  $(0,0)$ *is an equilibrium point, despite the fact that* f *is nonzero there, and the solution* ϕ_e *jumps infinitely many times from* $(0,0)$ *to* $(0,0)$*.*

- *The maximal solution from* $\phi_f(0,0) = (-1,0)$ *has the domain* $\operatorname{dom}\phi_f = \bigcup_{j=0}^{\infty}([t_j, t_{j+1}] \times \{j\})$, *where* $t_0 = 0$, $t_1 = 0$, $t_2 = \frac{1}{4}$, $t_3 = \frac{1}{4} + \frac{1}{8}$, *etc., so that* $t_{j+1} - t_j = \frac{1}{4}\left(\frac{1}{2}\right)^{j-1}$ *for* $j = 1, 2, \ldots$ *and is given by:*

$$\phi_f(0,0) = \begin{bmatrix} -1 \\ 0 \end{bmatrix},$$

$$\phi_f(t,j) = \begin{bmatrix} (t - t_j) - \frac{3}{4}\left(\frac{1}{2}\right)^{j-1} \\ (t - t_j) - \frac{1}{4}\left(\frac{1}{2}\right)^{j-1} \end{bmatrix}.$$

Solutions $\phi_a, \phi_b, \phi_c, \phi_d$ *and* ϕ_e *are maximal and complete. The solution* ϕ_a *is continuous,* ϕ_b *and* ϕ_c *are eventually continuous,* ϕ_d *is eventually discrete,* ϕ_e *is discrete, and* ϕ_f *is Zeno. The trajectories from different initial conditions are illustrated in Figure 2.7.* □

Completeness and maximality are distinct notions. A complete solution is maximal, but the converse implication does not hold. For instance, consider a solution ϕ that jumps outside $\mathcal{C} \cup \mathcal{D}$. In this case, the solution cannot be extended further and is therefore maximal, but at the same time, it does not evolve forever. Hence, it is not complete. The following example illustrates a case in which not all maximal solutions are complete.

Example 2.4.2

Consider a hybrid system in $\mathbb{R}$ *given by:*

$$\dot{x} = f(x) := x^2, \qquad x \in \mathcal{C} := \{x \in \mathbb{R} : |x| \geq 1\},$$
$$x^+ = g(x) := x - 1, \qquad x \in \mathcal{D} := [0,1].$$

Since the function f *is locally Lipschitz, the flow solutions are unique. The analysis begins by considering solutions starting from different initial conditions. Take the initial condition* $\phi_a(0,0) = 1$, *which belongs to the intersection* $\mathcal{C} \cap \mathcal{D}$. *From this point, two distinct solution trajectories are possible: one governed by the flow dynamics and another by the jump dynamics. Let us first consider the continuous solution. It is straightforward to verify that the following function satisfies the flow condition of the hybrid system:*

$$\phi_a(t,0) = (1-t)^{-1}, \ \forall t \in [0,1].$$

Due to the Lipschitz property of the flow dynamics, the solution described above is unique. This solution evolves continuously and is therefore referred to as a continuous solution. However, its time domain is bounded, as the state diverges to infinity when time approaches the critical value $t^* = 1$. *This behavior is known as finite escape time and leads to a maximal but not complete solution. Next, consider the same initial condition* $\phi_a(0,0) = 1$, *but focus on the solution that follows the jump dynamics:*

$$\bar{\phi}_a(0,1) = 0 \in \mathcal{D},$$
$$\bar{\phi}_a(0,2) = -1 \in \mathcal{C}.$$

At $x = -1$, the vector field $f(-1)$ points to the right; however, any attempt to flow from $x = -1$ would leave the flow set $\mathcal{C}$, which is not allowed. As a result, the solution cannot be extended further and is therefore maximal but not complete. □

To ensure that solutions of a hybrid system are well-behaved, it is necessary to impose some regularity assumptions on the hybrid data. These assumptions, commonly referred to as the hybrid basic conditions, play a key role in guaranteeing the existence of solutions and establishing robustness properties of stability results [3]. A hybrid system satisfying these assumptions is typically called well-posed.

Assumption 2.4.1 (*Hybrid basic conditions*)

The hybrid system $\mathcal{H} = (\mathcal{C}, F, \mathcal{D}, G)$ satisfies:

1. *$\mathcal{C}$ and $\mathcal{D}$ are closed subsets of $\mathbb{R}^n$;*
2. *F: $\mathbb{R}^n \rightrightarrows \mathbb{R}^n$ is outer semicontinuous, locally bounded relative to $\mathcal{C}$, and $F(x)$ is nonempty and convex for each $x \in \mathcal{C}$;*
3. *G: $\mathbb{R}^n \rightrightarrows \mathbb{R}^n$ is outer semicontinuous, locally bounded relative to $\mathcal{D}$, and $G(x)$ is nonempty for each $x \in \mathcal{D}$;*

□

A key notion in characterizing the possibility of flowing from a point in the flow set is the tangent cone.

Definition 2.4.8 (*Tangent cone*)

Given a set $\mathcal{S} \subset \mathbb{R}^n$ and a point $x \in \mathcal{S}$, the tangent cone to $\mathcal{S}$ at x, denoted $T_{\mathcal{S}}(x)$, is the set of all vectors $w \in \mathbb{R}^n$ for which there exist a sequence $x_i \in \mathcal{S}$, $\tau_i > 0$ with $x_i \to x$, such that:

$$w = \lim_{i \to \infty} \frac{x_i - x}{\tau_i}.$$

□

Using the tangent cone, the viability condition can be formulated as:

$$F(x) \cap T_{\mathcal{C}}(x) \neq \emptyset, \ \forall x \in \mathcal{C} \setminus \mathcal{D}.$$

Intuitively, this condition means that the flow map F does not point outside the flow set $\mathcal{C}$ at points where no jumps are allowed. Under these assumptions, and provided the viability condition holds, the existence of nontrivial solutions can be guaranteed.

Proposition 2.4.1 (*Basic existence*)

Consider the hybrid system $\mathcal{H} = (\mathcal{C}, F, \mathcal{D}, G)$. Let $\xi \in \overline{\mathcal{C}} \cup \mathcal{D}$. If $\xi \in \mathcal{D}$ or
(VC) there exists $\epsilon > 0$ and an absolutely continuous function $z : [0, \epsilon] \to \mathbb{R}^n$ such that $z(0) = \xi$, $\dot{z}(t) \in F(z(t))$ for almost all $t \in [0, \epsilon]$ and $z(t) \in \mathcal{C}$ for all $t \in (0, \epsilon]$, then there exists a nontrivial solution ϕ to $\mathcal{H}$ with $\phi(0, 0) = \xi$. If (VC) holds for every $\xi \in \overline{\mathcal{C}} \setminus \mathcal{D}$, then there exists a nontrivial solution to $\mathcal{H}$ from every point of $\overline{\mathcal{C}} \cup \mathcal{D}$, and

every $\phi \in \mathcal{S}_{\mathcal{H}}$ satisfies exactly one of the following:

1. *ϕ is complete,*
2. *dom ϕ is bounded and, with $J = \sup_j \text{dom } \phi$, the interval I^J has nonempty interior and is open to the right, and there does not exist an absolutely continuous function $z : [a, b] \to \mathbb{R}^n$ satisfying $\dot{z}(t) \in F(z(t))$ for almost all $t \in [a, b]$, $z(t) \in \mathcal{C}$ for all $t \in (a, b)$, and such that $I^j \subset [a, v)$ and $z(t) = \phi(t, J)$ for all $t \in I^J$,*
3. *dom ϕ is bounded and $\phi(T, J) \notin \overline{\mathcal{C}} \cup \mathcal{D}$, where $(T, J) = \sup \text{dom } \phi$.*

Furthermore, if $G(\mathcal{D}) \subset \overline{\mathcal{C}} \cup \mathcal{D}$, then (3) above does not occur. □

The first part of the proposition follows directly from the definition of a solution to the hybrid system $\mathcal{H}$. Specifically, if $\xi \in \mathcal{D}$, a jump can occur immediately; if instead, condition (VC) holds at ξ, then there exists a flow starting from ξ as specified by the definition of an absolutely continuous solution. Having established the basic existence properties of solutions, the next step is to study their qualitative behavior. In particular, stability analysis plays a central role, with Lyapunov-based methods providing powerful tools to assess robustness and performance of hybrid dynamical systems.

2.5 Stability of hybrid systems

Stability and convergence are fundamental properties of dynamical systems, and their analysis has been a central concern in control theory. In a classical linear system, such as $\dot{x} = Ax$, the homogeneity properties of solutions imply that if all solutions converge to a bounded set, then this set must be the origin. As a result, for linear systems, the notion of stability is often associated with a specific point or set, typically an equilibrium. In hybrid dynamical systems, solutions combine continuous-time and discrete-time evolution, which may prevent convergence to a single point. Therefore, it is natural to study the stability of closed sets rather than isolated equilibrium points. For example, in a sample-and-hold control system, the controlled state is expected to settle to an equilibrium. At the same time, the auxiliary timer variable does not converge to a point, but rather to an interval. In this context, asymptotic stability of an equilibrium point is a particular case of the more general notion of asymptotic stability of a closed set. The primary focus of this section is on uniform global asymptotic stability (UGAS), which provides strong guarantees on the convergence and robustness of solutions. To rigorously define stability properties of hybrid systems and formulate Lyapunov-based conditions, it is useful to introduce some standard preliminary notions. These concepts provide a way to measure the distance of the system state from a target set and to define comparison functions that quantify stability and convergence.

2.5.1 Preliminary definitions

Definition 2.5.1 (*Distance to a closed set*)

Given a vector $x \in \mathbb{R}^n$ and a closed set $\mathcal{A} \subset \mathbb{R}^n$, the distance of x to $\mathcal{A}$ is denoted by $|x|_{\mathcal{A}}$ and defined as:

$$|x|_{\mathcal{A}} := \inf_{y \in \mathcal{A}} \|x - y\|.$$

□

Definition 2.5.2 (*Positive definite function*)

A continuous function $\rho : \mathbb{R}_{\geq 0} \to \mathbb{R}_{\geq 0}$ is positive definite if $\rho(s) > 0$ for all $s > 0$ and $\rho(0) = 0$. Similarly, a continuous function $V : \mathbb{R}^n \to \mathbb{R}$ is positive definite with respect to a set $\mathcal{A} \subset \mathbb{R}^n$ if $V(x) = 0$ for all $x \in \mathcal{A}$ and $V(x) > 0$ for all $x \notin \mathcal{A}$. □

Definition 2.5.3 (*Class-$\mathcal{K}_\infty$ function*)

A function $\alpha : \mathbb{R}_{\geq 0} \to \mathbb{R}_{\geq 0}$ belongs to class-$\mathcal{K}_\infty$ if it is zero at zero, strictly increasing, continuous, and unbounded. □

Definition 2.5.4 (*Class-$\mathcal{KL}$ function*)

A function $\beta : \mathbb{R}_{\geq 0} \times \mathbb{R}_{\geq 0} \to \mathbb{R}_{\geq 0}$ belongs to class-$\mathcal{KL}$ if it is nondecreasing in its first argument, nonincreasing in its second argument, $\lim_{r \to 0^+} \beta(r, s) = 0$ for each $s \in \mathbb{R}_{\geq 0}$, and $\lim_{s \to \infty} \beta(r, s) = 0$ for each $r \in \mathbb{R}_{\geq 0}$. □

Definition 2.5.5 (*Proper indicator*)

Let $\mathcal{U} \subset \mathbb{R}^n$ be an open set. A function $\omega : \mathcal{U} \to \mathbb{R}_{\geq 0}$ is a proper indicator of the set $\mathcal{A} \subset U$ if it is continuous, positive definite with respect to $\mathcal{A}$, and $\omega(x_i) \to \infty$ as $i \to \infty$ if either $|x_i| \to \infty$ or the sequence $\{x_i\}_{i=1}^{\infty}$ approaches the boundary of $\mathcal{U}$. □

With these definitions, the stability of a hybrid dynamical system can be rigorously formalized. The analysis focuses on closed sets, often referred to as attractors, denoted by $\mathcal{A}$. Uniform global asymptotic stability is defined relative to such sets, and the subsequent sections provide equivalent characterizations and sufficient conditions for verification, primarily using Lyapunov functions.

2.5.2 Stability properties of hybrid systems

With the preliminary notions introduced above, the main stability properties of hybrid dynamical systems can now be rigorously defined. In this framework, the focus is not limited to isolated equilibrium points but extends to compact sets $\mathcal{A} \subset \mathbb{R}^n$. Depending on the level of generality, different notions of stability can be considered. The first concept is local asymptotic stability, which generalizes the classical Lyapunov stability of equilibria to compact sets and captures both Lyapunov stability and local attractivity.

Definition 2.5.6 (*Local asymptotic stability*)

Let $\mathcal{H}$ be a hybrid system in $\mathbb{R}^n$. A compact set $\mathcal{A} \subset \mathbb{R}^n$ is locally asymptotically stable (LAS) for $\mathcal{H}$ if:

- *(**Lyapunov stability**) for every $\epsilon > 0$ there exists $\delta > 0$ such that every solution ϕ to $\mathcal{H}$ with $|\phi(0,0)|_{\mathcal{A}} \leq \delta$ satisfies:*

$$|\phi(t,j)|_{\mathcal{A}} \leq \epsilon, \ \forall (t,j) \in \text{dom } \phi;$$

- *(**Local attractivity**) there exists $\mu > 0$ such that every complete solution ϕ to $\mathcal{H}$ with $|\phi(0,0)|_{\mathcal{A}} \leq \mu$ satisfies:*

$$\lim_{t+j\to\infty} |\phi(t,j)|_{\mathcal{A}} = 0.$$

□

LAS characterizes the behavior of solutions in a neighborhood of the attractor $\mathcal{A}$. In contrast, uniform global asymptotic stability extends these properties to the entire state space, providing uniform bounds on solutions and guaranteeing convergence from any initial condition. The following definition formalizes this stronger notion.

Definition 2.5.7 (*Uniform global asymptotic stability*)

Let $\mathcal{H}$ be a hybrid system in $\mathbb{R}^n$. A compact set $\mathcal{A} \subset \mathbb{R}^n$ is uniformly globally asymptotically stable (UGAS) for $\mathcal{H}$ if:

- *(**Uniform global stability**) there exists $\alpha \in \mathcal{K}_\infty$ such that any solution ϕ to $\mathcal{H}$ satisfies:*

$$|\phi(t,j)|_{\mathcal{A}} \leq \alpha(|\phi(0,0)|_{\mathcal{A}}), \ \forall (t,j) \in \text{dom } \phi;$$

- *(**Uniform global attractivity**) for each $\epsilon, r > 0$ there exists $T > 0$ such that, for any solution ϕ to $\mathcal{H}$ with $|\phi(0,0)|_{\mathcal{A}} \leq r$,*

$$(t,j) \in \text{dom } \phi, t + j \geq T \Rightarrow |\phi(t,j)|_{\mathcal{A}} \leq \epsilon.$$

□

Uniform global asymptotic stability not only ensures that solutions remain bounded with respect to the attractor $\mathcal{A}$, but also guarantees convergence from any initial condition in a uniform sense. An equivalent and often more convenient characterization of UGAS is given in terms of functions of class $\mathcal{KL}$, which provide an explicit bound on the decay of the distance to the attractor over time. This characterization is often convenient for analysis and Lyapunov-based verification. The following definition formalizes this notion.

Definition 2.5.8 (*Global $\mathcal{KL}$ stability*)

Let $\mathcal{H}$ be a hybrid system in $\mathbb{R}^n$. A compact set $\mathcal{A} \subset \mathbb{R}^n$ is globally $\mathcal{KL}$-stable if there exists $\beta \in \mathcal{KL}$ such that:

$$|\phi(t,j)|_{\mathcal{A}} \leq \beta(|\phi(0,0)|_{\mathcal{A}}, t + j), \ \forall (t,j) \in \text{dom } \phi,$$

for all solutions ϕ to $\mathcal{H}$. □

The definition of $\mathcal{KL}$ stability can be extended to the local case.

Definition 2.5.9 (*$\mathcal{KL}$ asymptotic stability*)

Let $\mathcal{H}$ be a hybrid system in $\mathbb{R}^n$, $\mathcal{A} \subset \mathbb{R}^n$ be a compact set, and $\mathcal{U}$ an open set such that $\mathcal{U} \subset \mathcal{A}$. The set $\mathcal{A}$ is $\mathcal{KL}$ asymtotically stable on $\mathcal{U}$ for $\mathcal{H}$ if, for every proper indicator ω of $\mathcal{A}$ on $\mathcal{U}$, there exists a function $\beta \in \mathcal{KL}$ such that:

$$\omega(\phi(t,j)) \leq \beta(\omega(\phi(0,0)), t+j), \ \forall (t,j) \in \text{dom } \phi,$$

for all solutions ϕ to $\mathcal{H}$ such that $\phi(0,0) \in \mathcal{U}$. □

2.5.3 Lyapunov functions for hybrid systems

Lyapunov functions are a powerful tool for analyzing the stability of hybrid systems. Due to the structure of the hybrid system, which imposes constraints on where jump and flow can occur, a Lyapunov function does not necessarily need to be defined on the entire space $\mathbb{R}^n$, nor continuously differentiable everywhere. It suffices to consider a function that is continuously differentiable on a neighborhood of the flow set $\mathcal{C}$. The following definitions formalize the conditions under which a function V can be considered a Lyapunov function candidate for establishing uniform global asymptotic stability of a closed set $\mathcal{A}$.

Definition 2.5.10 (*Lyapunov function candidate*)

A function V: dom $V \to \mathbb{R}$ is a Lyapunov function candidate for the hybrid system $\mathcal{H} = (\mathcal{C}, F, \mathcal{D}, G)$ if:

- *$\overline{\mathcal{C}} \cup \mathcal{D} \cup G(\mathcal{D}) \subset$ dom V;*
- *V is continuously differentiable on an open set containing $\overline{\mathcal{C}}$, where $\overline{\mathcal{C}}$ denotes the closure of $\mathcal{C}$.*

□

The following theorem provides sufficient conditions on a Lyapunov function candidate to guarantee uniform global asymptotic stability of a closed set $\mathcal{A}$.

Theorem 2.5.1 (*Sufficient Lyapunov conditions*)

Let $\mathcal{H} = (\mathcal{C}, F, \mathcal{D}, G)$ be a hybrid system and let $\mathcal{A} \subset \mathbb{R}^n$ be a closed set. If V is a Lyapunov function candidate for $\mathcal{H}$ and there exist $\alpha_1, \alpha_2 \in \mathcal{K}_\infty$, and a continuous $\rho \in \mathcal{PD}$ such that:

$$\alpha_1(|x|_\mathcal{A}) \leq V(x) \leq \alpha_2(|x|_\mathcal{A}) \ \forall x \in \mathcal{C} \cup \mathcal{D} \cup G(\mathcal{D}), \tag{2.6}$$

$$\langle \nabla V(x), f \rangle \leq -\rho(|x|_\mathcal{A}) \ \forall x \in \mathcal{C}, f \in F(x) \tag{2.7}$$

$$V(g) - V(x) \leq -\rho(|x|_\mathcal{A}) \ \forall x \in \mathcal{D}, g \in G(x), \tag{2.8}$$

then the set $\mathcal{A}$ is uniformly globally asymptotically stable for $\mathcal{H}$. □

Proof sketch. The proof combines standard arguments from Lyapunov stability theory with the invariance principle for hybrid systems. The conditions ensure a strict decrease of V along solutions that are not in $\mathcal{A}$, which guarantees uniform global attractivity. The upper and lower bounds on V ensure uniform global stability. □

The three inequalities in the Theorem 2.5.1 are referred to as:

- sandwich condition (S): ensures that V is bounded above and below by two class $\mathcal{K}_\infty$ functions of the distance to $\mathcal{A}$, thus providing a meaningful measure of how far the state is from the attractor;
- flow condition (F): requires that V decreases during flows in the set $\mathcal{C}$, i.e., along the continuous evolution of the system;
- jump condition (C): imposes that V decreases across jumps in the set $\mathcal{D}$, i.e., during discrete transitions.

Together, these three conditions guarantee the uniform global asymptotic stability of the set $\mathcal{A}$. In addition to Theorem 2.5.1, stability can also be established under weaker assumptions. In particular, when the hybrid system satisfies the hybrid basic conditions and the attractor is compact, the following theorem applies.

Theorem 2.5.2

Consider the hybrid system $\mathcal{H} = (\mathcal{C}, F, \mathcal{D}, G)$ satisfying the hybrid basic conditions, and let $\mathcal{A} \subset \mathbb{R}^n$ be a compact set such that $G(\mathcal{A} \cap \mathcal{D}) \subset \mathcal{A}$. If there exists a Lyapunov function candidate V such that:

$$\langle \nabla V(x), f \rangle < 0, \quad \forall x \in \mathcal{C} \setminus \mathcal{A}, \forall f \in F(x),$$

$$V(g) - V(x) < 0, \quad \forall x \in \mathcal{D} \setminus \mathcal{A}, \forall g \in G(x).$$

then the set $\mathcal{A}$ is globally asymptotically stable (GAS) for $\mathcal{H}$. □

Proof. The proof follows standard Lyapunov-based arguments for hybrid dynamical systems. Let $V : \mathbb{R}^n \to \mathbb{R}_{\geq 0}$ be the Lyapunov function introduced in Definition 2.5.10, satisfying the decrease conditions along flows and jumps. Along the continuous evolution, for all $x \in \mathcal{C}$, the time derivative of V satisfies

$$\dot{V}(x) \leq -\alpha(\|x\|)$$

for some class-$\mathcal{K}$ function α, ensuring decrease during flows.

Moreover, for all $x \in \mathcal{D}$, the jump map guarantees

$$V(x^+) - V(x) \leq 0,$$

which ensures non-increase of the Lyapunov function across discrete transitions. Therefore, by invoking the hybrid invariance principle and the main stability results for hybrid systems, the equilibrium point is stable (asymptotically stable, globally asymptotically stable, depending on the assumptions stated in the theorem. □

2.6 Summary

The fundamental framework for a hybrid dynamic system has been discussed, including its modeling through flow and jump dynamics, the notion of hybrid time domains and solutions, as well as the main concepts of stability. Hybrid systems constitute a powerful approach for modeling complex dynamical behaviors that combine continuous evolution with discrete transitions, and the associated stability tools are essential for guaranteeing reliable performance in practical applications. Among the various classes of hybrid systems, an important and widely studied subclass is that of switched systems, where the discrete dynamics are associated with switching among different continuous-time subsystems. The next section focuses on switched systems, introducing their mathematical formulation and discussing stability analysis under different switching signals.

Chapter 3

Switched systems

Abstract

This chapter provides a comprehensive overview of switched systems, a fundamental subclass of hybrid dynamical systems where the state evolution is determined by a family of continuous-time subsystems and a switching signal selecting the active dynamics at each instant. The discussion begins with the modeling of switched systems and proceeds to their classification based on the nature of the switching mechanism. The concept of solution is then formalized, highlighting the specific features induced by the presence of discontinuities. Special attention is given to stability analysis, including both general definitions and Lyapunov-based tools, as well as dwell-time conditions ensuring reliable behavior under switching. The interconnection between the switched and hybrid systems is also examined, clarifying their similarities and differences in both modeling and analysis. The chapter concludes with a summary and motivation for applications, emphasizing the relevance of switched systems in power electronics, robotics, and networked control, and setting the stage for the control design methodologies developed in the following chapters.

Contents

3.1 Introduction

In many real-world systems, continuous-time dynamics interact with discrete events such as mode changes, controller updates, or structural reconfigurations. These interactions are naturally described within the framework of hybrid systems, which combine both continuous evolution and discrete transitions. Hybrid systems are generally defined as dynamical systems resulting from the interaction between continuous dynamics, typically

represented by differential equations, and discrete dynamics, such as finite automata. For example, continuous dynamics may be modeled by a system like $\dot{x} = Ax + Bu$ with state $x \in \mathbb{R}^n$ and control input $u \in \mathbb{R}^m$. At the same time, the discrete part can be described by a variable q taking values in a finite set, where transitions between modes are triggered by changes in the continuous state or by external logic. A hybrid system arises when the continuous input depends on the discrete state, and vice versa. Traditionally, control theory has focused on either continuous or discrete behavior. However, most practical systems inherently involve both aspects. The field of hybrid systems reflects this interplay and has been approached from different perspectives. In computer science, the emphasis is often placed on the discrete event logic, with relatively simple continuous models, addressing questions such as verification and simulation. In contrast, the control theory community tends to emphasize the role of continuous dynamics, often viewing hybrid systems as continuous systems with switching. This viewpoint is primarily concerned with properties like stability and control design. A particularly structured subclass of hybrid systems is represented by switching systems. In these systems, the continuous dynamics evolve according to one of several predefined subsystems, and the discrete dynamics consist of transitions among a finite set of modes. From a modeling perspective, switching systems can be seen as special cases of hybrid systems, where the discrete component has a constrained and well-defined structure. While hybrid systems allow for more general forms of discrete behavior, switching systems restrict this behavior to a finite set of modes. Each mode is associated with a distinct vector field, and the switching signal selects the active one at any given time. Thus, the analysis focuses on continuous-time systems with isolated discrete switching events, commonly referred to as switched systems. Switched systems naturally arise in a wide range of engineering applications, including power electronics, automotive systems, robotics, and communication networks. In particular, many power conversion topologies, such as DC/DC and DC/AC inverters, are inherently switched due to the operation of semiconductor devices. The analysis and control of switched systems present significant challenges compared to conventional linear or nonlinear systems: the switching action can lead to complex dynamics, including discontinuities, chattering, and potential instability if the switching law is not properly designed. Moreover, performance objectives such as disturbance rejection, robustness to parameter variations, and harmonic minimization must be achieved despite the system's non-smooth nature. In the context of control design for switched systems, the characteristics of the switching mechanism often play a fundamental role. Nevertheless, in many cases, it is sufficient to consider only essential properties of the switching signal rather than its complete specification. Understanding the different behaviors and properties of switched systems requires a systematic classification of switching signals and mechanisms. Such classifications are essential for characterizing stability, performance, and robustness, and for guiding the design of effective control strategies [2], [13]. In the next section, a classification of switched systems is introduced based on switching rules, dwell-time conditions, and signal

properties, providing a fundamental framework for the stability and control analyses that follow.

3.2 Classification of switched systems

Switching systems can be classified based on the mechanism that determines the active subsystem at any given time [2], [5], [13]. The most common classifications include:

- **State-dependent switching**: The continuous state space (e.g., $\mathbb{R}^n$) is partitioned into a finite or infinite number of operating regions utilizing a set of switching surfaces (also called guards). Each area is associated with a specific continuous-time subsystem, typically described by differential equations with or without control inputs. When the system trajectory intersects one of the switching surfaces, the system may undergo a discrete transition. The continuous state jumps instantaneously to a new value, defined by a reset map. This map determines the latest value of the state after crossing a surface and is defined on the union of switching surfaces, possibly mapping into the full state space or a subset of it. In the simplest and most common case, the reset map is the identity. The concepts of reset maps and guard sets, fundamental in state-dependent switching, are thoroughly discussed in [3]. This means that the state trajectory is continuous everywhere, although it generally loses differentiability when it passes through a switching surface. Although such systems may not include a discrete state in the traditional sense, they are sometimes regarded as hybrid systems, especially when the switching mechanism depends on additional logic or memory, such as hysteresis.

- **Time-dependent switching**: Given a family f_p, $p \in \mathcal{P}$ of functions from $\mathbb{R}^n$ to $\mathbb{R}^n$, where $\mathcal{P}$ is, typically, a subset of a finite-dimensional linear vector space. This gives rise to a family of systems:

$$\dot{x} = f_p(x),\ p \in \mathcal{P}, \tag{3.1}$$

  evolving on $\mathbb{R}^n$. The functions f_p are assumed to be sufficiently regular (at least locally Lipschitz). A particularly relevant case arises when the systems are linear, i.e.:

$$f_p(x) = A_p x,\ A_p \in \mathbb{R}^{n\times n},\ p \in \mathcal{P}, \tag{3.2}$$

  and the index set $\mathcal{P}$ is finite: $\mathcal{P} = 1, 2, \ldots, m$. To define a switched system generated by the above family, it is useful to explain the notion of a switching signal. A switching signal is a piecewise constant function $\sigma : [0, \infty) \to \mathcal{P}$. Such a function has a finite number of discontinuities, called switching times, on every bounded time interval and takes a constant value on every interval between two consecutive switching times. For concreteness, assume that σ is continuous from the right everywhere: $\sigma(t) = \lim_{\tau \to t^+} \sigma(\tau)$ for each $\tau \geq 0$. Thus, a switched system with

time-dependent switching can be described by the following equation:

$$\dot{x}(t) = f_{\sigma(t)}(x(t)), \tag{3.3}$$

where $\sigma(t)$ is a piecewise constant function taking values in a finite set of modes. A particular case is a switched linear system:

$$\dot{x}(t) = A_{\sigma(t)}x(t), \tag{3.4}$$

which arises when all individual subsystems are linear, as in (3.2). To simplify the notation, omit the time arguments:

$$\dot{x} = f_{\sigma}(x), \tag{3.5}$$

and

$$\dot{x} = A_{\sigma}x, \tag{3.6}$$

respectively. While time-dependent switching may appear distinct from state-dependent switching, a connection exists between the two. Every trajectory of a state-dependent system can be viewed as a particular solution of a time-dependent switched system, for a suitably constructed switching signal. However, the reverse is not generally true. From this perspective, the time-dependent model offers a more general abstraction and is especially useful when the structure of the state-space partition or switching surface is unknown. The theory and analysis of switching signals are detailed in [2], [13].

- **Autonomous and controlled switching**: Autonomous switching refers to scenarios in which the switching mechanism that triggers discrete events is not under direct control. This category includes systems with state-dependent switching in which locations of the switching surfaces are predetermined, as well as systems with time-dependent switching, where the rule generating the switching signal is either unknown or intentionally abstracted during modeling. For instance, a discrete change in system dynamics may result from unpredictable environmental disturbances or component failures. Conversely, in many practical situations, the switching mechanism is actively imposed by the designer to achieve a desired behavior of the system. In these controlled switching systems, the designer has direct control over the switching mechanism (which can be state-dependent or time-dependent) and may adjust it as the system evolves. For various reasons, it may be natural to apply discrete control actions, which leads to systems with controlled switching. An important example, which provides motivation and serves as a unifying framework for studying systems with controlled switching, is that of an embedded system, where computer software interacts with physical devices. It is important to note that the distinction between autonomous and controlled switching, or between state-dependent and time-dependent switching, is not always

clear-cut. The distinction between autonomous and controlled switching is highly relevant not only for practical implementation but also for the development of appropriate control theory. Understanding whether the switching mechanism can be influenced or is driven by external factors informs the design of control strategies and stability analysis, shaping the theoretical framework within which switched systems are studied. Switched systems with controlled time-dependent switching can be described using the standard formalism of control theory. Assuming that $\mathcal{P}$ is a finite set. Then the switched system (3.5) can be reformulated as:

$$\dot{x} = \sum_{i=1}^{m} f_i(x)u_i, \tag{3.7}$$

where the admissible controls are of the form $u_k = 1$, $u_i = 0$ for all $i \neq k$ (this correspond to $\sigma = k$). In particular, the switched linear system (3.6) gives rise to the bilinear system:

$$\dot{x} = \sum_{i=1}^{m} A_i x u_i. \tag{3.8}$$

From a modeling perspective, switching systems can be viewed as structured hybrid systems, where the discrete component corresponds to a mode index and does not directly affect the continuous state during transitions. This is in contrast to more general hybrid systems, in which discrete events may cause discontinuities or resets in the continuous state, and the logic governing transitions may be significantly more complex. To rigorously analyze the behavior of switching systems, it is essential to formalize the notion of a solution. Due to the presence of discontinuities in the vector field, driven by the switching signal, solutions must be interpreted in a piecewise sense, where the system evolves according to a specific mode over each time interval between switches. The works [2], [5], [13] form the basis for the modern theory of switched and hybrid systems, combining rigorous mathematical foundations with practical relevance.

3.3 Solution of switched systems

The definition of a solution for a switched system requires careful treatment due to the possible discontinuities in the vector field introduced by the switching signal. Depending on the properties of the switching mechanism and the system's structure, different behaviors can arise. The most relevant aspects and modeling considerations include:

- **Ordinary differential equations**: On intervals where the switching signal remains constant, the system reduces to a standard ordinary differential equation governed by a smooth vector field. In such intervals, classical existence and uniqueness theorems for ODEs apply. At switching times, continuity of the solution is typically required, although differentiability may not be preserved. Consider the following system:

$$\dot{x} = f(t, x), \ x \in \mathbb{R}^n. \tag{3.9}$$

A solution $x(\cdot)$ is considered for the initial time t_0 and initial condition $x(t_0) = x_0$. It is common to assume that the function f is continuous in t and locally Lipschitz in x uniformly with respect to t. In addition, for every pair (t_0, x_0) there exists a constant $L > 0$ such that the following inequality:

$$|f(t,x) - f(t,y)| \leq L|x - y|, \tag{3.10}$$

holds for all (t, x) and (t, y) in some neighborhood of (t_0, x_0) in $[t_0, \infty) \times \mathbb{R}^n$. Under these conditions, it is well known that the system (3.9) has a unique solution for every initial condition (t_0, x_0). Considering the general system described by (3.9), the assumption of continuity of the function f in t is too restrictive. In fact, to guarantee the existence and uniqueness of solutions, it is sufficient to require that f be piecewise continuous in t. In this case, it is necessary to adopt a weaker concept of solution, namely a continuous function $x(\cdot)$ that satisfies the following integral equation:

$$x(t) = x_0 + \int_{t_0}^{t} f(\tau, x(\tau))d\tau.$$

A function with these properties is piecewise differentiable and satisfies the differential equation (3.9) almost everywhere. Such functions are known as absolutely continuous and provide solutions of (3.9) in the sense of Carathéodory [2], [14], [15]. Solutions of the switched system (3.5) will be interpreted in this way.

- **Zeno behavior**: This behavior occurs when a switched system undergoes an infinite number of discrete transitions in a finite time interval. This leads to a breakdown in the classical solution concept, since the trajectory cannot be extended beyond the so-called Zeno time. Such dynamics are relevant in switched and hybrid systems, especially when transitions are triggered by state-dependent conditions [3], [5]. These behaviors present difficulties for both analysis and implementation, and are typically avoided by imposing dwell-time or hysteresis constraints on the switching signal. The bouncing ball example illustrates a peculiar type of behavior that can occur in switched systems. Consider a ball bouncing on the floor. Denote by h its height above the floor and by v its velocity (taking the positive velocity direction to be upwards). Normalizing the gravitational constant, the following equations of motion, valid between the impact times, are obtained:

$$\begin{aligned} \dot{h} &= v, \\ \dot{v} &= -1. \end{aligned} \tag{3.11}$$

At the time of an impact, i.e., when the ball hits the floor, its velocity changes according to the following rule:

$$v(t) = -rv(t^-), \tag{3.12}$$

where $v(t^-)$ is the ball's velocity right before the impact, $v(t)$ is the velocity right after the impact, and $r \in (0, 1)$ is the restituition coefficient. This system can be

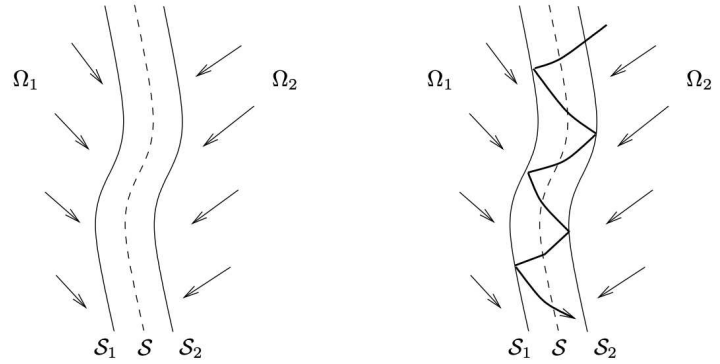

Figure 3.1: Hysteresis: (a) switching regions, (b) a typical trajectory.

viewed as a state-dependent switched system with impulse effects: the continuous dynamics are interrupted by discrete jumps in the velocity at each impact. Starting from an initial upward velocity, the ball rises and falls under gravity, repeatedly bouncing with decreasing amplitude due to energy loss at each impact. The sequence of impact times and velocities forms a geometric progression: each subsequent bounce is shorter and slower than the previous one. The impact times accumulate at a finite limit, resulting in infinitely many bounces occurring in a finite time interval. This phenomenon is known as Zeno behavior. After this accumulation point, it is natural to extend the solution by setting both height and velocity to zero, corresponding to the ball coming to rest.

- **Sliding modes**: In certain switched systems with state-dependent switching, the trajectory may exhibit a behavior in which it remains confined to a surface in the state space along which multiple vector fields are simultaneously active. This phenomenon is known as a sliding mode. It typically arises when the system trajectory reaches a switching surface $\mathcal{S}$ and the vector fields on either side of the surface point toward it. In this case, the trajectory does not leave the surface but evolves along it, generating tangent motion to the surface. This motion is referred to as sliding, and the corresponding vector field is known as the sliding vector field. From the viewpoint of switched systems, a sliding mode can be interpreted as an idealized representation of infinitely fast switching (also called chattering). Sliding modes are often undesirable in physical implementations due to wear and inefficiency caused by high-frequency switching. Nonetheless, they can also be exploited to solve control problems that are otherwise difficult, while enhancing robustness against model uncertainties and disturbances.

- **Hysteresis switching**: It is of interest to approximate sliding mode behavior while avoiding chattering and ensuring that a positive time interval separates any two consecutive switching events. The idea is to define two overlapping regions, each associated with one of the subsystems, as illustrated in Figure 3.1. The system follows $\dot{x} = f_1(x)$ in the first region and $\dot{x} = f_2(x)$ in the second. Switching occurs

only when the trajectory leaves one region and enters the other, ensuring a positive time interval between consecutive switches. This generates a piecewise constant discrete state σ that governs the switching, resulting in a hybrid system with reduced high-frequency switching [2], [16].

Note that switched systems can be viewed as a particular subclass of hybrid systems, in which the continuous state $x(t)$ evolves according to a family of differential equations selected by a discrete switching signal, while preserving the continuity of the state trajectory across switching instants. Despite their structural simplicity, switched systems can exhibit complex dynamical behaviors: even if each subsystem is stable in isolation, inappropriate switching may lead to instability. This highlights the need for specialized analytical tools capable of capturing the interaction between the switching signals and continuous dynamics. Having established how solutions to switched systems are defined and constructed, the next step is to analyze their behavior over time, with a particular focus on stability.

3.4 Stability of switched systems

Despite the structural simplicity compared to general hybrid systems, switched systems can exhibit complex dynamical behaviors. A system may become unstable due to the act of switching itself, even if all individual subsystems are stable when considered in isolation [2]. This phenomenon highlights that the stability of a switched system depends not only on the dynamics of the subsystems but also on the nature and timing of the switching. Indeed, unconstrained switching may destabilize the overall system, even if all the subsystems are stable. Conversely, appropriately designed switching rules may stabilize a switched system even when each individual subsystem is unstable. To analyze the stability of switched systems, several tools have been developed within the framework of Lyapunov theory [17]. Among the most widely adopted techniques are:

- the common Lyapunov function approach, which guarantees asymptotic stability under arbitrary switching,
- the multiple Lyapunov function method, which allows for mode-dependent analysis by assigning a distinct Lyapunov function to each subsystem,
- dwell time constraints, which impose lower bounds on the time spent in each mode, thus limiting the frequency of switching to prevent instability [18].

Two fundamental problems arise in the study of stability for switched systems:

- determine conditions under which a switched system is asymptotically stable for all admissible switching signals, including arbitrary ones;
- when stability under arbitrary switching cannot be guaranteed, identify classes of switching signals for which the system remains asymptotically stable.

The first problem is relevant when the switching mechanism is either unknown or too complicated to be useful in the stability analysis. In the context of the second problem, it is natural to distinguish between two situations. Suppose some or all of the individual subsystems are asymptotically stable. In that case, it is of interest to characterize the class of switching signals that preserve asymptotic stability. On the other hand, if all individual subsystems are unstable, then the task at hand is to construct at least one stabilizing switching signal, which may be quite difficult or even impossible. These two problems motivate a more detailed analysis of stability under different assumptions on the switching signals. In the following, the stability of switched systems is examined under both arbitrary switching and constrained switching.

3.4.1 Stability under arbitrary switching

In many practical cases, the switching signal is either unknown or varies in a way that is difficult to predict or control due to environmental factors, communication delays, or scheduling constraints. In such cases, it becomes crucial to determine whether the switched system remains stable for all possible switching signals. A widely used approach to addressing this problem involves the concept of a common Lyapunov function, which is a single function that decreases along the trajectories of all subsystems. If such a function can be found, it guarantees uniform asymptotic stability under arbitrary switching. While powerful, this approach can be conservative, as not all stable switched systems admit a common Lyapunov function. To address this limitation, alternative approaches have been developed based on additional structural properties of the subsystems. This subsection presents some of the main techniques and conditions that ensure stability in the presence of arbitrary switching signals.

- **Uniform stability via common Lyapunov functions**: Assume that all individual subsystems share a common equilibrium point, typically the origin. A necessary condition for asymptotic stability under arbitrary switching is that all of the individual subsystems are asymptotically stable. Indeed, if any subsystem is unstable for some $p \in \mathcal{P}$, then the entire switched system is unstable for $\sigma(t) \equiv p$. However, the asymptotic stability of all individual subsystems is not sufficient to guarantee the asymptotic stability of the switched system under arbitrary switching. The act of switching itself can introduce destabilizing behavior. Therefore, additional conditions must be imposed to ensure uniform asymptotic stability across all switching signals. A switched system is uniformly asymptotically stable if there exists a constant $\delta > 0$ and a function β such that for all switching signals σ, the solution of (3.5) with $|x(0)| \leq \delta$ satisfy the following inequality:

$$|x(t)| \leq \beta\left(|x(0)|, t\right) \quad \forall t \geq 0. \tag{3.13}$$

  If the function β takes the form $\beta(r, s) = cre^{-\lambda s}$ for some constants $c, \lambda > 0$, so

that the above inequality takes the form:

$$|x(t)| \leq c|x(0)|e^{-\lambda t} \quad \forall t \geq 0 \tag{3.14}$$

then the system (3.5) is called uniformly exponentially stable. If the inequalities (3.13) and (3.14) are valid for all switching signals and all initial conditions, the system is said to be globally uniformly asymptotically stable (GUAS) and globally uniformly exponentially stable (GUES), respectively. A central tool for proving GUAS is the existence of a common Lyapunov function [2], [17]. Specifically, given a positive definite continuously differentiable ($\mathcal{C}^1$) function $V : \mathbb{R}^n \to \mathbb{R}$, it is said to be a common Lyapunov function for the family of systems (3.1) if there exists a positive definite continuous function $W : \mathbb{R}^n \to \mathbb{R}$ such that the following inequality holds:

$$\frac{\partial V}{\partial x} f_p(x) \leq -W(x) \quad \forall x, \ \forall p \in \mathcal{P}. \tag{3.15}$$

This result, which generalizes Lyapunov's classical theorem to the switched setting, ensures that the rate of decrease of V is independent of the switching signal, thus guaranteeing uniform asymptotic convergence to the origin.

- **Stability under commuting subsystems**: Consider the switched linear system:

$$\dot{x}(t) = A_{\sigma(t)} x(t),$$

where $\sigma(t)$ is a piecewise constant switching signal taking values in a finite set $\mathcal{P} = \{1, 2, \ldots, m\}$, and each matrix $A_p \in \mathbb{R}^{n \times n}$, $p \in \mathcal{P}$, is Hurwitz, meaning all its eigenvalues have strictly negative real parts. Two matrices A_i and A_j commute if:

$$[A_i, A_j] := A_i A_j - A_j A_i = 0.$$

Under this condition, the corresponding matrix exponentials also commute:

$$e^{A_i t} e^{A_j \tau} = e^{A_j \tau} e^{A_i t}, \ \forall t, \tau > 0.$$

When $\mathcal{P} = 1, 2$, with commuting matrices A_1 and A_2, the solution can be expressed as:

$$x(t) = e^{A_2(\tau_1 + \tau_2 + \ldots)} e^{A_1(t_1 + t_2 + \ldots)} x(0). \tag{3.16}$$

t_i and τ_i denote the durations of the time intervals in which the switching signal equals 1 and 2, respectively. Since both matrices are Hurwitz, the corresponding matrix exponentials decay to zero exponentially as time increases, provided that the cumulative activation time of each subsystem diverges. As a result, the solution converges to the origin for any switching signal, implying global asymptotic stability. This property can also be established by constructing a common quadratic Lyapunov function. Given a set $\{A_1, A_2, \ldots, A_m\}$ of commuting Hurwitz matrices, define P_1 as the unique positive definite symmetric solution to the Lyapunov equation:

$$A_1^\top P_1 + P_1 A_1 = -I.$$

Then, for $i = 2, \ldots, m$, recursively define P_i as the unique solution to:

$$A_i^\top P_i + P_i A_i = -P_{i-1}.$$

Define the candidate Lyapunov function as:

$$V(x) = x^\top P_m x. \tag{3.17}$$

This function is a common Lyapunov function for all subsystems, since for each i the following relation is satisfied:

$$A_i^\top P_m + P_m A_i = -Q_i,$$

where Q_i is a positive definite matrix resulting from the recursive construction (in particular, $Q_1 = I$ and, for $i \geq 2$, $Q_i = P_{i-1}$). Hence, V decreases along the trajectories of every subsystem, confirming global stability.

- **Stability of switched systems with special dynamical structure**: In some cases, specific structural properties of the system can be exploited to derive less conservative or more general stability results. One notable class of structured systems is that of triangular systems. In the linear case, if $\{A_p : p \in \mathcal{P}\}$ is a compact set of Hurwitz matrices in upper-triangular form, then the switched linear system (3.6) is GUES. Under these hypotheses, the linear system $\dot{x} = A_p x$, $p \in \mathcal{P}$ admits a common quadratic Lyapunov function. The result extends naturally to lower-triangular matrices due to symmetry [2], [17]. For switched nonlinear systems, suppose that $\mathcal{P}$ is a compact set and the family of systems (3.1) is such that for each $p \in \mathcal{P}$, the vector field f_p takes the upper-triangular form:

$$f_p(x) = \begin{bmatrix} f_{p1}(x_1, x_2, \ldots, x_n) \\ f_{p2}(x_2, \ldots, x_n) \\ \vdots \\ f_{pn}(x_n) \end{bmatrix}. \tag{3.18}$$

Assume that the Jacobian matrices $\frac{\partial f_p}{\partial x}(x)$ are Hurwitz at the origin and depend continuously on p. By Lyapunov's indirect method [19], it then follows that the switched nonlinear system (3.5) is locally uniformly exponentially stable. However, a triangular structure alone does not guarantee GUAS. One way to guarantee GUAS is to require that, along solutions of the individual subsystems (3.1), each component of the state vector remain small if the subsequent components are small. Then, a sufficient condition for GUAS in such a case involves the concept of input-to-state stability (ISS) [20].

In conclusion, the stability under arbitrary switching represents a fundamental and challenging problem in the analysis of switched systems. However, arbitrary switching assumptions are inherently conservative, and ensuring stability under all possible switching

signals often imposes stringent requirements on subsystem properties. This motivates the exploration of less restrictive switching scenarios, such as stability under constrained switching, where additional information or rules governing the switching process can be exploited to obtain more precise and less conservative stability results.

3.4.2 Stability under constrained switching

When stability cannot be guaranteed under arbitrary switching, or when no common Lyapunov function exists, stability under constrained switching is considered. This approach leverages subsystem properties and switching logic, often imposing dwell time constraints to prevent instability caused by rapid switching. Another technique is the use of multiple Lyapunov functions, where suitable conditions on their evolution across switching times ensure overall system stability. These techniques make it possible to analyze a broader class of systems, including those with unstable subsystems.

- **Multiple Lyapunov functions**: Multiple Lyapunov functions are a useful tool for providing stability when a common Lyapunov function does not exist [2], [5], [21]. Each subsystem $p \in \mathcal{P}$ has its own Lyapunov function V_p, which decreases when that subsystem is active but may increase during inactivity. Stability then depends on the switching signal σ and the behavior of V_p at switching times. A sufficient condition for stability is that the sequence of values of each V_p at the switching times when subsystem p activates is decreasing. This idea can be formalized through the following sufficient condition for global asymptotic stability, which is based on the decrease of the Lyapunov functions at the switching instants. The next theorem shows that, even in the absence of a common Lyapunov function, suitable conditions on the evolution of mode-dependent Lyapunov functions can guarantee that the switched system remains globally asymptotically stable.

Theorem 3.4.1

Let (3.1) *be a finite set of globally asymptotically stable systems, and let* V_p, $p \in \mathcal{P}$ *be a family of corresponding radially unbounded Lyapunov functions. Suppose that there exists a family of positive definite continuous functions* W_p, $p \in \mathcal{P}$, *with the property that for every pair of switching times* (t_i, t_j), $i < j$, *such that* $\sigma(t_i) = \sigma(t_j) = p \in \mathcal{P}$ *and* $\sigma(t_k) \neq p$ *for* $t_i < t_k < t_j$, *then*

$$V_p(x(t_j)) - V_p(x(t_i)) \leq -W_p(x(t_i)). \tag{3.19}$$

The switched system (3.5) *is globally asymptotically stable.* □

Proof. Consider nested sublevel sets of the Lyapunov functions V_p, defining neighborhoods around the origin. By assumption (3.19), the values of V_p decrease across intervals when subsystem p is active, implying that trajectories enter progressively smaller sets. Since $\mathcal{P}$ is finite, at least one subsystem q is active

infinitely often, and the sequence $V_q(x(t_{ij}))$ converges to zero. Positive definiteness of W_p and radial unboundedness of V_p then guarantee global asymptotic stability of the switched system. □

- **Stability under slow switching**: In many practical situations, it is difficult or impossible to evaluate or estimate Lyapunov function values at every switching signal. However, under suitable constraints on the switching signal, such as dwell-time conditions, stability can still be ensured without requiring a common Lyapunov function. Dwell-time constraints limit the frequency of switching, ensuring that each subsystem has sufficient time to contribute positively to the overall stability before the next switch. Several types of constraints can be imposed on the switching signal to ensure stability. The most common include:

  – **Dwell time**: The simplest constraint is to introduce a positive number τ_d and restrict the class of admissible switching signals to signals with the property that the switching times satisfy the inequality $t_{i+1} - t_i \geq \tau_d$ for all i. The dwell time τ_d is the minimum time each mode remains active. If all subsystems are asymptotically stable, the switched system is also stable for sufficiently large τ_d, whose lower bound can be explicitly computed from the decay rates of each mode [2], [18]. Under suitable conditions, a sufficiently large dwell time also guarantees asymptotic stability of the switched system in the nonlinear case. One of the most effective approaches to establishing such results is through the use of multiple Lyapunov functions. Assume, for simplicity, that all systems in the family (3.1) are globally exponentially stable. Then for each $p \in \mathcal{P}$ there exists a Lyapunov function V_p which for some positive constants a_p, b_p, and c_p satisfies:

$$a_p|x|^2 \leq V_p(x) \leq b_p|x|^2, \tag{3.20}$$

and

$$\frac{\partial V_p}{\partial x} f_p(x) \leq -c_p|x|^2. \tag{3.21}$$

Combining (3.20) and (3.21), the following inequalities can be derived:

$$\frac{\partial V_p}{\partial x} f_p(x) \leq -2\lambda_p V_p(x), \ p \in \mathcal{P}$$

where $\lambda_p := \frac{c_p}{2b_p}$. This implies that $V_p(x(t_0 + \tau_d)) \leq e^{-2\lambda_p \tau_d} V_p(x(t_0))$ provided that $\sigma(t) = p$ for $t \in [t_0, t_0 + \tau_d)$. Consider the case with two modes, $\mathcal{P} = \{1, 2\}$, and σ takes the value 1 on $[t_0, t_1)$ and 2 on $[t_1, t_2)$. From the previous inequalities, it follows that:

$$V_2(t_1) \leq \frac{b_2}{b_1} V_1(t_1) \leq \frac{b_2}{a_1} e^{-2\lambda_1 \tau_d} V_1(t_0),$$

and furthermore:

$$V_1(t_2) \leq \frac{b_1}{a_2} V_2(t_2) \leq \frac{b_1}{a_2} e^{-2\lambda_2 \tau_d} V_2(t_1) \leq \frac{b_1 b_2}{a_1 a_2} e^{-2(\lambda_1 + \lambda_2)\tau_d} V_1(t_0). \tag{3.22}$$

It is then possible to compute an explicit lower bound on the dwell time τ_d that ensures global asymptotic stability of the switched system. In particular, a sufficient condition is:

$$\tau_d > \frac{1}{2(\lambda_1 + \lambda_2)} \log \frac{b_1 b_2}{a_1 a_2}. \tag{3.23}$$

This provides a concrete lower bound on the dwell time required to ensure stability. Even when the estimates are not quadratic, for example, when using quartic Lyapunov functions, the same reasoning remains valid, as long as there exists a positive constant μ such that the inequality:

$$V_p(x) \leq \mu V_q(x) \ \forall x \in \mathbb{R}^n, \ \forall p, q \in \mathcal{P}, \tag{3.24}$$

holds globally. If this condition holds locally, then only local asymptotic stability can be established. Dwell time constraints are particularly relevant in practical systems, where switching frequency is naturally limited by physical, computational, or communication constraints. To address this limitation, the concept of average dwell time allows for more flexible switching by bounding the average switching rate over time.

– **Average dwell time**: Instead of requiring a fixed minimum time interval between consecutive switches, the average dwell time limits the average number of switches over a given time interval. This allows for fast switching when necessary while requiring slower switching behavior on average, thus ensuring stability without compromising responsiveness. Denote the number of discontinuities of a switching signal σ on an interval (t, T) by $N_\sigma(T, t)$. A switching signal σ is said to have average dwell time τ_a if there exist two positive numbers N_0 and τ_a such that:

$$N_\sigma(T, t) \leq N_0 + \frac{T - t}{\tau_a} \ \forall \ T \geq t \geq 0. \tag{3.25}$$

At every time interval (t, T), the number of switches is strictly bounded by $\frac{(T-t)}{\tau_a}$, thus excluding frequent instances of fast switching. It is of interest to investigate whether the property of asymptotic stability under sufficiently large dwell time can be extended to switching signals satisfying an average dwell time condition.

Theorem 3.4.2

Consider the family of systems (3.1). *Suppose that there exist* $\mathcal{C}^1$ *functions* $V_p : \mathbb{R}^n \to \mathbb{R}$, $p \in \mathcal{P}$, *two class* $\mathcal{K}_\infty$ *functions* α_1 *and* α_2, *and a positive number* λ_0 *such that:*

$$\alpha_1(|x|) \leq V_p(x) \leq \alpha_2(|x|) \ \forall x, \ \forall p \in \mathcal{P} \tag{3.26}$$

and

$$\frac{\partial V_p}{\partial x} f_p(x) \leq -2\lambda_0 V_p(x) \ \forall x, \ \forall p \in \mathcal{P}. \tag{3.27}$$

Suppose also that (3.24) *holds. Then the switched system* (3.5) *is globally asymptotically stable for every switching signal* σ *with the following average dwell time:*

$$\tau_a > \frac{log\mu}{2\lambda_0}. \tag{3.28}$$

□

If all systems in the family (3.1) are globally exponentially stable, then for each $p \in \mathcal{P}$ there exists a Lyapunov function V_p which for all x satisfies $\alpha_{1,p}(|x|) \leq V_p(x) \leq \alpha_{2,p}(|x|)$ and:

$$\frac{\partial V_p}{\partial x} f_p(x) \leq -W_p(x), \tag{3.29}$$

where W_p is positive definite. The average dwell time condition imposes a bound on the number of switches over any time interval, not only those starting from the initial time. This ensures that the state trajectory exhibits uniform decay properties across the entire time horizon. In the case of linear systems, this property also guarantees the boundedness of induced input-output norms, which is essential for performance analysis in the presence of external inputs.

While time-based constraints, such as dwell time and average dwell time, limit the switching frequency uniformly over time, another class of strategies bases the switching decisions on the current state of the system. This leads to the concept of stability under state-dependent switching.

- **Stability under state-dependent switching**: In many applications, the switching logic is not purely time-driven but explicitly depends on the system state. In a state-dependent switching scheme, a switch event occurs only when the system trajectory crosses a predefined surface in the state space, known as the switching surface. Each subsystem affects the system only within the region where it is active. A common approach to ensure stability in this setting is to associate a Lyapunov function $V_p(x)$ with each mode $p \in \mathcal{P}$, and define the switching signal so that the active subsystem at each time either selects the mode minimizing $V_p(x)$ or the one in which it decreases most rapidly. Such strategies can lead to global asymptotic stability even without enforcing dwell time conditions, provided that the Lyapunov functions satisfy appropriate compatibility and decrease conditions at the switching surfaces. The following example illustrates this phenomenon.

Example 3.4.1

Consider matrices A_1 *and* A_2 *of the form:*

$$A_1 := \begin{bmatrix} \gamma & -1 \\ 2 & \gamma \end{bmatrix}, \; A_2 := \begin{bmatrix} \gamma & -2 \\ 1 & \gamma \end{bmatrix} \tag{3.30}$$

where γ *is a negative number sufficiently close to zero. Define a state-dependent*

switched linear system in the plane by:

$$\dot{x} = \begin{cases} A_1 x \text{ if } x_1 x_2 \leq 0 \\ A_2 x \text{ if } x_1 x_2 > 0. \end{cases} \tag{3.31}$$

One can verify that the function $V(x) := x^\top x$ satisfies $\dot{V} < 0$ along all nonzero solutions of this switched system. Therefore, the original is globally asymptotically stable. Notably, neither A_1 nor A_2 needs to be asymptotically stable on its own. This is because the Lyapunov function only needs to decrease along solutions of each subsystem in an appropriate region, and not necessarily everywhere. Even if $\gamma = 0$, V still decreases along all non-zero solutions of the switched system (3.31). By continuity, the system remains stable even for small $\gamma > 0$, despite the instability of each subsystem. If one changes the switching rule to:

$$\dot{x} = \begin{cases} A_1 x \text{ if } x_1 x_2 > 0 \\ A_2 x \text{ if } x_1 x_2 \leq 0, \end{cases}$$

then the resulting switched system becomes unstable. This highlights the critical role of the switching rule in determining the global behavior. The state-dependent switching strategy considered in the above example can be converted to time-dependent ones, because the time needed for a linear time-invariant system to cross a quadrant can be explicitly calculated and is independent of the trajectory. In cases where a single Lyapunov function is insufficient for stability analysis, multiple Lyapunov functions can be used. □

- **Stabilization by state-dependent switching**: Consider a finite family of continuous-time linear systems. The objective is to design a state-dependent switching law that ensures the asymptotic stability of the resulting switched system. If one subsystem is asymptotically stable, stabilization is trivial via constant switching. However, more interesting scenarios arise when none of the individual subsystems is stable. A natural first case to examine involves stable convex combinations of the subsystem matrices.

  - **Stable convex combinations**: Even if the individual subsystems are not globally stabilizing, stability can be achieved through a convex combination of their dynamics. In particular, if there exists $\alpha \in (0, 1)$ such that the matrix $A := \alpha A_1 + (1 - \alpha) A_2$ is Hurwitz, then the switched system can be stabilized by a suitable state-dependent strategy. This condition guarantees the existence of a quadratic Lyapunov function $V(x) = x^\top P x$ whose derivative is negative in conic regions of the state space associated with each subsystem. Defining:

$$\Omega_i := \{x : x^\top (A_i^\top P + P A_i) x < 0\}, \ i = 1, 2,$$

one can design a hysteresis-based switching law: the active subsystem remains unchanged while the state stays inside Ω_i, and a switch occurs only when the trajectory exits this region. This prevents chattering and ensures exponential decay of the Lyapunov function. As a consequence, the switched system satisfies:

$$\dot{V}(x) < -\epsilon |x|^2 \ \forall x \neq 0, \tag{3.32}$$

for some $\epsilon > 0$, which implies quadratic stability, a stronger property than global asymptotic stability for switched linear systems. The same reasoning extends to cases with more than two subsystems. If a Hurwitz convex combination can be found for a subset of the system matrices, the same construction applies with minor modifications. Moreover, it can be shown that the existence of a quadratic Lyapunov function for a two-mode state-dependent switched system necessarily implies the existence of a Hurwitz convex combination of the two matrices. Thus, in this setting, the convex combination criterion is both sufficient and necessary for quadratic stabilization.

– **Unstable convex combinations**: In some cases, no convex combination of the subsystem dynamics is stable. In such cases, arguments based on convexity alone are insufficient. Nevertheless, global asymptotic stabilization via state-dependent switching can still be achieved by exploiting the nonlinear nature of the switching logic. A common approach is to use multiple Lyapunov functions. Each subsystem is associated with its own Lyapunov function, decreasing in a suitable conic region of the state space. If the union of these regions covers $\mathbb{R}^n \setminus \{0\}$, a switching strategy can be defined that always selects the subsystem for which the corresponding Lyapunov function decreases. Formally, let:

$$V_1(x) = x^\top P_1 x, \quad V_2(x) = x^\top P_2 x, \quad P_i = P_i^\top > 0.$$

If the following conditions hold:

$$x^\top (A_1^\top P_1 + P_1 A_1) x < 0 \ \text{ whenever } \ x^\top P_1 x \leq x^\top P_2 x \text{ and } x \neq 0, \tag{3.33}$$

$$x^\top (A_2^\top P_2 + P_2 A_2) x < 0 \ \text{ whenever } \ x^\top P_1 x \geq x^\top P_2 x \text{ and } x \neq 0, \tag{3.34}$$

then a stabilizing switching signal can be defined as:

$$\sigma(t) := \arg \min_{i \in \{1,2\}} V_i(x(t)).$$

Assuming no sliding motion occurs on the switching surface $S := \{x : x^\top P_1 x = x^\top P_2 x\}$, the function V_σ is continuous and decreases along solutions, ensuring global asymptotic stability.

3.5 The interconnection between switching systems and hybrid systems

Switching systems and hybrid systems are two fundamental frameworks for modeling dynamical systems exhibiting both continuous evolution and discrete changes. Although often studied separately in the literature [2], [3], [22], these frameworks share a strong interconnection but also important distinctions. This section highlights their main similarities and differences in terms of modeling, solution concepts, stability analysis, and practical applications.

- **Modeling framework**: Switching systems can be viewed as a particular class of hybrid systems where the discrete dynamics are limited to changes in the active mode, without involving additional discrete state variables or events. In general, a switching system is described by a finite set of differential equations, each associated with a discrete mode $q \in \mathcal{Q}$, where $\mathcal{Q}$ is a finite set. The continuous state $z(t) \in \mathbb{R}^n$ evolves according to:

$$\dot{z} = f_{\sigma(t)}(z(t)),$$

  with mode changes driven by the switching signal $\sigma(t)$. In a hybrid framework, the state is $x = \begin{bmatrix} z & q \end{bmatrix}^\top$, with z evolving during flows and q changing at jumps. Thus, the switching systems embed naturally into hybrid systems. Hybrid systems, however, encompass a much broader modeling paradigm. Beyond mode indices, they may include additional discrete states, guards, and reset maps that allow autonomous transitions triggered by the continuous state. This structure allows modeling phenomena such as instantaneous state resets, impulses, hysteresis, or logic-based rules, which cannot be represented within the classical switching framework. Another key distinction concerns the triggers for discrete changes. In switching systems, transitions are usually driven by an external signal, while in hybrid systems, they may occur autonomously when the trajectory intersects a guard set. These differences also affect analysis and design. When the switching signal is known or externally imposed, switching system offer a simpler description, while hybrid models are advantageous when timing constraints or state-triggered events must be captured explicitly. A practical illustration of the interplay between switching and hybrid systems is found in power electronics, where converters switch between different circuit topologies. If the switching instants are externally controlled (e.g., by a PWM signal), the system can be modeled as a switching system. However, if the switching depends on the state (e.g., voltage or current crossing a threshold), a hybrid model with autonomous transitions better captures the behavior.

- **Concept of solution**: The notion of solutions differs fundamentally between switching and hybrid systems due to the nature of their discrete dynamics and how these interact with the continuous evolution. For switching systems, solutions are defined

piecewise on time intervals where the switching signal σ remains constant. In each interval, the system behaves as a standard continuous-time dynamical system following a differential equation corresponding to the active mode. Therefore, the overall solution is obtained by concatenating the trajectories of these continuous subsystems at the switching instants $\sigma(t)$. In contrast, hybrid systems adopt a more general notion of solution based on hybrid time domains, which allow rigorous modeling of the interplay between continuous flows and discrete jumps. Solutions are defined as hybrid arcs $(t, j) \mapsto x(t, j)$ where t represents the ordinary time variable and j counts the number of discrete jumps. This formalism explicitly captures both continuous evolution (on intervals of constant j) and discrete transition (where j increments while t may stay constant). Consequently, the hybrid system solution concept generalizes the switched system one, providing a unified framework for describing trajectories that combine continuous and discrete behaviors in a state-dependent way.

- **Stability analysis**: For switching systems, stability analysis typically focuses on conditions ensuring stability under arbitrary switching, constrained switching (e.g., minimum dwell-time), or switching signals belonging to a specified class. Common tools include multiple Lyapunov functions, average dwell-time conditions, and specific stability theorems for switched systems. For hybrid systems, stability theory is broader. It accounts for both flows and jumps, using hybrid Lyapunov functions and invariance principles to handle resets, impulses, and logic-based transitions. In practice, the stability analysis of switching systems can often be embedded within the more general framework of hybrid systems, especially when discrete transitions depend on state conditions or timing constraints, allowing for a unified approach to stability verification.

- **Applications and modeling flexibility**: Switching systems are typically used when mode changes are planned or externally commanded, as in gain-scheduled controllers, supervisory schemes, or fault-tolerant designs. Hybrid systems, on the other hand, are better suited for scenarios where discrete changes arise autonomously from the evolution of the system state or logical conditions. Examples include automotive transmissions with gear changes triggered by vehicle speed, robotic systems with contact or impact dynamics, power electronics converters with state-triggered switching (e.g., current-mode control), and cyber-physical systems with safety logics or mode-dependent constraints. The modeling capabilities of hybrid systems, including guards, resets, and autonomous jumps, enable richer and more accurate descriptions of complex real-world phenomena that cannot be captured within the classical switching systems framework alone. This modeling flexibility makes hybrid systems a powerful tool for analyzing and designing controllers for modern engineering systems where continuous and discrete dynamics interact.

3.6 Summary and motivation for applications

The theoretical foundations developed in the first part of this thesis are essential for the analysis and design of advanced control strategies for systems that combine continuous dynamics and discrete switching behaviors, as commonly encountered in electric drives and power electronic converters. Based on this theoretical background, the second part of the thesis focuses on power converter control, where the hybrid nature of the systems is evident due to switching operations and state-dependent logic. This includes DC-DC synchronous boost converters, multi-input converters, and differential boost inverters, with a particular focus on challenges related to switching behavior and system robustness. These systems inherently combine continuous-time dynamics (e.g., current and voltage dynamics) with discrete decision logic (e.g., switching modes or protection mechanisms), making the hybrid systems framework particularly suitable. The third part addresses control strategies for electric drives, which also exhibit hybrid features due to mode switching, commutation events, and interactions between estimation and control processes, often involving logic-driven transitions based on measured or estimated quantities. The transition from theoretical analysis to advanced control applications highlights the flexibility and effectiveness of hybrid system modeling and control, demonstrating its capability to address complex behavior arising from the interaction of continuous and discrete dynamics.

Part II
Applications in Power Electronics

Chapter 4

Min-type hybrid control strategy of DC-DC boost converters

Abstract

This part of the thesis presents the hybrid control of a synchronous boost converter operating in continuous conduction mode (CCM), focusing on a min-type control strategy formulated within a hybrid dynamical systems framework. The converter is modeled as a hybrid system, where the continuous-time evolution of the inductor current and output voltage is interleaved with discrete switching actions driven by a state-dependent control logic. The proposed strategy employs a nonlinear switching surface to induce a change in topology within the converter, and is analyzed using a sliding mode control (SMC) approach. Subsequently, the min-type strategy is modified by a hybrid control formulation, which introduces a hysteresis band and a dwell-time constraint. These additions guarantee finite switching frequency during start-up and steady-state operation, respectively, and reduce component stress and enable practical digital implementation. The hybrid control strategy is implemented digitally through a microprocessor, which processes discrete-time samples of inductor current and capacitor voltage to generate the switching signal that activates the power switch. Experimental results in a prototype validate the effectiveness of the proposed control strategy, demonstrating accurate regulation, fast dynamic response, and consistent hybrid behavior across a wide range of operating conditions, such as transient time and steady-state.

Contents

4.1 Motivation and literature review

Power converters, specifically DC-DC converters, play a crucial role in modern electrical and electronic systems due to their capability to efficiently transform voltage levels to accommodate varying load and source requirements. These devices are widely used in applications such as renewable energy systems, electric vehicles, and portable electronics [23]. Effective control of a DC-DC converter is critical for ensuring the overall system's stability, reliability, and efficiency [24]. However, these converters are inherently nonlinear systems, due to the switching behavior of semiconductor devices. The switching behavior introduces hybrid dynamics, where the continuous-time evolution of the system states is interrupted with discrete events corresponding to mode transitions [1]. Such a hybrid structure necessitates control methodologies capable of simultaneously addressing the continuous and discrete aspects of the system to achieve optimal performance and robustness. The main objectives in controlling a DC-DC converter include maintaining a regulated output voltage within limits despite variations in input voltage and load conditions, ensuring system stability under frequent switching action, optimizing energy efficiency by minimizing losses, and dynamic performance by achieving fast transient response and reduced overshoot during load input changes [2], [24], [25]. Traditionally, control strategies, such as voltage-mode control and current-mode control, are based on continuous-time models and implemented through analog or digital feedback loops. These approaches treat the system as approximately continuous and often rely on linearization around steady-state operating points. Although widely adopted, these approaches can face limitations due to system nonlinearities, mode transitions, and parameter uncertainties. In systems where continuous and discrete dynamics coexist, like power converters, this approach enables more accurate analysis and control. Boost converters are widely employed in industrial applications such as battery charging and renewable energy systems, owing to their high power density and soft-switching capabilities [23]. However, traditional control approaches for such converters, such as frequency and amplitude modulation, suffer from nonlinear control-to-output characteristics, which complicate control design [24]. As an alternative, state-plane control approaches, where the switching decision is based on current and voltage measurements within the converter, can improve controller design. These approaches simplify system dynamics, improve regulation performance, and offer straightforward implementation. In recent years, the control problem for

switching power electronics has been successfully expressed as a hybrid dynamical control design problem, wherein the system state comprises both physical quantities, such as voltage and current that take real values, and logical quantities, such as the position of switches that take discrete values [1]. Within this hybrid framework, the continuous state evolution represents the continuous-time behavior of currents and voltages during intervals where the logical states remain constant. The discrete state evolution, on the other hand, corresponds to instantaneous changes in the switch position or modes, with the physical states remaining unchanged during these jumps. This hybrid formalism provides a rigorous foundation for control design, connecting the gap between practical power converters and advanced system theory. To better understand the role of hybrid control in complex energy conversion systems, this chapter focuses on a single-input single-output (SISO) topology, namely the synchronous boost converter. The boost converter represents an ideal starting point for hybrid control design due to its relatively simple structure and well-understood nonlinear behavior, while still exhibiting the hybrid characteristics that make such control strategies necessary. Analyzing this converter allows us to isolate and study the key features of hybrid control, such as mode transitions, continuous-discrete interaction, and state-dependent switching, in a controlled setting. Moreover, the SISO nature of the system allows for a focused implementation of min-type hybrid control without the additional complexity of source coordination, which is addressed in the next chapter on multi-input converters. This progression, from SISO to multi-input systems, and later to inverted-based output control, follows the natural evolution of real-world power conversion architectures. To demonstrate this application of hybrid system theory to SISO converters, the next section introduces a min-type control strategy of a DC-DC synchronous boost converter, which proposes a novel hybrid control method for power converters that leverages the state-plane framework in conjunction with an input-dependent coordinate transformation within hybrid systems theory to achieve efficient, robust, and high-performance control in power electronics converters. Non-minimum phase converters, such as boost converters, are traditionally controlled in industrial applications by a cascade regulation scheme [24]. This approach typically consists of an inner loop regulating the inductor current and an outer loop regulating the output voltage by providing an appropriate reference to the inner loop. Implementations often rely on analog circuits or commercial chips and differ in the processing of the inductor current, using peak, valley, or average current values, as well as the modulation technique, which can be pulse-width modulation (PWM) or hysteresis [26], [27]. Digital control of DC-DC converters has gained momentum in recent years due to advances in digital processors, enabling implementations of cascade control with PWM or hysteresis modulation. Inner loop control strategies range from current prediction methods, which reduce continuous sampling requirements, to discrete-time SM control [28], [29]. In conventional methods, the transition between switch states is triggered by comparing the inductor current waveform indices with predefined thresholds, often independently of the

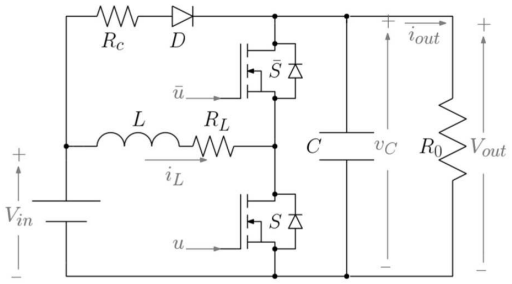

Figure 4.1: Synchronous boost converter.

output voltage. In contrast, the min-type control approach drives the switching based on a combined state error involving both voltage and current, and optimizing the system's response through an online minimization procedure over the state-space evolution [30], [31]. The min-type strategy, when formulated within a hybrid dynamical systems framework, addresses limitations such as variable switching frequency and startup transients, providing a systematic method for digital implementation and enhanced regulation performance and robustness, while inherently ensuring stability without requiring additional design conditions.

4.2 Dynamic model of synchronous boost converter

The synchronous boost converter depicted in Fig. 4.1 can be described by the set of parameters (V_{in}, L, C, R_0, R_L), where V_{in} is the input voltage, L and C are the inductance and capacitance, respectively, R_0 is the load resistance, and R_L is the parasitic resistance of the inductor. The dynamic behavior of the converter in CCM can be described in compact form as follows:

$$\frac{di_L}{dt} = -\frac{R_L}{L} i_L - \frac{v_C}{L}(1-u) + \frac{V_{in}}{L}, \tag{4.1}$$

$$\frac{dv_C}{dt} = \frac{i_L}{C}(1-u) - \frac{1}{CR_0} v_C, \tag{4.2}$$

where i_L is the inductor current, v_C is the capacitor voltage, and u is a control binary signal ($\bar{u} = 1 - u$) such that $u = 1$ ($\bar{u} = 0$) during T_{on}, interval of energy absorption from the input source, and $u = 0$ ($\bar{u} = 1$) during T_{off}, interval of energy transfer to the output load. Note that the converter shown in Fig. 4.1 is bidirectional because it allows the flow of power in both directions, from the input to the load and vice versa. Therefore, the inductor current can assume negative values. For this reason, the converter is analyzed only in CCM because the discontinuous mode is automatically not allowed. On the other hand, diode D charges the capacitor during start-up, avoiding a large inrush current. Note that this diode is not active when the output voltage becomes higher than the input one. Moreover, the charging resistance R_c does not affect the efficiency of the system, because during normal operation, the output voltage is always higher than the input one, and the diode D blocks the current from flowing through R_c. The switching converter's

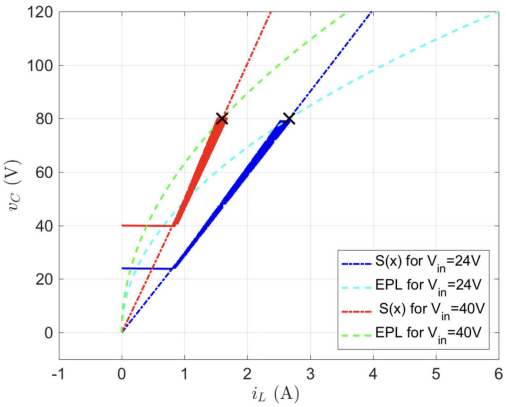

Figure 4.2: Simulation of the converter start-up for $V_{\text{in}} = 24V$ (blue trajectory) and $V_{\text{in}} = 40V$ (red trajectory) and min-type control with nonlinear switching surface $S(x)$.

equilibrium point locus (EPL) is the set of points in the plane $i_L - v_C$ that the converter state variables can take in steady-state. In the converter considered here, the EPL is given by the following equation:

$$v_C^2 + R_L R_0 i_L^2 - R_0 V_{in} i_L = 0. \tag{4.3}$$

Understanding the EPL is fundamental for designing the control law and predicting the steady-state behavior of the converter.

4.3 Design of the min-type hybrid control law

The min-type control strategy continuously evaluates a set of candidate discrete control inputs and selects the one that minimizes a state-dependent cost function, typically associated with regulation error or energy efficiency. This selection mechanism induces discrete switching behavior, resulting in a hybrid dynamical system where continuous-time evolution of the converter's states is interrupted by discrete switching events of the control input [30], [31]. Direct implementation of the min-type control strategy may lead to infinitely fast switching, especially during transient responses and steady-state operation, which is physically infeasible and can cause excessive stress in the power components. To mitigate this limitation, the control strategy is extended using a hybrid control framework that incorporates two critical features:

- a hysteresis band around the switching surface to eliminate the chattering;
- a dwell-time constraint that enforces a minimum time interval between consecutive switching events.

This hybrid approach ensures a finite switching frequency, reduces component stress, and enhances overall system efficiency, while also providing a computationally efficient method to drive the system to the desired equilibrium with guaranteed convergence properties, without requiring explicit trajectory planning or solving differential equations online. This

makes the min-type control law a suitable alternative to more complex strategies such as nonlinear model predictive control (MPC) in real-time applications.

4.3.1 Mathematical formulation and optimization

The min-type control strategy based on a nonlinear switching surface can be expressed as follows:

$$\sigma(x) = \arg \min_{u\in\{0,1\}} (x - X_E)^\top P(A_u x + BV_{\text{in}}). \tag{4.4}$$

Matrices A_u and B relate the state vector $x = \begin{bmatrix} i_L & v_C \end{bmatrix}^\top$ and its time derivative, i.e., $\dot{x} = A_u x + BV_{in}$. Specifically, $B = \begin{bmatrix} \frac{1}{L} & 0 \end{bmatrix}^\top$, and matrices A_u are:

$$A_0 = \begin{bmatrix} -\frac{R_L}{L} & -\frac{1}{L} \\ -\frac{1}{C} & -\frac{1}{R_0 C} \end{bmatrix} \text{ for } u = 0 \ (T_{\text{off}} \text{ interval}), \tag{4.5}$$

$$A_1 = \begin{bmatrix} -\frac{R_L}{L} & 0 \\ 0 & -\frac{1}{R_0 C} \end{bmatrix} \text{ for } u = 1 \ (T_{\text{on}} \text{ interval}). \tag{4.6}$$

$X_E(I_E, V_E)$ is the desired equilibrium point in EPL, and P is a symmetric positive-definite matrix given by:

$$P = \begin{bmatrix} \alpha & \beta \\ \beta & \gamma \end{bmatrix}, \tag{4.7}$$

and satisfying:

$$A^\top P + PA_u + 2Q \leq 0, \quad u = 0, 1 \tag{4.8}$$

where Q is an auxiliary symmetric positive-definite matrix. To find a strictly positive definite matrix P such that (4.8) is satisfied, the following optimization problem is solved:

$$\begin{aligned} P^* = \arg \min_{P=P^\top} & \text{ trace}(P) \text{ subject to} \\ & A_u^\top P + PA_u + 2Q \leq 0, \ \forall u \in \{0, 1\} \\ & P \geq I_2. \end{aligned} \tag{4.9}$$

Inequality $P \geq I_2$ has been used instead of $P > 0$. This choice has been made to avoid numerical problems and solutions that lead to small values of P because its trace is minimized. In any case, any matrix P solution to (4.9) is also a solution to the problem with $P > 0$ because it has relaxed constraints. The cost function J of the transition from the initial state $x(0)$ to the equilibrium point X_E is bounded and given by:

$$J = \int_0^\infty (x(t) - X_E)^\top Q\,(x(t) - X_E)\,dt < (x(0) - X_E)^\top P\,(x(0) - x_e)\,. \tag{4.10}$$

Note that $X_E = \begin{bmatrix} I_E & V_E \end{bmatrix}^\top$, where I_E and V_E are the mean values of the inductor current i_L and output voltage V_{out} at steady-state, respectively. Moreover, the minimization of the trace of P, as given in (4.9), leads to the minimization of the cost function J.

The first term in (4.10) is the time integral of the weighted square error of the state vector trajectory for the desired equilibrium point, while the second term is the weighted Euclidean distance between the start point and the equilibrium point.

4.3.2 Switching surface and simulation

The interpretation of (4.4) results in two possible cases:

$$\sigma(x) = 0 \iff (x - X_E)^\top P(A_0 x + BV_{\text{in}}) = M_0 \text{ is minimum,} \tag{4.11a}$$

$$\sigma(x) = 1 \iff (x - X_E)^\top P(A_1 x + BV_{\text{in}}) = M_1 \text{ is minimum.} \tag{4.11b}$$

By defining the switching surface as $S(x) = M_1 - M_0$, from equation (4.11a) the following expression is obtained:

$$S(x) = (x - X_E)^\top P(A_1 - A_0)x. \tag{4.12}$$

Therefore, the control law (4.4) can be interpreted as follows:

$$u = 0 \text{ if } S(x) > 0, \; u = 1 \text{ if } S(x) < 0. \tag{4.13}$$

Introducing the expression of X_E, P, A_0 and A_1 in (4.12) yields:

$$S(x) = \frac{\beta v_C^2}{L} - \frac{\beta i_L^2}{C} + \left(\frac{\alpha}{L} - \frac{\gamma}{C}\right) i_L v_C - \left(\frac{\alpha I_E}{L} + \frac{\beta V_E}{L}\right) v_C + \left(\frac{\beta I_E}{C} + \frac{\gamma V_E}{C}\right) i_L. \tag{4.14}$$

The expression (4.14) is a conic curve that passes through the origin of the plane $i_L - v_C$

Table 4.1: Circuit parameters values

Symbol	Value	Unit
V_{in}	[24, 40]	V
L	470	μH
R_L	3	mΩ
C	20	μF
R_0	[100, 150]	Ω

and the equilibrium point $X_E(I_E, V_E)$. Fig. 4.2 shows a MATLAB simulation of the converter start-up in the plane $i_L - v_C$ for the set of parameters C, L, and R_L shown in Table 4.1, $R_0 = 100\Omega$, $V_E = 80V$, and two possible input voltages, i.e., $V_{\text{in}} = 24V$ (blue trajectory) and $V_{\text{in}} = 40V$ (red trajectory). Matrix P used in the simulation is the solution of the optimization problem (4.9), with $Q = \text{diag}(R_L, \frac{\rho}{R_0})$ and $\rho = 1000$,

$$P^* = \begin{bmatrix} \alpha^* & \beta^* \\ \beta^* & \gamma^* \end{bmatrix} = \begin{bmatrix} 2.3108 & -0.0097 \\ -0.0097 & 1.0001 \end{bmatrix}. \tag{4.15}$$

In both cases, the initial voltage of the output capacitor coincides with the input voltage to reduce the inrush current as demonstrated in [32]. The proposed switching surface leads to a negligible inrush current regardless of the input voltage value. This is a significant advantage during the start-up phase, where an uncontrolled inrush current may otherwise damage the converter or reduce its efficiency. Also, it has to be pointed out that the

coordinate V_E is the same in both cases, while the coordinate I_E changes according to $I_E = \frac{v_E^2}{R_0 V_{\text{in}}}$, neglecting the losses in the resistor R_L. This switching surface defines a nonlinear boundary in the $i_L - v_C$ state-space that determines the active control input. Specifically, it separates the operating region into two domains, each corresponding to one of the binary control actions. The control law selects $u = 1$ or $u = 0$ based on which trajectory leads to a faster convergence to the desired equilibrium point in a quadratic sense.

4.3.3 Comparison with conventional control methods

Equations (4.13) and (4.14) have been introduced to give an interpretation of the control strategy in the framework of a nonlinear switching surface, which might initially be interpreted as the SMC approach. However, several fundamental differences must be emphasized. The proposed control technique is formulated using a new framework of hybrid dynamical systems. Unlike classic SMC, where the control law is directly derived from a discontinuous feedback rule to maintain the state on a predefined sliding surface, the control input u in this case is obtained via the arg-min strategy in equation (4.4). This optimization-based selection ensures that the system always follows the direction that minimizes the local quadratic cost in the state space. Moreover, in strategy (4.4) there is embedded a second optimization problem related to the selection of matrix P, obtained by solving the convex combination problem in (4.9). In particular, the matrix Q can be arbitrarily chosen to provide any performance level of the converter by suitably weighting both output voltage and inductor current errors. For instance, selecting a scalar weight ρ such that $\frac{\rho}{R_0} > R_L$ (where $Q = \text{diag}(R_L, \frac{\rho}{R_0})$ as in equation (4.8)) implies that higher priority is assigned to the output voltage error compared to the inductor current error. This choice typically results in faster voltage regulation, possibly at the cost of a larger current ripple. Once Q is selected, the optimal matrix P is computed by minimizing the trace of P, which in turn minimizes the upper bound of the cost function J in equation (4.10). Traditional SMC techniques do not include any optimization procedure, nor do they provide an explicit performance tuning mechanism based on a cost function. The min-type control law described above offers an effective trade-off between implementation simplicity and dynamic performance. Unlike conventional PWM strategies based on fixed or modulated duty cycles, the hybrid control approach responds instantaneously to the system's state, ensuring faster responses and improved regulation in the presence of disturbances. Moreover, its structure enables real-time implementation on embedded hardware without the computational overhead associated with MPC. The analysis of the switching surface provides an intuitive and graphical understanding of the control action and its relation to the design parameters and equilibrium point. This naturally leads to a hybrid system representation, where the continuous dynamics of the converter are combined with discrete-time logic for switching control decisions. In the following, a

formal hybrid model is introduced to describe this interaction and support the real-time implementation of the proposed strategy.

4.4 Hybrid system approach with hysteresis-based control

A practical implementation of the min-type control law described in (4.13) requires careful implementation of the switching mechanism. In particular, the idealized control law leads to infinitely fast switching between the two modes $u = 0$ and $u = 1$, which is not feasible in physical systems due to limitations in the power stage and switching devices. To mitigate this, a hysteresis mechanism is introduced around the switching surface to enforce a finite and bounded switching frequency, making the control strategy suitable for real-world applications. The hysteresis can be implemented in two main ways:

- analogically, through dedicated electronic components [33];
- digitally, by leveraging microcontroller features such as comparators and timers [34].

However, the resulting closed-loop behavior with hysteresis only approximates the ideal min-type strategy. The resulting dynamics and the sliding dynamics become equivalent to the ideal case only when the hysteresis width tends to zero. This motivates a more rigorous treatment of the system using a hybrid systems framework, where both the continuous evolution of the state and the discrete switching logic are captured in a unified mathematical model. A preliminary attempt to indirectly introduce a hysteresis for a switched affine system was explored in [35] under the perspective of a hybrid control formulation.

4.4.1 Hybrid system representation

The synchronous boost converter described by (4.1)-(4.3) can be considered as a switching system, i.e., a differential equation whose right-hand side dynamics is chosen from a family of functions based on a switching signal $u \in [0, 1]$. This class of systems can naturally be contextualized in the hybrid dynamical system framework, which is well-suited for modeling circuits that combine continuous-time with discrete-time dynamics. According to the hybrid system formalism (see Chapter 2), the system is defined by:

$$\mathcal{H} \quad \begin{cases} z \in \mathcal{C} & \dot{z} = f(z), \\ z \in \mathcal{D} & z^+ = g(z). \end{cases} \tag{4.16}$$

As suggested by (4.16), the state of the hybrid system z can evolve according to a differential equation $\dot{z} = f(z)$, (where the vector field f is called flow map) if the state z belongs to the flow set $\mathcal{C}$, or it can change according to a difference equation $z^+ = g(x)$ (where the vector field g is called jump map) is the state z belongs to the jump set $\mathcal{D}$.

The notation z^+ is the value of the state after the jump, i.e., the value assumed by $g(z)$ when z belongs to $\mathcal{D}$. In our case, the hybrid state vector is defined as:

$$z = \begin{bmatrix} i_L & v_C & u \end{bmatrix}^\top. \tag{4.17}$$

The dynamics are given by:

$$f(z) = \begin{bmatrix} -\frac{R_L}{L} i_L - \frac{v_C}{L}(1-u) + \frac{V_{\text{in}}}{L} \\ -\frac{i_L}{C}(1-u) - \frac{1}{CR_0} v_C \\ 0 \end{bmatrix}, \quad g = \begin{bmatrix} i_L \\ v_C \\ 1-u \end{bmatrix}. \tag{4.18}$$

In this formulation, the control input u is treated as a discrete state variable, which remains constant during flows ($\dot{u} = 0$), and toggles its value during jumps.

4.4.2 Design of flow and jump sets

To properly define the hybrid behavior of the converter, the sets $\mathcal{C}$ and $\mathcal{D}$ must be chosen to enforce the desired switching logic. Based on the approach proposed in [35], the following definitions are used:

$$\mathcal{C} := \left\{(x,u) : (x - X_E)^\top P(A_u x + B V_{\text{in}}) \leq \eta (x - X_E)^\top Q (x - X_E)\right\}, \tag{4.19}$$

$$\mathcal{D} := \left\{(x,u) : (x - X_E)^\top P(A_u x + B V_{\text{in}}) > \eta (x - X_E)^\top Q (x - X_E)\right\}, \tag{4.20}$$

where $0 < \eta \leq 1$ is a tunable scalar parameter used to introduce hysteresis, and $Q = \text{diag}(R_L, \frac{\rho}{R_0})$, with $\rho > 0$. Note that η is strictly greater than zero to avoid Zeno behaviors. As proven in [35, Th. 1], the choice $\eta > 0$ precludes Zeno behavior, ensuring well-posedness of the hybrid model. The scalar η controls the sensitivity of the switching mechanism:

- for small η, the switching surface is close to the ideal one, leading to more frequent switching;
- for η closer to 1, a larger hysteresis band is introduced, reducing the switching frequency and making the behavior more robust against noise and uncertainties.

The switching logic defined by the flow and jump sets in (4.19)-(4.20) ensures that the system remains in the current converter topology when (4.19) holds, and changes to the alternative topology when (4.20) is satisfied. This construction, based on the hybrid systems framework, provides a systematic way to implement hysteresis consistent with the min-type control law and guarantees the avoidance of undesirable behaviors such as Zeno phenomena (i.e., infinitely fast switching in finite time).

4.4.3 Hysteresis band and limit cycle analysis

The introduction of hysteresis does not compromise the convergence guarantees provided by the original min-type strategy, while allowing practical implementation with controlled

switching frequency. By interpreting the control law (4.19)-(4.20) in the i_L-v_C plane as in the case of the min-type control (4.13), the hybrid system dynamics can be visualized as trajectories that cross a nonlinear conic switching surface with an added hysteresis band, which smooths the transitions between topologies and improves robustness. Defining $S_0(x)$ and $S_1(x)$ as:

$$S_0(x) = (x - X_E)^\top P(A_0 x + BV_{\text{in}}) + \eta(x - X_E)^\top Q(x - X_E), \tag{4.21}$$

$$S_1(x) = (x - X_E)^\top P(A_1 x + BV_{\text{in}}) + \eta(x - X_E)^\top Q(x - X_E). \tag{4.22}$$

The corresponding expressions of $S_0(x)$ and $S_1(x)$ in terms of state variables and system parameters are given by:

$$S_1(x) = \eta R_L(i_L - I_E)^2 + \eta\frac{\rho}{R_0}(v_C - V_E)^2 + (\alpha\frac{V_{\text{in}} - R_L i_L}{L} - \frac{\beta v_C}{CR_0})(i_L - I_E), \tag{4.23}$$

$$S_0(x) = S_1(x) - \frac{\alpha}{L}(i_L - I_E)v_C + \frac{\beta}{C}(i_L - I_E)i_L - \frac{\beta}{L}(v_C - V_E)v_C + \frac{\gamma}{C}(v_C - V_E)i_L. \tag{4.24}$$

From (4.21) or equivalently from (4.23)-(4.24), it can be observed that X_E is a point of both $S_0(x) = 0$ and $S_1(x) = 0$, confirming that the equilibrium point lies on both switching surfaces. These constructions define a nonlinear hysteresis band around the ideal switching surface $S(x) = 0$ introduced in the min-type law (4.13). The state trajectory oscillates between these two boundaries, generating a cyclic behavior where transitions between modes $u = 0$ and $u = 1$ occur based on the system's state relative to these surfaces. This interpretation allows the control law to be reformulated as a set of conditional switching rules, where the decision to switch is governed by the sign of $S_0(x)$ or $S_1(x)$, depending on the current value of the control input u. Specifically, the switching strategy (4.19)-(4.20) can be interpreted as follows:

$$\text{if } u(t) = 0 \text{ and } S_0(x) > 0, \text{ then } u^+ = 1, \tag{4.25a}$$

$$\text{if } u(t) = 0 \text{ and } S_0(x) < 0, \text{ then } u^+ = 0, \tag{4.25b}$$

$$\text{if } u(t) = 1 \text{ and } S_1(x) > 0, \text{ then } u^+ = 0, \tag{4.25c}$$

$$\text{if } u(t) = 1 \text{ and } S_1(x) < 0, \text{ then } u^+ = 1. \tag{4.25d}$$

Here, u^+ denotes the control input immediately after the time instant t, i.e., $u^+ = \lim_{h\to 0^+} u(t + h)$. According to the switching logic defined in (4.21)-(4.24), all trajectories corresponding to the T_{on} interval (i.e., when $u = 1$) begin on the switching surface $S_0(x) = 0$ and evolve toward $S_1(x) = 0$, at which point a switch to the T_{off} interval (i.e., $u = 0$) occurs. Conversely, during the T_{off} phase, the trajectory starts from $S_1(x) = 0$ and returns to $S_0(x) = 0$, completing a full hysteresis cycle. This alternating behavior ensures regular switching between topologies based on the system's state relative to the conic switching surfaces. This behavior is graphically depicted in Fig. 4.3. Moreover, it has been simulated for different values of parameter η (see Fig. 4.4, $\rho = 1000$, and the

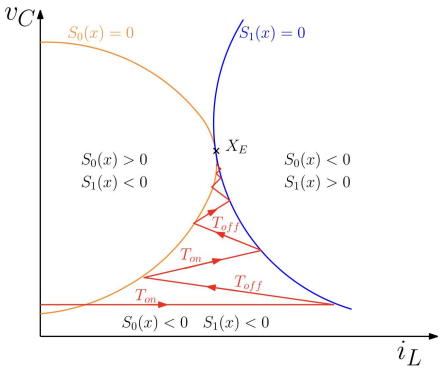

Figure 4.3: Graphical representation of the state trajectory according to the control law (4.25a).

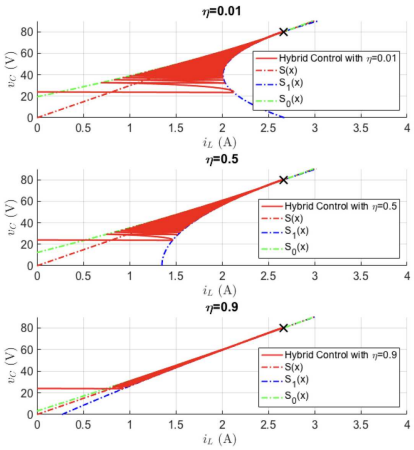

Figure 4.4: Simulation of the converter start-up for $V_{\text{in}} = 24V$ (blue trajectory) and $V_{\text{in}} = 40V$ (red trajectory) and hybrid control with $\eta = 0.5$.

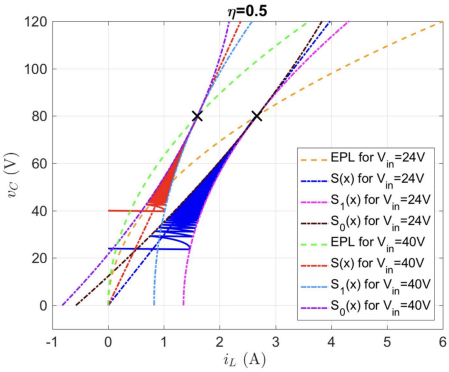

Figure 4.5: Simulation of the converter start-up in the case of hybrid control, $V_{\text{in}} = 24V$ and different values of parameters η.

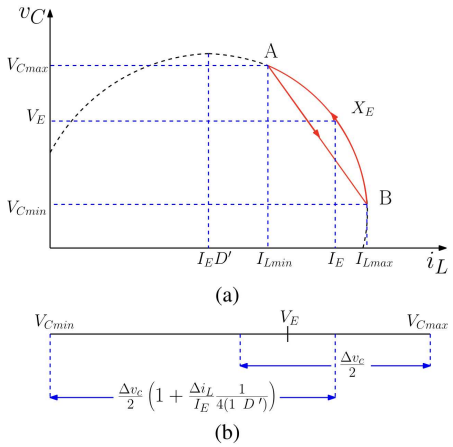

Figure 4.6: (a) Limit cycle representing the steady-state converter behavior. (b) V_E bounds.

same set of parameters used in the simulations of Fig. 4.2. The resulting hysteresis width, that is, the separation between the two switching surfaces $S_0(x) = 0$ and $S_1(x) = 0$, is directly influenced by the value of η. For small values of η, the width is maximum, which reduces the switching frequency during transients but may introduce a higher deviation from the equilibrium (larger inrush current). On the other hand, a larger value of η reduces the hysteresis band, leading to faster switching and reduced deviation but potentially higher switching stress and power losses. As the state trajectory approaches the equilibrium point X_E, the hysteresis band becomes narrower and eventually converges to zero, since both switching surfaces satisfy $S_0(X_E) = S_1(X_E) = 0$. This results in an infinite switching frequency at steady state, which corresponds to the behavior of the ideal min-type control (4.13). The reduction of initial switching frequency results in a slight increase of the inrush current since the switching surface $S(x) = 0$ of Fig. 4.2 is located between $S_0(x) = 0$ and $S_1(x) = 0$, the two switching surfaces only having in common the equilibrium point X_E. The increase of the inrush current is illustrated in Fig. 4.5, which reproduces the conditions of the simulations of Fig. 4.2 for the case of hybrid control and $\eta = 0.5$. While this phenomenon is theoretically well-behaved, it is unfeasible in real systems due to the finite switching capability of power devices. Consequently, practical operation settles on a finite-frequency limit cycle. The trade-off introduced by η is therefore fundamental in practical implementations. A low switching frequency during transients may be desirable to reduce switching losses and electromagnetic interference (EMI). Still, it comes at the cost of a larger inrush current due to the delay in reaching the target switching surface. The parameter η provides the designer a flexible tool for tuning system performance during transient behavior: by adjusting η, one can manage the number of switching events during start-up or disturbance, effectively balancing switching effort for current overshoot. This feature makes the hybrid control strategy more suitable for real-world implementations, especially in applications where switching cost, thermal constraints, or EMI are significant concerns. Although both the min-type and hybrid control strategies ultimately result in infinite switching frequency at the equilibrium point,

real converters operate at finite frequencies. As a result, the idealized infinite-frequency behavior translates in practice into periodic oscillations (or ripple) in the inductor current and output voltage around their equilibrium values I_E and V_E. These periodic oscillations form a limit cycle around the equilibrium point, as illustrated in Fig. 4.6(a). In this figure, the linear segment corresponds to the evolution under the T_{on} interval (constant control input $u = 1$). At the same time, the parabolic arc reflects the dynamics during the T_{off} interval (control input $u = 0$). The closed trajectory evolves between two characteristic points:

- $A = (I_{L,min}, V_{C,max})$,
- $B = (I_{L,max}, V_{C,min})$.

The sub-indexes *min* and *max* indicate the minimum and maximum values of the respective state variables, due to ripple. This representation clarifies how switching frequency, ripple amplitude, and control dynamics are connected in both analysis and practical implementation of the hybrid control law. A classical steady-state analysis reveals that the segments of the limit cycle can be expressed as:

- for T_{on} interval:

$$v_C = V_{C,max} + \frac{L}{C}\frac{I_E}{V_{\text{in}}}D'(I_{L,min} - i_L); \tag{4.26}$$

- for T_{off} interval:

$$v_C = V_{C,min} - \frac{L(I_{L,max} - I_E D')}{C(V_E - V_{\text{in}})}(i_L - I_{L,max}) - \frac{L}{2C(V_E - V_{\text{in}})}(i_L - I_{L,max})^2; \tag{4.27}$$

where $I_E = \frac{I_{Lmax}+I_{Lmin}}{2}$ is the average of the minimum and maximum inductor currents, $V_E = I_E D' R_0$ as the steady-state output voltage, and $D' = 1 - D = 1 - \frac{T_{\text{on}}}{T}$, where T_{on} and T being the respective durations of ON interval and switching period in steady-state. During the ON interval (T_{on}), the capacitor voltage evolves linearly, while during the OFF interval (T_{off}) it follows a parabolic trajectory. Defining $\Delta i_L = I_{Lmax} - I_{Lmin}$ and $\Delta v_C = V_{Cmax} - V_{Cmin}$, it can be demonstrated that V_E is bounded as shown in Fig. 4.6(b), where the current and voltage ripple, Δi_L and Δv_C, are given by:

$$\Delta i_L = \frac{V_{\text{in}}}{L}DT, \tag{4.28}$$

$$\Delta v_C = \frac{I_E}{C}DD'T. \tag{4.29}$$

Both the horizontal and vertical excursions of the limit cycle are proportional to the switching period T. As $T \to 0$, both $\Delta i_L \to 0$ and $\Delta v_C \to 0$, or equivalently $I_{Lmax} = I_{Lmin} = I_E$, and $V_{Cmax} = V_{Cmin} = V_E$, which implies that the limit cycle collapses in the equilibrium point X_E. Therefore, in hybrid control schemes, it becomes essential to define a minimum switching period to ensure proper behavior of the converter. Practically, this means the switching frequency must be sufficiently high, at least one

or two decades above the system's natural frequency $\frac{1}{2\pi\sqrt{LC}}$. The above-mentioned steady-state study is particularly important as it enables the analysis of the experimental results. Note that the theoretical results shown in Figs. 4.4-4.5 cannot be reproduced at steady-state since it would imply an infinite switching frequency.

4.4.4 Minimum dwell-time implementation

The need to establish a minimum switching period in steady state introduces a new constraint on the hybrid controller, which directly affects system stability. This fact has been analyzed in [36], where a modification of the hybrid control is considered based on the introduction of a dwell-time, denoted as T_{DT}, which defines the minimum duration the system must remain in a given topology before a switch can occur. This modification extends the state of the system by including an auxiliary timing variable τ, which acts as an internal clock. The state vector thus becomes $z = \begin{bmatrix} i_L & v_C & u & \tau \end{bmatrix}^\top$, and the flow and jump maps and the flow and jump sets are modified as follows:

$$f = \begin{bmatrix} -\frac{R_L}{L} i_L - \frac{v_C}{L}(1-u) + \frac{V_{\text{in}}}{L} \\ -\frac{i_L}{C}(1-u) - \frac{1}{CR_0} v_C \\ 0 \\ 1 \end{bmatrix}, \quad g = \begin{bmatrix} i_L \\ v_C \\ 1-u \\ 0 \end{bmatrix}, \tag{4.30}$$

$$\mathcal{C} := \left\{ (x, u, \tau) : (x - X_E)^\top P(A_u x + B V_{\text{in}}) \leq \eta (x - X_E)^\top Q (x - X_E) \wedge \tau \in \mathbb{R}_+ \right\}, \tag{4.31a}$$

$$\mathcal{D} := \left\{ (x, u, \tau) : (x - X_E)^\top P(A_u x + B V_{\text{in}}) > \eta (x - X_E)^\top Q (x - X_E) \wedge \tau > T_{DT} \right\}. \tag{4.31b}$$

This enhanced model ensures that the converter remains in the current topology given by (4.31a) at least T_{DT} seconds, after that, the change of topology derived from (4.31b) has taken place. Despite this additional dwell-time constraint, it has been formally proven ([36], Th. 3) that the equilibrium point X_E remains uniformly globally asymptotically stable, thereby confirming the robustness of the hybrid approach even under practical timing limitations.

4.5 Advantages of the proposed strategy

Beyond enabling the enforcement of a minimum dwell-time, the proposed min-type hybrid control strategy offers three key advantages over conventional control techniques:

- **Direct control of voltage and current trajectories in the phase-plane voltage/current**: unlike standard methods such as SMC or PI controllers, which often regulate only the inductor current in the inner loop, the proposed strategy directly governs the complete state trajectory. This design ensures both zero inrush current during

startup and a good tracking of the voltage reference, since system trajectories are constrained between the surfaces $S_0(x)$ and $S_1(x)$, which intersect only at the equilibrium point (see Figs. 4.4-4.5). Indeed, in SMC or PI control, the inner loop is driven only by the error of the inductor current, without considering the error of the output voltage, which is often controlled by a second loop. Here, in the proposed control technique, the inner loop is driven by the state error $(x - X_E)$, which contains both the output voltage and the inductor current. Moreover, matrix P is selected by solving the optimization problem (4.9), leading to the minimization of the cost function J.

- **Tuning flexibility via the parameter** η: The tuning parameter η allows the designer to shape the control trajectory within the hysteresis band. By decreasing η, the distance between S_0 and S_1 narrows (see Fig. 4.6), which in turn increases the switching frequency and reduces the ripple amplitude. This provides an effective trade-off mechanism between switching effort and dynamic performance, making the controller adaptable to application-specific requirements such as thermal constraints or EMI reduction.
- **Natural integration within the hybrid control framework**: The use of the hybrid formalism [1] provides a natural framework for this class of systems and offers a mathematically rigorous and structurally consistent approach for modeling and controlling systems that exhibit both continuous-time and discrete-event dynamics. In the context of power converters, this dual nature is inherent and must be explicitly handled. Hybrid control provides both the theoretical tools and practical means to ensure system stability, even in the presence of real-world constraints such as limited switching frequency or dwell-time requirements.

In conclusion, the min-type hybrid control law provides a robust and flexible framework for power converter regulation, ensuring controlled switching, accurate trajectory shaping, and stability under practical constraints. It combines phase-plane trajectory control, parameter tunability, and formal stability guarantees, making it particularly suited for applications where efficiency, reliability, and compliance with physical limitations are critical.

4.6 Experiments

To validate the effectiveness of the proposed min-type hybrid control strategy with hysteresis, a series of experimental tests has been conducted on a synchronous boost converter. The experiments aim to assess the controller's performance in real-world conditions, focusing on key aspects such as switching behavior, transient response, voltage and current trajectories, and the impact of the hysteresis parameter η. Both startup and steady-state operation are examined to demonstrate the controller's ability to maintain

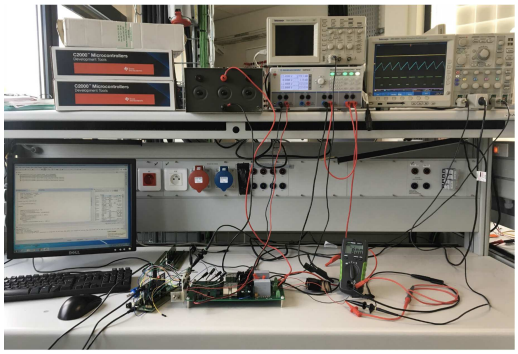

Figure 4.7: Picture of the test bench.

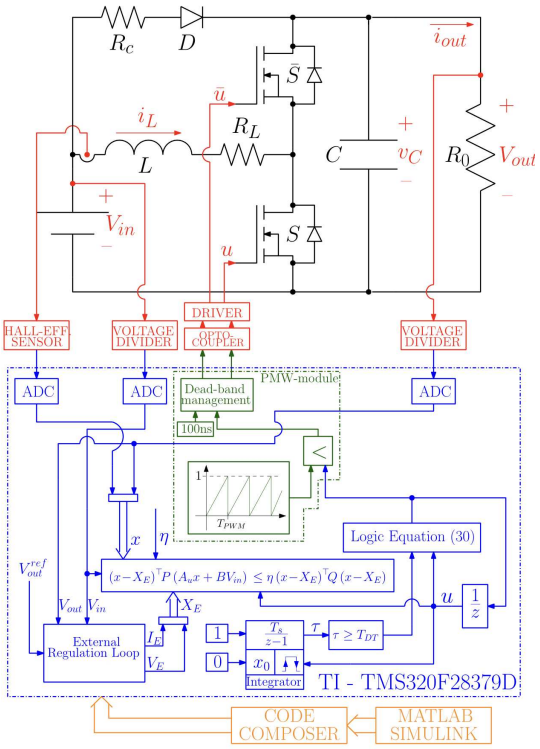

Figure 4.8: Block diagram of the experimental setup.

stability, limit inrush currents, and achieve precise tracking of the desired output voltage. In the following, the experimental setup is presented, highlighting the components, instrumentation, and configuration used for implementation.

4.6.1 Experimental setup

An experimental setup was developed to bridge the gap between theoretical modeling and practical implementation, providing a platform to evaluate the performance of the min-type hybrid control strategy under real operating conditions. The picture of the test bench is shown in Fig. 4.7. The converter under test is shown in Fig. 4.1, and the general architecture of the experimental setup is shown in Fig. 4.8. The nominal power is 60 W, and the components used for the experimental prototype are:

- Inductor L: AGP4233-473ME.
- Capacitor C: MKP1848620094P4.
- Switches $S - \bar{S}$: SiC MOSFET C3M0065090D.
- Auxiliary diode D: 8TQ100S.

The passive elements have the same nominal values used in the simulations in Figs. 4.2-4.5 These component choices, including the SiC MOSFETs and high-quality passive components, are critical to achieving high switching frequencies and maintaining overall efficiency in the prototype. The MOSFETs are sourced by means of a power-driven MGJ2D121505SC, which provides the correct amount of current for the turning on and off of the components. To ensure galvanic isolation between the signal and power parts of the circuit, two optocouplers, ADUM3401CRWZ, have been used. The inductor current i_L is measured using a Hall-effect sensor (LEM LTS-15-N). In contrast, the output voltage v_C is calculated using a cascade between a voltage divider and an operational amplifier (LM324) configured as a buffer. Both signals are sampled at 1.5 MHz by the respective analog-to-digital converters to be subsequently processed by the microcontroller, providing real-time data for the control algorithm. The controller has been digitally implemented on a TI TMS320F28379D microcontroller, as shown in the block diagram of Fig. 4.8. The latter uses the MATLAB/Simulink information developed in the simulation described above to generate the control signal u. In particular, it provides the coordinates of the equilibrium point X_E for a desired value of the output voltage V_E and input voltage, and the sampled values of $S_0(x)$ and $S_1(x)$ for the mentioned sampling frequency.

Table 4.2: Logic table of the communications

Inputs			**Output**
$u(kT_{sa})$	$S_u\,(x(u(kT_{sa})) < 0)$	$\tau \geq T_{DT}$	$u((k+1)T_{sa})$
0	0	0	0
0	0	1	1
0	1	0	0
0	1	1	0
1	0	0	1
1	0	1	0
1	1	0	1
1	1	1	1

4.6.1.1 Discrete control law

To implement the proposed control law in real-time, a logical representation of the switching behavior is required, as summarized in Table 4.2. The proposed control law is digitalized by considering Table 4.2, where $\frac{1}{T_{sa}} = 1.5$ MHz is the sampling frequency. The switching input $u(kT_{sa})$ is determined according to the logical relation derived in

Table 4.2, summarized as:

$$u\left((k+1)T_{sa}\right) = (\neg u(kT_{sa}) \wedge \neg s(kT_{sa}) \wedge t(kT_{sa})) \vee (u(kT_{sa}) \wedge \neg s(kT_{sa}) \wedge \neg t(kT_{sa})) \vee (u(kT_{sa}) \wedge s(kT_{sa})) \tag{4.32}$$

where $s(kT_{sa})$ and $t(kT_{sa})$ represent the logic status respectively of relations $S_u\left(x(u(kT_{sa}))\right) < 0$ and $\tau \geq T_{DT}$. A dwell-time $T_{DT} = 3\mu s$ is enforced to ensure a minimum switching period of $5\mu s$, which corresponds to a maximum switching period of $10\mu s$.

4.6.1.2 PWM signal generation

Once the switching logic has been established, the controller must translate this logic into gate-driving signals through PWM. As a consequence, the computed discrete control input signal $u(kT_s)$, calculated according to (4.32), results in a two-level square signal with a switching frequency ranging from 100 to 200 kHz. This internal signal of the microcontroller is compared with a 10 MHz periodic triangular internal signal of the PWM module to obtain the signal u and $\bar{u}$ that activate the optocouplers and hence the power switch. The high level of signal $u(kT_{sa})$, representing the binary value 1, is always higher than the periodic triangular signal, so that the comparison will always yield a binary value 1 at the output of the PWM during the interval of time in which $u(kT_{sa}) = 1$. On the contrary, the low level of $u(kT_{sa})$, representing the binary value 0, is always below the periodic triangular signal, which leads to a binary value 0 at the output of the PWM. Thus, the output of the PWM reproduces the variable switching frequency signal generated by the min-type control strategy and provides the necessary level of current to activate the optocouplers. While the inner loop ensures fast and stable switching, an outer regulation loop is required to cope with slow variations in input voltage or load. The PWM frequency, which is constant and equal to $\frac{1}{T_{PWM}}$, has been chosen high enough to reduce possible static errors since the proposed min-type control strategy generates a variable switching frequency that will be an integer multiple of the PWM frequency. A dead-band of 100 ns is introduced to prevent simultaneous conduction of the complementary switches S and $\bar{S}$. This mechanism is represented in Fig. 4.8.

4.6.1.3 Robustness to input and load variations

To enhance robustness against variations in the input voltage and load conditions, a PI regulator processes the output voltage error. The regulator updates the reference output voltage V_E, which in turn modifies the equilibrium point (I_E, V_E). As shown in Fig. 4.9, the PI controller processes the output voltage error and gives a reference value of V_E. By using this value of V_E and the measured value of the input voltage, the equilibrium value of the current is computed using (4.3). The min-type control algorithm then uses these update values, along with the measured input voltage V_{in}, to solve the arg-min problem

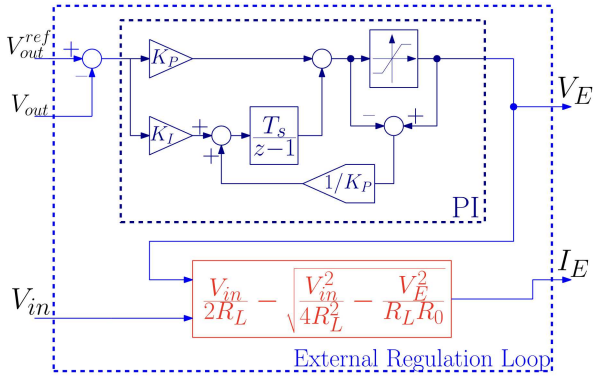

Figure 4.9: Block diagram of the external regulation loop.

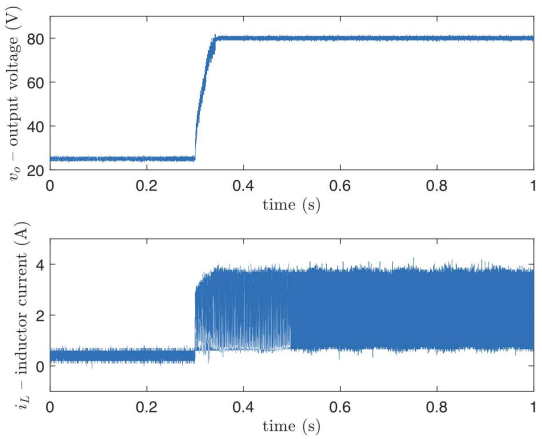

Figure 4.10: Output voltage v_0 and inductor current i_L during a start-up test using the proposed min-type control strategy.

described in (4.4), ensuring adaptive and stable performance under varying operating conditions. The combined operation of the inner hybrid controller and the outer PI regulator enables the system to maintain performance across a wide range of conditions.

4.6.1.4 Hardware implementation

The proposed control technique does not depend on the particular hardware used for the implementation. The digital implementation on a microcontroller confirms the method's flexibility and ability to handle high-frequency switching signals. This approach can be easily deployed on field programmable gate array (FPGA) platforms, which are particularly suitable for applications requiring even higher switching frequencies or more complex control algorithms. Overall, the experimental implementation highlights the natural suitability of hybrid modeling frameworks for power electronics systems, effectively capturing the coexistence of continuous-time dynamics and discrete-time switching logic, leading to improved performance and robustness in practical applications. These implementation details provide the foundation for the experimental evaluation of the hybrid control strategy under a range of operating conditions.

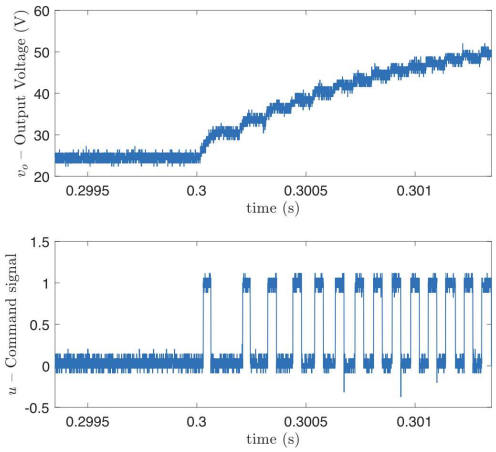

Figure 4.11: Zoom of the output voltage v_0 and the corresponding control input u, during a start-up test using the proposed min-type control strategy.

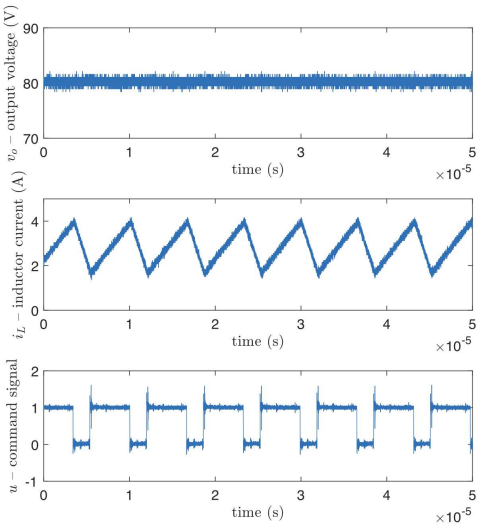

Figure 4.12: Output voltage v_0, inductor current i_L, and control signal u at steady-state using the proposed min-type control strategy.

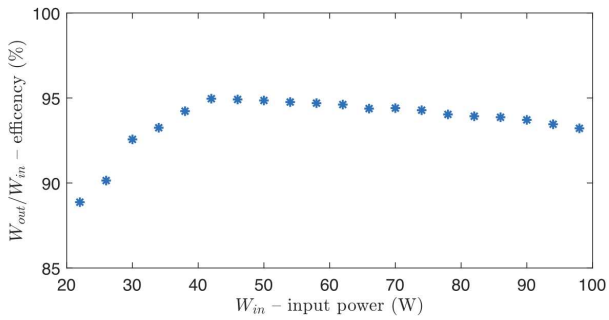

Figure 4.13: Efficiency of the system at steady-state for different values of input power.

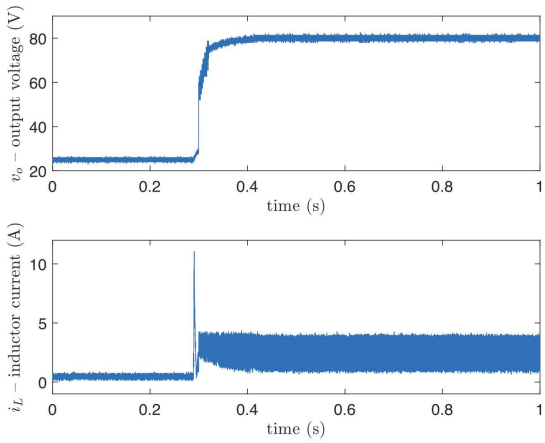

Figure 4.14: Output voltage v_0 and inductor current i_L during a start-up test using SMC strategy.

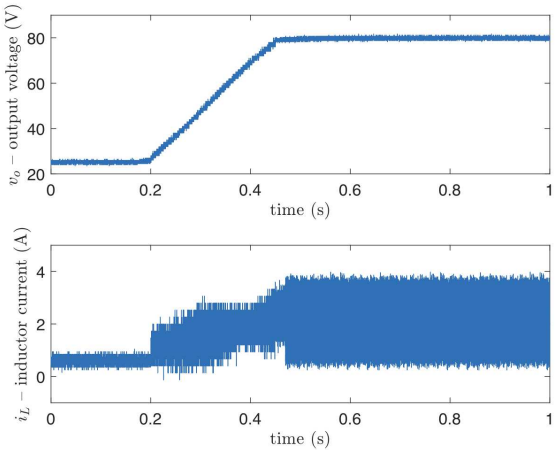

Figure 4.15: Output voltage v_0 and inductor current i_L during a start-up test using PI control strategy.

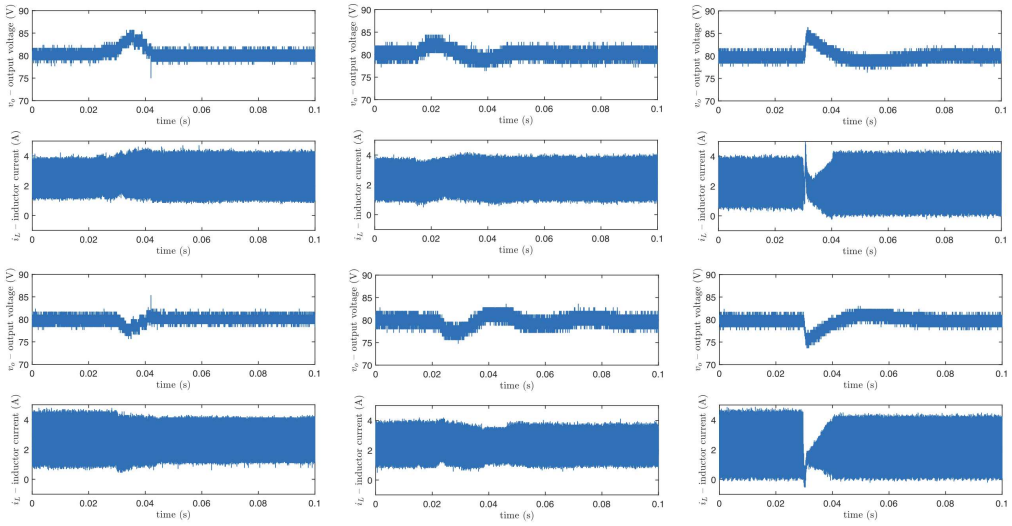

Figure 4.16: Output voltage v_0 and inductor current i_L with an additional outer regulation loop during a step variation in the input voltage V_{in} from 24 to 29 V (upper plots), and from 29 to 24 V (bottom plots) by using: (a) proposed min-type control strategy, (b) SM controller, and (c) PI controller.

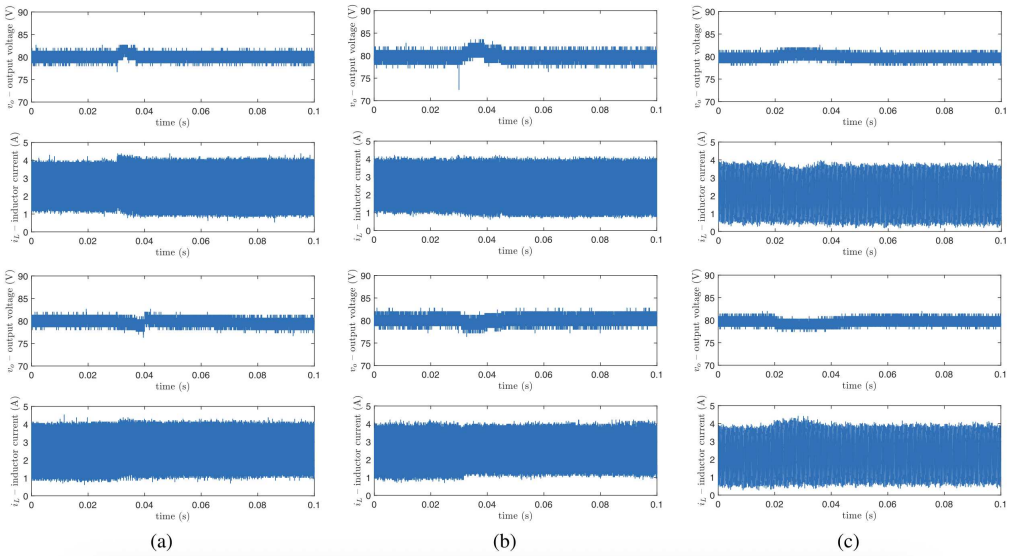

Figure 4.17: Output voltage v_0 and inductor current i_L with an additional outer regulation loop during a step variation in the load resistance R_L from 100 to 150 Ω (upper plots), and from 150 to 100 Ω (bottom plots) by using: (a) proposed min-type control strategy, (b) SM controller, and (c) PI controller.

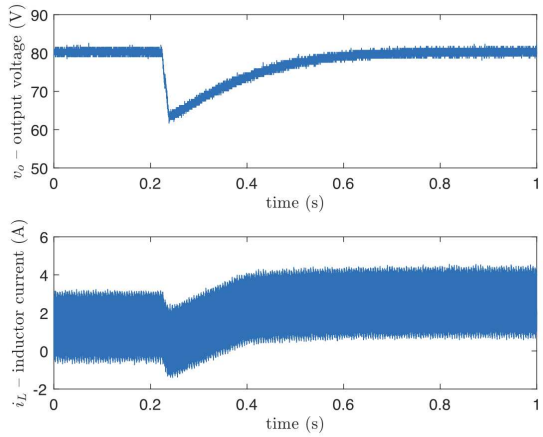

Figure 4.18: Output voltage v_0 and inductor current i_L with an additional outer regulation loop during a step variation in the input voltage V_{in} from 48 to 24 V with the proposed min-type control strategy.

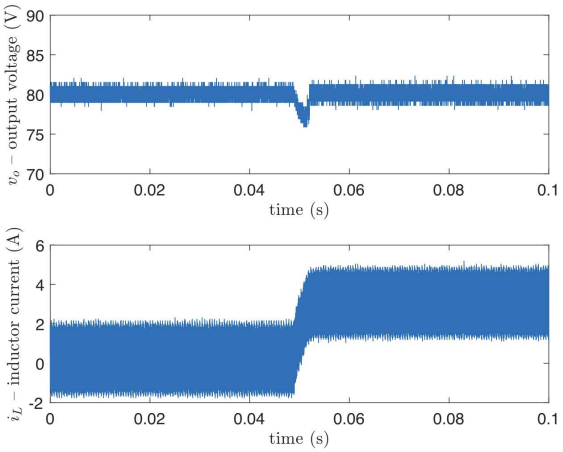

Figure 4.19: Output voltage v_0 and inductor current i_L with an additional outer regulation loop during a step variation in the load resistance R_L from no load to 100 Ω with the proposed min-type control strategy.

4.6.2 Experimental results

To validate the theoretical analysis, the converter prototype was experimentally tested. These experimental tests aim to demonstrate the effectiveness, robustness, and real-time feasibility of the proposed min-type hybrid control strategy under various operating conditions, including start-up, steady-state, and input and load variations tests.

- **Start-up test**: Fig. 4.10 shows the experimental waveforms of the output voltage and inductor current during a start-up. The initial instant in the oscilloscope capture corresponds to 0.3 ms, and the min-type hybrid controller is configured with the design parameter $\eta = 0.5$. The converter reaches the desired equilibrium point corresponding to the output voltage coordinate $V_E = 80V$ for an input voltage $V_{\text{in}} = 24V$. Moreover, no inrush current is observed, even after a fast transient state. To highlight the behavior of the min-type strategy implemented by the proposed controller, a zoomed view of the capacitor voltage and the corresponding control input u during start-up is shown in Fig. 4.11. The experimental response aligns with the theoretical predictions, confirming the accurate implementation of the min-type logic and switching conditions.
- **Steady-state test**: Fig. 4.12 shows the steady-state waveforms of the output voltage and inductor current. The converter operates at an output power of approximately 65 W, with an average inductor current $I_E = 2.75A$, a current ripple $\Delta i_L = 3A$, and a switching frequency of about 150 kHz. The converter operates in CCM, since the topology of the boost converter is bidirectional and never enters discontinuous-conduction mode because the inductor current can also be negative. The relatively high current ripple is not a drawback but a consequence of the system design, optimized for a fast response. It is possible to reduce the ripple by decreasing the dwell-time T_{DT} (during steady-state), or tuning the design parameter η (during transient). Experimentally, it was observed that the switching frequency remains approximately constant at $\frac{1}{2\lambda T_{DT}}$, where $\lambda \in [1, 1.5]$. This frequency is maintained almost constant despite the equilibrium point changes, offering a significant advantage over traditional hysteresis controllers, where the switching frequency varies based on load and input voltage. Fig. 4.13 illustrates the measured system efficiency under various input power levels. The results show good energy performance, with a peak efficiency of around 94% under nominal operating conditions. This demonstrates that the proposed hybrid strategy not only ensures dynamic performance but also maintains high power conversion efficiency.
- **Input and load variation test**: Fig. 4.16(a) shows the converter's response to an input voltage variation from 24 V to 29 V and from 29 V to 24 V. The output voltage quickly recovers the desired value of 80 V after a fast transient and a minimal overshoot. At the same time, the inductor current absorbs the energy variation introduced by the fluctuation in the input voltage. The same test was performed

using the SMC and the PI controller, shown in Fig. 4.16(b) and (c), respectively. In both cases, the min-type strategy showed a lower settling time and a higher dynamic precision. Similarly, Fig. 4.17(a) presents the converter response to a load variation from 100 to 150 Ω and from 150 to 100 Ω. The system immediately adjusts the inductor current and restores the output voltage. The results obtained with the SMC and the PI controller under the same variations of the output load are shown in Fig. 4.17(b) and (c), respectively.

4.6.2.1 Comparison with conventional controllers

To compare the performance of the proposed control method with other control solutions, comparative tests were carried out using the SMC and a PI controller under the same operating conditions. Figs. 4.14 and 4.15 show the waveforms of the output voltage and the inductor current during the start-up for the SMC strategy and PI control strategy, respectively. By comparing Figs. 4.14 and 4.15 with Fig. 4.10, it is evident that the min-type control strategy offers a better transient in terms of settling time, higher transient accuracy, and dynamic precision. The PI controller results in a higher settling time, while the SMC exhibits a lower dynamic precision during the transient time. This difference arises because the SMC acts only on the inductor current in the sliding surface definition, whereas the min-type strategy operates on both voltage and current trajectories in the phase-plane voltage-current, ensuring more accurate tracking. Additionally, the min-type controller ensures a smooth start-up without inrush current and enables accurate tracking of the voltage reference.

4.6.3 Robustness under stress scenarios

To evaluate the proposed min-type control strategy under highly challenging operating conditions, two stress scenarios were presented:

- Fig. 4.18 illustrates the first scenario where the system's behavior during a large input voltage variation, from 48 to 24 V.
- Fig. 4.19 presents the second scenario where the system's response to a load resistance variation, from no load to 100 Ω.

In both cases, the min-type controller maintains system stability, achieves fast output voltage recovery, and handles the inductor current dynamics effectively.

4.7 Summary

An analytical model of a min-type control strategy based on a nonlinear switching surface was developed and applied to a synchronous boost converter within the framework of SMC. To address the practical constraint of finite switching frequency in power devices,

the original control approach was extended to a hybrid formulation, which differentiates between the continuous dynamics inherent in the current converter topology and the discrete dynamics associated with switching events and topology changes. This hybrid formulation introduces a hysteresis width during start-up, which decreases from its maximum value, corresponding to the first T_{on} trajectory, until zero when the equilibrium point is attained. A dwell-time constraint further limits the switching frequency and imposes an upper bound, preventing the infinite switching behavior that would otherwise occur in steady-state operation and ensuring a predictable and finite frequency profile. Experimental validation was performed on a hardware prototype, where the hybrid control algorithm was implemented on a microcontroller platform. Real-time measurements of inductor current and capacitor voltage were processed to generate the control signal, adapted via PWM and optocouplers to interface with the power stage. Results confirm that the system rapidly reaches the desired equilibrium point with a fast transient response and without inrush current. The inclusion of a PI controller ensured effective regulation of the output voltage under both input voltage and load disturbances. Overall, the min-type hybrid control approach demonstrates a robust and practical solution for power converter applications. It combines the fast transient response characteristic of SMC with the predictable and limited switching frequency of hybrid control. By combining continuous phase-plane dynamics with discrete logic based on dwell-time and state-based conditions, the approach successfully addresses challenges that are difficult to handle with traditional linear or purely switching-based controllers. The experimental results validate its feasibility, robustness, and effectiveness, while also highlighting its adaptability for digital implementation on microcontrollers or FPGA platforms.

Chapter 5

Hybrid control strategy of multi-input converters using dynamic input allocation

Abstract

This chapter addresses the current sharing and voltage regulation challenges in multi-input energy conversion systems as part of a broader control architecture for DC microgrids. The focus is on the Multi-Input Converter (MIC) topology consisting of two voltage sources connected to a common DC bus with a bulk capacitor through two parallel synchronous boost converters and an aggregated load modelled as an ideal current source connected to the DC bus. It is shown that the dynamics related to current distribution can be controlled without impacting voltage regulation. The decoupling is performed without relying on traditional frequency separation methods, which typically degrade transient response and limit overall system performance. Instead, a novel control structure is introduced, allowing the voltage regulation task to operate independently from current distribution. The approach is based on dynamic allocation theory. The strategy achieves a fast voltage response with optimal current distribution among the converters, considering the current limits, the dynamic response, and the efficiency of the individual converters. Numerical simulations in a MATLAB/Simulink environment validate the effectiveness of the proposed approach, demonstrating fast voltage tracking, robustness against load and input disturbances, and an accurate current allocation across the input branches. The proposed strategy represents a key component of the intermediate control stage within the hybrid system architecture, coupling energy sourcing with robust output regulation.

Contents

5.1 Motivation and literature review

In recent years, the increasing demand for high-efficiency and flexible power electronic systems has led to the development of advanced control strategies that can manage complex converter topologies. Among these, MICs have gained significant attention due to their ability to interface multiple energy sources, such as photovoltaic panels, batteries, or fuel cells, within a single power processing stage. However, their structural complexity requires advanced control mechanisms to guarantee optimal source control, maintain system stability, and achieve high performance across a wide range of operating conditions. This part of the thesis addresses the control of over-actuated systems, where multiple energy sources must be coordinated to supply a common load. It lays the foundation for the final part of the thesis, where the control of output-side DC/AC conversion through boost inverters will be explored. In the context of DC microgrids, where multiple energy sources, such as batteries, photovoltaic panels, and fuel cells, must be coordinated to supply power to a shared load, MICs play a fundamental role [37], [38]. Ensuring coordinated operation among these sources is crucial for maximizing energy efficiency, guaranteeing system stability, and preserving the lifespan of the components involved. Nowadays, connecting multiple power converters in parallel to supply the load has become more common. Despite the higher number of electrical components, this parallel interconnection of converters offers several advantages, including higher reliability, ease of maintenance and repair, improved thermal management, and reduced output ripple due to Pulse Width Modulation (PWM) phase interleaving. Traditionally, this structure has been used for low-voltage/high-current power supplies, where the parallelization of the converters allows for an increase in the maximum current that can be supplied. In addition, this configuration has become increasingly used with the development of microgrids, i.e., energy distribution networks that combine local consumption, storage, and electricity production [39]. Such devices are connected to the microgrid through power converters, whose operation must be suitably coordinated to ensure seamless integration. For example, it is advisable to operate a fuel cell at nearly constant current since both ripple current and wide current variations reduce the lifespan of such a device [40]. Furthermore, microgrids are often supervised by Energy Management Systems (EMS) to optimize the power flows among the devices, aiming to pursue goals such as minimum microgrid operating, maximum microgrid self-sufficiency, the minimum fuel consumption of diesel generators, etc. [41], [42]. In this context, the EMS determines the optimal power reference for the microgrid devices, which the control systems must

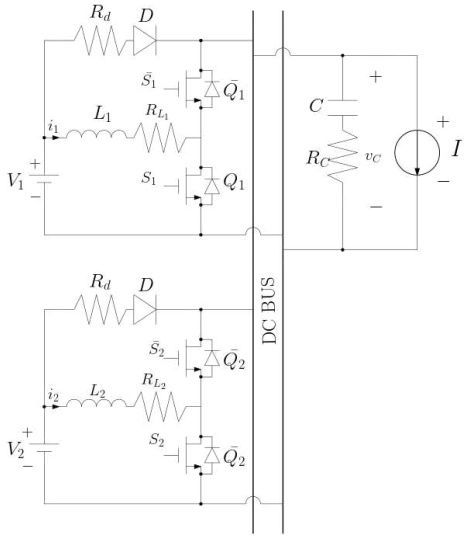

Figure 5.1: Electrical scheme of the MIC.

enforce. However, from a control standpoint, the parallel operation of converters is a complex problem, as it leads to a redundant system at the input when each converter is considered an actuator. The primary control challenge is to separately regulate the output voltage, which is the primary control objective, and the current distribution, which is the secondary control objective. These objectives are inherently coupled, making controller design a nontrivial task. To address this problem, a control design procedure based on several SISO-shaped transfer functions is often resorted to. Moreover, the closed-loop stability in this framework is more complex, and frequency separation is usually employed, which reduces performance by imposing slow current distribution dynamics, especially under dynamic loading or source variation conditions. In literature, some works address these problems [43], [44], [45]. However, in recent literature, dynamic control allocation techniques have been developed, and they appear very promising for controlling such over-actuated systems [46], [47]. This chapter proposes a hybrid control strategy based on dynamic input allocation, designed specifically for MIC operating in parallel. This technique is totally different from the other techniques presented in the literature for MIC, and it seems very promising.

5.2 Description of the MIC and problem statement

In MIC, each power stage acts as an actuator contributing to a common control objective: regulating the output voltage while coordinating the sharing of the load current. When more actuators are available than strictly necessary, the system is overactuated. In such configurations, the control problem is inherently redundant, as multiple input combinations can achieve the same output behavior. Dynamic input allocation resolves this redundancy by dynamically assigning control efforts to the available inputs in a manner that optimizes secondary objectives, such as efficiency, thermal distribution, or long-term reliability,

while ensuring the primary goal of voltage regulation. The control system can be naturally modeled as a hybrid dynamical system, where the output voltage evolves continuously and the current allocation decisions are made through discrete switching logic. This hybrid nature allows for real-time adaptation to varying operating conditions, input constraints, or source availability, effectively decoupling voltage regulation from current sharing. The MIC under study consists of two synchronous boost converters connected to a common DC bus and supplying a shared load, as shown in Fig. 5.1. The two voltage sources are assumed to be a battery and a fuel cell due to their relevance in microgrid applications. An ideal current generator is also connected in parallel to the DC bus capacitor to model both passive and active loads, depending on the current sign. This architecture enables the flexible management of energy flows from heterogeneous sources. Fuel cells achieve optimal performance when operated under slowly varying or nearly constant current profiles, minimizing degradation [40], whereas batteries are well-suited to rapidly respond to load fluctuations. The proposed hybrid control strategy combines continuous-time voltage regulation with discrete-time dynamic allocation. A discrete-time supervisor embedded alongside continuous feedback loops enforces real-time coordination without relying on slow dynamic loops or frequency separation, while min-type logic determines, in real-time, how the load current should be distributed among the available sources, respecting constraints such as current limits, dynamic behavior, and efficiency profiles. The main goal is to effectively control both the DC bus voltage and the currents along the inductors of the MIC. Small variations in duty cycle can unbalance the parallel branches, leading to inefficiencies or potential stress on components. To maintain circuit balance, the hybrid control strategy dynamically selects the equilibrium point that satisfies the voltage regulation constraint while automatically distributing currents to achieve optimal load sharing. This structure enhances transient performance, improves robustness, and allows operational constraints, such as maintaining nearly current from the fuel cell, to be directly enforced through the allocation logic.

5.3 Dynamic modeling and equilibrium characterization of MIC

To effectively design a hybrid control strategy, it is essential to derive an accurate mathematical model of the MIC. The dynamic model of the MIC is introduced and reformulated in a state-space representation suitable for analysis and control design. The continuous-time dynamics of the system are governed by the following differential equations:

$$\frac{di_1}{dt} = -\frac{R_{L_1} + R_s + S_1(R_d - R_s + R_C)}{L_1} i_1 - \frac{S_1 S_2 R_C}{L_1} i_2 - \frac{S_1}{L_1} v_C + \frac{1}{L_1} V_1 + \frac{S_1 R_C}{L_1} I; \tag{5.1a}$$

$$\frac{di_2}{dt} = -\frac{R_{L_2} + R_s + S_2(R_d - R_s + R_C)}{L_2} i_2 - \frac{S_1 S_2 R_C}{L_2} i_1 - \frac{S_2}{L_2} v_C + \frac{1}{L_2} V_2 + \frac{S_2 R_C}{L_2} I; \tag{5.1b}$$

$$\frac{dv_C}{dt} = \frac{S_1}{C} i_1 + \frac{S_2}{C} i_2 - \frac{1}{C} I; \tag{5.1c}$$

where R_{L_1} and R_{L_2} are the parasitic resistances of the inductances L_1 and L_2 respectively, R_s represents the MOSFET'S conduction resistance, R_d represents the body diode's resistance, R_C is the parasitic resistance of the capacitor C, S_1 and S_2 represent the state of the switches Q_1 and Q_2 and they can assume the value 0 or 1 depending on the operating condition, V_1 and V_2 represent the voltages of the battery and fuel-cell respectively, I represents the current of the ideal generator, i_1 and i_2 represent the currents along the inductances L_1 and L_2 and, finally, v_C is the voltage capacitor. This system is switching-affine, and it can be written in a suitable hybrid state-space form as follows:

$$\dot{x} = A(u)x + BV_{in}, \tag{5.2a}$$

$$y = Cx, \tag{5.2b}$$

where $x = \begin{bmatrix} L_1 i_1 & L_2 i_2 & C v_c \end{bmatrix}^\top$ is the state-vector, $V_{in} = \begin{bmatrix} V_1 & V_2 & I \end{bmatrix}^\top$ is the input vector, $y = v_C$ is the output. Matrices B and C are given by:

$$B = \begin{bmatrix} 1 & 0 & 0 \\ 0 & 1 & 0 \\ 0 & 0 & -1 \end{bmatrix}, \quad C = \begin{bmatrix} 0 & 0 & 1 \end{bmatrix},$$

while matrix $A(u)$ is parametrized as follows:

$$A(u_1, u_2) = A_0 + \sum_{i=1}^{2} u_i A_i \tag{5.3}$$

where:

$$A_0 = \begin{bmatrix} -\frac{R_1}{L_1} & 0 & 0 \\ 0 & -\frac{R_2}{L_2} & 0 \\ 0 & 0 & 0 \end{bmatrix}, \; A_1 = \begin{bmatrix} -\frac{R}{L_1} & 0 & -\frac{1}{C} \\ 0 & 0 & 0 \\ \frac{1}{L_1} & 0 & 0 \end{bmatrix}, \; A_2 = \begin{bmatrix} 0 & 0 & 0 \\ 0 & -\frac{R}{L_2} & -\frac{1}{C} \\ 0 & \frac{1}{L_2} & 0 \end{bmatrix},$$

with: $R_1 = R_{L_1} + R_s$, $R_2 = R_{L_2} + R_s$, $R = R_d - R_s$ and R_C has been assumed equal to zero. Model (5.2) is a convenient way to represent the original model. Indeed, when $u_1 = S_1$ and $u_2 = S_2$, the original model (5.1) is obtained. On the other hand, u_1 and u_2 can be considered as the duty cycles of the two branches. This means that fixing the values of $u_1 = \bar{u}_1$ and $u_2 = \bar{u}_2$, with $0 \leq \bar{u}_1 \leq 1$ and $0 \leq \bar{u}_2 \leq 1$, matrix (5.3) is a constant matrix, representing the convex combination of matrices A_0, A_1 and A_2. Model (5.2) becomes a standard LTI system that describes the averaged behavior of the original switching system when the converter is operated at constant duty-cycles equal to $\bar{u}_1$ and $\bar{u}_2$. The practical control inputs will be u_1 and u_2 while V_1, V_2, and I are uncontrolled inputs. This formulation captures the hybrid nature of the system; the continuous dynamics evolve according to a parameter-dependent linear model, while the duty cycles are selected by a discrete supervisory controller embedded within the

hybrid framework. By interpreting u_1 and u_2 as piecewise constant signals updated by a logic-based min-type selector, the model becomes well-suited for hybrid control design. Due to the overactuation of the system, with two control inputs but only one directly regulated output, there exists an infinite set of equilibrium points. Model (5.2) allows the determination of a set of equilibrium states, defined as:

$$X_e = \{x_e(u_1, u_2) \ : \ A(u_1, u_2)x_e + BV_{in} = 0, u_1, u_2 \in]0, 1[\}. \tag{5.4}$$

These equilibria correspond to combinations of i_1, i_2, and v_C that satisfy the desired output voltage while distributing current among sources. Their explicit expression is given by:

$$x_1 = \frac{CV_1L_1\eta_1}{u_1} - \eta_1 L_1 \frac{C(\eta_1 V_1 + \eta_2 V_2) - I}{u_1\eta_1 + u_2\eta_2}; \tag{5.5a}$$

$$x_2 = \frac{CV_2L_2\eta_2}{u_2} - \eta_2 L_2 \frac{C(\eta_1 V_1 + \eta_2 V_2) - I}{u_1\eta_1 + u_2\eta_2}; \tag{5.5b}$$

$$x_3 = \frac{C(\eta_1 V_1 + \eta_2 V_2) - I}{u_1\eta_1 + u_2\eta_2}; \tag{5.5c}$$

where $\eta_1 = \frac{u_1}{C(R_1+Ru_1)}$ and $\eta_2 = \frac{u_2}{C(R_2+Ru_2)}$. From a hybrid perspective, this redundancy enables the system to dynamically select the most appropriate equilibrium in real-time via dynamic allocation logic, considering performance metrics such as efficiency, component degradation, or fuel cell limitations. For example, the fuel cell current i_1 can be constrained to remain nearly constant, while the battery current i_2 adjusts dynamically. To ensure the reliability and predictability of this equilibrium-based allocation, it is crucial to analyze the internal stability properties of the associated averaged system model.

5.4 Lyapunov-based stability analysis

The stability of the system under model (5.2) is guaranteed for all $u_1, u_2 \in]0, 1[$, as proven in the following Lemma.

Lemma 5.4.1

A suitable Lyapunov function is constructed using a positive definite matrix $P(u_1, u_2)$, and its properties are verified through Linear Matrix Inequalities (LMI), ensuring that the origin is globally exponentially stable for the averaged system. For any u_1 and u_2 belonging to the set $]0, 1[$, and for any positive constant γ satisfying $\gamma > \max\{1, \xi\}$, with

$$\xi = -\frac{(\alpha^2 C - L_1 u_1^2)}{2L_1 u_1^2} + \frac{\sqrt{\Delta}}{8\alpha\beta L_1 u_1^2}, \tag{5.6}$$

and

$$\alpha = R_1 + Ru_1, \ \beta = R_2 + Ru_2,$$

$$\Delta = \left(4\alpha^3\beta C - 4\alpha\beta L_1 u_1^2\right)^2 + \left(16\alpha^3\beta L_1 u_1^2\right)\left(4\alpha\beta C + L_1 u_2^2\right),$$

then any matrix $P(u_1, u_2)$ defined as follows:

$$P(u_1,u_2)=\begin{bmatrix}\gamma u_1 & 0 & \alpha \\ 0 & \frac{C\alpha^2}{L_2u_1}+\frac{L_1}{L_2}u_1\gamma & 0 \\ \alpha & 0 & \frac{\alpha^2}{u_1}+\frac{L_1}{C}u_1\gamma\end{bmatrix}, \tag{5.7}$$

is positive definite and satisfies:

$$P(u_1,u_2)A(u_1,u_2)+A^\top(u_1,u_2)P(u_1,u_2)<0. \tag{5.8}$$

□

Proof. Matrix $P(u_1, u_2)$ defined in (5.7) has the following structure:

$$P(u_1,u_2)=\begin{bmatrix}p_1 & 0 & p_4 \\ 0 & p_2 & 0 \\ p_4 & 0 & p_3\end{bmatrix}, \tag{5.9}$$

and it is positive definite because:

$$p_3=\frac{\alpha^2}{u_1}+\frac{L_1}{C}u_1\gamma>0, \tag{5.10a}$$

$$p_2p_3=\left(\frac{C\alpha^2}{L_2u_1}+\frac{L_1}{L_2}u_1\gamma\right)\left(\frac{\alpha^2}{u_1}+\frac{L_1}{C}u_1\gamma\right)>0, \tag{5.10b}$$

$$p_1p_3-p_4^2=(\gamma-1)\alpha^2+\frac{L_1}{C}u_1^2\gamma^2>0, \tag{5.10c}$$

where the last comes from the consideration that $\gamma > \max\{1, \xi\}$ for hypothesis. By calculating the following matrix:

$$\begin{aligned}H_e\big(P(u_1,u_2)A(u_1,u_2)\big)&=\begin{bmatrix}\frac{2}{L_1}(\alpha p_1-u_1p_4) & -\frac{u_2}{L_2}p_4 & \frac{\alpha}{L_1}p_4-\frac{u_1}{L_1}p_3+\frac{u_1}{C}p_1 \\ -\frac{u_2}{L_2}p_4 & 2\frac{\beta}{L_2}p_2 & u_2(\frac{p_2}{C}-\frac{p_3}{L_2}) \\ \frac{\alpha}{L_1}p_4-\frac{u_1}{L_1}p_3+\frac{u_1}{C}p_1 & u_2(\frac{p_2}{C}-\frac{p_3}{L_2}) & 2\frac{u_1}{C}p_4\end{bmatrix} \\ &=p_1\begin{bmatrix}\frac{2\alpha}{L_1\gamma}(\gamma-1) & -\frac{u_2\alpha}{L_2u_1\gamma} & 0 \\ -\frac{u_2\alpha}{L_2u_1\gamma} & \frac{2\beta CL_1}{L_2^2u_1}(\frac{\alpha^2}{\gamma u_1L_1}+\frac{u_1}{C}) & 0 \\ 0 & 0 & \frac{2\alpha}{C\gamma}\end{bmatrix},\end{aligned} \tag{5.11a}$$

which is positive definite, because:

$$\frac{2\alpha}{C\gamma}>0, \tag{5.12a}$$

$$4\alpha\beta L_1u_1^2\gamma+4\alpha^3\beta C>0, \tag{5.12b}$$

$$\det(H_e(\cdot))=(4\alpha\beta L_1u_1^2)\gamma^2+4\alpha\beta(\alpha^2C-L_1u_1^2)\gamma-\alpha^2(4\alpha\beta C+L_1u_2^2)>0, \tag{5.12c}$$

where the last comes from the consideration that $\gamma > \xi$ where ξ is defined as in (5.6). Model (5.2) is composed of three state variables i_1, i_2, and v_C, and each of these variables represents a different source. This modeling framework provides the foundation for the hybrid control strategy proposed in this chapter. The primary goal is to control both the voltage on the bus, v_C, and the internal current variables, i_1 and i_2. To this end, discrete

allocation decisions are embedded into the continuous control loop, enabling efficient coordination of the source currents and maintaining voltage stability. In particular, it is necessary to manage the fuel-cell current i_1, as it should be maintained as constant as possible due to performance and lifespan considerations. In contrast, the battery current i_2 can vary accordingly to the setting value of v_C. To achieve these goals, a hybrid min-type control law is employed in combination with a dynamic input allocation strategy, which ensures that the appropriate equilibrium point is selected in real time based on system conditions.

5.5 Hybrid min-type control design for MIC

Following the modeling and stability analysis of the averaged MIC, this section focuses on the design of a hybrid control strategy aimed at stabilizing the system around a desired operating point. Due to the overactuated nature of the MIC, multiple combinations of control inputs can achieve the same output voltage, introducing a level of redundancy that can be effectively leveraged. To exploit this feature, a hybrid min-type control approach is proposed. This method integrates continuous-time regulation with discrete logic-based switching, allowing the system to dynamically select the most suitable configuration among the available switching states to ensure robust and stable operation.

5.5.1 Equilibrium selection and control objectives

Starting from the continuous-time averaged MIC model, described by the state variables i_1, i_2, and v_C, representing the fuel cell, battery, and common DC bus voltage, respectively, the control objective is to stabilize the system around a desired equilibrium point. Due to the overactuated nature of the MIC, multiple combinations of duty cycles u_1, u_2 can lead to the same output voltage, resulting in input redundancy. To resolve this redundancy, a specific equilibrium operating point is selected. Considering the explicit expression of the set of equilibrium points (5.5), by imposing $v_C = V_C^*$ and $i_1 = I_1^*$, the corresponding equilibrium values of u_1 and u_2 are:

$$u_1^* = \frac{(V_1 - R_1 I_1^*)}{(V_C^* + R I_1^*)}, \tag{5.13a}$$

$$u_2^* = \frac{(I - u_1^* I_1^*)}{I_2^*}, \tag{5.13b}$$

where

$$I_2^* = \frac{V_2 - R(I - u_1^* I_1^*)}{2R_2} - \frac{\sqrt{\Gamma}}{2R_2},$$

with

$$\Gamma = [V_2 - R(I - u_1^* I_1^*)]^2 - 4R_2 V_C^* (I - u_1^* I_1^*).$$

This selection balances both performance and physical constraints of the energy sources. The resulting equilibrium defines a compact attractor set $\mathcal{A}$, representing the desired

dynamic behavior. Define the compact attractor $\mathcal{A}$ as follow:

$$\mathcal{A} := \{(x, v) : x = x_e(u_1^*, u_2^*), v \in \mathcal{Q}\}, \tag{5.14}$$

where x_e is the desired equilibrium point, and Q is a set representing all the possible configuration of $[S_1\ S_2]^\top$, defined as:

$$\mathcal{Q} = \left\{ \begin{bmatrix} 0 \\ 0 \end{bmatrix}, \begin{bmatrix} 0 \\ 1 \end{bmatrix}, \begin{bmatrix} 1 \\ 0 \end{bmatrix}, \begin{bmatrix} 1 \\ 1 \end{bmatrix} \right\}. \tag{5.15}$$

The set $\mathcal{A}$ in (5.14) is referred to as a compact attractor, since it is both bounded and closed, i.e., compact, and represents the equilibrium set toward which the state x is intended to converge.

5.5.2 Hybrid min-type control law and stability analysis

To ensure convergence toward the set $\mathcal{A}$, a min-type hybrid control law is applied. This control mechanism dynamically selects the discrete switching vector $v \in \mathcal{Q}$ based on the minimization of a Lyapunov function derivative, ensuring stability and robustness. This hybrid strategy enables the continuous-time controller to operate effectively within a discrete switching environment. The integration of logic-based decision-making and Lyapunov-based design guarantees Uniform Global Asymptotic Stability (UGAS) of the set $\mathcal{A}$, under suitable conditions on the control parameters. Before giving the main results, the following Lemma is considered:

Lemma 5.5.1

Consider $e = x - x_e$ as the tracking error, and also consider a set Q defined in (5.15), then for any matrix $P(u_1, u_2)$ defined in (5.7) it holds that $e \neq 0$ implies:

$$\min_{v \in Q} e^\top P(u_1, u_2) \left(\left(A_0 + \left[\begin{array}{c|c} A_1 & A_2 \end{array} \right] [v \otimes \mathcal{I}_3] \right) x + BV_{in} \right) < 0. \tag{5.16}$$

□

where $\otimes$ denotes the Kronecker product and $\mathcal{I}_3$ is the identity matrix.

Proof. Inequality (5.16) can be proved by using Lemma 5.4.1 and the same consideration given in [[36], Lemma 1]. The proposed min-type control strategy can be expressed by the following Theorem.

Theorem 5.5.1

Consider $e = x - x_e$ and matrix $P(u_1, u_2)$ defined in (5.7). Then, defining:

$$\mu(v) = -\min\left\{0, \eta(e)\right\},\ \forall v \in Q \tag{5.17}$$

where

$$\eta(e) = e^\top P(u_1, u_2) \left(\left(A_0 + \left[\begin{array}{c|c} A_1 & A_2 \end{array} \right] [v \otimes \mathcal{I}_3] \right) x + BV_{in} \right),$$

the input u chosen as $u = u_{stab}$ with:

$$u_{stab} = \left(\sum_{v \in Q} \mu(v) \right)^{-1} \left(\sum_{v \in Q} \mu(v) v \right), \tag{5.18}$$

ensure that $\mathcal{A}$ is UGAS. □

Proof Let us consider the following quadratic Lyapunov function

$$V = \frac{1}{2} e^\top P(u_1, u_2) e. \tag{5.19}$$

Then:

$$\begin{aligned}
\dot{V} &= e^\top P(u_1,u_2)\dot{e} = e^\top P(u_1,u_2) \left[\left(A_0 + \left[\begin{array}{c|c} A_1 & A_2 \end{array} \right] \left(\begin{bmatrix} u_1 \\ u_2 \end{bmatrix} \otimes \mathcal{I}_3 \right) \right) x + BV_{in} \right] \\
&= e^\top P(u_1,u_2) \left[\left(A_0 + \left[\begin{array}{c|c} A_1 & A_2 \end{array} \right] \left(\left(\frac{\sum_{v \in Q} \mu(v) v}{\sum_{v \in Q} \mu(v)} \right) \otimes \mathcal{I}_3 \right) \right) x + BV_{in} \right] \\
&= \left(\sum_{v \in Q} \mu(v) \right)^{-1} \sum_{v \in Q} \mu(v) \left[e^\top P(u_1,u_2) \left(\left(A_0 + \left[\begin{array}{c|c} A_1 & A_2 \end{array} \right] [v \otimes \mathcal{I}_3] \right) x + BV_{in} \right) \right] \leq 0.
\end{aligned} \tag{5.20}$$

where the last inequality derives from (5.17) and Lemma 5.5.1. Finally, to conclude the proof, it is trivial to note that $v \in C_o(Q)$. The min-type hybrid control strategy presented here plays a central role in the proposed hierarchical control framework. It enables accurate regulation of both the DC bus voltage and the source currents, addressing the challenges due to the overactuated nature of the MIC. To further enhance the flexibility and performance of the MIC, it is necessary to develop a dynamic allocation method that enables decoupled regulation of the source currents while maintaining the DC bus voltage constant.

5.6 Hybrid dynamic allocation strategy

To enhance the flexibility and performance of the MIC within the hierarchical control architecture, a hybrid dynamic allocation strategy is proposed to regulate source currents without altering the bus voltage. Considering the averaged model (5.2) and rewriting it in a suitable way:

$$\dot{x} = A_0 x + \left[\begin{array}{c|c} A_1 x & A_2 x \end{array} \right] \begin{bmatrix} u_1 \\ u_2 \end{bmatrix} + BV_{in} = f_0(x,u), \tag{5.21}$$

where V_{in} is the uncontrolled constant input, and u_1, u_2 are the control inputs. Due to the overactuated nature of the MIC, multiple input combinations can lead to the same bus voltage v_C. This redundancy is exploited here to introduce a second layer of control logic that dynamically shapes the current profile. To ensure that a variation of u_1 and u_2 does not affect v_C, a decoupling condition is imposed. Specifically, it is necessary that

the quantities $A_0x + u_1A_1x + u_2A_2x$ have the third component equal to zero, as u_1 and u_2 undergo an allocation transient. Consider now selecting $u = u_{\text{stab}} + \tilde{u}$ with:

$$\tilde{u} = \begin{bmatrix} L_1x_2 \\ -L_2x_1 \end{bmatrix} \bar{u},$$

where $\bar{u}$ is a scalar generic allocation-oriented input and u_{stab} is given in (5.18). Then:

$$\dot{x} = f_0(x, u_{\text{stab}}) + \begin{bmatrix} -L_1x_2(\frac{R}{L_1}x_1 + \frac{1}{C}x_3) \\ L_2x_1(\frac{R}{L_2}x_2 + \frac{1}{C}x_3) \\ 0 \end{bmatrix} \bar{u}. \tag{5.22}$$

Note that, according to (5.22), any constant or time-varying selection of $\bar{u}$ does not induce any perturbation of v_C as compared to what should be induced by the stabilizer u_{stab}. This property enables the use of $\bar{u}$ as a modulation signal within a dynamic allocation mechanism, allowing for the adjustment of internal current references while preserving the voltage regulation achieved at the previous control level. For this reason, the quantity $\bar{u}$ is used in our dynamic allocation strategy, where a cost function, penalizing the current splitting error, is minimized through a gradient-based selection of the artificial input $\bar{u}$. In particular, if the current associated with the fuel-cell source (i_1) has to be maintained constant, it is possible to define the cost function J as follows:

$$J = \zeta(x_1 - x_{1,ref})^2, \tag{5.23}$$

where ζ is a positive constant gain, which allows to regulate the speed of convergence of the current loop. The selection of the cost function (5.23) leads to the following gradient-based selection:

$$\dot{\bar{u}} = -\zeta \nabla J, \tag{5.24}$$

where ∇J is the gradient of cost function J, computed as:

$$\nabla J = 2\dot{x}_1 = -2L_1x_2\left(\frac{R}{L_1}x_1 + \frac{1}{C}x_3\right).$$

Based on the allocator dynamics (5.24), the allocation-modified input can finally be selected as:

$$u = u_{\text{stab}} + \begin{bmatrix} L_1x_2 \\ -L_2x_1 \end{bmatrix} \bar{u},$$

where u_{stab} is given in (5.18), which allows minimizing the cost J without affecting at all the voltage output v_C, due to the dynamical constraint highlighted in (5.22). This control logic introduces a dynamic reference shaping mechanism embedded within the existing hybrid architecture. The modulation of $\bar{u}$ does not interfere with the DC bus voltage v_C thanks to the decoupling condition, preserving the layered structure of the control system.

Remark 5.6.1

The introduction of the auxiliary input $\bar{u}$ serves as a dynamic allocation mechanism,

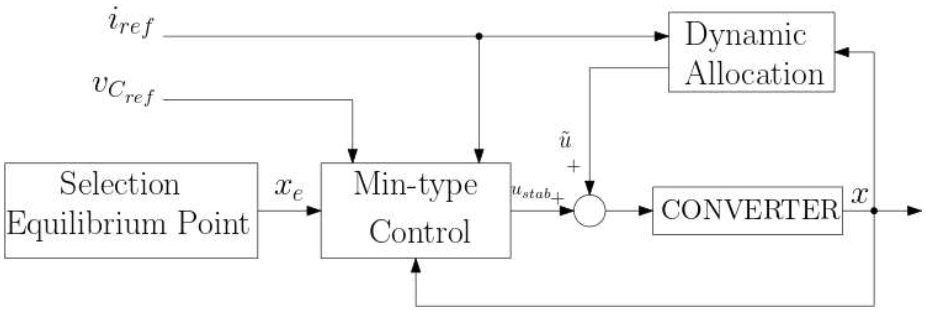

Figure 5.2: Block diagram of the proposed control algorithm.

Table 5.1: Parameters

Parameter	Value
Voltage of the battery V_1	13.3 V
Voltage of the fuel-cell V_2	14.8 V
Inductance L_1	1040 µH
Inductance L_2	1000 µH
Parasitic resistances of the inductance L_1 R_{L_1}	43 mΩ
Parasitic resistances of the inductance L_2 R_{L_2}	73 mΩ
Capacitance C	1880 µF
Parasitic resistances of the capacitor R_C	6.75 mΩ
MOSFET'S conduction resistance R_s	55 mΩ
Body diode's resistance R_d	55 mΩ

enabling decoupled regulation of source currents while maintaining overall voltage stability. This approach enhances the flexibility of the MIC controller, allowing it to adapt to changing operating conditions or source priorities without compromising system-level objectives. When the input $\bar{u}$ is added to the original input u, it becomes possible to minimize the cost function J and consequently to regulate the current i_1 without affecting the voltage v_C. Indeed, any variation induced by $\bar{u}$ induces $\dot{v}_C = 0$. □

The block diagram of the proposed control algorithm is shown in Fig. 5.2. This strategy completes the intermediate level of the hybrid control architecture by enabling the MIC to operate not only as a power-processing unit but also as a dynamic energy allocator. Through this mechanism, the system can adapt to varying operational conditions and distribute source contributions efficiently, without compromising voltage stability.

5.7 Experiments

The effectiveness of the proposed hybrid control strategy has been validated through numerical simulations in the MATLAB/Simulink environment. Circuit-level implementation was carried out using the Power System Toolbox to ensure high modeling accuracy and greater reliability of the electrical dynamics. The parameters used for the simulation setup are summarized in Table 5.1.

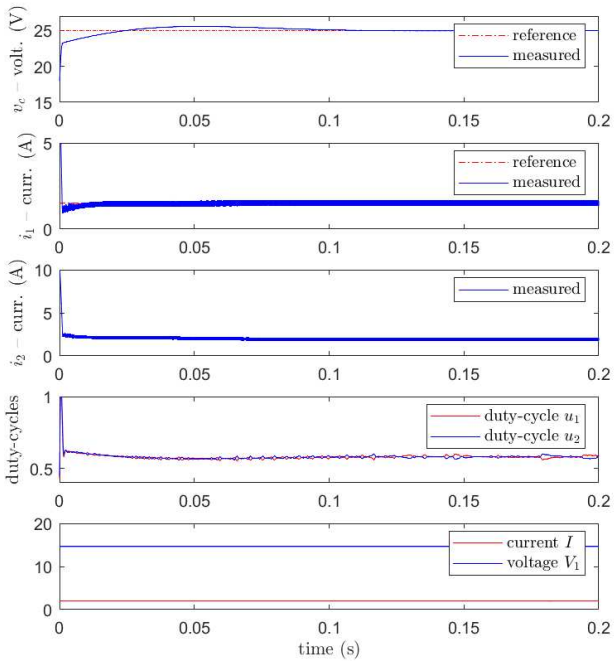

Figure 5.3: Transient time waveforms of the bus voltage v_C, current i_1, current i_2, duty-cycles u_1 and u_2, input voltage V_1 and load current I during a step variation of the bus voltage reference from 18 V to 25 V.

5.7.1 Simulation results

To comprehensively evaluate the system behavior under different operating scenarios, and to highlight both voltage regulation and dynamic current allocation capabilities of the MIC under hybrid control, four different kinds of tests have been performed:

- **Bus voltage reference step response test**: Fig. 5.3 illustrates the transient response of the bus voltage v_C, current i_1, current i_2, duty-cycles u_1 and u_2, input voltage V_1, and load current I during a step variation of the bus voltage reference from 18 V to 25 V. The controller successfully manages the transient by modulating the control inputs u_1 and u_2, ensuring coordinated current injection from the two sources i_1 and i_2. The DC bus voltage v_C converges smoothly to the new setpoint, confirming the correct operation of the voltage regulation loop.
- **Dynamic current allocation test**: Fig. 5.4 shows the same simulations as Fig. 5.3 but for a variation, after 0.1 sec, of the reference current i_1 from 1.5 A to 3 A, while the bus voltage v_C remains constant. As expected, the internal dynamic allocation mechanism rebalances the source currents without disturbing the regulated output voltage. This confirms the decoupling property achieved by auxiliary input $\bar{u}$. The small voltage variation observed in v_C is due to the idealized assumption that the parasitic capacitance resistance R_C is negligible and therefore not explicitly modeled.
- **Load disturbance rejection test**: In Fig. 5.5, the same simulations as in the previous figure are performed, but with a variation of the load current I from 2 A to 8 A.

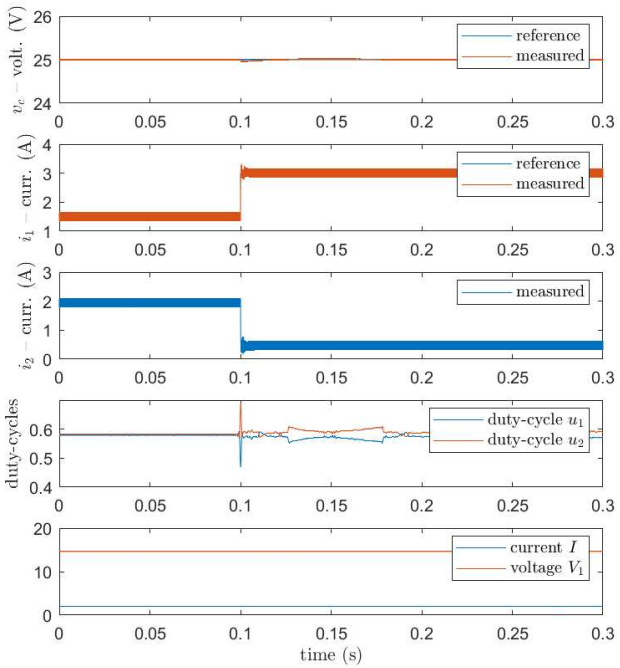

Figure 5.4: Transient time waveforms of the bus voltage v_C, current i_1, current i_2, duty-cycles u_1 and u_2, input voltage V_1, and load current I during a variation, after 0.1 sec, of the current reference from 1.5 A to 3 A.

In this test, both the bus voltage reference v_C and the reference currents i_1 and i_2 remain constant. Despite the step load disturbance, the MIC quickly restores the bus voltage to its nominal value (25 V), demonstrating the robustness of the hybrid control strategy. Additionally, the fuel cell current i_1 remains effectively constant, confirming the stability and effectiveness of the current regulation loop.

- **Input voltage variation rejection test**: Finally, Fig. 5.6 presents the system behavior under a 10% variation in the input voltage V_1. The hybrid control framework successfully compensates for the disturbance, maintaining stable bus voltage and correctly regulated source currents. The ability to reject such perturbations further confirms the robustness and flexibility of the proposed control strategy.

By analyzing the results, it is evident that a variation in the reference current does not affect the output, so dynamic allocation works exactly as expected. From Fig. 5.4, it can be observed that the bus voltage v_C remains constant even though the currents in the two branches have changed; only a small variation of the voltage v_C is observed, as the parasitic resistance R_C of the capacitance C is negligible. From Fig. 5.5, it is possible to observe that a variation of the load current I leads to a variation of the output voltage, as it is logical to expect. However, the system still manages to reject this disturbance and returns to the correct voltage level of 25 V. Furthermore, the current i_1 remains constant and equal to its reference value, indicating that the current control is working as expected. Finally, from Fig. 5.6 it is possible to make similar comments to those made for Fig. 5.5: the control system successfully rejects the disturbance, corresponding here

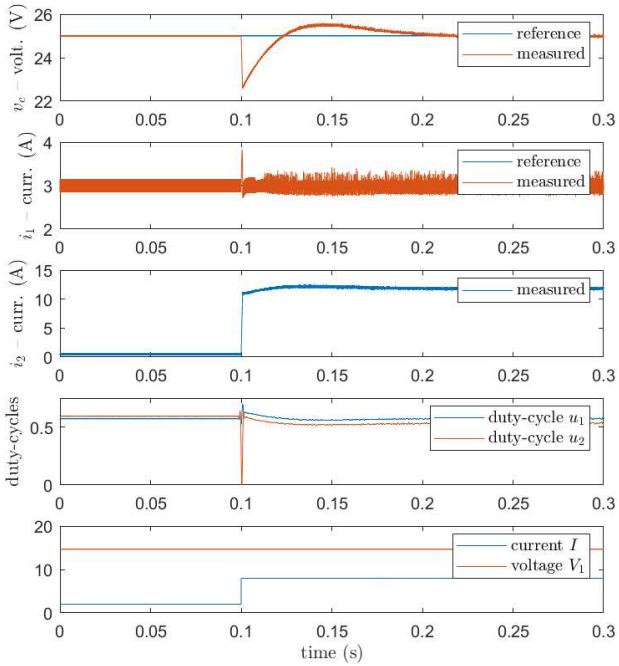

Figure 5.5: Transient time waveforms of the bus voltage v_C, current i_1, current i_2, duty-cycles u_1 and u_2, input voltage V_1 and load current I during a variation of the load current from 2 A to 8 A.

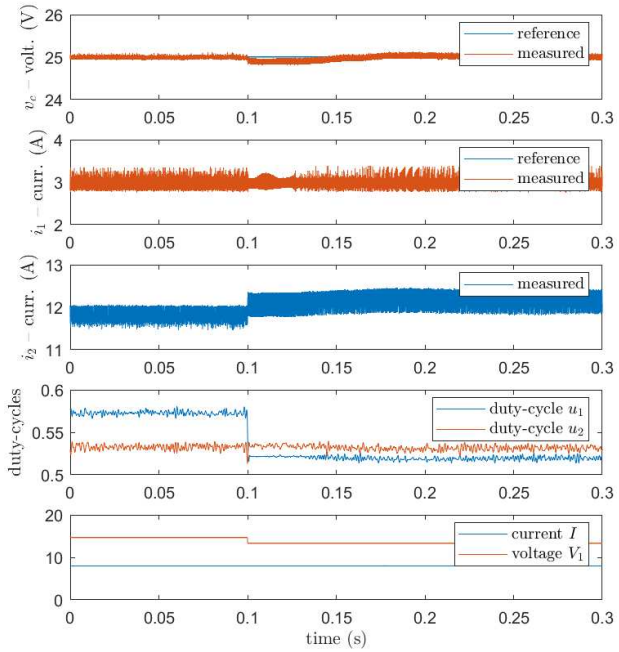

Figure 5.6: Transient time waveforms of the bus voltage v_C, current i_1, current i_2, duty-cycles u_1 and u_2, input voltage V_1 and load current I during a variation of the input voltage.

to a variation of the input voltage V_1. The simulation results confirm that the proposed hybrid control framework satisfies both voltage regulation and dynamic current shaping requirements. The decoupling of current dynamics from voltage control enables flexible energy management while maintaining stability. These features enable MIC to operate as a dynamic energy interface within a broader hybrid control architecture, allowing it to

efficiently address varying operational demands.

5.8 Summary

A dynamic allocation control technique for a MIC is proposed, where both the output voltage and source currents are suitably regulated. The proposed control strategy enables precise management of the current dynamics through automatic control techniques, ensuring that variations in current references do not affect the bus voltage. This decoupling significantly enhances the overall performance and flexibility of the system. The simulation results confirm the effectiveness of the approach. Despite the variations in the reference current, the control system demonstrates strong robustness against parameter variations, successfully rejecting disturbances such as load current changes and input voltage fluctuations. This ensures reliable operation under varying operating conditions. By enabling independent current regulation without compromising voltage stability, the proposed strategy transforms the MIC from a basic power interface into a dynamic energy allocator capable of adapting to various and evolving operational demands. This lays a solid foundation for practical applications in hybrid energy systems and smart grid integration.

Chapter 6

Advanced nonlinear robust control of a DC/AC differential boost inverter with active disturbance compensation and sliding mode component

Abstract

This chapter addresses the nonlinear robust control of a DC/AC Differential Boost Inverter (DBI), leveraging a combination of dynamic feedback linearization, active disturbance rejection, and sliding mode control (SMC) techniques. The considered inverter topology comprises two interleaved synchronous boost converters connected through a resistive load, forming a differential configuration. The control methodology is based on transforming each boost converter into Brunovsky's canonical form via nonlinear feedback, thus isolating the control-affine dynamics from nonlinear disturbance terms. These disturbances contain both endogenous nonlinearities and exogenous influences such as parameter uncertainties or supply/load variations. Each disturbance is estimated by an extended state observer (ESO) and compensated through a control law designed for tracking the desired trajectory, according to the active disturbance rejection control (ADRC) technique. To further enhance the robustness, especially in the presence of model uncertainties or imperfect disturbance estimation, SMC is added to the control law. This hybrid control structure ensures accurate tracking of the desired output voltage trajectory while maintaining resilience to uncertainties in system parameters and external perturbations. The effectiveness of the proposed approach is validated through experimental results, which confirm the controller's ability to maintain stability and performance under challenging operating conditions.

Contents

6.1 Motivation and literature review

As the final stage of the hybrid control architecture developed in this thesis, the output interface plays a critical role in shaping the quality and stability of the energy delivered to the load or the grid. After controlling the power input and regulating the internal energy flow, the DBI represents the concluding part in the control architecture, where nonlinear dynamics, switching behavior, and disturbances must be addressed with high precision and robustness. Model-based control methods for boost DC/DC and DC/AC converters are widely discussed in the scientific literature. The boost converter, usually employed in DC/DC applications, can also be used for directly converting a DC input voltage into a sinusoidal AC voltage with assigned amplitude and frequency superimposed on a mean value different from zero [48]. However, many applications require that the sinusoidal voltage has a mean value equal to zero. In this context, a converter topology named the DBI is a suitable choice. It consists of two synchronous boost converters connected through a central AC load, enabling the generation of bipolar sinusoidal output with zero average value, which is essential for grid compatibility and many AC applications. The scientific literature presents a wide range of strategies for controlling boost and inverter topologies, from small-signal linearized models [49], [50], [51], which employ control methods based on the transfer function, and those based on the sliding mode control [52], [53], [54], [55], [56], [57] based on the state space model. A recent interesting overview of differential single-phase inverter topologies with active power decoupling and their main control technique is given in [58]. In [49], the controller for each boost converter is designed starting from a mathematical model of the boost converter. A transfer function is obtained by linearizing this mathematical model, and a controller is designed in the frequency domain. The controller is implemented via a hardware circuit consisting of an operational amplifier and an RC network. In [50], the same approach is followed, designing two control loops for each boost; the outer loop gives the reference current for the inner loop, and the inner loop gives the duty cycle. Both loops are controlled using PI controllers. In [59], a fractional order PID-type control algorithm for a boost converter is proposed. A suitable procedure for computing the parameters of the fractional controller is given, together with a discretizing method for

implementing it in a floating-point digital signal processing (DSP) unit. In [60], a new topology of a fractional order PID controller is proposed to control a boost converter with minimum overshoot and undershoot. The fractional controller parameters are tuned using a genetic algorithm with a combined cost function composed of the integral of time-weighted absolute error (ITAE) and time-weighted square error (ITSE). In [51], the problem of generating a sinusoidal waveform at high frequency is addressed. It is shown that using a particular nonlinear feedback linearization technique, it is possible to generate a sinusoidal waveform at 2 kHz using the DBI topology mentioned above. In [61], the controller for each boost converter is designed according to the SMC method, assuming as a sliding function a linear combination of the tracking errors of the reference current and voltage. While the reference voltage is well-defined, the reference current is not an exogenous, well-defined signal, and this current is assumed to be the output of a high-pass filter. The implementation of the controller is carried out via hardware through an electronic circuit. In [62], SMC is designed for the whole system, assuming that only two configurations occur among the four conduction configurations of the DBI converter. The sliding function is chosen according to the current-mode design method, and the controller is implemented at a constant frequency using the equivalent control corresponding to the chosen sliding function. In [63], a two-loop control system is illustrated, where the inner loop is controlled using the SMC method with the same sliding function as in [62], the outer loop is PI-type and gives the reference signal for the inner loop so that the output voltage error converges to zero. In [54], a global sliding mode current control scheme for a grid-connected DBI is presented. In [55], the controller for the boost converter is designed according to the SMC based on switched capacitors with high DC gain and low-voltage stress. In [56], a sliding mode backstepping control is proposed for boost converters in real-time for LED lighting applications. The sliding surface in the backstepping control procedure ensures the robustness of the system by attaining an asymptotically stable system. A sliding mode backstepping controller is formulated to address uncertainties resulting from load and input supply variations. In [57], a control law is proposed in terms of the duty cycle. This law is derived by employing the dynamic SMC method applied to the conventional averaged model, where the control variables are the duty cycles; the sliding function is obtained according to the current mode method, adding a term proportional to the integral of the tracking voltage error. For each boost converter, the duty cycle consists of two terms: a continuous term given by the equivalent control corresponding to the chosen sliding function and a discontinuous term proportional to the sign of the sliding function itself. While extensive research has been conducted on both linear and nonlinear control strategies for boost and inverter topologies, challenges persist, particularly in ensuring robust performance under parameter uncertainties, disturbances, and rapidly changing operating conditions.

6.2 Comparison with state-of-the-art control strategies

This chapter introduces an advanced hybrid control scheme for the DBI, including dynamic feedback linearization (FL), ADRC, and SMC. This composite structure provides a high degree of flexibility and robustness, enabling the system to handle all possible conduction modes of the DBI while maintaining accurate tracking and disturbance rejection. In the literature, the control of the boost inverter is typically analyzed using the ADRC without an additional SMC component. A key advantage of the strategy proposed in this chapter lies in its robust-to-disturbance design: the control law includes a dedicated SMC component that compensates for both parametric uncertainties (e.g., changes in input voltage, load resistance) and structural inaccuracies (e.g., estimation error in the ESO). This results in a highly stable closed-loop system, capable of maintaining tracking performance even under significant deviations from nominal operating conditions. To enable implementation, two linear differentiators are employed to compute the derivatives of the current, required for FL. The overall structure remains modular and can be seamlessly embedded in a digital control platform. Both simulation and experimental validation confirm the controller's ability to maintain performance and robustness under real-world disturbance, including those originating from switching ripple, input supply fluctuations, and load transients. Several recent studies have explored ADRC for DC/DC converters [64], [65], [66], [67]. However, these contributions are mainly limited to the control of single boost converter configurations for DC/DC applications and do not address the DBI topology considered in this work. Moreover, none of these studies integrates an additional SMC component, which is crucial for enhancing robustness against a mismatch of the electrical parameters, parametric deviations, and input voltage and load variations, as better described in the approach proposed in this chapter. By comparing the present method with dynamic SMC strategies already presented in the literature, some relevant differences exist. Indeed, the proposed control method introduces a novel formulation where disturbances, both endogenous and exogenous, are actively estimated and compensated using ADRC, and, differently from previously cited papers about SMC ([52], [53], [54], [55], [56], [57]), here the dynamic control method is achieved by extending the state, including the duty-cycle, and defining an auxiliary control variable which is the derivative of the duty-cycle itself. Therefore, the SMC component is added to this auxiliary control variable instead of the duty cycle, which implies that problems due to the chattering are highly attenuated because an integration stage filters out the discontinuous component; this avoids the implementation of suitably designed filters like in [57]. Another important distinction lies in the validity of the proposed control law: it is not restricted to small-signal variations and ensures accurate tracking of the desired output trajectory, minimal waveform distortion, and strong robustness properties under uncertain operating conditions. In summary, the proposed control technique combines three powerful methodologies:

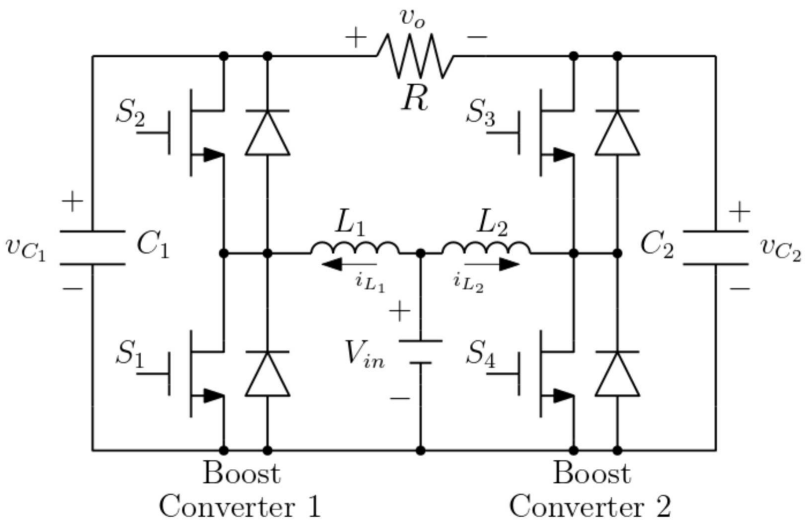

Figure 6.1: Scheme of the differential boost inverter.

- Dynamic FL, to transform the nonlinear model into the linear Brunovski canonical form;
- ADRC, to estimate and compensate internal and external disturbances present in the linearized model through an ESO;
- SMC, added as an auxiliary robustness mechanism to mitigate the effects of disturbance estimation errors and model uncertainties.

Unlike the approaches that rely on simplified assumptions or hardware-based implementation of SMC strategies, the proposed control law is fully PWM-compatible, eliminating issues related to analog signal quantization or discontinuous switching.

6.3 Dynamic model of the DBI and control problem formulation

The scheme of the DBI is shown in Fig. 6.1. The system consists of two synchronous boost converters that share a common DC input source and are connected through a load resistance. The DBI operates in continuous conduction mode (CCM), and for modeling purposes, parasitic elements such as the resistances of the inductors and capacitors are neglected. The differential equations describing the dynamics of the boost inverter can be written using the averaged state-space mathematical model [68] as follows:

$$\dot{i}_{L_1} = -\frac{1}{L_1}(1-\lambda_1)v_{C_1} + \frac{1}{L_1}V_{in}, \tag{6.1a}$$

$$\dot{v}_{C_1} = -\frac{1}{RC_1}(v_{C_1} - v_{C_2}) + \frac{1}{C_1}(1-\lambda_1)i_{L_1}, \tag{6.1b}$$

$$\dot{i}_{L_2} = -\frac{1}{L_2}(1-\lambda_2)v_{C_2} + \frac{1}{L_2}V_{in}, \tag{6.1c}$$

$$\dot{v}_{C_2} = -\frac{1}{RC_2}(v_{C_2} - v_{C_1}) + \frac{1}{C_2}(1-\lambda_2)i_{L_2}, \tag{6.1d}$$

where i_{L_1} and i_{L_2} are the inductor currents flowing in the inductors L_1 and L_2, respectively, v_{C_1} and v_{C_2} are the voltages on the capacitors C_1 and C_2, respectively, V_{in} is the DC supply voltage and R is the load resistance. In this model, the main state variables are the inductor currents i_{L_1} and i_{L_2}, and the capacitor voltages v_{C_1} and v_{C_2}, corresponding to the two boost stages. Moreover, λ_1 and λ_2 represent the duty cycles. In particular, by defining a modulation period equal to T_{PWM}, the switches S_1 and S_4 are managed by considering a turn-on period equal to $T_{1,ON} = \lambda_1 T_{PWM}$ for S_1, and $T_{2,ON} = \lambda_2 T_{PWM}$ for S_4; while the turn off period is, respectively, $T_{1,OFF} = (1-\lambda_1)T_{PWM}$, and $T_{2,OFF} = (1-\lambda_2)T_{PWM}$. The switches S_2 and S_3 are managed in a complementary way concerning S_1 and S_4. The DBI can be considered as two coupled synchronous boost converters (indicated in Fig. 6.1 as Boost Converter 1 and Boost Converter 2) sourced from the same input. To simplify the notation, the synchronous boost converter 1 (left side) will be indicated with Boost-1, and the synchronous boost converter 2 (right side) will be indicated with Boost-2. It is useful to observe that equations (6.1a) and (6.1b) constitute the model of the Boost-1, where the interaction with Boost-2 is represented by the variable v_{C_2}, whereas the model of the Boost-2 is given by (6.1c) and (6.1d), where the interaction with Boost-1 is due to v_{C_1}. The dynamics of Boost-1 are influenced by the output of Boost-2 through the capacitor voltage v_{C_2}, and vice versa, making the system inherently coupled. This mutual interaction must be considered when designing the control strategy. The main goal of this work is to design a controller for the DBI so that the output voltage v_O, defined as:

$$v_O = v_{C1} - v_{C2}, \tag{6.2}$$

tracks a sinusoidal reference (i.e., $v_O = V_O \sin(\omega_o t)$), rejecting both exogenous and endogenous disturbances and ensuring the robustness and stability of the closed loop system. Based on the above considerations, the described goal can be modified by separately controlling the two boost converters and considering their interactions. For this reason, the following desired output voltages, $v^*_{C_1}$ and $v^*_{C_2}$, for the two converters will be considered:

$$v^*_{C_1} = V_{dc} + \frac{V_o}{2} sin(\omega_o t), \tag{6.3}$$

$$v^*_{C_2} = V_{dc} - \frac{V_o}{2} sin(\omega_o t), \tag{6.4}$$

where V_{dc} is the average output voltage required to maintain CCM and is typically greater than the peak of the reference signal V_o (i.e., $V_{dc} > \frac{V_o}{2}$). By designing independent controllers to track these reference signals for each boost converter, the overall system naturally ensures that the output differential voltage v_o follows the desired sinusoidal reference. This decomposition approach also simplifies the control design and enhances robustness by isolating the effects of coupling.

6.4 Design of the control algorithm

The controller is designed starting from the nonlinear averaged state-space mathematical model, with two independent control variables consisting of the duty cycle of the two converters. Although the proposed controller is more complex than those considered in [62], it is more versatile, since it provides a high degree of flexibility and robustness, allowing the system to manage all possible conduction configurations of the converter and enabling separate control of the two boost stages. Moreover, it can be directly implemented through a PWM strategy, thus avoiding the deterioration of regulation properties that typically arises from the transformation of SMC into the PWM one, as in [69]. More in detail, the model of each boost converter is put in Brunovski's canonical form through dynamic FL, defining an auxiliary input that depends on both endogenous and exogenous variables. Each disturbance is estimated by an ESO and compensated through a control law designed for tracking the desired trajectory, according to the ADRC technique. In addition, the SMC component is designed and added to the previous control law to ensure the robustness of the closed-loop system against uncertainties due to electric parameters, supply voltage, load resistance deviations, and disturbance estimation errors. The control law for trajectory tracking requires knowledge of the derivatives of currents, which is carried out using two linear differentiators. The primary objective of the proposed control strategy is to independently control Boost-1 and Boost-2, while effectively managing their dynamic interactions. Within the ADRC framework, the mutual influence between the two converters is considered as an exogenous disturbance that can be estimated through an ESO and subsequently compensated. More precisely, ADRC is structured around an extended dynamic model of order $n + 1$, where n is the order of the original system. The additional state variable represents the total disturbance acting on the system, which includes both internal model uncertainties and external influences. From a hybrid systems perspective, the DBI can be naturally interpreted as a switched nonlinear system, where the power stage dynamics evolve continuously while the control action is implemented through discrete switching signals. Although the control design is presented in a nonlinear continuous-time framework, the overall closed-loop behavior inherently exhibits hybrid characteristics, as discussed in Chapters 2 and 3. In particular, the interaction between the extended state observer, the sliding-mode component, and the switching logic of the inverter results in a hybrid control architecture combining continuous estimation and discrete control actions. The robustness properties of the proposed controller can be interpreted using hybrid stability concepts, where sliding-mode activation and disturbance compensation introduce switching behaviors that can be analyzed through multiple Lyapunov functions and invariance principles for hybrid systems. Based on this model, an ESO is designed to estimate the total disturbance, while the control law is composed of two components:

- the first component compensates for the total disturbance;

- the second component assigns the desired behaviors and assures the desired robustness property.

Since the two converters share the same structure, only one controller is detailed here (Boost-1). The same approach is then symmetrically applied to Boost-2.

6.4.1 Brunovsky canonical transformation with integral dynamic input

To apply the ADRC technique, it is necessary to express the extended model in the Brunovsky canonical form. According to [70], Brunovsky's canonical form can be obtained by introducing an auxiliary control input δ_1, defined as the derivative of the duty cycle λ_1:

$$\dot{\lambda}_1 = \delta_1. \tag{6.5}$$

The output voltage of Boost-1 is expressed as a "flat output":

$$z_1 := C_1 v_{C_1}^2 + L_1 i_{L_1}^2. \tag{6.6}$$

A new state vector is defined based on the successive derivatives of z_1:

$$\boldsymbol{z} = \begin{bmatrix} z_1 \\ z_2 \\ z_3 \end{bmatrix} = \begin{bmatrix} z_1 \\ \dot{z}_1 \\ \ddot{z}_1 \end{bmatrix}, \tag{6.7}$$

where

$$z_2 = 2V_{in} i_{L_1} - \frac{2}{R} v_{C_1}(v_{C_1} - v_{C_2}), \tag{6.8a}$$

$$z_3 = \frac{2}{R^2 C_1}\big(v_{C_1} - v_{C_2}\big)\big(2v_{C_1} - v_{C_2}\big) + \frac{2}{RC_2} v_{C_1}\left[\frac{1}{R}\big(v_{C_1} - v_{C_2}\big) + \big(1 - \lambda_2\big) i_{L_2}\right] + \\ - 2\big(1 - \lambda_1\big)\left[\frac{1}{RC_1}\big(2v_{C_1} - v_{C_2}\big) i_{L_1} + \frac{V_{in}}{L_1} v_{C_1}\right] + \frac{2}{L_1} V_{in}^2. \tag{6.8b}$$

From (6.7), the dynamics of the Boost-1 in terms of $\boldsymbol{z}$-variables are described by linear dynamic model expressed as:

$$\dot{\boldsymbol{z}} = \boldsymbol{A}_z \boldsymbol{z} + \boldsymbol{b}_z \mu_1, \tag{6.9a}$$

$$y_z = z_1, \tag{6.9b}$$

where

$$\boldsymbol{A}_z = \begin{bmatrix} 0 & 1 & 0 \\ 0 & 0 & 1 \\ 0 & 0 & 0 \end{bmatrix}, \boldsymbol{b}_z = \begin{bmatrix} 0 \\ 0 \\ 1 \end{bmatrix},$$

$$\mu_1 = \alpha_1 \delta_1 + \eta_1, \tag{6.10}$$

$$\alpha_1 = \frac{2}{L_1} V_{in} v_{C_1} + \frac{2}{RC_1}(2v_{C_1} - v_{C_2}) i_{L_1}, \tag{6.11}$$

$$
\begin{aligned}
\eta_1 =& 2\Big[-\frac{1}{RC_1}\big(v_{C_1}-v_{C_2}\big)+\frac{1}{C_1}\big(1-\lambda_1\big)i_{L_1}\Big]\Big[\frac{1}{R^2C_1}\big(4v_{C_1}-3v_{C_2}\big)-\frac{2}{RC_1}\big(1-\lambda_1\big)i_{L_1}+\\
&+\frac{1}{R^2C_2}\big(2v_{C_1}-v_{C_2}\big)+\frac{1}{RC_2}\big(1-\lambda_2\big)i_{L_2}-\frac{V_{in}}{L_1}\big(1-\lambda_1\big)\Big]+2\Big[-\frac{1}{RC_2}\big(v_{C_2}-v_{C_1}\big)+\\
&+\frac{1}{C_2}(1-\lambda_2)i_{L_2}\Big]\Big[-\frac{1}{R^2C_1}(3v_{C_1}-2v_{C_2})+\frac{1}{RC_1}(1-\lambda_1)i_{L_1}-\frac{1}{R^2C_2}v_{C_1}\Big]+\\
&-\frac{2}{RC_1L_1}(1-\lambda_1)\big[V_{in}-(1-\lambda_1)v_{C_1}\big](2v_{C_1}-v_{C_2})-\frac{2}{RC_2}v_{C_1}i_{L_2}\dot{\lambda}_2+\\
&+\frac{2}{RC_2L_1}(1-\lambda_2)\big[V_{in}-(1-\lambda_2)v_{C_2}\big]v_{C_1}.
\end{aligned}
\tag{6.12}
$$

α_1 and η_1 are nonlinear and time-variant functions of the original state vector, in particular the variables v_{C2}, which represent the interaction of Boost-2 on Boost-1, and the circuital parameters. Model (6.9) is the Brunovski canonical form of Boost-1 in the $\boldsymbol{z}$-domain. This transformation is needed to linearize the boost model through a nonlinear state feedback. This feedback allows, under certain conditions, to transform the original nonlinear model of the Boost-1 into a linear model in the $\boldsymbol{z}$-domain, a chain of integrators:

$$
\dddot{y}_z = \mu_1. \tag{6.13}
$$

This technique is sensitive to parameter variations, as evident from the complex expressions of α_1 and η_1 in (6.11) and (6.12). The transformation introduces nonlinear, time-varying functions α_1 and η_1, which depend on the full state vector, the coupling voltage v_{C_2}, and physical parameters. In particular:

- α_1 acts as a time-varying control gain;
- η_1 represents the total equivalent disturbance, including modeling errors and inter-converter interactions.

Remark 6.4.1

The Brunovsky canonical form (6.9) has never been presented in literature since it considers the interaction effects between Boost-1 and Boost-2. Indeed, past works considered only isolated DC-DC boost converters, whose canonical form is much simpler. Interestingly, the interaction effects between the two converters can be included in the equivalent disturbance η_1, and the function α_1 does not contain the input variable related to Boost-2. For this reason, an ESO can be designed to estimate the function η_1 as shown in the following subsection, independently of the control input of Boost-2. □

6.4.2 Design of the ESO

To estimate the unknown disturbance η_1, the Brunovsky model is extended by including it as an additional state variable, resulting in an augmented model of fourth order. The ESO is based on model (6.9), including an extra state variable defined as $z_4 = \eta_1$. The resulting extended model is given by:

$$
\dot{\boldsymbol{z}}_e = \boldsymbol{A}_{ze}\boldsymbol{z}_e + \boldsymbol{b}_{ze}\alpha_1\delta_1 + \boldsymbol{b}_{\eta_1}\dot{\eta}_1, \tag{6.14}
$$

where:

$$\boldsymbol{A}_{ze} = \begin{bmatrix} 0 & 1 & 0 & 0 \\ 0 & 0 & 1 & 0 \\ 0 & 0 & 0 & 1 \\ 0 & 0 & 0 & 0 \end{bmatrix}, \ \boldsymbol{z}_e = \begin{bmatrix} z_1 \\ z_2 \\ z_3 \\ z_4 \end{bmatrix}, \ \boldsymbol{b}_{ze} = \begin{bmatrix} 0 \\ 0 \\ 1 \\ 0 \end{bmatrix}, \ \boldsymbol{b}_{\eta_1} = \begin{bmatrix} 0 \\ 0 \\ 0 \\ 1 \end{bmatrix}.$$

A Linear Extended State Observer (LESO) is designed to estimate the state $\boldsymbol{z}_e$, as shown in the following:

$$\dot{\hat{z}}_1 = \hat{z}_2 + \epsilon^{-1}\beta_1 e_z, \tag{6.15a}$$

$$\dot{\hat{z}}_2 = \hat{z}_3 + \epsilon^{-2}\beta_2 e_z, \tag{6.15b}$$

$$\dot{\hat{z}}_3 = \hat{z}_4 + \epsilon^{-3}\beta_3 e_z + \alpha_1\delta_1, \tag{6.15c}$$

$$\dot{\hat{z}}_4 = \epsilon^{-4}\beta_4 e_z, \tag{6.15d}$$

where:

- $\dot{\hat{z}}_i$ denotes the estimated states;
- $e_z = z_1 - \hat{z}_1$ is the output estimation error;
- β_i are observer gains designed such that the polynomial

$$s^4 + \beta_4 s^3 + \beta_3 s^2 + \beta_2 s + \beta_1 = 0, \tag{6.16}$$

  is Hurwitz (i.e., all roots have negative real parts);
- ϵ is a small positive tuning parameter affecting convergence speed.

The parameter ϵ plays a crucial role in balancing speed and noise sensitivity, and must be chosen as low as possible. The lower ϵ, the lower the convergence time, the higher the bandwidth of the observer, and the lower the steady-state estimation errors. However, note that the drawback of a small ϵ is a high noise level on the estimated variables, and, consequently, a good compromise between speed of convergence and noise level should be considered. Therefore, its value should be selected carefully to ensure reliable estimation under real operating conditions.

6.4.3 Controller design using the estimated states

The controller design is carried out starting from the Brunovsky canonical form (6.9), imposing that the output, $y_z = z_1 = C_1 v_{C_1}^2 + L_1 i_{L_1}^2$, tracks the desired trajectory. If the boost converter has to work as a DC/DC converter, with output voltage equal to V_{dc}, the reference value of z_1 is perfectly known and given by:

$$z_{1,ref} = C_1 V_{dc}^2 + L_1 I_{dc}^2,$$

where $I_{dc} = \frac{V_{dc}^2}{RV_{in}}$. A problem arises when the converter must track a time-varying reference voltage, as in (6.3), since determining the real-time reference value of the current

is challenging. Several strategies have been proposed in the literature to determine the inductor current reference. In [49] and [50], the current reference is obtained as the output of a suitably designed high-pass filter. In [48], a systematic procedure is illustrated that allows the determination of the inductor current reference using a differential function of finite order. In [71], the reference state trajectory to be tracked is obtained using the equations of the stable system center, deriving from the ideal internal dynamics, corresponding to a model where these dynamics describe the time evolution of the flat output, i.e., the variable z_1. In this case, the inductor current is equal to the measured current, and its derivatives, up to the third order, are estimated through a fourth-order linear differentiator, whose details are given below. This approach is different from that used in [49] and [50] because, for control purposes, the measured current is passed through a differentiator, i.e., a low-pass filter able to reproduce very well the mean waveform of the current itself, canceling at the same time the high-frequency components while retaining its average dynamic behavior. At the start of the sampling period, the inductor current is measured, and the reference variable $z_{1,ref}$ is computed from the value of the reference voltage $y_{1,ref}$ and the measured current. Then, the controller will calculate the appropriate duty cycle to be applied at the start of the successive sampling interval, following the control law illustrated below.

6.4.3.1 Design of the differentiator

To compute the derivatives of the inductor current i_{L_1}, a fourth-order linear differentiator is considered, described by the following model:

$$\dot{\boldsymbol{\chi}} = \boldsymbol{A}_\chi \boldsymbol{\chi} + p_0 \boldsymbol{h} i_{L_1}, \tag{6.17}$$

where:

$$\boldsymbol{A}_\chi = \begin{bmatrix} 0 & 1 & 0 & 0 \\ 0 & 0 & 1 & 0 \\ 0 & 0 & 0 & 1 \\ -p_0 & -p_1 & -p_2 & -p_3 \end{bmatrix}, \boldsymbol{h} = \begin{bmatrix} 0 \\ 0 \\ 0 \\ 1 \end{bmatrix}.$$

The parameters p_i, $i = 0, \ldots, 3$, are chosen such that the characteristic polynomial

$$s^4 + p_3 s^3 + p_2 s^2 + p_1 s + p_0 = 0, \tag{6.18}$$

is Hurwitz, ensuring system stability. The components of $\boldsymbol{\chi}$, χ_1, χ_2, χ_3 and χ_4, represent, respectively, estimates of the current i_{L_1}, i_{L_1F}, and its derivatives up to the third order $\dot{i}_{L_1F}$, $\ddot{i}_{L_1F}$ and $\dddot{i}_{L_1F}$. Using these values of the inductor current and its derivatives, the reference variable z_{1ref} can be computed as follows:

$$\dot{z}_{1ref} = 2C_1 v_{C_1 ref} \dot{v}_{C_1 ref} + 2L_1 i_{L_1F} \dot{i}_{L_1F}, \tag{6.19a}$$

$$\ddot{z}_{1ref} = 2C_1 (\dot{v}^2_{C_1 ref} + v_{C_1 ref} \ddot{v}_{C_1 ref}) + 2L_1 (\dot{i}^2_{L_1F} + i_{L_1F} \ddot{i}_{L_1F}), \tag{6.19b}$$

$$\dddot{z}_{1ref} = 2C_1 (3\dot{v}_{C_1 ref} \ddot{v}_{C_1 ref} + v_{C_1 ref} \dddot{v}_{C_1 ref}) + 2L_1 (3\dot{i}_{L_1F} \ddot{i}_{L_1F} + i_{LF} \dddot{i}_{L_1F}). \tag{6.19c}$$

6.4.3.2 Design of the control law

According to non-linear control theory [72], the control law that stabilizes and assigns the steady-state and dynamic behavior to a model (6.13) can be determined as follows:

$$\mu_1 = \dddot{y}_{z,ref} - \gamma_{z2}(\ddot{y}_z - \ddot{y}_{z,ref}) - \gamma_{z1}(\dot{y}_z - \dot{y}_{z,ref}) - \gamma_{z0}(y_z - y_{z,ref}). \tag{6.20}$$

Defining the tracking error $e_{yz} = y_z - y_{z,ref}$, and substituting (6.20) into (6.13), the following equation is obtained:

$$\dddot{e}_{yz} + \gamma_{z2}\ddot{e}_{yz} + \gamma_{z1}\dot{e}_{yz} + \gamma_{z0}e_{yz} = 0, \tag{6.21}$$

which is a third-order stable tracking error dynamic and implies that $\lim_{t\to\infty} e_{yz} = 0$ if the polynomial $s^3 + \gamma_{z2}s^2 + \gamma_{z1}s + \gamma_{z0} = 0$ is Hurwitz. Finally, δ_1 can be derived as follows:

$$\delta_1 = \alpha_1^{-1}\left(-\eta_1 + \mu_1\right). \tag{6.22}$$

α_1 and η_1 in (6.22) are known with a certain margin of uncertainty. This consideration suggests modifying the control law (6.22) by adding the SMC designed to cope with these uncertainties (cf. [72]). In particular, to enhance robustness against parameter deviations and/or variations of the supply DC voltage V_{in} and the load resistance R, the control law in terms of δ_1 is modified as follows:

$$\delta_1 = \frac{1}{\hat{\alpha}_1}(\mu_1 - \hat{\eta}_1 + u_{sm1}), \tag{6.23}$$

where $\hat{\alpha}_1$ is the nominal value of α_1, $\hat{\eta}_1$ is the estimated value of η_1 by means of ESO, and

$$u_{sm1} = -k_{sm1}\text{sign}(s_1), \tag{6.24}$$

with:

$$s_1 = \ddot{e}_{yz} + k_1\dot{e}_{yz} + k_0 e_{yz}, \tag{6.25}$$

and k_{sm1} is a positive constant designed as shown in the following Proposition 6.4.1. Before giving the Proposition for determining the gain k_{sm1} the following Assumption 6.4.1 is required:

Assumption 6.4.1

It is assumed that the maximum error between η_1 and its estimate $\hat{\eta}_1$ is

$$\left|\tilde{\eta}_1\right| = \left|\eta_1 - \hat{\eta}_1\right| \leq \epsilon_\eta\left|\hat{\eta}_1\right|, \tag{6.26}$$

for some positive constant ϵ_η. Moreover, it is assumed that $\alpha_1 \in [\alpha_{1min}, \alpha_{1max}]$ where α_{1min} and α_{1max} are the minimum and the maximum values, respectively, of the control gain α_1 and are obtained assuming deviations of the electric parameters from their nominal ones starting from the tolerances of the components employed for realizing the two converters. In this case, α_{1min} and α_{1max} were chosen considering the 30% tolerance of the circuit components from their nominal values. □

Proposition 6.4.1

Assuming:

$$\hat{\alpha}_1 = \sqrt{\alpha_{1min}\alpha_{1max}},\ \text{and}\ \beta = \sqrt{\frac{\alpha_{1max}}{\alpha_{1min}}}.$$

If the gain k_{sm1} is designed as follows:

$$k_{sm1} \geq |\mu_1 - \hat{\eta}_1| + \beta\epsilon_\eta|\hat{\eta}_1| + \beta|\hat{\eta}_1 + k_1\ddot{e}_{yz1} + k_0\dot{e}_{yz1} - \dddot{y}_{z1ref}|, \tag{6.27}$$

then the sliding condition is verified, and the system slides on the surface $s_1 = 0$, for each value of the uncertainties satisfying Assumption 6.4.1. □

Proof. Assuming:

$$\hat{\alpha}_1 = \sqrt{\alpha_{1min}\alpha_{1max}},\ \text{and}\ \beta = \sqrt{\frac{\alpha_{1max}}{\alpha_{1min}}},$$

it follows that

$$\frac{\alpha_1}{\hat{\alpha_1}} \in [\beta^{-1}, \beta], \quad \text{and} \quad \frac{\hat{\alpha_1}}{\alpha_1} \in [\beta^{-1}, \beta]. \tag{6.28}$$

Substituting (6.23) into (6.9), the following equation is obtained:

$$\dot{z}_3 = \left(\eta_1 - \frac{\alpha_1}{\hat{\alpha}_1}\hat{\eta}_1\right) + \frac{\alpha_1}{\hat{\alpha}_1}\big(\mu_1 - k_{sm1}\,\mathrm{sign}(s_1)\big). \tag{6.29}$$

The Lyapunov candidate function is defined as follows:

$$V(s_1) = \frac{1}{2}s_1^2. \tag{6.30}$$

Computing the derivative of (6.30) yelds:

$$\dot{V}(s_1) = s_1\dot{s}_1.$$

Consequently, for obtaining $\dot{V}(s_1) < 0$, the following sliding conditions have to be satisfied:

$$\begin{cases} \dot{s}_1 > 0 & \text{for} \quad s_1 < 0, \\ \dot{s}_1 < 0 & \text{for} \quad s_1 > 0. \end{cases} \tag{6.31}$$

From (6.24) and (6.25), it follows that:

$$\begin{aligned} \dot{s}_1 = {} & \dddot{y}_z - \dddot{y}_{z,ref} + k_1(\ddot{y}_z - \ddot{y}_{z,ref}) + k_0(\dot{y}_z - \dot{y}_{z,ref}) = \\ & = \tilde{\eta}_1 + \left(1 - \frac{\alpha_1}{\hat{\alpha}_1}\right)\hat{\eta}_1 + \frac{\alpha_1}{\hat{\alpha}_1}\big(\mu_1 - k_{sm1}\mathrm{sign}(s_1)\big) + k_1(\ddot{y}_z - \ddot{y}_{z,ref}) + k_0(\dot{y}_z - \dot{y}_{z,ref}) + \\ & - \dddot{y}_{z,ref}. \end{aligned} \tag{6.32}$$

Then, from (6.31), it is obtained that:

- for $s > 0$:

$$\tilde{\eta}_1 + \left(1 - \frac{\alpha_1}{\hat{\alpha}_1}\right)\hat{\eta}_1 + \frac{\alpha_1}{\hat{\alpha}_1}\big(\mu_1 - k_{sm1}\big) + k_1(\ddot{y}_z - \ddot{y}_{z,ref}) + k_0(\dot{y}_z - \dot{y}_{z,ref}) - \dddot{y}_{z,ref} < 0; \tag{6.33}$$

- for $s < 0$:

$$\tilde{\eta}_1 + \left(1 - \frac{\alpha_1}{\hat{\alpha}_1}\right)\hat{\eta}_1 + \frac{\alpha_1}{\hat{\alpha}_1}\left(\mu_1 + k_{sm1}\right) + k_1(\ddot{y}_z - \ddot{y}_{z,ref}) + k_0(\dot{y}_z - \dot{y}_{z,ref}) - \dddot{y}_{z,ref} > 0. \tag{6.34}$$

Both of which are satisfied for:

$$k_{sm1} > \max_{\tilde{\eta}_1,\alpha_1} \left| \mu_1 - \hat{\eta}_1 + \frac{\hat{\alpha}_1}{\alpha}\left(\tilde{\eta}_1 + \hat{\eta}_1 + k_1(\ddot{y}_z - \ddot{y}_{z,ref}) + k_0(\dot{y}_z - \dot{y}_{z,ref}) - \dddot{y}_{z,ref}\right)\right|. \tag{6.35}$$

Using the conditions given in Assumption 6.4.1, (6.35) can be maximized as follows:

$$\begin{aligned}
&\left| \mu_1 - \hat{\eta}_1 + \frac{\hat{\alpha}_1}{\alpha}\left(\tilde{\eta}_1 + \hat{\eta}_1 + k_1(\ddot{y}_z - \ddot{y}_{z,ref}) + k_0(\dot{y}_z - \dot{y}_{z,ref}) - \dddot{y}_{z,ref}\right)\right| \leq \\
&\left|\mu_1 - \hat{\eta}_1\right| + \frac{\hat{\alpha}_1}{\alpha_1}\left|\tilde{\eta}_1\right| + \frac{\hat{\alpha}_1}{\alpha_1}\left|\hat{\eta}_1 + k_1(\ddot{y}_z - \ddot{y}_{z,ref}) + k_0(\dot{y}_z - \dot{y}_{z,ref}) - \dddot{y}_{z,ref}\right| \leq \\
&\left|\mu_1 - \hat{\eta}_1\right| + \beta\epsilon_\eta\left|\hat{\eta}_1\right| + \beta\left|\hat{\eta}_1 + k_1(\ddot{y}_z - \ddot{y}_{z,ref}) + k_0(\dot{y}_z - \dot{y}_{z,ref}) - \dddot{y}_{z,ref}\right|.
\end{aligned} \tag{6.36}$$

From (6.36) follows that (6.31) is satisfied if k_{sm1} is as shown in (6.27). This concludes the proof. □

The condition (6.35) does not depend on the electromagnetic parameters as it occurs, for example, in [49], simplifying robustness analysis. This is important because it is challenging to verify a priori if the sliding conditions are satisfied for all the values of the parameters in the cases where they depend on the parameters themselves. In contrast with [71], where the coordinate transformation leads to a canonical form nonlinear model having an internal dynamics unstable of order 1, the coordinate transformation used here leads to a linear model having no internal dynamics.

Remark 6.4.2

From the Proof 6.4.3.2, it is evident that condition (6.35) can be satisfied using two procedures:

- *estimate an upper bound of k_{sm1}, which satisfies the sliding condition in all the possible operating situations;*
- *select, online, the time-variant gain k_{sm1}, computing the second member of (6.27), including β_1, which is computed as indicated in Proposition 6.4.1, considering the maximum and minimum values for the electromagnetic parameters, and assuming that the measured voltages and currents are not affected by errors.*

The first choice is too conservative and results in an increase in chattering. The second choice has been adopted in this case. If the gain is time-varying, it does not depend on the particular values of α_1 or η_1, which are unknown. Instead, only the value of ϵ_η has to be chosen because the other variables in (6.27) are computed online. □

Table 6.1: Parameters of the converter

Name	Value	Component	Description
V_{IN}	48V		Input Voltage
R	150Ω		Load Resistor
$L_{1,2}$	470μH	AGP4233-474ME	Inductors
$C_{1,2}$	10μF	MKP1848610094P	Capacitors
$S_{1,2,3,4}$	-	SCTWA90N65G2V	Switch
Driver	-	STGAP2SCIC	Switch Driver

Remark 6.4.3

The proposed control law is not influenced by the power range of the converter; therefore, there are no limitations, and it can be employed both in low-power and high-power applications. □

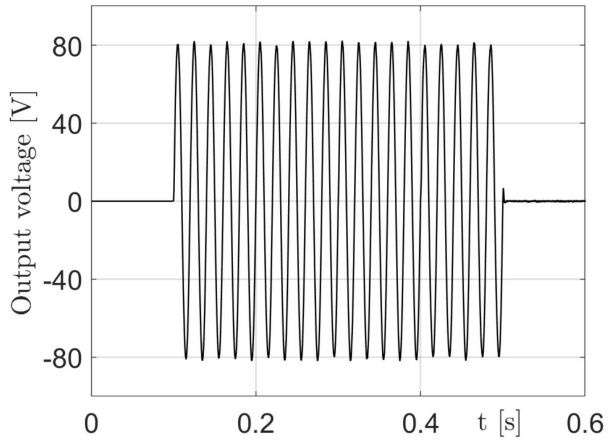

Figure 6.2: Output voltage generated during the test with nominal parameters.

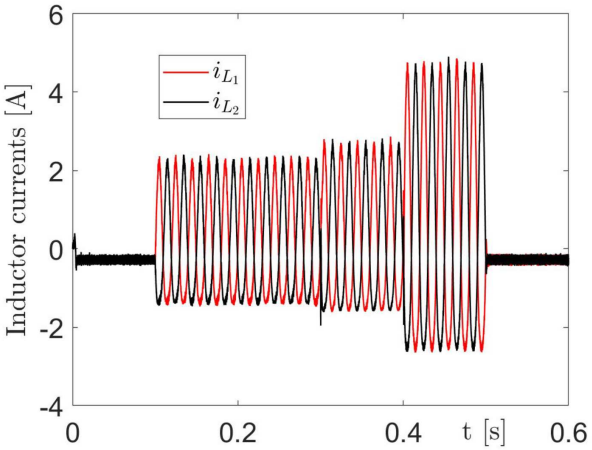

Figure 6.3: Currents in the inductors of the two boost converters, generated during the test with nominal parameters.

6.5 Experiments

This section presents the validation of the proposed control strategy for the DBI through both numerical simulations and laboratory experiments. First, the simulation results

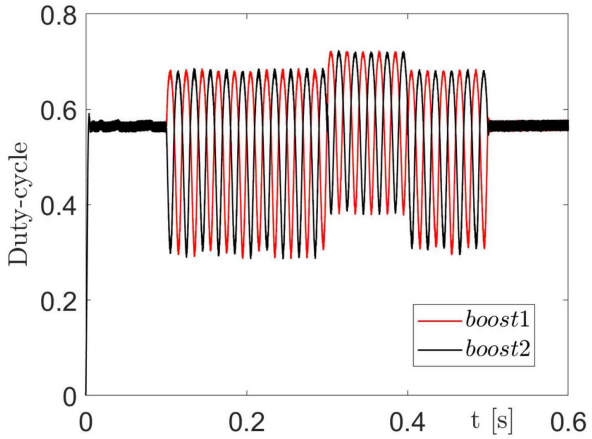

Figure 6.4: Duty cycles generated during the test with nominal parameters.

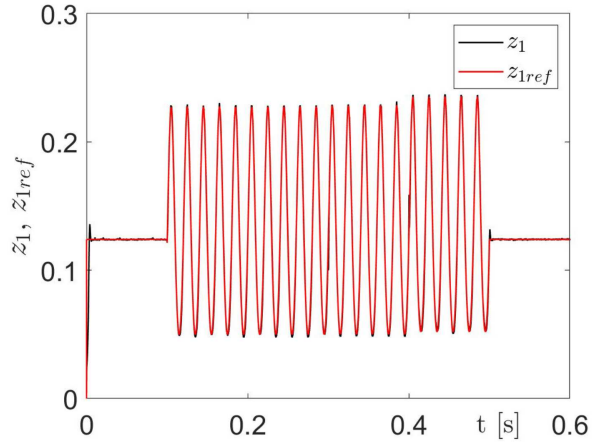

Figure 6.5: Reference variable $z_{1,ref}$ and variable z_1 generated during the test with nominal parameters.

are reported, evaluating the controller's performance under nominal conditions and its robustness under parameter mismatches. Next, the experimental setup is described, including the hardware configuration and measurement instrumentation, designed to reproduce realistic operating conditions and provide accurate measurements of electrical quantities such as inductor currents and capacitor voltages. Then, the experimental results are presented, including start-up test behavior, steady-state operation, load variation test, and input voltage variation test. Finally, a comparison between experimental and simulation results is provided.

6.5.1 Simulation results

To validate the performance of the proposed nonlinear robust control strategy, simulation experiments were carried out in the MATLAB-Simulink environment, where both the plant model and the controller were implemented. To test the behavior of the boost inverter and its robustness against input voltage and load variations, two test scenarios were designed:

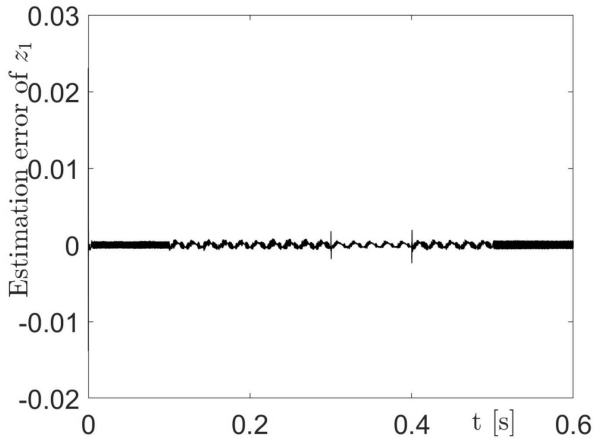

Figure 6.6: Estimation error of the variable z_1 generated from the ESO 1 during the test with nominal parameters.

- performance with nominal parameters;
- robustness under parameter mismatch.

6.5.1.1 Performance with nominal parameters

In the first test, the converter parameters were set to their nominal values. In particular:

- At $t = 0.1$ sec., two sinusoidal voltage references with 50 Hz of frequency and 40 V of amplitude are imposed on both the converters, according to (6.3) and (6.4), with $V_{dc} = 110V$. This produced a sinusoidal differential output voltage with a peak amplitude of $80V$.
- At $t = 0.3$ sec., a step variation of 12.5% was applied to the input voltage.
- At $t = 0.4$ sec., a variation of the load resistance, equal to -50%, is applied, restoring, at the same time, the nominal input voltage.
- Finally, at $t = 0.5$ sec., the reference voltage was set to zero to test transient shutdown behavior.

The parameters of the boost inverter are given in Table 6.1. From the datasheets of the inductors and capacitors, the maximum value deviations are $\pm 20\%$ for the inductance and $\pm 10\%$ for the capacitance. The parameters of the controller are chosen such that:

- **Controller**: the roots of polynomial (6.21) are real, negative and equal to $\omega_{contr} = 10150$ rad/s;
- **ESO**: the roots of polynomial (6.16) are real, negative and equal to $\omega_{eso} = 100$ rad/s;
- **Differentiator**: the roots of polynomial (6.18) are real, negative and equal to $\omega_{diff} = 20000$ rad/s;

- **Sliding function**: the roots of polynomial (6.25) are real, negative and equal to $\omega_{sl} = 1000$ rad/s.

The simulation results are shown in the Figures 6.2-6.6. These results show that the DBI can generate a sinusoidal voltage with a maximum amplitude error of 0.65% in all situations. The harmonic content of the output voltage consists of odd harmonics, with the third harmonics, the biggest one, about 1% of the fundamental frequency, and a fifth harmonic less than 0.4%. The total harmonic distortion (THD) depends on the bandwidth of the differentiator and, in this test, is equal to 2.05%. The currents do not have a sinusoidal waveform due to the nonlinear characteristic of the boost converters, and their peak-to-peak value increases to compensate for the variations of the input voltage and load. The measured inductor currents assume the significance of reference currents and, consequently, it is possible to generate the reference variable $z_{1,ref}$ and the state variable z_1, both useful for the control loop of the FL system. Figure 6.5 shows the tracking high capability of this control loop, where the state variable is superimposed on the reference one. Fig. 6.6 shows the high capability of the ESO in the estimation of the state variable z_1, which is a necessary condition for a good estimation of the total disturbance η_1, useful in the computation of δ_1 and then of the duty cycle λ_1. The smooth waveforms of the duty cycles, due to the presence of the dynamic input, produce smooth forms in the voltage v_{C_1} and v_{C_2}, and then in the output voltage, by avoiding the main issue of other standard SMCs. Finally, the results described in this test show that the output voltage is practically insensitive to input voltage variations and load resistance variations. Naturally, the inductor currents vary in the presence of the above variations, as illustrated in Fig. 6.3.

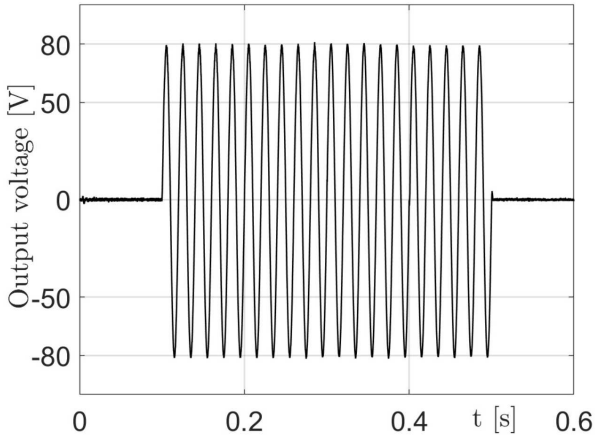

Figure 6.7: Output voltage generated during a test with strong parameter variation

6.5.1.2 Robustness under parameter mismatch

Since one strength of the proposed algorithm is its robustness against electrical parameter variations, to demonstrate the performance of the proposed control technique, a second

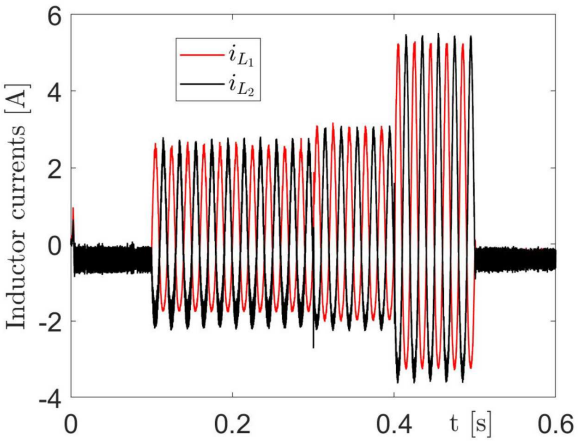

Figure 6.8: Currents in the inductors of the two boost converters, generated during a test with strong parameter variation.

test was carried out by imposing a strong mismatch of the two boost parameters. In particular, the values of L_1, L_2, C_1, and C_2 are varied with an increment of 30% for the Boost-1 and a decrement of 30% for the Boost-2. Moreover, the parasitic resistances of both inductances and capacitors were considered in the circuit. The type of test in terms of reference output voltage, input, and load variations is the same as the previous one shown in the Figures 6.2-6.3. The simulation results are given in Figs. 6.7 and 6.8. Examination of these figures shows that the robustness of the output voltage is maintained for variations of input voltage and load resistance, whereas a mismatch of the inductor currents appears. In particular, peak values of the current i_{L_1} diminish, whereas those of i_{L_2} increase. The total harmonic distortion, equal to 2.92%, increases slightly compared with the test with nominal parameters, but it is widely acceptable. This performance improvement is due to the proposed control scheme since the equivalent disturbance is estimated and compensated online, and the SMC action allows it to gain robustness against possible exogenous disturbances and input errors of the ESOs, thus confirming the effectiveness of the proposed approach.

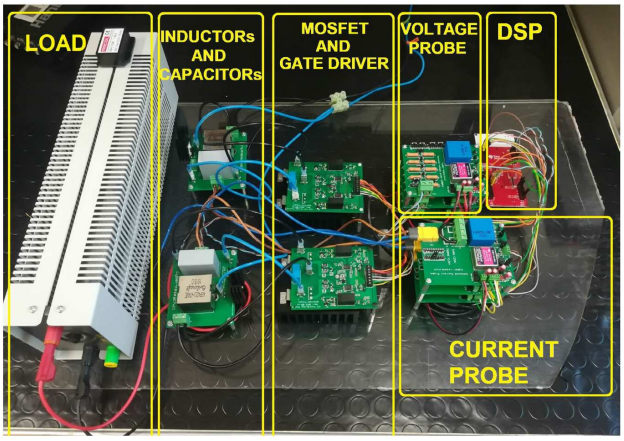

Figure 6.9: Picture of the overall test setup.

6.5.2 Experimental setup

This section presents the experimental setup suitably built to validate the proposed controller. The converter under test is shown in Fig. 6.1, while in Fig. 6.9, a photo of the overall test bench is given. Moreover, Table 6.1 shows the components and their values used to conduct the experiments. The controller has been implemented on the F28379D LaunchPad development kit for the C2000 Delfino MCU by Texas Instruments, a low-cost evaluation and development board for the TMS320F28379D microcontroller. The board features a 32-bit microcontroller with a dedicated coprocessor for optimizing floating point calculations, the CLA (Control Law Accelerator). The processor, in particular, features a dual-core architecture with two C28x CPUs and two CLAs, operating at 200MHz with a total processing capability of 800 MIPS. It includes 1024 kB of flash memory, 204 kB of RAM, and supports advanced functionalities such as 12- and 16-bit ADC resolution, 24 PWM channels, and 8 SPI interfaces. In particular, the implementation has been made so that the CLA executes the control algorithm at 100kHz. In contrast, other tasks, which do not need to be executed with strict timings, are executed on the main CPU. The source files necessary for implementing the algorithm have been developed employing MATLAB-Simulink software. The MOSFETs' gates are logically driven through the PWM generator modules available on the processor. Specific attention has been given to the design of the driver circuitry using the STGAP2SICS driven by ST-Microelectronics. In particular, the implementation follows the application diagram with Miller Clamp and negative gate driving. The Miller Clamp function allows control of the Miller current during power stage switching in half-bridge configurations. When the external power transistor is in the OFF state, the driver operates to avoid the induced turn-on phenomenon that may occur when the other switch in the same leg is being turned on. During the turn-off period, the gate of the external switch is monitored through the CLAMP pin. The CLAMP switch is activated when the gate voltage goes below the voltage threshold, thus creating a low impedance path between the switch gate and the GNDISO pin. System state, specifically the voltages on the output capacitors v_{C_1}, v_{C_2}, and the currents through the inductors i_{L_1} and i_{L_2}, were measured using some LA 25-NP LEM Hall effect sensors. These sensors were installed on custom boards built explicitly for the implementation of this experimental setup. All signals are sampled and converted by the four parallel on-board analog-to-digital converters. For acquisition via oscilloscope, and to generate the graphs related to the experimental tests, two Teledyne T3CP100-2 current probes, configured with 0.1V/A scale, and two Tektronix P5200 voltage probes, were used in conjunction with the Lecroy Wavepro 7200A DSO. A digital pin on the CPU was also used to trigger the startup sequence and the load and voltage variation tests.

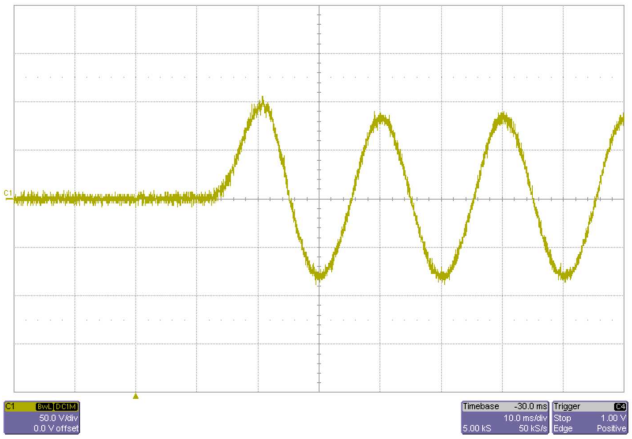

Figure 6.10: Output voltage v_O during a start-up sequence.

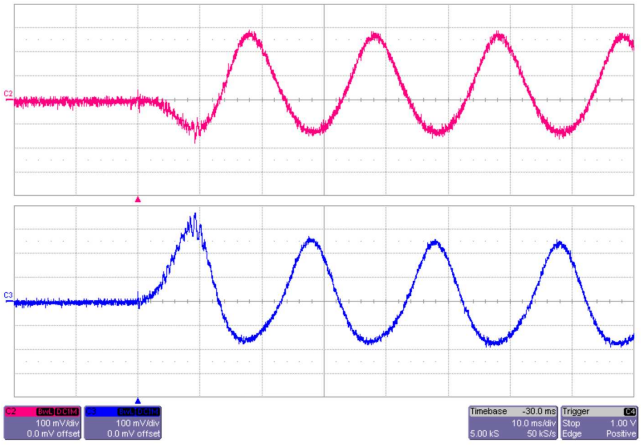

Figure 6.11: Inductor currents i_{L_1} (purple) and i_{L_2} (blue) during a start-up sequence.

6.5.3 Experimental results

This section presents the experimental results obtained to validate the effectiveness proposed hybrid control strategy for the DBI. Four experimental tests were performed:

- **Start-up response analysis**: The system's behavior during the start-up sequence, i.e., the initial transient from zero to the generation of a sinusoidal waveform with a peak-to-peak amplitude of 160 V and a frequency of 50 Hz, is illustrated. In particular, the results of this test are shown in Figures 6.10 and 6.11. Fig. 6.10 shows the waveform of the output voltage v_O, while Fig. 6.11 shows the i_{L_1} and i_{L_2} inductor currents trends. These results show that the system perfectly tracks the sinusoidal reference, the overshoot is negligible, and the steady-state is reached after less than 50 ms, demonstrating excellent transient performance.
- **Steady-state performance evaluation**: Fig. 6.12 shows the waveform of the output voltage v_O in a steady-state condition, while in Fig. 6.13, the FFT components were reported. In Fig. 6.14, the waveforms of the inductor currents i_{L_1} and i_{L_2} are shown for the same operating conditions. The system can follow correctly the

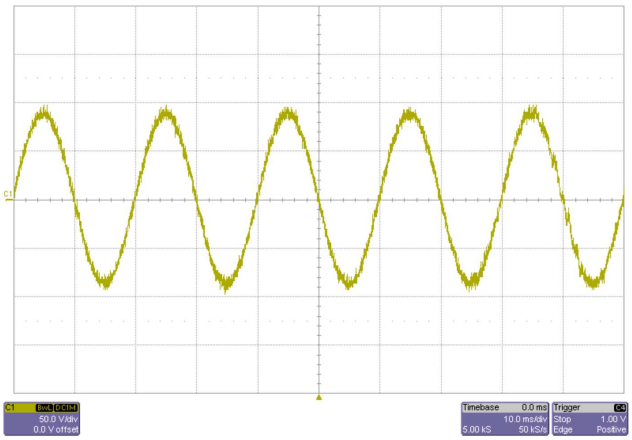

Figure 6.12: Output voltage v_O during a steady-state operating condition.

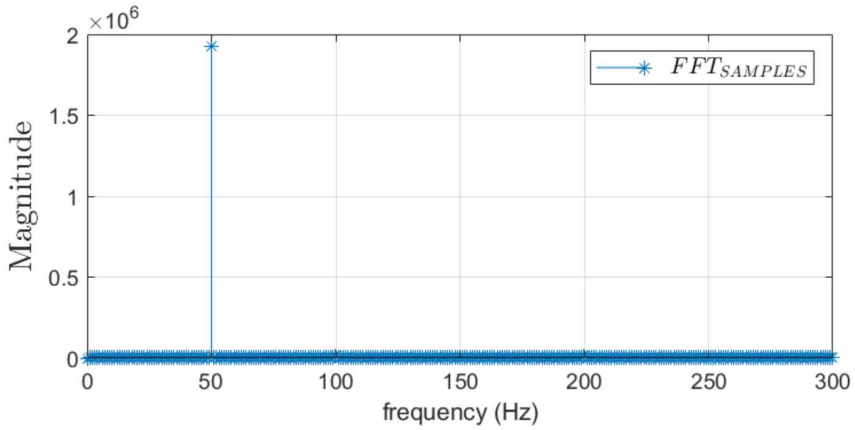

Figure 6.13: FFT samples in a steady-state operating condition.

sinusoidal reference. Furthermore, in this test, the FFT was performed. From the results shown in Fig. 6.13, it is possible to see that there is a negligible distortion with the third harmonics about 1.3% of the fundamental frequency, and a fifth harmonics less than 0.5%. The THD is equal to 2.45%. These values confirm the ability of the proposed control to maintain high power quality in the generated AC voltage.

- **Load variation robustness test**: To assess robustness against load disturbance, the load resistance R was changed from an initial value of $100\,\Omega$ to a final value of $50\,\Omega$. The results are shown in Figures 6.15-6.16, where the waveforms of the output voltage v_O and inductor currents i_{L_1} and i_{L_2} are shown during a load variation. The control system can reject the disturbance; in fact, the output voltage v_O is not affected by load variation, i.e., the influence on v_O is negligible, and the inductor currents i_{L_1} and i_{L_2} rise instantaneously, as can be seen from Fig. 6.16, coherently with the load variation. This confirms the fast dynamic capability and disturbance rejection of the proposed control.

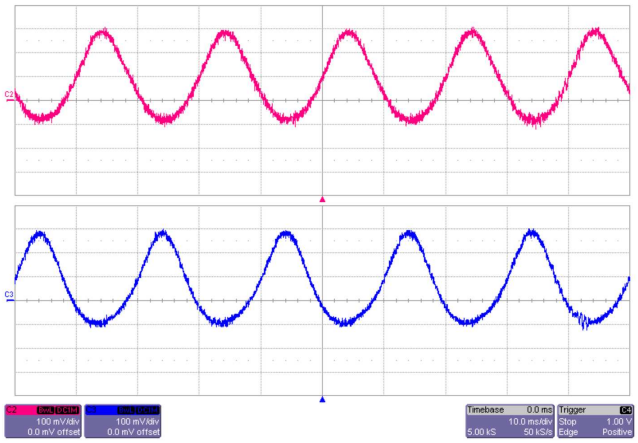

Figure 6.14: Inductor currents i_{L_1} (purple) and i_{L_2} (blue) in a steady-state operating condition.

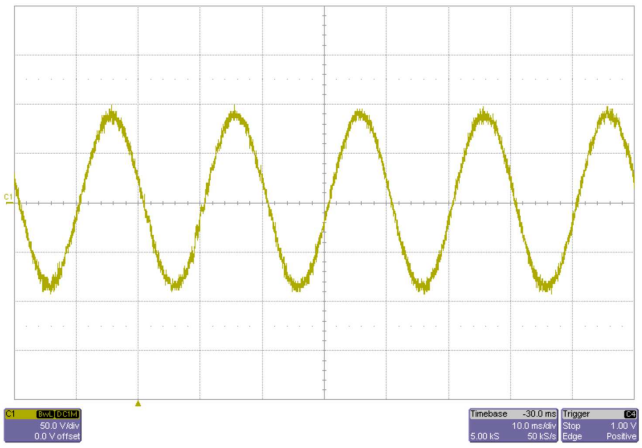

Figure 6.15: Output voltage v_O in a load variation transient.

- **Input voltage variation robustness test**: An input voltage variation test was performed by decreasing the input voltage V_{in} from the nominal 48 V value to 42 V. Results are shown in Figures 6.17-6.18. Also, the output voltage is almost insensitive to input voltage variations, and the currents attain their steady-state values quickly. This demonstrates that the controller effectively compensates for fluctuations in the supply voltage.

The results confirm the controller's ability to ensure stable operation, precise reference tracking, and strong disturbance rejection under various operating conditions.

6.5.4 Comparison between experimental and simulation results

Across all operating scenarios, start-up transient, steady-state operation, load variation, and input voltage variation, the experimental waveforms show an excellent match with the simulated ones. In particular:

- **Waveform shape and tracking**: The output voltage v_O and inductor currents i_{L_1} and i_{L_2} exhibit the same sinusoidal profiles predicted in simulation, with negligible

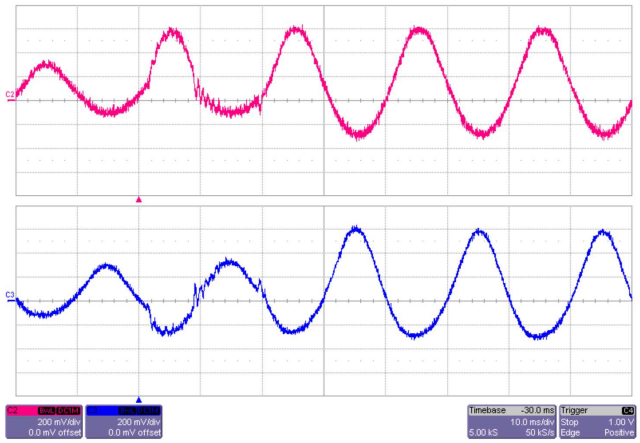

Figure 6.16: Inductor currents i_{L_1} (purple) and i_{L_2} (blue) in a load variation transient.

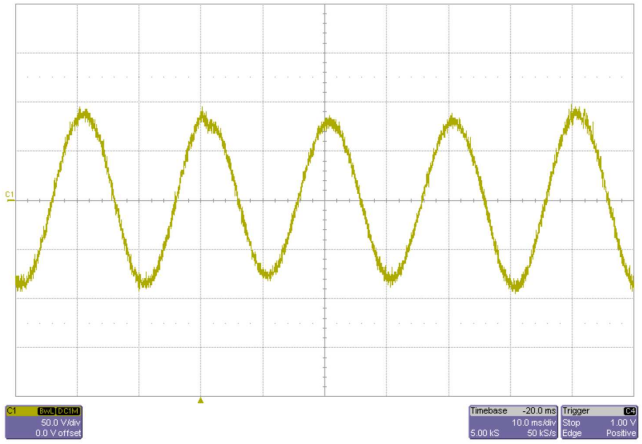

Figure 6.17: Output voltage v_O in an input voltage variation transient.

phase shift and amplitude deviation.

- **Transient response**: The measured settling time after a disturbance is within a ±5% range of the simulated value, with the system reaching steady-state in under 50 ms during start-up and within a few milliseconds after load or supply variations.
- **Harmonic distortion**: The experimentally measured THD (2.45%) is only slightly higher than the simulated value (2.05%). This minor discrepancy is expected, as the experimental setup introduces additional parasitic effects (switching device non-idealities, PCB parasitic inductances/capacitances, and sensor noise) not fully captured in the idealized simulation model.
- **Disturbance rejection**: Both experimental and simulated results show that the output voltage remains unaffected by step changes in load or input voltage. The inductor currents adjust instantaneously in both cases, confirming that the ESOs and the SMC method behave as designed.

From an implementation perspective, these results validate the real-time feasibility of the control algorithm, originally developed and tested in the MATLAB-Simulink simulation

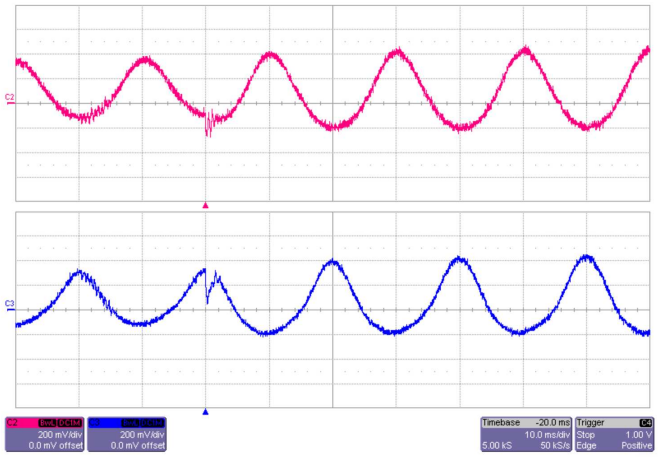

Figure 6.18: Inductor currents i_{L_1} (purple) and i_{L_2} (blue) in an input voltage variation transient.

environment and later deployed on the Texas Instruments F28379D LaunchPad. The consistency between the two domains (simulation and hardware) demonstrates that the discretization process, execution on the CLA coprocessor, and integration with the sensing and driving circuits do not degrade performance. Overall, the excellent agreement between simulation and experimental data confirms:

- accuracy of the mathematical model used for the inverter and controller design;
- effectiveness of the proposed hybrid control strategy in real-world conditions;
- robustness against hardware non-idealities, ensuring performance stability without the need for excessive parameter tuning after deployment.

This high level of agreement is crucial for practical applications, as it implies that future system designs can rely heavily on the simulation model to predict field performance, significantly reducing prototyping time and costs.

6.6 Summary

This chapter addresses the control of a DBI for DC/AC operations. The approach combines ESO for nonlinear disturbance compensation with an additional SMC component to enhance robustness against load and supply voltage variations. In particular, a rigorous procedure is shown to put the system in Brunovski's canonical form and to derive suitable developed ESOs to compensate for nonlinear disturbances. A key design feature is the use of dynamic input modeling, where the control variables, the duty cycles of the two boost converters, are obtained as the integrals of auxiliary control inputs. This prevents the occurrence of chattering effects while preserving the robustness of the SMC approach. Both simulation and experimental results confirmed that the system works well and can effectively reject internal load variation disturbances. Moreover, the reproduced waveforms are good, the inverter successfully generates high-quality sinusoidal output voltages with negligible harmonic distortion (THD $\approx 2.45\%$), fast transient response,

and strong rejection of both exogenous (input voltage fluctuations) and endogenous (load variations) disturbances, which confirms the effectiveness of the proposed control technique. The proposed control strategy not only improves the operational reliability of the DBI but also makes it suitable for practical applications in renewable energy systems, distributed generation, and smart grid integration. Its combination of robustness, precision, and implementation feasibility lays the foundation for further developments in high-performance power conversion systems.

Part III
Applications in Electric Drives

Chapter 7

Adaptive robust nonlinear control strategies for high-performance induction motor drives

Abstract

This chapter presents a robust nonlinear control strategy for induction motor (IM) drives based on adaptive disturbance compensation. Unlike conventional Active Disturbance Rejection Control (ADRC), which relies on the Extended State Observer (ESO), the proposed method employs a high-gain Unknown Input Observer (UIO) that is interconnected with the controller through the tracking error. This structure enhances robustness against parameter uncertainties, inverter nonlinearities, and external disturbances. The control law is derived from the IM dynamic model, and its stability is formally analyzed. Both simulation and experimental results confirm high dynamic performance, accurate flux and speed tracking, and effective disturbance rejection.

Contents

7.1 Motivation and literature review

Induction motor (IM) drives play a fundamental role in industrial applications thanks to their robustness and reliability. However, achieving high dynamic performance in IM drives is challenging, mainly due to the nonlinear nature of their dynamics, parameter uncertainties, and the presence of inverter nonlinearities and external disturbances. The industrial standard for high-performance control of IM drives is the field-oriented control (FOC), proposed and rearranged in various forms in the scientific literature [73], [74]. FOC guarantees optimal dynamic performance and full decoupling of the speed and flux loops under constant flux operation. However, when flux variation is required, for example, when an electrical losses minimization technique (ELMT) is integrated into the drive control, FOC cannot ensure complete decoupling of the speed and flux loops, with a consequent reduction of the dynamic performance [75]. To overcome this limit, several nonlinear control techniques have been proposed. Among them, feedback linearization (FL) represents a classical solution [75], [76], [77], [78]. Although FL is, in principle, applicable, once the dynamic model of the plant is known, it still presents some problems to be faced, either related to rotating or linear IMs. A typical problem arises when there is no precise knowledge either of the mathematical model or unmodeled dynamics. To address this issue, in [79], the linear controller has been substituted with a suitable controller designed to be robust to the variations of the main parameters of the IM, like stator and rotor resistances and the three-phase magnetizing inductance. In some works, more complex models have been adopted [80], [81]. Alternatively, the FL has been integrated with a suitable online parameter estimation method [81], [82], [83]. An alternative and increasingly popular approach is the Active Disturbance Rejection Control (ADRC) [84], [85], [86], [87]. In [88], the problem of three-phase asynchronous motors regulating energy savings is analyzed using ADRC. In the field of electrical drives, ADRC has been applied several times to control Permanent Magnet Synchronous Motors (PMSM) [89], [90], [91], [92], [93]. In [89], a novel parallel structure to improve dynamic responses that replaces the traditional cascade structure of position and speed loops has been proposed; [90] proposes an enhanced linear ADRC-based rotor position sensorless FOC scheme; [91] investigates a class of linear-nonlinear switching ADRC to design speed controllers and current controllers for PMSM in servo systems, which aims at enhancing the ability of disturbance rejection of speed and current controllers. In contrast, [92] deals with performance deterioration due to DC and AC disturbances. It proposes a discrete-time repetitive control-based ADRC for the current loop, and finally, [93] proposes a linear ADRC with a variable gain load torque sliding mode observer to reduce the effects of the load torque disturbance of interior PMSMs. The ADRC method is a robust adaptive extension of the input-output FL control. It performs the exact linearization of the IM model by a suitable nonlinear state transformation based on the online estimation of the corrective term by the Extended State Observer (ESO). Consequently, any unmodeled

dynamics or uncertainty in the parameters are properly addressed. However, parameter variations and errors in estimating the total disturbance cannot be estimated by the ESO, which may deteriorate the performance of the ADRC method. To overcome these drawbacks, an enhanced ADRC scheme has been proposed in [94]. In particular, an advanced ADRC controller was developed by adding a sliding mode (SM) component. However, as it is well known, the SM contribution induces chattering and current ripples that, in turn, imply torque oscillations in the input voltage. In this chapter, a novel robust nonlinear control structure for IM drives is presented. The classical ESO is replaced with a high-gain Unknown Input Observer (UIO), interconnected with the controller through a driving term depending on the tracking error. In more detail, in the classical ADRC, there is a cascade between the controller and the ESO, and the controller does not influence the ESO. On the contrary, in the proposed approach, there is an interconnection between the observer and the controller due to the driving term, so the observer can be considered embedded in the controller. As a result, the controller and the UIO influence each other. This results in a more complicated designing phase, but, on the other side, the proposed observer structure does not contain the input u applied to the motor (as for the ESO in ADRC); in this way, all uncertainties associated with inverter nonlinearities, delays, and parameter variation of the input gain are automatically eliminated. Although the induction motor dynamics are modeled in continuous time, the proposed adaptive robust control strategy gives rise to a hybrid closed-loop system. In particular, the adaptation mechanisms and disturbance estimation introduce internal dynamics whose activation depends on operating conditions, effectively resulting in a switching behavior among different dynamic regimes. This structure is consistent with the hybrid system framework introduced in Chapter 2, where continuous flows are combined with discrete events associated with changes in control structure or estimation dynamics. Moreover, the stability analysis relies on Lyapunov arguments that can be interpreted as common or multiple Lyapunov functions for switched systems, as discussed in Chapter 3. As a result, the proposed approach ensures robustness against both parameter uncertainties and external disturbances, while avoiding the drawbacks of SM components.

7.2 Dynamic model of the induction motor

To design advanced control strategies for IM drives, it is essential to start from a suitable mathematical description of the system dynamics. In this work, the model is expressed in the rotating rotor flux reference frame, which allows a natural decoupling between torque and flux components and is widely adopted in high-performance control schemes. The continuous-time state-space model of the IM can be written as follows:

$$\dot{\mathbf{x}} = \begin{bmatrix} \dot{i}_{sx} \\ \dot{i}_{sy} \\ \dot{\psi}_{rx} \\ \dot{\omega} \end{bmatrix} = f\left(\mathbf{x}, u_{sx}, u_{sy}\right) = \begin{bmatrix} -a_{11} i_{sx} + \left(\omega + a_{21} \frac{i_{sy}}{\psi_{rx}}\right) i_{sy} + a_{12} \psi_{rx} + c_1 u_{sx} \\ -a_{11} i_{sy} - \left(\omega + a_{21} \frac{i_{sy}}{\psi_{rx}}\right) i_{sx} - c_1 \omega \psi_{rx} + c_1 u_{sy} \\ a_{21} i_{sx} - a_{22} \psi_{rx} \\ -a_m \omega + b_m \left(\frac{2}{3} p i_{sy} \psi_{rx} - t_l\right) \end{bmatrix} \tag{7.1}$$

where:

$$a_{11} = \frac{1}{L_e}\left(R_s + \frac{L_s - L_e}{\tau_r}\right), a_{12} = \frac{1}{\tau_r L_e}, a_{21} = \frac{L_s - L_e}{\tau_r},$$
$$a_{22} = \frac{1}{\tau_r}, c_1 = \frac{1}{L_e}, a_m = \frac{\rho_v}{J_m}, b_m = \frac{1}{J_m}$$

The variables i_{sx}, i_{sy}, u_{sx}, u_{sy} and ψ_{rx}, ψ_{sy} are respectively the stator current, the stator voltage and the rotor flux components along the x- and y-axis of the rotor flux reference frame, ω is the rotor speed, R_s and L_s are the stator resistance and the stator inductance, ρ_v is the viscous friction coefficient, t_l is the load torque, J_m is the inertia coefficient, $\tau_r = \frac{L_r}{R_r}$ is the rotor time constant, where L_r and R_r are the rotor inductance and the rotor resistance, $L_e = L_s - \frac{L_m^2}{L_r}$ is the stator transient inductance, where L_m is mutual inductance and finally p represents the pole pairs. This formulation makes explicit the nonlinear coupling between electrical and mechanical dynamics. In particular, the stator currents and voltages determine the rotor flux evolution; the electromagnetic torque depends on both the flux and the stator current quadrature component; the mechanical dynamics are governed by the balance between the electromagnetic torque, the load torque, and the viscous friction.

7.3 Problem statement and control objectives

The design of robust control strategies for IM drives must account for several challenges. Classical FOC achieves decoupling between torque and flux only under constant flux conditions [75], [95]. In the presence of flux variations, as in the case of energy optimization techniques, the decoupling is lost, resulting in degraded dynamic performance. It is known from the scientific literature that a technique to overcome this drawback is the FL approach (cf. [75], [96], [97]). However, the FL technique has several critical limitations, since its effectiveness strongly depends on precise knowledge of the motor parameters and on the accuracy of the mathematical model. In practice, unmodeled dynamics, parameter uncertainties, and inverter nonlinearities can significantly degrade performance. To address these issues, an adaptive control law inspired by the ADRC structure has been proposed, which estimates and compensates disturbances through an ESO. However, ADRC itself is affected by limitations, since some disturbances cannot be correctly estimated by the ESO, and performance may deteriorate in the presence of parameter variations or input nonlinearities. The objective of this work is to design a robust nonlinear control law for IM drives, capable of:

- ensuring accurate flux and speed tracking under both constant and variable flux conditions;
- rejecting external disturbances such as load torque variations;
- preserving robustness with respect to parameter uncertainties and inverter nonlinearities;
- avoiding chattering and torque oscillations associated with SM-based approaches.

To this end, a new control structure is proposed, inspired by ADRC but based on a high-gain UIO instead of the classical ESO. The key features of this approach are the direct interconnection between observer and controller through a driving term depending on the tracking error, which enhances robustness and rejection, particularly under parameter uncertainties and inverter nonlinearities.

7.4 Design of the robust nonlinear controller

In order to derive the proposed robust control law, the IM dynamics are reformulated into simplified canonical forms for both the rotor flux and speed subsystems. This allows the use of a unified structure that facilitates both analysis and control design.

7.4.1 Flux and speed models

Considering IM model (7.1), defining the flux-related states as:

$$x_{\psi 1} = \psi_{rx}, \quad \text{and} \quad x_{\psi 2} = \dot{\psi}_{rx},$$

so that the flux dynamics can be expressed in the canonical form:

$$\dot{x}_{\psi 1} = x_{\psi 2}, \tag{7.2a}$$

$$\dot{x}_{\psi 2} = h_{\psi}(\boldsymbol{x}) + b_{\psi} u_{sx}, \tag{7.2b}$$

where $b_{\psi} = a_{21} c_1$ and $h_{\psi}(\boldsymbol{x})$ is the total disturbance given by:

$$h_{\psi}(\boldsymbol{x}) = \big(a_{22}^2 + a_{21} a_{12}\big)\psi_{rx} - a_{21}\big(a_{22} + a_{11}\big) i_{sx} + a_{21}\left(\omega + a_{21}\frac{i_{sy}}{\psi_{rx}}\right) i_{sy}.$$

The same procedure is used in order to obtain the speed model. Considering model (7.1), the mechanical acceleration equation is:

$$\ddot{\omega} = -a_m \dot{\omega} - \frac{2}{3}\, p\, b_m \Big(\big(a_{11} + a_{22}\big)\, i_{sy} + \omega\, \big(i_{sx} + c_1 \psi_{rx}\big)\Big)\psi_{rx} - b_m \dot{t}_l + \frac{2}{3}\, p\, c_1 b_m \psi_{rx} u_{sy}. \tag{7.3}$$

By defining $x_{\omega 1} = \omega$, and $x_{\omega 2} = \dot{\omega}$, the speed model is obtained:

$$\dot{x}_{\omega 1} = x_{\omega 2}, \tag{7.4a}$$

$$\dot{x}_{\omega 2} = h_{\omega}(\boldsymbol{x}) + b_{\omega}(\boldsymbol{x}) u_{sy}, \tag{7.4b}$$

where $b_\omega(\boldsymbol{x}) = \frac{2}{3}\, p\, c_1 b_m \psi_{rx}$, and $h_\omega(\boldsymbol{x})$ is the total disturbance and is given by:

$$h_\omega(\boldsymbol{x}) = -a_m \dot{\omega} - \frac{2}{3}\, p\, b_m \Big(\left(a_{11} + a_{22}\right) i_{sy} + \omega \left(i_{sx} + c_1 \psi_{rx}\right) \Big) \psi_{rx} - b_m \dot{t}_l. \tag{7.5}$$

The flux and speed models have the same structure, given by:

$$\dot{x}_1 = x_2, \tag{7.6a}$$

$$\dot{x}_2 = h(\boldsymbol{x}) + bu, \tag{7.6b}$$

where $h(\boldsymbol{x})$ represents the total disturbance (including modeling uncertainties and load effects), and u is the control input. Based on this model, the proposed control strategy employs an adaptive disturbance estimation through the UIO, leading to a closed-loop system capable of achieving the desired tracking objectives with high robustness.

7.4.2 Control law formulation

Based on the general model (7.6), the control variable structure is chosen as follows:

$$u = \frac{1}{b} \left(-\hat{h}(\boldsymbol{x}) + \nu \right), \tag{7.7}$$

where $\hat{h}(\boldsymbol{x})$ is the estimate of the disturbance $h(\boldsymbol{x})$, and ν is the auxiliary control variable designed so that the speed and rotor flux can evolve according to the desired dynamics. The control law (7.7) leads to the following model:

$$\dot{x}_1 = x_2, \tag{7.8a}$$

$$\dot{x}_2 = \big(h(\boldsymbol{x}) - \hat{h}(\boldsymbol{x}) \big) + \nu. \tag{7.8b}$$

Since model (7.8) is observable and reachable, a state-feedback control law can be applied to achieve the desired eigenvalue placement. However, to guarantee zero steady-state error in tracking constant references, a third state variable is added to model (7.8), whose dynamics are described as follows:

$$\dot{r} = x_1^* - x_1, \tag{7.9}$$

where x_1^* is the desired value of x_1. The model (7.8) becomes:

$$\dot{x}_1 = x_2, \tag{7.10a}$$

$$\dot{x}_2 = \big(h(\boldsymbol{x}) - \hat{h}(\boldsymbol{x}) \big) + \nu, \tag{7.10b}$$

$$\dot{r} = x_1^* - x_1. \tag{7.10c}$$

To assign the internal dynamics of the system, the auxiliary control variable ν is chosen as follows:

$$\nu = -\boldsymbol{k} \left[x_1 \; x_2 \; r \right]^\top, \tag{7.11}$$

where $\boldsymbol{k} = [k_1 \; k_2 \; k_3]$ is a constant matrix, suitably selected to ensure closed-loop stability.

7.4.3 Disturbance estimation using unknown input observer

Starting from model (7.10)-(7.11), the dynamics are suitably extended to estimate the external disturbance $h(x)$, but differently from ADRC, where a classical ESO sourced by the input u is used, a high-gain UIO is considered, with a driving term that is a function of the tracking error. The complete controlled system dynamics is therefore given by:

$$\dot{x}_1 = x_2, \tag{7.12a}$$

$$\dot{x}_2 = \big(h(\boldsymbol{x}) - z_3\big) - k_1 x_1 - k_2 x_2 - k_3 r, \tag{7.12b}$$

$$\dot{r} = x_1^* - x_1, \tag{7.12c}$$

$$\dot{z}_1 = z_2 + \epsilon^{-1} g_1 \left(x_1 - z_1\right), \tag{7.12d}$$

$$\dot{z}_2 = z_3 + \epsilon^{-2} g_2 \left(x_1 - z_1\right) + \rho \text{sign}(x_1^* - x_1), \tag{7.12e}$$

$$\dot{z}_3 = \epsilon^{-3} g_3 \left(x_1 - z_1\right), \tag{7.12f}$$

where z_1, z_2 and z_3 represent an estimate of x_1, x_2 and $h(\boldsymbol{x})$ respectively, while ϵ, ρ, g_i, i=1, 2, 3, and k_i, i=1, 2, 3, are constant parameters. They will be chosen to ensure the stability of the closed-loop system (7.12) with sufficiently high margins.

Remark 7.4.1

The proposed observer structure (7.12) *does not require the input* u *in its dynamics. This eliminates the effects of inverter nonlinearities, delays, and parameter variations of the input gain, which are typically critical at low speeds. Furthermore, since no sliding-mode component is employed, chattering and associated torque oscillations are avoided.* □

7.5 Stability and robustness analysis

In this section, the stability of the closed-loop system described in (7.12) is analyzed. The analysis is carried out by defining an extended error space that includes both the tracking errors and the estimation errors from the UIO:

$$e_1 = -r, \tag{7.13a}$$

$$e_2 = x_1^* - x_1, \tag{7.13b}$$

$$e_3 = -x_2, \tag{7.13c}$$

$$e_4 = x_1 - z_1, \tag{7.13d}$$

$$e_5 = x_2 - z_2, \tag{7.13e}$$

$$e_6 = h(x) - z_3. \tag{7.13f}$$

The extended error dynamics are computed by means of equations (7.12) and are given by:

$$\dot{e}_1 = -e_2, \tag{7.14a}$$

$$\dot{e}_2 = \dot{x}_1^* + e_3, \tag{7.14b}$$

$$\dot{e}_3 = -k_3 e_1 - k_1 e_2 - k_2 e_3 - e_6 + k_1 x_1^*, \tag{7.14c}$$

$$\dot{e}_4 = -\epsilon^{-1} g_1(e_4) + e_5, \tag{7.14d}$$

$$\dot{e}_5 = k_3 e_1 + k_1 e_2 + k_2 e_3 - \epsilon^{-2} g_2(e_4) + 2e_6 - \rho \text{sign}(e_2) - k_1 x_1^* - h(x), \tag{7.14e}$$

$$\dot{e}_6 = \dot{h}(x) - \epsilon^{-3} g_3(e_4), \tag{7.14f}$$

that can be rewritten in a suitably compact form as follows:

$$\dot{e} = Fe + B_1 \text{sign}(e_2) + B_2 \mu, \tag{7.15}$$

where

$$F = \begin{bmatrix} 0 & -1 & 0 & 0 & 0 & 0 \\ 0 & 0 & 1 & 0 & 0 & 0 \\ -k_3 & -k_1 & -k_2 & 0 & 0 & -1 \\ 0 & 0 & 0 & -\epsilon^{-1} g_1 & 1 & 0 \\ k_3 & k_1 & k_2 & -\epsilon^{-2} g_2 & 0 & 2 \\ 0 & 0 & 0 & -\epsilon^{-3} g_3 & 0 & 0 \end{bmatrix}, B_1 = \begin{bmatrix} 0 & 0 & 0 & 0 & -\rho & 0 \end{bmatrix}^T, \tag{7.16}$$

$$B_2 = \begin{bmatrix} 0 & 0 & 0 & 0 \\ 0 & 0 & 0 & 1 \\ 0 & 0 & k_1 & 0 \\ 0 & 0 & 0 & 0 \\ -1 & 0 & -k_1 & 0 \\ 0 & 1 & 0 & 0 \end{bmatrix}, \text{ and } \mu = \begin{bmatrix} h(x) & \dot{h}(x) & x_1^* & \dot{x}_1^* \end{bmatrix}^T.$$

The stability of the estimation error can be ensured by choosing the parameters of the matrix F such that all its eigenvalues have a negative real part. The proposed control method structure offers several robustness advantages:

- the control input does not appear in the observer dynamics, eliminating sensitivity to input nonlinearities and delays;
- the absence of SM components avoids chattering and associated torque oscillations.
- by appropriately tuning the observer gain ϵ and ρ, the closed-loop system can tolerate bounded external disturbance $h(\boldsymbol{x})$ without loss of stability.

7.5.1 Stability proof

The following analysis demonstrates the asymptotic stability of the extended error space corresponding to the error variables. In particular, it is shown that the system (7.15)

reaches a steady state asymptotically and that the steady-state value of the tracking error (7.13b) is zero.

Assumption 7.5.1

It is assumed that input μ in (7.15) is bounded. Specifically, there exists constants M and N, such that:

$$|\dot{h}(x)| < M, \tag{7.17a}$$

$$|\dot{x}_1^*| < N. \tag{7.17b}$$

□

Inequality (7.17a) is a standard assumption when ADRC is considered, while inequality (7.17b) refers to the reference input, and therefore it is easy to verify in practical applications. Under Assumption 7.5.1, system (7.15) is stable if the matrix F is Hurwitz. Since μ and sign(e_2) are bounded, stability can be ensured by selecting the parameters g_i, i=1, 2, 3, and k_i, i=1, 2, 3 such that all eigenvalues of the matrix F have a negative real part. To simplify the design process, the eigenvalues can be chosen considering the following characteristic polynomial of F:

$$\begin{aligned}\Delta(\lambda) = &\lambda^6 + (k_2 + g_1\epsilon^{-1})\lambda^5 + (k_1 + g_1k_2\epsilon^{-1} + g_2\epsilon^{-2})\lambda^4 \\ &+ (-k_3 + g_1k_1\epsilon^{-1} + g_2k_2\epsilon^{-2} + 2g_3\epsilon^{-3})\lambda^3 \\ &+ (-g_1k_3\epsilon^{-1} + g_2k_1\epsilon^{-2} + g_3k_2\epsilon^{-3})\lambda^2 \\ &+ (-g_2k_3\epsilon^{-2} + g_3k_1\epsilon^{-3})\lambda - g_3k_3\epsilon^{-3}.\end{aligned} \tag{7.18}$$

Consequently, it is possible to assign the convergence dynamics of the variables e by choosing a suitable six-order characteristic polynomial and subsequently parameters g_i, i=1, 2, 3, and k_i, i=1, 2, 3, are chosen such that the desired polynomial matches polynomial (7.18). Note that for the moment, parameter ϵ constitutes one more degree of freedom, but its choice will be clearer with the steady state analysis given in the following.

Remark 7.5.1

The negative sign in the constant term of the characteristic polynomial (7.18) originates from the feedback structure of the closed-loop system and from the definition of the estimation error dynamics. In particular, it results from the product of the tracking feedback gain k_3 and the observer gain g_3, and is therefore structurally consistent with the high-gain UIO formulation. □

7.5.2 Steady-state analysis

Based on the previous analysis, stability is ensured, and the desired dynamics of the variables e during the transient can be selected. However, e does not converge exactly to zero due to the forcing terms B_1sign(e_2) and $B_2\mu$. For this reason, a steady-state analysis

is performed in order to evaluate the final error and how the extra parameters ϵ and ρ can be suitably chosen. In particular, system (7.15) can be transformed in the Laplace domain as follows:

$$E(s) = (sI - F)^{-1}BU(s), \tag{7.19}$$

where s is the Laplace variable, $E(s)$ is the Laplace transform of the error vector $e(t)$, $B = \begin{bmatrix} B_1 & B_2 \end{bmatrix}$ and $U(s)$ is the Laplace transform of the input vector $u(t) = \begin{bmatrix} \text{sign}(e_2) & \mu \end{bmatrix}^\top$. If F is Hurwitz, the steady-state value of the error vector $E(s)$, e_{ss}, can be obtained as:

$$\begin{aligned} e_{ss} &= \lim_{s\to\ 0} E(s) = \lim_{s\to\ 0} (sI - F)^{-1}BU(s) = \\ &= \begin{bmatrix} (2k_1x_1^*) - (h + \rho + k_1x_1^*) + (k_2N) - \frac{M\epsilon g_2}{g_3} \\ 0 \\ -N \\ \frac{M\epsilon^3}{g_3} \\ \frac{M\epsilon^2 g_1}{g_3} \\ h + \rho + (\frac{M\epsilon g_2}{g3}) \end{bmatrix} \end{aligned} \tag{7.20}$$

The second component of e_{ss} in (7.20) is identically zero, therefore the tracking error (7.13b) converges asymptotically to zero. This guarantees that the IM follows correctly the speed and flux references with zero steady-state error, which represents the main design objective. Moreover, from this computation, more information regarding the choice of ϵ and ρ can be inferred. In particular, ϵ is a positive parameter and is chosen as low as possible, considering that the lower ϵ implies a lower steady-state estimation error (7.13d), (7.13e), and (7.13f). Finally, it is noted that the error variable (7.13a), corresponding to the integral of the tracking error, does not converge to zero. However, this does not represent a problem for the proposed application, as it does not compromise the effectiveness of the control scheme.

Remark 7.5.2

The function sign$(e_2(t))$ is nonlinear and discontinuous, so its Laplace transform is not defined in the classical sense. In this analysis, we only consider that sign(e_2) is bounded ($|$sign$(e_2)| \leq 1$) and apply the final value theorem of the Laplace transform to the stable linear system (with F Hurwitz) to determine the steady-state value of the error. This allows obtaining e_{ss} without explicitly computing the Laplace transform of the nonlinear function. □

7.6 Experiments

This section presents the experimental validation of the proposed control strategy for IM drives. The experiments were carried out on the laboratory test bench described below, specifically designed to reproduce realistic operating conditions and to provide accurate measurements of both mechanical and electrical quantities. The first subsection

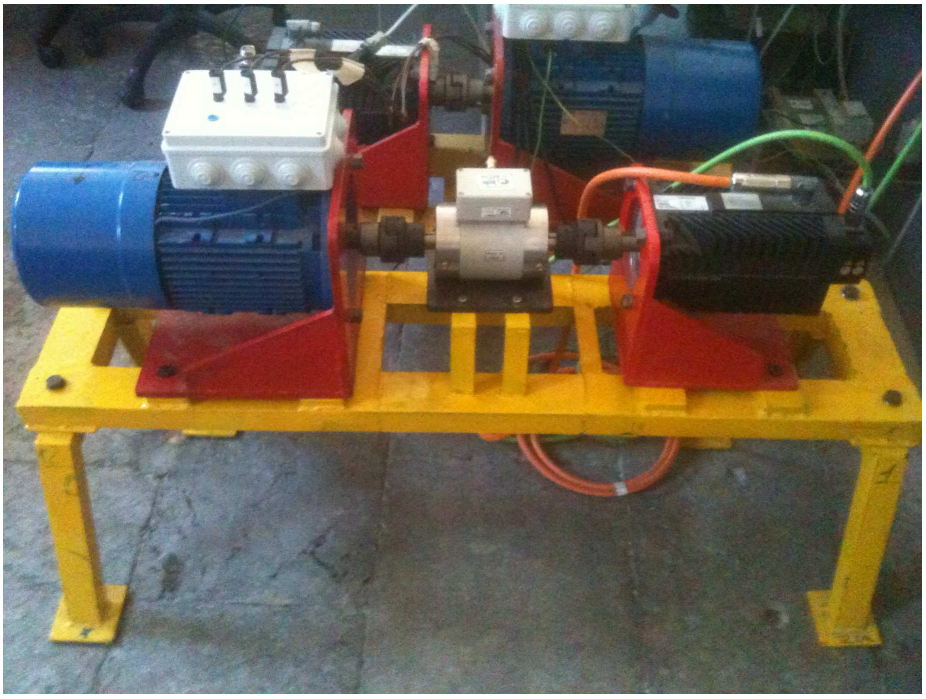

Figure 7.1: Photograph of the experimental test set-up

Table 7.1: Motor parameters

Parameter	Value
stator inductance, L_s	0.2030 H
stator leakage, σL_s	0.01798 H
stator resistance, R_s	2.9 Ω
rotor time constant, τ_r	0.135 s
viscous friction, f_v	0.0023 Nms
inertia momentum, J_m	0.0088 Nms^2
pole-pairs, p	2

introduces the test setup, while the second discusses the experimental results obtained under different operating scenarios, highlighting the transient response and disturbance rejection capabilities of the proposed approach. The experiments were performed using the parameter values listed in Table 7.1.

7.6.1 Experimental setup

In order to validate the effectiveness of the proposed control strategy, an experimental test bench was developed. The system is designed to reproduce realistic operating conditions for an IM drive while allowing accurate measurement of the main electrical and mechanical quantities. The machine under test is a 2.2 kW, three-phase IM (SEIMEC model HF 100LA 4 B5), equipped with an incremental encoder for rotor position and speed measurement. The employed test setup consists of the following:

- a three-phase 2.2 kW IM;

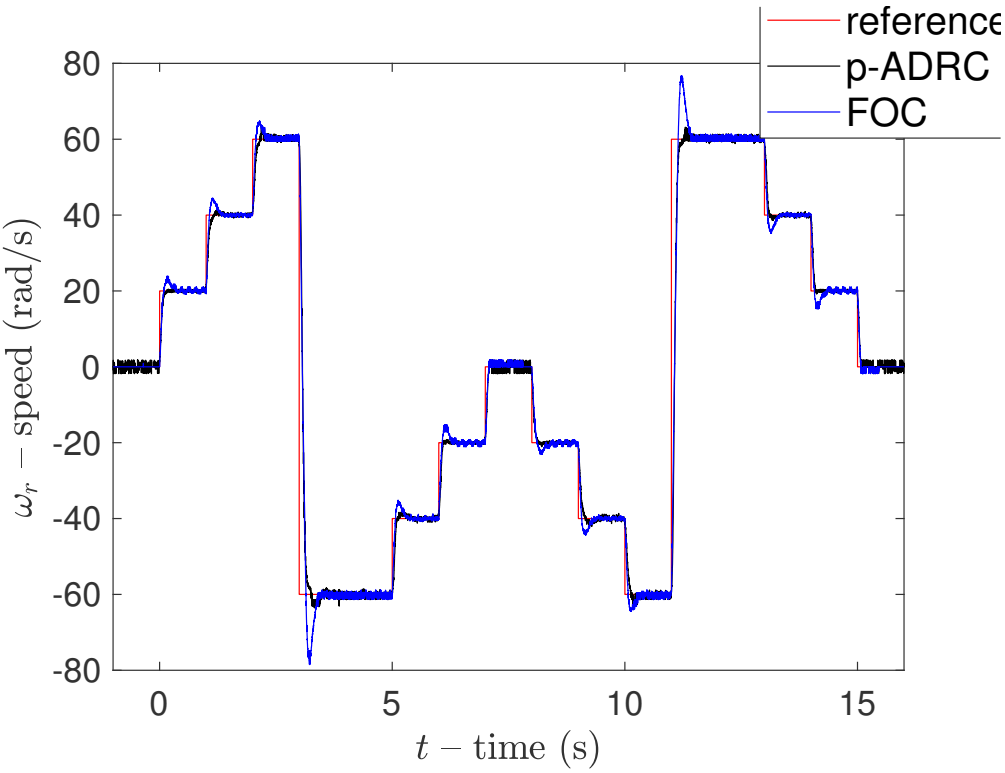

Figure 7.2: Transient response at no load and constant flux, speed

- a frequency converter that consists of a three-phase diode rectifier and a $7.5\,kVA$, three-phase VSI;
- a dSPACE card (DS1103) with a PowerPC 604e at $400\,MHz$ and a floating-point DSP TMS320F240.

The sampling frequency of the control loop is set to $12\,kHz$, which ensures a sufficiently fast response for the considered dynamics. To provide a controllable mechanical load, the induction motor is mechanically coupled to a torque-controller PMSM (Emerson Unimotor FM series). The PMSM acts as an active load, allowing the emulation of different operating conditions. The electromagnetic torque on the shaft is measured by means of a torque transducer (Himmelstein 59003V(4-2)-N-F-N-L-K), ensuring high accuracy in the validation of the proposed control technique. A schematic representation of the test set-up is shown in Fig. 7.1.

7.6.2 Experimental results

The proposed robust nonlinear ADRC control scheme was experimentally validated on the test bench described above. Two kinds of tests have been performed. The first test is a transient response at no load, while the second test is a load rejection test at a constant speed. Both tests have been performed twice, respectively in constant flux and variable flux operation. As for the constant flux operation, the reference flux of the drive has been set equal to the rated value (0.8 Wb for the machine under test). As for the variable flux

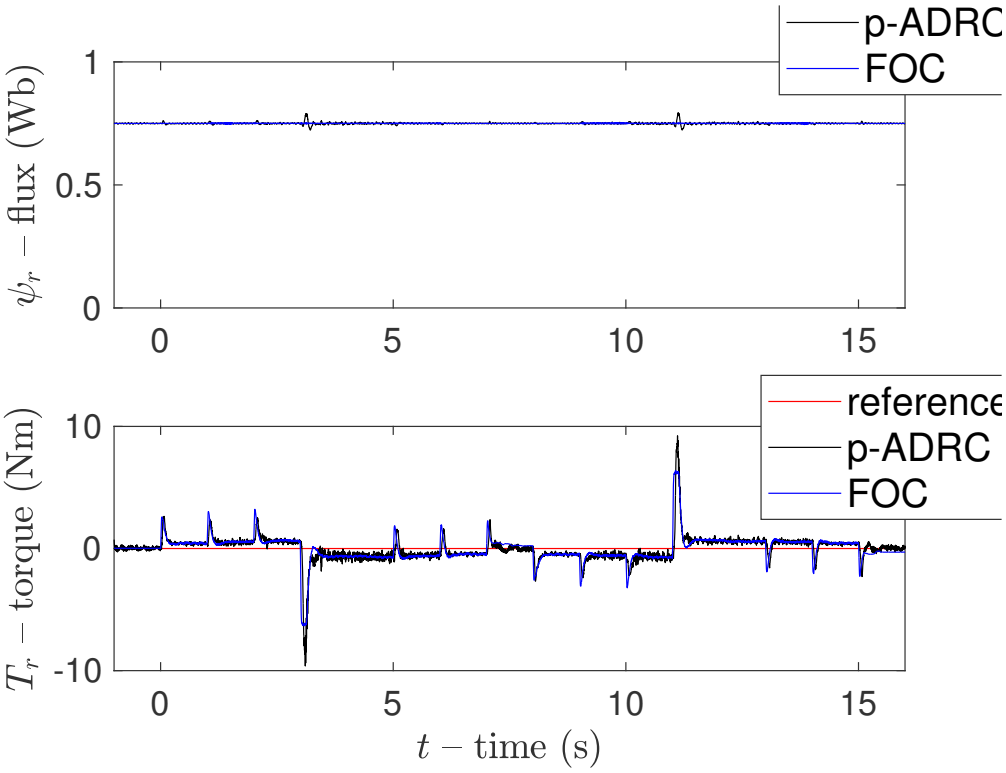

Figure 7.3: Transient response at no load and constant flux, flux and torque

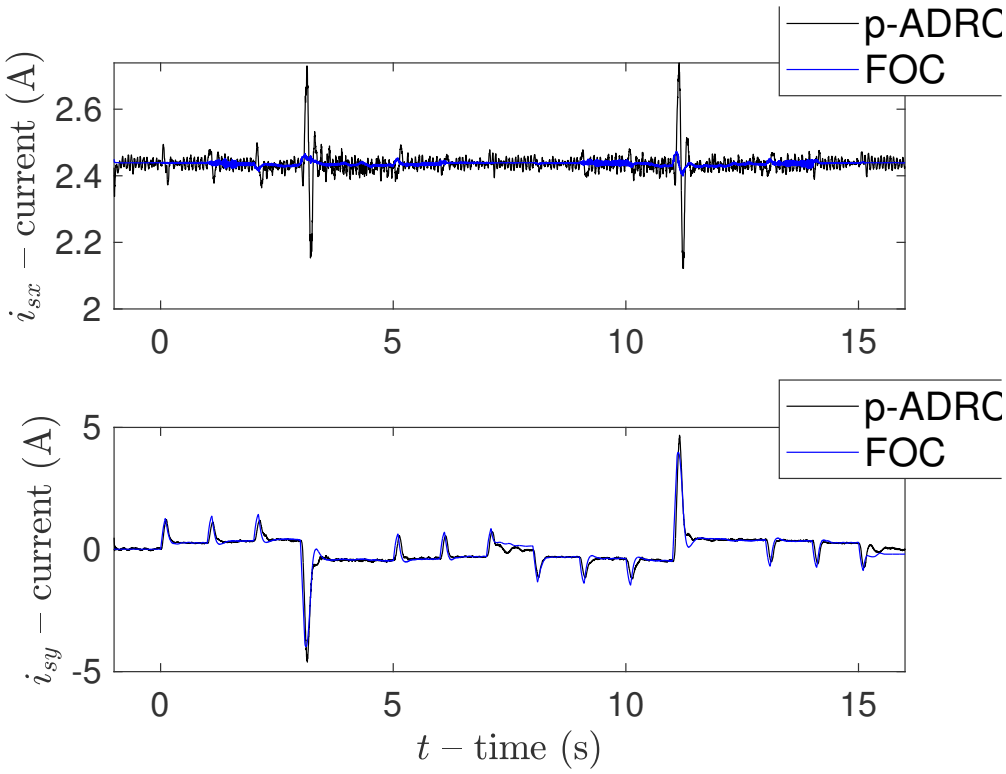

Figure 7.4: Transient response at no load and constant flux, currents

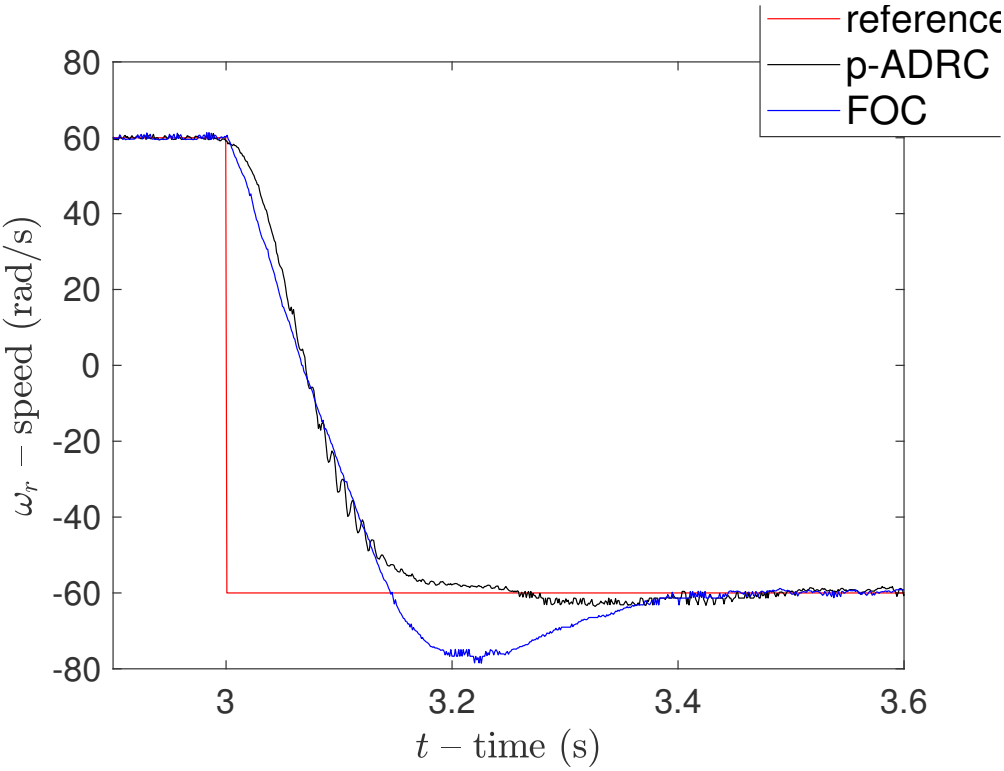

Figure 7.5: Transient response at no load and constant flux, speed (particular)

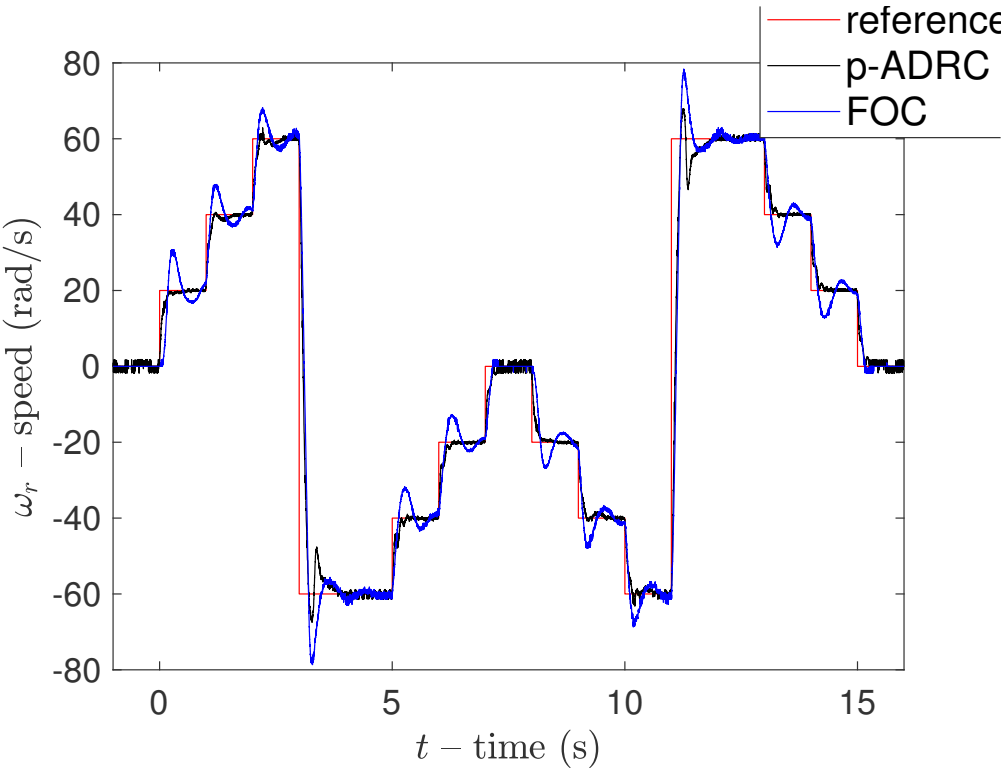

Figure 7.6: Transient response at no load and ELMT, speed

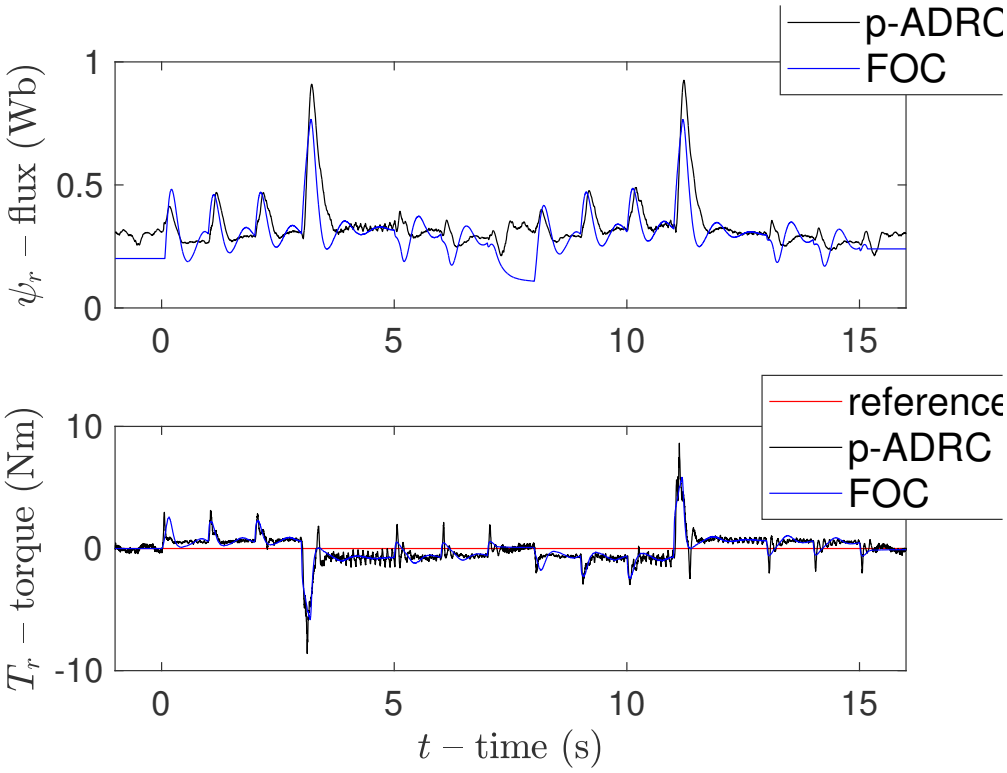

Figure 7.7: Transient response at no load and ELMT, flux and torque

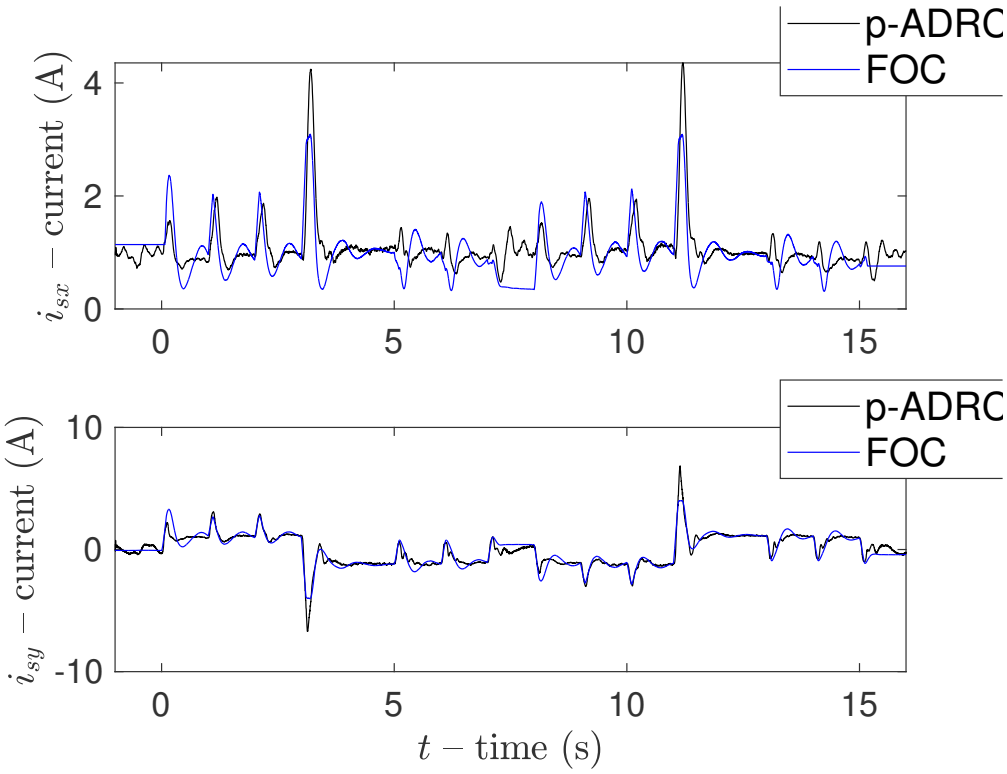

Figure 7.8: Transient response at no load and ELMT, currents

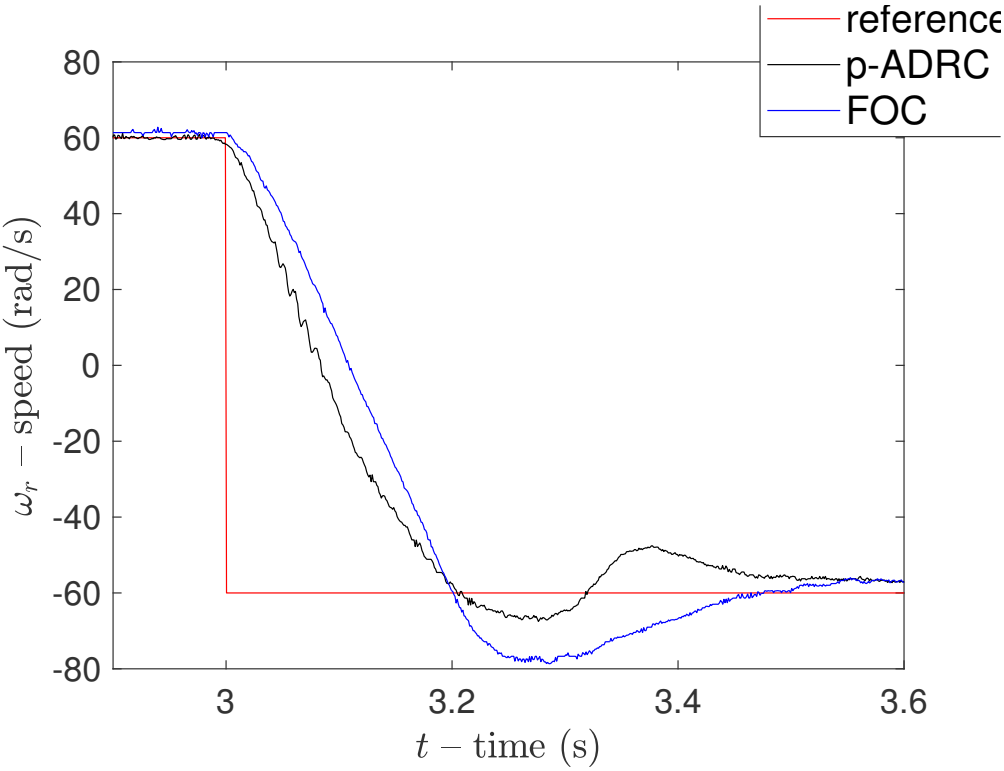

Figure 7.9: Transient response at no load and ELMT, speed (particular)

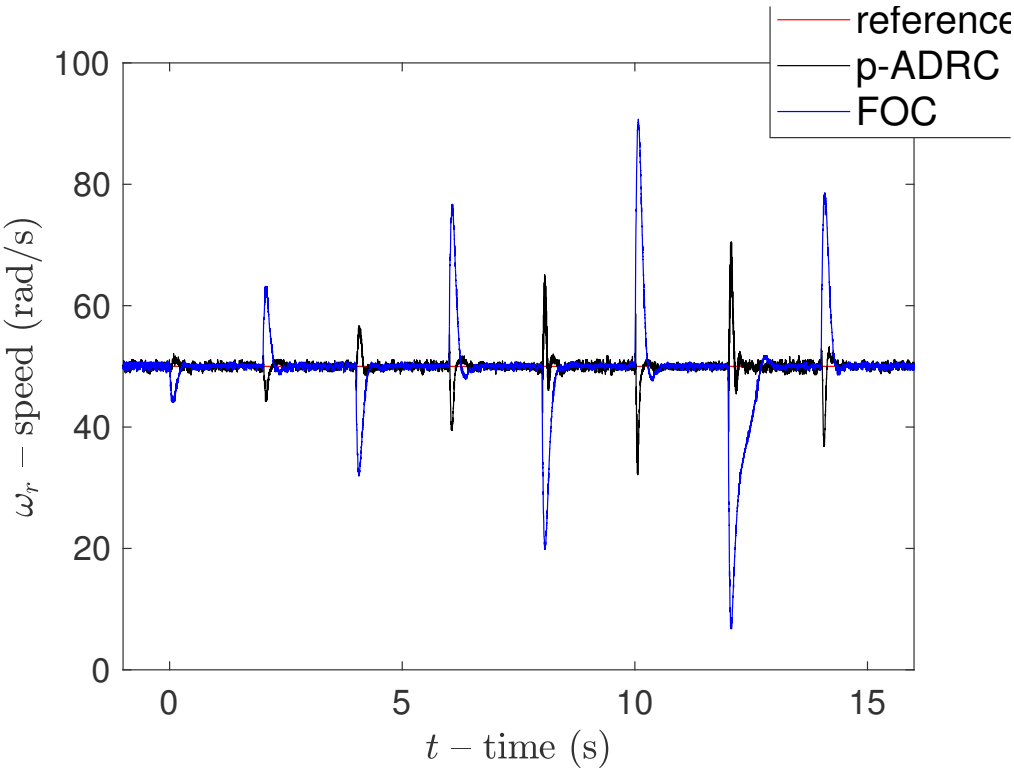

Figure 7.10: Load rejection test at 50 rad/s and constant flux, speed

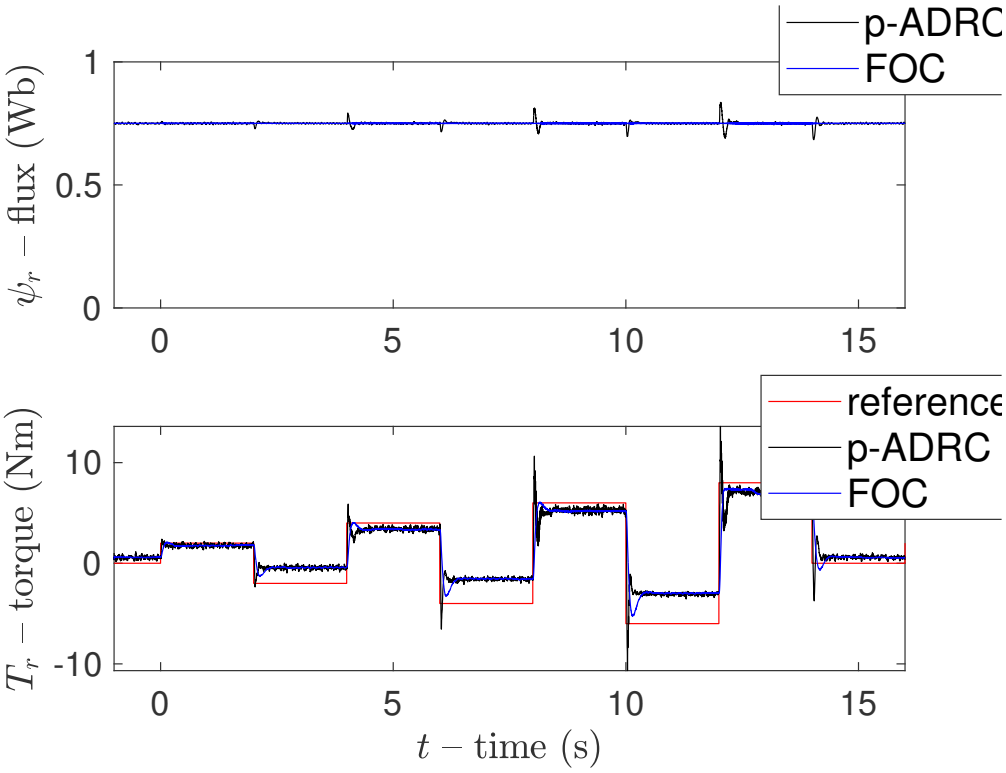

Figure 7.11: Load rejection test at 50 rad/s and constant flux, flux and torque

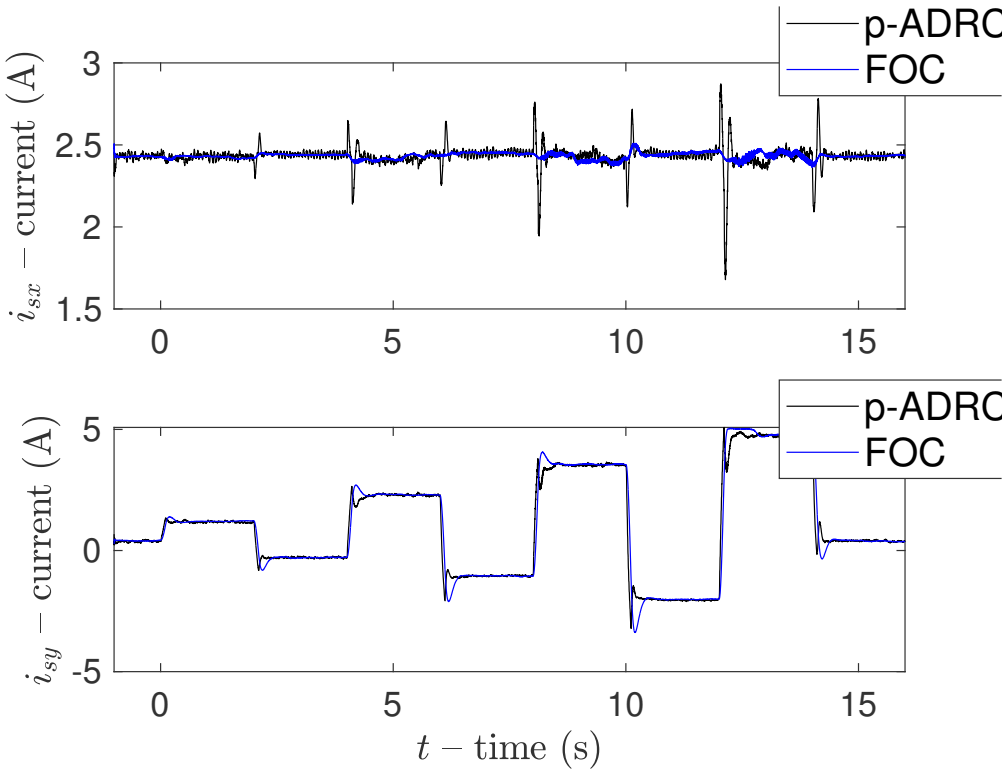

Figure 7.12: Load rejection test at 50 rad/s and constant flux, currents

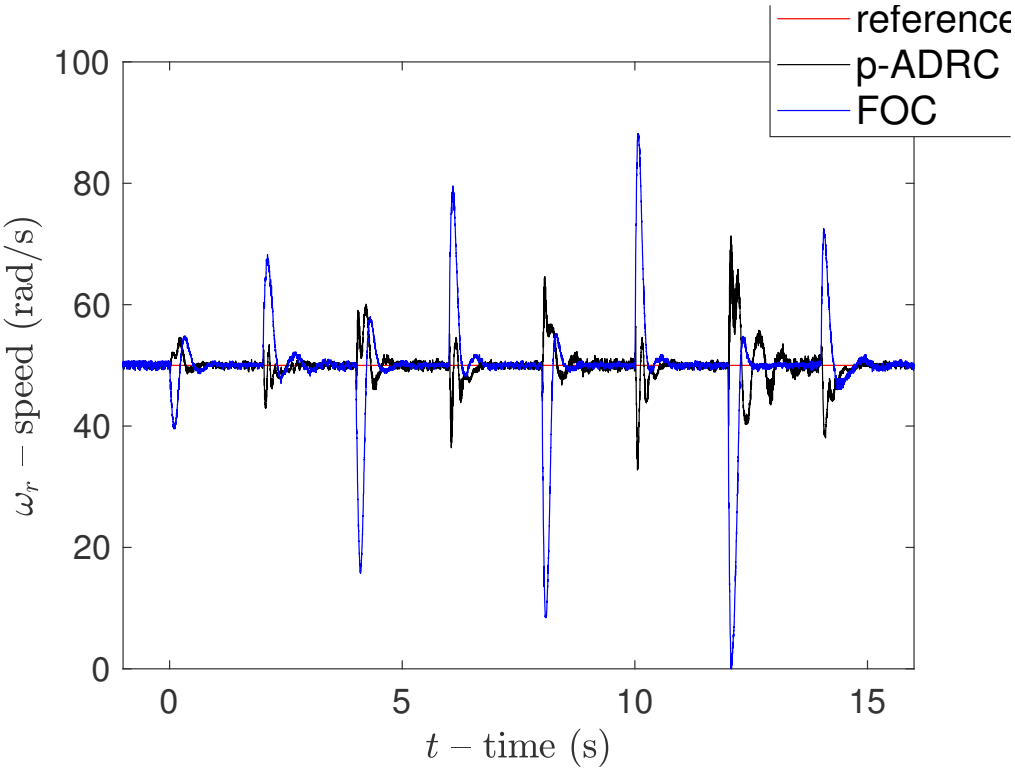

Figure 7.13: Load rejection test at 50 rad/s and ELMT, speed

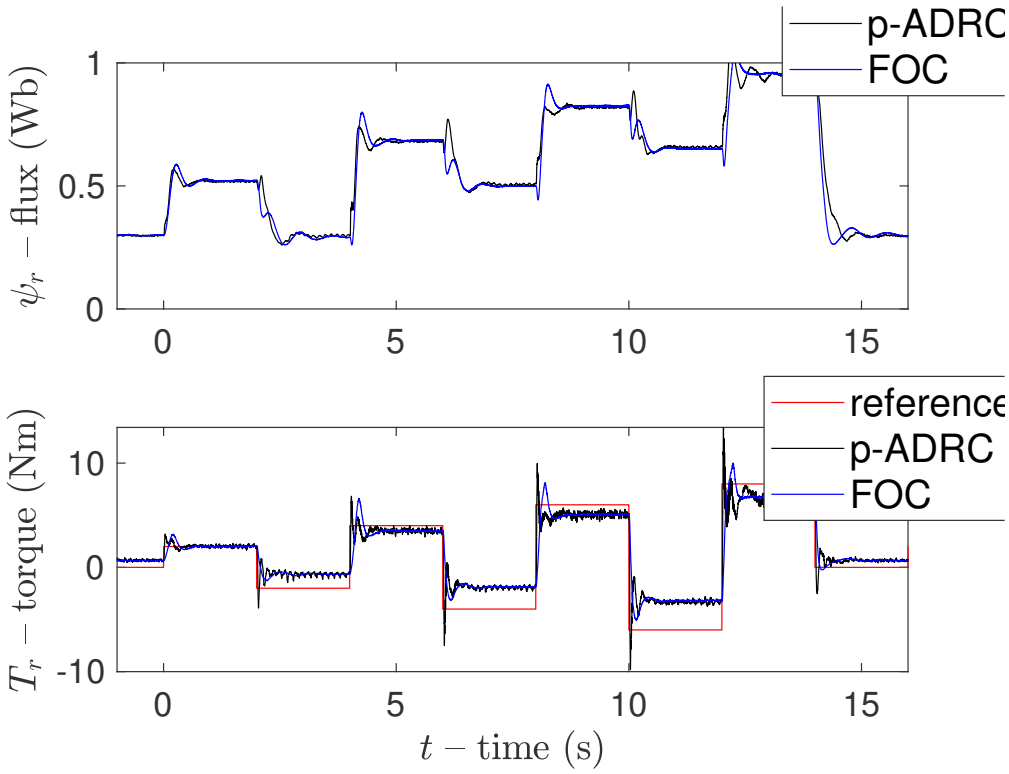

Figure 7.14: Load rejection test at 50 rad/s and ELMT, flux and torque

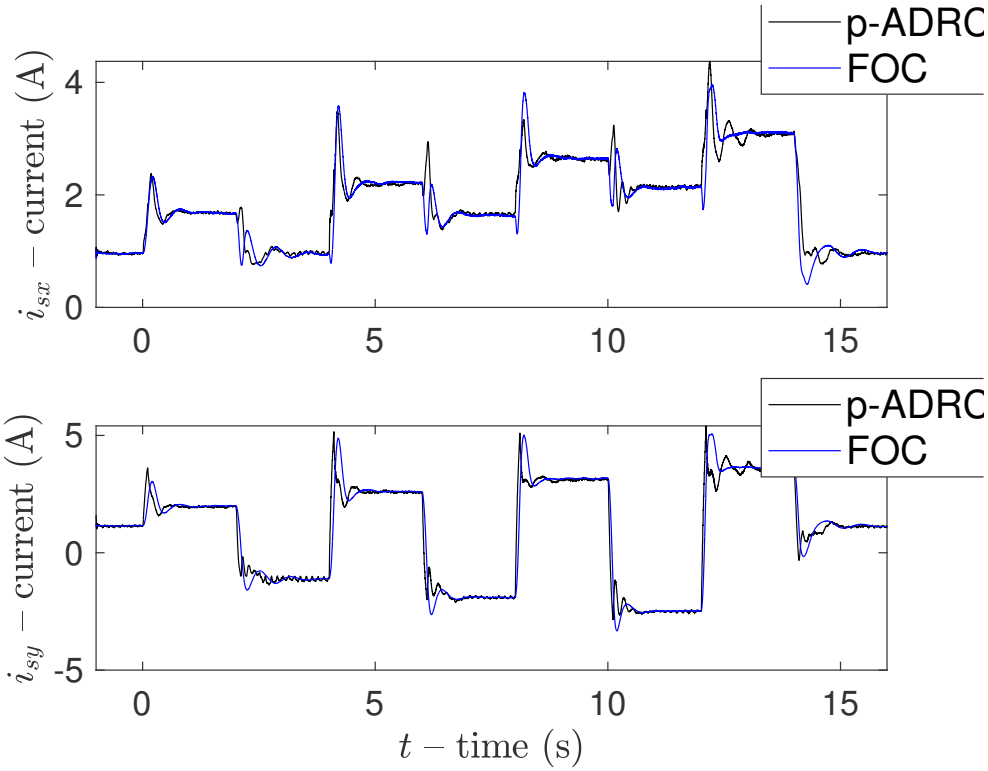

Figure 7.15: Load rejection test at 50 rad/s and ELMT, currents

operation, the drive has been operated by integrating the ADRC control system with the ELMT proposed in [98]. In both experimental tests, the proposed ADRC control system has been compared with the classic FOC [73].

7.6.2.1 Transient response test

The first test aims to evaluate the transient performance of the proposed ADRC scheme in comparison with the conventional FOC strategy. To this end, the motor was operated under no-load conditions and subjected to a sequence of speed step references. Fig. 7.2 shows the reference and measured speed obtained during such a test, with both the ADRC and the FOC. Fig. 7.3 shows the corresponding waveforms of the reference and estimated rotor flux linkage as well as the electromagnetic torque. Fig. 7.4 shows the corresponding waveforms of the i_{sx}, i_{sy} stator current in the rotor flux reference frame. All the above figures show that both ADRC and FOC properly work, permitting the speed and rotor flux to track their references, acting on the corresponding references of the stator current components i_{sx}, i_{sy}. It can be observed that i_{sx} is controlled to a constant value, permitting the rotor flux to be controlled to the constant rated value of 0.8 Wb. On the contrary, i_{sy} shows a step-like waveform, with peaks occurring at each variation of the speed reference. The rotor flux and electromagnetic torque waveform exhibit the same shape as the corresponding i_{sx}, i_{sy}, as expected. Fig. 7.5 shows a zoom of the speed reversal and highlights that, even in constant flux operation, the proposed

ADRC presents better dynamic performance with a lower overshoot and lower settling time. Figures 7.6 to 7.9 show the analogous waveforms obtained by integrating the ELMT into both control systems. Different from the constant flux operation, in this case, at each speed transient not only a peak of i_{sy} (electromagnetic torque) occurs, but also a corresponding peak of i_{sx} (rotor flux) occurs, due to the regular working of the ELMT. Fig. 7.9, showing a zoom of the speed reversal under ELMT operation, clearly highlights that the proposed ADRC presents better dynamic performance with a lower overshoot and lower settling time.

7.6.2.2 Load disturbance rejection test

The second test investigates the disturbance rejection capability of the proposed ADRC controller compared to the conventional FOC strategy. In this test, the drive was operated at a constant speed of 50 rad/s, while a sequence of load torque steps was applied by means of the torque-controlled PMSM used as active load. Figures 7.10 to 7.15 show the reference and measured speed, the reference and estimated rotor flux, the electromagnetic torque, and finally the direct and quadrature components of the stator currents i_{sx}, i_{sy} in constant flux operation. The figures show that both the proposed ADRC and the FOC exhibit good load rejection capabilities, with the electromagnetic torque quickly tracking the load one, thus permitting a fast recovery of the measured speed to its reference. It can be observed that, as for the load rejection capabilities, the proposed ADRC significantly overcomes the classic FOC. In fact, the ADRC not only results in significantly smaller speed deviations under load application, but it also reacts so rapidly that the electromagnetic torque temporarily exceeds the applied load torque. As a consequence, the resulting speed variation is governed by the electromagnetic torque rather than by the load torque, unlike in the case of FOC. This is even more visible in the load rejection test under ELMT operation, as clearly visible in Figs. 7.13 to 7.15.

7.7 Summary

In this chapter, a robust nonlinear ADRC scheme for IM drives has been presented. The proposed approach relies on a high-gain UIO, driven by the tracking error, which replaces the classical ESO. This design eliminates the dependence on the control input, thus overcoming typical ADRC limitations such as sensitivity to inverter nonlinearities and chattering phenomena. A detailed stability and robustness analysis was provided, showing that the closed-loop system achieves asymptotic stability with guaranteed convergence of the tracking error. The analysis also highlighted how proper parameter tuning allows the system to achieve high robustness margins while preserving steady-state accuracy. The proposed control strategy was experimentally validated on a laboratory test bench, both under constant flux and variable flux operation. Two sets of experiments were carried out, focusing respectively on transient response and load disturbance rejection. The results

confirmed that the proposed ADRC achieves better dynamic performance and robustness compared to the classical FOC, with faster transients, reduced overshoot, and improved disturbance rejection capabilities.

Chapter 8

Dual three-phase induction motor control for harmonic loss reduction using dynamic input allocation

Abstract

This chapter presents a control strategy aimed at minimizing harmonic losses in dual three-phase induction motors through a dynamic input allocation technique. These motors, increasingly employed in high-reliability and high-performance applications, exhibit complex interactions among their multiple subspaces due to inverter-induced voltage harmonics and inherent system nonlinearities. The proposed control method compensates for undesirable harmonic components in the auxiliary z_1, z_2 subspace by generating control inputs within the null space of the transformation matrix, ensuring that the main sD, sQ subspace remains unaffected. This approach enhances overall system efficiency by reducing harmonic losses and mitigating their impact on motor operation. The effectiveness of the proposed strategy has been validated experimentally on a dedicated test setup, demonstrating its potential for practical implementation in advanced electric drive systems.

Contents

8.1 Motivation and literature review

Harmonic losses in dual three-phase induction motors can arise from inverter operation, parameter variations, and inherent system nonlinearities. Multi-phase induction motors have attracted significant attention due to their advantages in terms of fault tolerance, smoother torque production, and improved efficiency compared to conventional three-phase machines. While three-phase AC drives remain the standard for industrial applications, multi-phase drives have gained increased interest in recent years, especially for high-power, high-current, high-reliability, and power-density applications such as aerospace applications, ship propulsion, electric/hybrid vehicles, and offshore wind generation. One of the main benefits of multi-phase systems is the ability to distribute power across more inverter legs, improving their thermal management and reliability [99], [100]. Among the different multi-phase drive solutions, the dual three-phase induction machine is the most interesting and widely discussed in the literature [101], [102]. Several control strategies for dual three-phase machines have been reviewed in the literature, with significant focus on modeling techniques and PWM strategies. In [103], a comprehensive review of control strategies for dual three-phase induction machines is presented. In particular, it discusses various modeling approaches, PWM modulation techniques, and advanced control methods such as field-oriented control (FOC) and direct torque control. However, the increased complexity of these systems requires more advanced modeling and control frameworks to fully exploit their potential. For the analysis of multi-phase machines, several transformations have been proposed in the past [104], [105], [106], [107], [108]. Symmetrical component theory and matrix theory have served as the theoretical foundations for these transformations. Traditional modeling approaches are based on space vector decomposition, which transforms the six-phase system into three orthogonal subspaces:

- the main sD, sQ subspace;
- the auxiliary z_1, z_2 subspace;
- the homopolar o_1, o_2 subspaces.

This decomposition is fundamental for control strategies as extensively described in [109], and further compared in [110] for different current control approaches in multi-phase machines. However, the inverter adopted to supply the motor is an intrinsic time-harmonic generator. Among the various contributions to the modeling of dual three-phase machines, [109] proposes a transformation method based on matrix theory and vector space decomposition. In this framework, the six-dimensional stator and rotor current-voltage vectors are mapped into three two-dimensional orthogonal subspaces, leading to a simplified and decoupled representation of the system dynamics. While this approach provides valuable insights, it is subject to several limitations that reduce its applicability in control design:

- rotor variables are often expressed in the rotor reference frame, leading to time-varying mutual inductance matrices due to the difference between stator and rotor frequency;
- rotor currents, commonly used as state variables, are not directly measurable;
- the model is not formulated in state-space form, which complicates its integration with modern control strategies.

To overcome these issues, it is necessary to reformulate the model in the stator reference frame and to replace the rotor current with rotor flux linkages as state variables. Traditional control strategies typically focus on the main sD, sQ subspace, regulating mechanical and electrical variables. Moreover, due to nonlinearities, parameter variations, and other disturbances, current components may also appear in the auxiliary z_1, z_2 subspace, which ideally should remain zero under balanced operation with sinusoidal voltages. For these reasons, active harmonic compensation is required to increase the system's efficiency. Recent approaches that address harmonic minimization under parameter variations and nonlinearities are discussed in [111], emphasizing adaptive control methods. The main problem is that the system is multi-input, and dynamics in all subspaces are coupled. Therefore, it is very complex to minimize the harmonics in the z_1, z_2 subspace, and simultaneously control the mechanical variables without influencing each other, which results in a reduction of performance. This work presents a harmonic losses minimization by a dynamic input allocation approach [47] designed to compensate undesirable components in the z_1, z_2 subspace. In particular, by considering the null space (kernel) of the transformation matrix, the proposed method generates control inputs that effectively eliminate undesired harmonic components in the z_1, z_2 subspace without interfering with the main sD, sQ subspace. This approach improves overall system efficiency by reducing losses and mitigating the impact of undesired harmonic components.

8.2 Dynamic model of the dual three-phase induction motor

8.2.1 Phase equations

The dynamic model of the dual three-phase induction motor is derived under the assumption of a structurally balanced machine, and considering the following hypothesis:

- machine windings have been assumed sinusoidally distributed;
- mutual leakage inductances have been neglected;
- unity turn ratio between the stator and the rotor has been assumed;
- magnetic saturation of the iron core has been neglected;
- iron losses have been neglected.

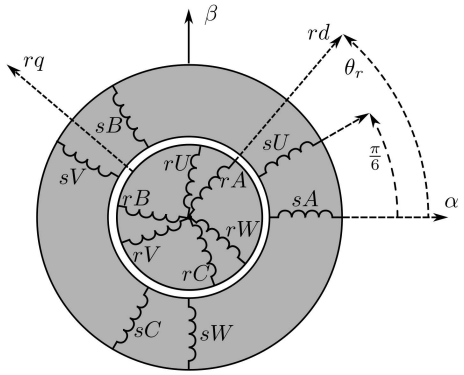

Figure 8.1: Cross-section of the dual three-phase induction motor.

Fig. 8.1 illustrates the cross-section of the motor, where the two sets of three-phase stator windings (sA, sB, sC and sU, sV, sW) are spatially shifted by $\frac{\pi}{6}$ rad. Similarly, the corresponding three-phase rotor windings (rA, rB, rC and rU, rV, rW, respectively) are mutually shifted by $\frac{\pi}{6}$ rad and shifted by the rotor electrical angle θ_r with respect to the stator windings. In this framework, sD, sQ, and rd, rq denote the direct and quadrature axes of the stator and rotor. In the original six-dimensional phase domain, the stator and rotor voltage equations can be expressed as:

$$\begin{cases} u_{sp} = R_{sp} i_{sp} + \frac{d\Phi_{sp}}{dt} = R_{sp} i_{sp} + \frac{d}{dt}(L_{sp} i_{sp} + L_{srp} i_{srp}), \\ u_{rp} = R_{rp} i_{rp} + \frac{d\Phi_{rp}}{dt} = R_{rp} i_{rp} + \frac{d}{dt}(L_{rp} i_{rp} + L_{rsp} i_{rsp}). \end{cases} \tag{8.1}$$

where u_{sp} and u_{rp} are the stator and rotor phase voltage vectors, Φ_{sp} and Φ_{rp} are the stator and rotor phase flux linkage, i_{sp} and i_{rp} are the stator and rotor phase current, R_{sp} and R_{rp} are the stator and rotor phase resistance, L_{sp} and L_{rp} are the stator and rotor phase self-inductance and, L_{srp} and L_{rsp} are the stator and rotor phase mutual-inductance defined as:

$$L_{srp} = L_m \begin{bmatrix} \cos(\theta_r) & \cos(\theta_r + \frac{\pi}{6}) & \cos(\theta_r + \frac{4\pi}{6}) & \cos(\theta_r + \frac{5\pi}{6}) & \cos(\theta_r + \frac{8\pi}{6}) & \cos(\theta_r + \frac{9\pi}{6}) \\ \cos(\theta_r + \frac{11\pi}{6}) & \cos(\theta_r) & \cos(\theta_r + \frac{3\pi}{6}) & \cos(\theta_r + \frac{4\pi}{6}) & \cos(\theta_r + \frac{7\pi}{6}) & \cos(\theta_r + \frac{8\pi}{6}) \\ \cos(\theta_r + \frac{8\pi}{6}) & \cos(\theta_r + \frac{9\pi}{6}) & \cos(\theta_r) & \cos(\theta_r + \frac{\pi}{6}) & \cos(\theta_r + \frac{4\pi}{6}) & \cos(\theta_r + \frac{5\pi}{6}) \\ \cos(\theta_r + \frac{7\pi}{6}) & \cos(\theta_r + \frac{8\pi}{6}) & \cos(\theta_r + \frac{11\pi}{6}) & \cos(\theta_r) & \cos(\theta_r + \frac{3\pi}{6}) & \cos(\theta_r + \frac{4\pi}{6}) \\ \cos(\theta_r + \frac{4\pi}{6}) & \cos(\theta_r + \frac{5\pi}{6}) & \cos(\theta_r + \frac{8\pi}{6}) & \cos(\theta_r + \frac{9\pi}{6}) & \cos(\theta_r) & \cos(\theta_r + \frac{\pi}{6}) \\ \cos(\theta_r + \frac{3\pi}{6}) & \cos(\theta_r + \frac{4\pi}{6}) & \cos(\theta_r + \frac{7\pi}{6}) & \cos(\theta_r + \frac{8\pi}{6}) & \cos(\theta_r + \frac{11\pi}{6}) & \cos(\theta_r) \end{bmatrix}, \tag{8.2}$$

$$L_{rsp} = L_m \begin{bmatrix} \cos(-\theta_r) & \cos(-\theta_r + \frac{\pi}{6}) & \cos(-\theta_r + \frac{4\pi}{6}) & \cos(-\theta_r + \frac{5\pi}{6}) & \cos(-\theta_r + \frac{8\pi}{6}) & \cos(-\theta_r + \frac{9\pi}{6}) \\ \cos(-\theta_r + \frac{11\pi}{6}) & \cos(-\theta_r) & \cos(-\theta_r + \frac{3\pi}{6}) & \cos(-\theta_r + \frac{4\pi}{6}) & \cos(-\theta_r + \frac{7\pi}{6}) & \cos(-\theta_r + \frac{8\pi}{6}) \\ \cos(-\theta_r + \frac{8\pi}{6}) & \cos(-\theta_r + \frac{9\pi}{6}) & \cos(-\theta_r) & \cos(-\theta_r + \frac{\pi}{6}) & \cos(-\theta_r + \frac{4\pi}{6}) & \cos(-\theta_r + \frac{5\pi}{6}) \\ \cos(-\theta_r + \frac{7\pi}{6}) & \cos(-\theta_r + \frac{8\pi}{6}) & \cos(-\theta_r + \frac{11\pi}{6}) & \cos(-\theta_r) & \cos(-\theta_r + \frac{3\pi}{6}) & \cos(-\theta_r + \frac{4\pi}{6}) \\ \cos(-\theta_r + \frac{4\pi}{6}) & \cos(-\theta_r + \frac{5\pi}{6}) & \cos(-\theta_r + \frac{8\pi}{6}) & \cos(-\theta_r + \frac{9\pi}{6}) & \cos(-\theta_r) & \cos(-\theta_r + \frac{\pi}{6}) \\ \cos(-\theta_r + \frac{3\pi}{6}) & \cos(-\theta_r + \frac{4\pi}{6}) & \cos(-\theta_r + \frac{7\pi}{6}) & \cos(-\theta_r + \frac{8\pi}{6}) & \cos(-\theta_r + \frac{11\pi}{6}) & \cos(-\theta_r) \end{bmatrix}. \tag{8.3}$$

L_{sp} and L_{rp} are the stator and rotor phase self-inductance matrices, defined as follows:

$$L_{sp} = L_{\sigma s} I_6 + L_m \begin{bmatrix} 1 & \frac{\sqrt{3}}{2} & -\frac{1}{2} & -\frac{\sqrt{3}}{2} & -\frac{1}{2} & 0 \\ \frac{\sqrt{3}}{2} & 1 & 0 & -\frac{1}{2} & -\frac{\sqrt{3}}{2} & -\frac{1}{2} \\ -\frac{1}{2} & 0 & 1 & \frac{\sqrt{3}}{2} & -\frac{1}{2} & -\frac{\sqrt{3}}{2} \\ -\frac{\sqrt{3}}{2} & -\frac{1}{2} & \frac{\sqrt{3}}{2} & 1 & 0 & -\frac{1}{2} \\ -\frac{1}{2} & -\frac{\sqrt{3}}{2} & -\frac{1}{2} & 0 & 1 & \frac{\sqrt{3}}{2} \\ 0 & -\frac{1}{2} & -\frac{\sqrt{3}}{2} & -\frac{1}{2} & \frac{\sqrt{3}}{2} & 1 \end{bmatrix}, \tag{8.4}$$

$$L_{rp} = L_{\sigma r} I_6 + L_m \begin{bmatrix} 1 & \frac{\sqrt{3}}{2} & -\frac{1}{2} & -\frac{\sqrt{3}}{2} & -\frac{1}{2} & 0 \\ \frac{\sqrt{3}}{2} & 1 & 0 & -\frac{1}{2} & -\frac{\sqrt{3}}{2} & -\frac{1}{2} \\ -\frac{1}{2} & 0 & 1 & \frac{\sqrt{3}}{2} & -\frac{1}{2} & -\frac{\sqrt{3}}{2} \\ -\frac{\sqrt{3}}{2} & -\frac{1}{2} & \frac{\sqrt{3}}{2} & 1 & 0 & -\frac{1}{2} \\ -\frac{1}{2} & -\frac{\sqrt{3}}{2} & -\frac{1}{2} & 0 & 1 & \frac{\sqrt{3}}{2} \\ 0 & -\frac{1}{2} & -\frac{\sqrt{3}}{2} & -\frac{1}{2} & \frac{\sqrt{3}}{2} & 1 \end{bmatrix}, \tag{8.5}$$

where $L_{\sigma s}$ and $L_{\sigma r}$ are the stator and rotor leakage inductances, L_m is the three-phase mutual inductance, and I_6 denotes the 6×6 identity matrix.

8.2.2 Equations in the sD, sQ-z_1, z_2-o_1, o_2 subspaces

To simplify the analysis, the space-vector decomposition method proposed in [109] has been adopted, which transforms the dynamic equations of the dual three-phase induction motor into three orthogonal two-dimensional subspaces:

- the sD, sQ subspace, responsible for electromechanical energy conversion;
- the z_1, z_2 subspace, associated with harmonic effects and losses;
- the o_1, o_2 subspace, corresponding to the homopolar components.

If the machine is structurally balanced and all the phases are regularly supplied, to pass from the subspace of the phases to the sD, sQ-z_1, z_2-o_1, o_2 subspaces, the following transformation matrix must be adopted:

$$T = \frac{1}{\sqrt{3}} \begin{bmatrix} 1 & \cos(\theta) & \cos(4\theta) & \cos(5\theta) & \cos(8\theta) & \cos(9\theta) \\ 0 & \sin(\theta) & \sin(4\theta) & \sin(5\theta) & \sin(8\theta) & \sin(9\theta) \\ 1 & \cos(5\theta) & \cos(8\theta) & \cos(9\theta) & \cos(\theta) & \cos(4\theta) \\ 0 & \sin(5\theta) & \sin(8\theta) & \sin(9\theta) & \sin(\theta) & \sin(4\theta) \\ 1 & 0 & 1 & 0 & 1 & 0 \\ 0 & 1 & 0 & 1 & 0 & 1 \end{bmatrix}, \tag{8.6}$$

where $\theta = \frac{\pi}{6}$ rad represents the angular shift between the two three-phase stator (rotor) windings. The main physical characteristics of the sD,sQ-z_1,z_2-o_1,o_2 subspaces are described in [103], [109], [112], [113]. If the matrix T is pre-multiplied by each term of

the stator and rotor phase equations given in 8.1, the following expressions are obtained:

$$\begin{cases} Tu_{sp} = TR_{sp}T^{-1}Ti_{sp} + T\frac{d\Psi_{sp}}{dt} = TR_{sp}T^{-1}Ti_{sp} + \frac{d}{dt}\Big(TL_{sp}T^{-1}Ti_{sp} + TL_{srp}T^{-1}Ti_{rp}\Big), \\ Tu_{rp} = TR_{rp}T^{-1}Ti_{rp} + T\frac{d\Psi_{rp}}{dt} = TR_{rp}T^{-1}Ti_{rp} + \frac{d}{dt}\Big(TL_{rp}T^{-1}Ti_{rp} + TL_{rsp}T^{-1}Ti_{sp}\Big), \end{cases} \tag{8.7}$$

with

$$Tu_{sp} = \begin{bmatrix} u_{sD} \\ u_{sQ} \\ u_{sz_1} \\ u_{sz_2} \\ u_{so_1} \\ u_{so_2} \end{bmatrix}, \qquad Ti_{sp} = \begin{bmatrix} i_{sD} \\ i_{sQ} \\ i_{sz_1} \\ i_{sz_2} \\ i_{so_1} \\ i_{so_2} \end{bmatrix}, \qquad Tu_{rp} = \begin{bmatrix} u_{rD} \\ u_{rQ} \\ u_{rz_1} \\ u_{rz_2} \\ u_{ro_1} \\ u_{ro_2} \end{bmatrix}, \qquad Ti_{rp} = \begin{bmatrix} i_{rD} \\ i_{rQ} \\ i_{rz_1} \\ i_{rz_2} \\ i_{ro_1} \\ i_{ro_2} \end{bmatrix}.$$

In the following, the final dynamic equations in the sD,sQ-z_1,z_2-o_1,o_2 subspaces are presented, with all variables referred to the stator reference frame. Furthermore, a state-space formulation of the model is proposed, in which the selected state variables are the stator currents and the rotor flux linkages, since these quantities are particularly relevant for FOC.

8.2.2.1 Equations in the sD, sQ subspace

By applying the transformation (8.6) to the stator and rotor voltage phase equations (8.7), the following stator and rotor equations can be obtained in the sD, sQ subspace, where each variable is expressed in its natural reference frame, i.e., stator or rotor:

$$\begin{cases} u_s = R_s i_s + \frac{d\Phi_s}{dt} = R_s i_s + L_s\frac{di_s}{dt} + \frac{d}{dt}(L_{sr}i_r), \\ u_r = R_r i_r + \frac{d\Phi_r}{dt} = R_r i_r + L_r\frac{di_r}{dt} + \frac{d}{dt}(L_{rs}i_s), \end{cases} \tag{8.8}$$

where R_s and R_r are the stator and rotor resistance matrices. Under the assumption of a structurally balanced machine, the stator-to-rotor and rotor-to-stator mutual inductance submatrices are:

$$L_{sr} = L_{rs}^T = M_2 \begin{bmatrix} \cos\theta_r & -\sin\theta_r \\ \sin\theta_r & \cos\theta_r \end{bmatrix}, \tag{8.9}$$

with $M_2 = 3L_m I_2$. Similarly, the stator and rotor self-inductance matrices can be expressed as:

$$L_s = L_{\sigma s}I_2 + M_1, \quad \text{and} \quad L_r = L_{\sigma r}I_2 + M_1,$$

where $M_1 = 3L_m I_2$. For structurally balanced machines, $M_1 = M_2$. Equations 8.8, that have been proposed in [114], are not useful for control purposes for three reasons:

- rotor variables are expressed in the rotor reference frame, implying that stator and rotor quantities present different frequencies and, consequently, all mutual inductance matrices are time-dependent quantities;

- rotor current is chosen as a model variable, but is not a measurable quantity;
- equation 8.8 is not expressed in state form.

To make 8.8 useful for control purposes, rotor variables have to be converted from the rotor to the stator reference frame, and the rotor flux linkage should be chosen in place of the rotor current as a state variable. To convert the rotor current from the rotor (i_r) to the stator ($i_r^{'}$) reference frame, the following vector rotation must be applied to the rotor current space vector:

$$i_r = \begin{bmatrix} \cos\theta_r & \sin\theta_r \\ -\sin\theta_r & \cos\theta_r \end{bmatrix} i_r^{'},$$

where θ_r is the rotor electrical angle. When all rotor-related variables are represented in the stator reference frame using a consistent transformation, the rotor flux linkage can be expressed as $\Phi_r^{'} = L_r i_r^{'} + M_r^{\top} i_s$, where L_r is the rotor inductance matrix in the stator reference frame, and M_r is the mutual inductance matrix. From this relationship, the rotor current space vector can be expressed as a function of the stator current and the rotor flux, $i_r^{'} = L_r^{-1}\Phi_r^{'} - L_r^{-1}M_r^{\top} i_s$. By substituting this expression into equation (8.8), and introducing the global leakage inductance matrix, defined as $L_\sigma = L_s(I_2 - L_s^{-1}L_r^{-1}M_2M_2^{\top})$, where L_s denotes the stator inductance matrix, the matrix representation of the global leakage inductance of three-phase machines is obtained. After some manipulations with matrix algebra, the following dynamic equations can be obtained and expressed in state-space form:

$$\begin{aligned} \frac{di_s}{dt} =& L_\sigma^{-1}\{-[R_s + L_r^{-1}T_r^{1}M_2M_2^{\top}]i_s + M_2L_r^{-1}(T_r^{-1} - J\omega_r)\Phi_r^{'} + u_s\}, \\ \frac{d\Phi'_r}{dt} =& T_r^{-1}M_2^{\top} i_s - (T_r^{-1} - J\omega_r)\Phi_r^{'} \end{aligned} \tag{8.10}$$

where T_r is the rotor time constant matrix and $J = \begin{bmatrix} 0 & -1 \\ 1 & 0 \end{bmatrix}$. In equation (8.10), not all the inductance matrices are time-dependent, since the model is expressed in the stator reference frame. These matrices are diagonal, with no dependence on time or current (assuming magnetic saturation is neglected), and have identical values along the sD, sQ axes. In conclusion, equation (8.10) is coincident with the classic dynamic equation of the three-phase induction motor.

8.2.2.2 Equations in the z_1, z_2 subspace

By properly processing equations (8.7), the dynamic equations of the dual three-phase induction motor in the z_1, z_2 subspace can be expressed in state-space form as follows:

$$\begin{cases} \frac{di_s^{z_1z_2}}{dt} = & -\frac{R_s}{L_{\sigma s}} i_s^{z_1z_2} + \frac{1}{L_{\sigma s}} u_s^{z_1z_2}, \\ \frac{d\Phi_r^{z_1z_2}}{dt} = & -\frac{R_r}{L_{\sigma r}} \Phi_r^{z_1z_2}, \end{cases} \tag{8.11}$$

These equations indicate that the z_1, z_2 subspace does not contribute to the energy conversion process. Instead, it is only responsible for power losses when a voltage component exists within this subspace.

8.2.2.3 Equations in the o_1, o_2 subspace

By properly processing equations (8.7), the dynamic equations of the dual three-phase induction motor in the o_1, o_2 subspace can be expressed in state-space form as follows:

$$\begin{cases} \frac{di_s^{o_1o_2}}{dt} = & -\frac{R_s}{L_{\sigma s}} i_s^{o_1o_2} + \frac{1}{L_{\sigma s}} u_s^{o_1o_2}, \\ \frac{d\Phi_r^{o_1o_2}}{dt} = & -\frac{R_r}{L_{\sigma r}} \Phi_r^{o_1o_2}. \end{cases} \tag{8.12}$$

These equations indicate that the o_1, o_2 subspace does not contribute to energy conversion but is a source of power losses when a voltage component exists in that subspace. Equations (8.10), (8.11), (8.12) represent the dynamic model of the structurally balanced dual three-phase induction machine represented in state-space form, assuming the rotor flux and the stator current as state variables and expressed in the stator reference frame.

8.3 Simplifying assumptions on the proposed model

The proposed dynamic model of the dual three-phase induction motor is comprehensive and particularly valuable for the development of control strategies. One of its main advantages comes from its formulation within a single reference frame, the stator frame, which significantly simplifies implementation. Moreover, it preserves a consistent mathematical structure regardless of whether the machine is balanced or unbalanced, healthy or faulty. The model is based on several simplifying assumptions characteristic of the classical dynamic model of the induction motor. Specifically, it neglects the magnetic saturation of the iron core, iron losses, slotting effects, and mutual leakage inductances between phases. Magnetic saturation, in particular, becomes significant in variable flux operating conditions, such as in the field weakening region, or when control schemes aimed at minimizing electrical losses (e.g., Electrical Loss Minimization Techniques, ELMT) are applied. These assumptions simplify the model without significantly affecting its suitability for control design and analysis, while preserving the essential dynamics of the dual three-phase induction motor.

8.4 Design of dynamic input allocation control

The control strategy proposed in this work aims to minimize harmonic distortions in the dual three-phase induction motor by regulating currents in the auxiliary z_1, z_2 subspace, while preserving optimal performance in the main sD, sQ subspace responsible for electromechanical dynamics. These distortions can significantly degrade system performance by increasing losses, reducing overall efficiency, and introducing unwanted

torque oscillations. The unavoidable additional harmonic components present in the phase voltages introduce disturbance components in both the sD, sQ, and z_1, z_2 subspaces. In particular, harmonic components in the source voltage generate currents along the z_1, z_2 subspace, which should be zero.

8.4.1 Controller design

To regulate the currents in the auxiliary z_1, z_2 subspace and minimize harmonic losses, the current errors are defined as:

$$e_{z1} := i_{z1ref} - i_{z1}, \tag{8.13}$$

$$e_{z2} := i_{z2ref} - i_{z2}, \tag{8.14}$$

where the reference currents i_{z1ref} and i_{z2ref} are the reference values of i_{z1} and i_{z2}, and are set to zero to directly achieve the minimization of harmonic losses. The main goal of the proposed method is to design two control inputs $\bar{\nu}_{z1}$ and $\bar{\nu}_{z2}$ that independently drive e_{z1} and e_{z2} such that:

$$\begin{cases} \bar{\nu}_{z1} \text{ is s.t. } e_{z1} = i_{z1ref} - i_{z1} \to 0 \quad \text{as } t \to +\infty \\ \bar{\nu}_{z2} \text{ is s.t. } e_{z2} = i_{z2ref} - i_{z2} \to 0 \quad \text{as } t \to +\infty \end{cases} \tag{8.15}$$

The effects of these two inputs must not be projected in the sD, sQ null space, because they should not influence the control of the mechanical variables; otherwise, it would result in a reduction of performance. For this reason, a suitable voltage injection map $G(\bar{\nu}_{z1}, \bar{\nu}_{z2})$ is designed such that the voltage generated by this map:

$$\bar{V} := \begin{bmatrix} \bar{V}_{abc} \\ \bar{V}_{xyz} \end{bmatrix} = G(\bar{\nu}_{z1}, \bar{\nu}_{z2}), \tag{8.16}$$

that will be added to the voltage reference generated by the main control system (which controls the electromechanical variables), is such that:

$$\mathrm{T}\bar{V} = \begin{bmatrix} 0 & 0 & \bar{\nu}_{z1} & \bar{\nu}_{z2} & 0 & 0 \end{bmatrix}^\top. \tag{8.17}$$

If (8.17) is satisfied, it means that the two currents in the z_1, z_2 subspace can be controlled independently by acting on $\bar{\nu}_{z1}$ $\bar{\nu}_{z2}$, and that their effect on the sD, sQ subspace is null as desired. A block diagram of the entire control system is shown in Fig. 8.2. By considering the transformation matrix T defined in (8.6) and imposing the condition (8.17), it is possible to construct an injection map $G(\bar{\nu}_{z1}, \bar{\nu}_{z2})$ that derives from the projection into the nullspace. This leads to the following expression:

$$G(\bar{\nu}_{z1}, \bar{\nu}_{z2}) = \begin{bmatrix} -\frac{\sqrt{3}}{2} & -\frac{1}{2} \\ -\frac{1}{2} & \frac{\sqrt{3}}{2} \\ \frac{\sqrt{3}}{2} & -\frac{1}{2} \\ -\frac{1}{2} & \frac{\sqrt{3}}{2} \end{bmatrix} \begin{bmatrix} \bar{\nu}_{z1} \\ \bar{\nu}_{z2} \end{bmatrix}, \tag{8.18}$$

where $\bar{\nu}_{z1}$ and $\bar{\nu}_{z2}$ are the outputs of two independent controllers, whose inputs are the current tracking errors e_{z1} and e_{z2}, respectively, as defined in equations (8.13) and (8.14). The corresponding control actions, $\bar{\nu}_{z1}$ and $\bar{\nu}_{z2}$, are implemented as PI controllers:

$$\bar{\nu}_{z1}(t) = K_P e_{z1}(t) + K_I \int_0^t e_{z1}(\tau) d\tau, \tag{8.19}$$

$$\bar{\nu}_{z2}(t) = K_P e_{z2}(t) + K_I \int_0^t e_{z2}(\tau) d\tau. \tag{8.20}$$

These control actions generate a voltage vector that is injected into the system through the map $G(\bar{\nu}_{z1}, \bar{\nu}_{z2})$, ensuring that the harmonic components of the currents in the z_1, z_2 subspace are independently regulated without interfering with the electromechanical dynamics control in the sD, sQ subspace.

8.4.2 Controller tuning

To ensure closed-loop stability and achieve a desired dynamic performance in the control of the i_{z1} and i_{z2} current components, the parameters of the two controllers (8.19) and (8.20) can be tuned by analyzing the first-order dynamics of the system described in the equation (8.11), which represent the behavior of the currents in the z_1, z_2 subspace. The frequency response function describing the dynamics of the current in the z_1, z_2 subspace is given by:

$$G_i(j\omega) = \frac{1}{R_s + j\omega L_{\sigma s}}, \tag{8.21}$$

while the general frequency response function of the two controllers (8.19) and (8.20) can be expressed as:

$$G_c(j\omega) = \frac{j\omega K_P + K_I}{j\omega}. \tag{8.22}$$

The two controllers were designed to impose suitable values of the crossover frequency $\bar{\omega}_t$ and phase margin $\bar{m}_\phi$. To this end, the controller parameters K_P and K_I were selected to satisfy the following tuning conditions:

$$\|G_i(j\bar{\omega}_t)\| \|G_c(j\bar{\omega}_t)\| = 1, \tag{8.23}$$

$$\arg(G_c(j\bar{\omega}_t)) = -180^\circ + \bar{m}_\phi - \arg(G_i(j\bar{\omega}_t)). \tag{8.24}$$

These relations allow for straightforward computation of the controller parameters K_P and K_I, guaranteeing both stability and optimal dynamic performance in current regulation. Following the tuning conditions in (8.23) and (8.24), both were tuned using identical parameters, with gains set to $K_P = 32$ and $K_I = 750$ to ensure the desired stability margins and dynamic response, respectively $\bar{m}_\phi \approx 90^\circ$ and $\bar{\omega}_t \approx 3kHz$. The dynamic input allocation strategy adopted in this chapter represents a clear application of hybrid and switched system principles. The allocation mechanism introduces a supervisory logic that dynamically redistributes control inputs among redundant degrees of freedom, resulting in a hybrid control structure combining continuous current regulation with discrete reallocation decisions. This approach directly builds upon the dynamic allocation

Table 8.1: Parameters of the dual three-phase induction motor under test

Stator Resistance R_s	$7\,\Omega$
Stator Inductance L_s	$0.765\,\mathrm{H}$
Rotor Resistance R_s	$1.5240\,\Omega$
Rotor Inductance L_r	$0.776\,\mathrm{H}$
Magnetizing Inductance L_m	$0.754\,\mathrm{H}$
Rotor time constant T_r	$0.5092\,\mathrm{s}$
Rotor Leakage Inductance L_{dr}	$0.0220\,\mathrm{H}$
Stator Leakage Inductance L_{ds}	$0.0110\,\mathrm{H}$
Moment of Inertia J	$0.0072\,\mathrm{kg\,m^2}$
Pole Pairs number p	1

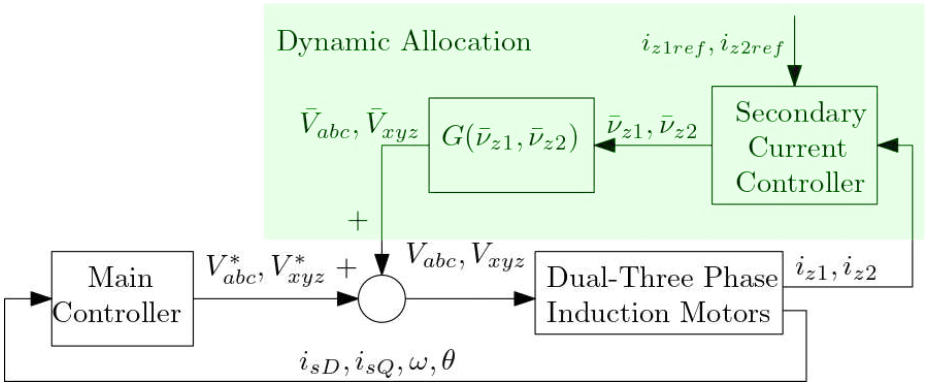

Figure 8.2: Block diagram of the proposed control algorithm.

framework discussed in Chapters 2 and 3, where the switching among allocation modes can be analyzed within a hybrid system formulation, ensuring stability and performance through appropriate Lyapunov-based arguments.

8.5 Experiments

This section presents the experimental validation of the proposed control strategy for harmonic loss reduction in dual three-phase induction motors. The main objective of the experiments is to demonstrate that the dynamic input allocation controller is capable of suppressing undesired harmonic currents in the z_1, z_2 subspace, without interfering with the electromechanical dynamics in the sD, sQ subspace. To this end, the control algorithm has been implemented on a dedicated laboratory test bench and experimentally tested under controlled operating conditions. The experiments were performed using the parameter values given in Table 8.1.

8.5.1 Experimental setup

The experimental setup has been developed starting from a standard three-phase induction motor, which has been modified by redesigning the stator winding in order to realize a dual three-phase prototype. A photograph of the test bench is shown in Fig. 8.3. The

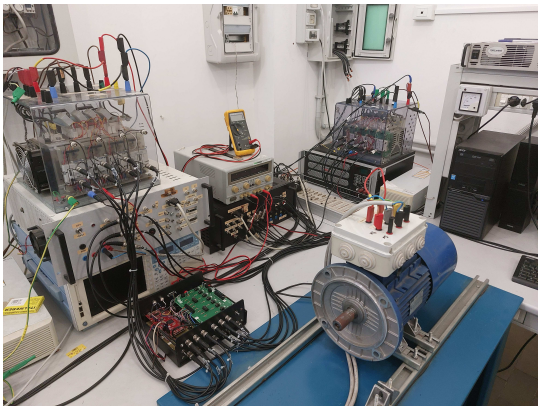

Figure 8.3: Photo of the experimental setup.

machine is supplied by a six-leg voltage source inverter (VSI) using Semikron SKM 50 GB 123 IGBT devices, and a sinusoidal PWM technique. The drive is controlled by a classical FOC scheme, specifically a rotor flux-oriented control, where current control is performed in the rotor flux-oriented reference frame by PI controllers. The rotor flux amplitude and phase angle are estimated using the classical flux model based on the rotor equation in the rotor reference frame [115]. The stator current components in the stator reference frame are obtained from the measured phase currents using the matrix transformation T (see eq. 8.6), which projects the six-phase system into the decoupled subspaces used in the control. The proposed dynamic allocation controller is integrated into the FOC framework as illustrated in Fig. 8.2. It operates in parallel with the main controller to suppress undesired harmonic currents in the z_1, z_2 subspace without affecting the sD, sQ subspace. Both the FOC and the PWM have been implemented on a Texas Instruments LAUNCHXL-F28379D real-time development board. The control loop sampling frequency is set to 10 kHz, while the PWM frequency is fixed at 5 kHz, ensuring sufficient bandwidth for accurate current regulation and real-time harmonic compensation.

8.5.2 Experimental results

The effectiveness of the proposed controller has been evaluated through dedicated experimental tests. The drive is initially running at a constant speed of 150 rad/s at no load. The reference voltage at the output of the controller is purposely injected with 5^{th} and 7^{th} voltage harmonics, with amplitudes of $\frac{1}{5}$ and $\frac{1}{7}$ of the fundamental, respectively. The dynamic allocation controller is initially deactivated. At $t = 4s$, the controller is activated. Fig. 8.4 (a) shows, respectively, the measured rotor speed, the estimated electromagnetic torque, and the direct and quadrature components of the rotor flux in the stator reference frame. As expected, neither the rotor speed, the electromagnetic torque, nor the rotor flux components are affected by the activation of the dynamic allocation controller, confirming the proper separation of the subspaces in which the FOC and the controller operate. Fig. 8.4 (b) shows the six-phase stator currents. Before activating

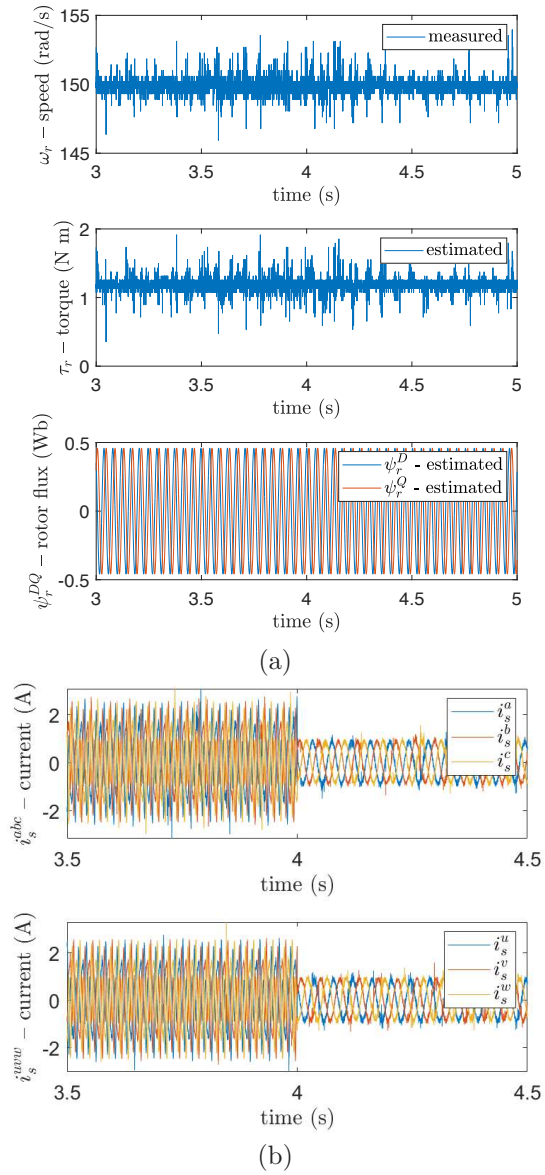

Figure 8.4: (a) shows respectively the mechanical speed, the torque, and the rotor flux, (b) shows respectively the current along the sD-sQ, z_1-z_2, o_1-o_2 subspaces.

the dynamic allocation controller, the phase currents are highly distorted due to the injected 5^{th} and 7^{th} harmonic voltages. After activation, the currents become almost sinusoidal, confirming the effectiveness of the proposed controller. This behavior is further highlighted in Fig. 8.5 (a), which shows the direct and quadrature components of the stator current in the three working subspaces, respectively, the sD, sQ, the z_1, z_2, and the o_1, o_2 subspaces. The i_s^{DQ} components are not affected by the activation of the dynamic allocation controller, as desired. On the contrary, the $i_s^{z_1 z_2}$ current components, present a considerable amplitude before the activation of the dynamic allocation controller because of the purposely added 5^{th} and 7^{th} harmonic voltages, which drastically reduce close to zero when the dynamic allocation controller is activated, confirming the correct working of the proposed controller. The effectiveness of the proposed controller is also confirmed by

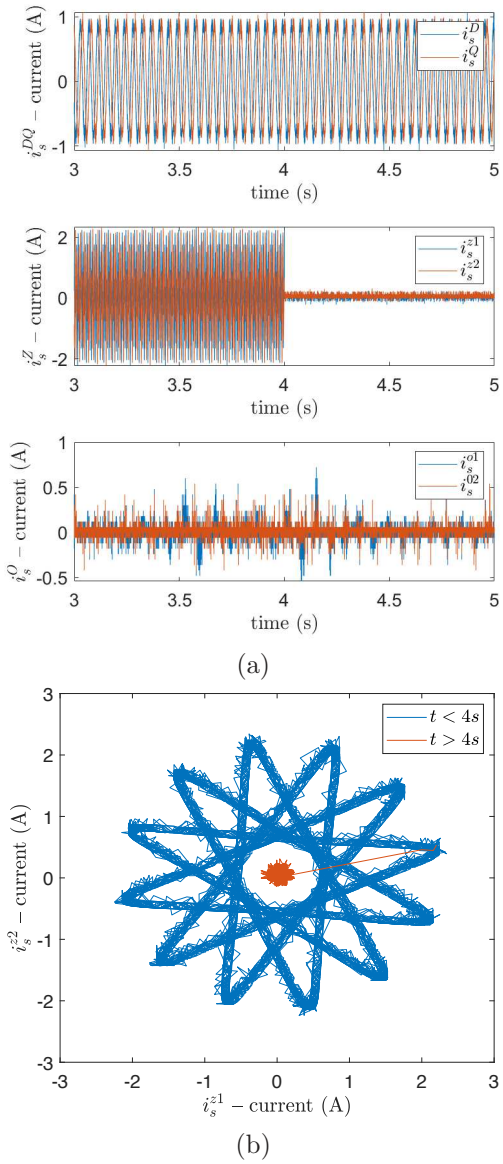

Figure 8.5: (a) shows respectively the six-phase currents, (b) shows the locus $i_s^{z_1}$-versus-$i_s^{z_1}$.

the locus describing $i_s^{z_2}$-versus-$i_s^{z_1}$ shown in Fig. 8.5 (b). When the controller is disabled ($t < 4s$, blue trace), the trajectory reflects the influence of the injected harmonics. Once the controller is activated ($t > 4s$, red trace), the trajectory degenerates to the origin, demonstrating the complete suppression of the undesired harmonic components. The $i_s^{o_1 o_2}$ current components are not affected by the application of the proposed controller, as expected and desired.

8.6 Summary

This chapter has addressed the design and experimental validation of a control strategy for minimizing harmonic losses in a dual three-phase induction motor. The proposed approach relies on a dynamic input allocation technique, which regulates the auxiliary z_1,

z_2 subspace while preserving the electromechanical dynamics in the main sD, sQ subspace. A suitable injection map and nullspace projection ensure that the harmonic mitigation action does not influence torque production or flux regulation. A systematic procedure has been presented for controller design, including the formulation of current error dynamics and the tuning of PI regulators for harmonic current suppression. The method guarantees stability and a suitable dynamic response while mitigating performance degradation in the fundamental subspace. The proposed controller has been implemented on a real-time DSP platform and experimentally tested on a custom dual three-phase induction motor prototype. The results confirm that the control strategy effectively suppresses unwanted harmonic components in the auxiliary subspace, improves current waveform quality, and reduces losses, without affecting the motor's mechanical performance. Overall, the proposed dynamic input allocation method enhances efficiency and current quality in multiphase drives, making it suitable for applications where reliability and minimization of losses are critical requirements.

Chapter 9

Sensorless control strategies for high-speed permanent magnet synchronous motor in exhaust energy recovery

Abstract

This chapter addresses the sensorless control of a Permanent Magnet Synchronous Motor (PMSM) designed for use in a turbo-generator, aiming to recover exhaust gas energy from an Internal Combustion Engine (ICE). The primary challenge in this application arises from the high rotational speeds required by the turbo-generator, which complicates the installation of a physical speed sensor. Consequently, sensorless control is highly recommended. However, conventional sensorless techniques suffer from limitations due to their computational complexity and sensitivity to model parameter uncertainties. This chapter presents a comparative study of two principal sensorless techniques for rotor speed estimation: a deterministic approach based on a Model Reference Adaptive System (MRAS) observer, and a stochastic approach utilizing an Extended Kalman Filter (EKF). The analysis evaluates the effectiveness of each method in terms of computational load, robustness to parameter variations, and resilience to measurement noise.

Contents

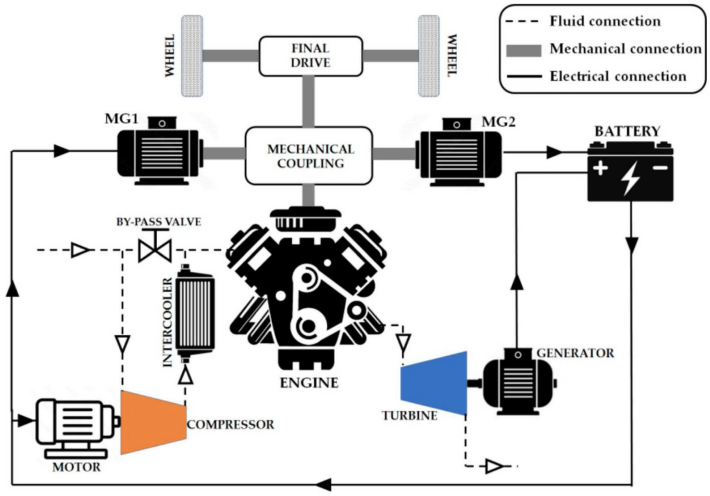

Figure 9.1: Schematic representation of the separated electric compound system.

9.1 Motivation and literature review

Recent concerns about environmental problems and the increasing impact of climate change highlight the need to adopt effective strategies to reduce fossil fuel consumption. In particular, the recovery of energy and emissions from vehicles equipped with an ICE represents a significant challenge. The European Union must drastically reduce greenhouse gas (GHG) emissions around the world to keep global warming below 2 Celsius-degrees. For this reason, the European Parliament adopted strong measures, with a target of 55% overall GHG emissions reduction (concerning the 1990 level) by 2050 in the European Union. Great attention is paid to the transport sector. The goal is to make vehicles suitable for compliance with current and future environmental regulations by pushing toward market solutions that combine respect for the environment with vehicle fuel savings. Consequently, numerous measures have been proposed to reduce polluting emissions across road, rail, air, and maritime transport. In this context, the study presented in this chapter investigates and designs a system that allows better exploitation of the chemical energy in the fuel of ICEs. Hybrid Electric Vehicles (HEV) have demonstrated considerable potential in reducing fuel consumption compared to traditional ICE vehicles. Although ICE technology is well-established, engines based on Otto or Diesel cycles are inherently limited, as they cannot fully expand the combustion gases inside the cylinder, resulting in the loss of approximately 20% of the total energy. Several solutions have been proposed in the literature to recover this unexpanded gas energy [116], [117]. A commonly adopted approach is conventional turbocharging, where the unexpanded gas energy is recovered by a gas turbine (usually a radial in-flow turbine) mechanically connected to a compressor to increase the inlet air pressure and engine power. In this configuration, the turbine only provides the mechanical power required by the compressor, which reduces the amount

of energy recovered. Additionally, the shared shaft between the turbine and compressor imposes rotational speed constraints that reduce the overall efficiency to approximately 20-30%. Alternative solutions include the integration of an electric generator on the turbocharger shaft to capture excess energy [118], [119], [120], [121], achieving efficiency improvements of up to 6%; Another approach is represented by electric turbo-compound systems, where a turbine-generator group is installed downstream of the main turbine, providing gains of around 4% [122], [123]. In [124], [125], an auxiliary turbo generator is implemented in parallel with the main turbocharger, allowing for efficiency improvements of up to 9%. The system investigated in this work adopts a novel architecture suitable for hybrid propulsion systems [126]. As shown in Fig. 9.1, the proposed architecture is an innovative compound system in which a suitably designed exhaust gas turbine connected to a proper electric generator converts the unexpanded exhaust gas energy into electric energy delivered to the vehicle storage system. The energy content of the unexpanded gas could significantly improve the overall efficiency of the propulsion system. The difference, compared to other systems, is that in the proposed thermal unit, the entire exhaust gas flow from the combustion engine completes the expansion (from the exhaust pressure of the engine to the pressure of the exhaust pipe) inside the turbine, whose output power is transformed into electricity by the generator. This system is named a separated electric compound engine since the compressor used for engine charging is not connected to the turbine employed for exhaust gas energy recovery, thus letting their operating conditions be independent of each other. In the propulsion system proposed, the turbine always operates with the entire engine exhaust mass flow to recover as much energy as possible; on the contrary, the compressor, which is mechanically independent of the turbine, is driven by its electric motor only when supercharging is required, i.e., for the higher engine loads. As discussed in [126], [127], to satisfy the required wide range of mass flow rates and pressure ratio (i.e., the ratio between the turbine inlet and outlet pressure), the exhaust gas turbine adopted is a variable nozzle turbine; this kind of turbine allows an efficient adaptation to several operating conditions (i.e. mass flow rate and pressure ratio) by adequately setting the distributor blade position. The electrical power produced by the turbo-generator group could contribute to the total power delivered for vehicle traction, thus increasing the vehicle's fuel economy. To maximize efficiency and minimize the size of the turbo-generator unit, high-speed electric drives are required. PMSM is the preferred choice for hybrid systems due to its high energy density and efficiency, particularly in high-speed applications [128]. This chapter focuses on evaluating the feasibility of two sensorless control strategies (EKF and MRAS observer), usually employed for standard PMSM, for the exhaust gas energy recovery from the internal combustion engine. These methods were selected due to their representation of stochastic and deterministic frameworks, respectively, allowing an analysis of how explicit modeling of uncertainties affects performance under challenging conditions such as high rotational speeds, significant disturbances, and parameter variations.

9.2 System description and problem formulation

This section focuses on modeling a high-speed PMSM, which represents the core of the turbo-generator system used for exhaust gas energy recovery. As discussed in the previous section, the role of the turbo-generator in the proposed separated electric compound propulsion architecture is to convert the residual energy of the exhaust gases, unexpanded in the cylinder, into electrical energy with the highest possible efficiency. Achieving this objective requires an optimal control strategy that simultaneously acts on two separate parameters: the distributor nozzle angle and the rotor speed of rotation. In the turbine considered, the nozzle blade position is typically varied within a narrow operating range of $2.9 - 11.2$ degrees and can be efficiently regulated using a stepper motor, which provides adequate response time and robustness. Conversely, the rotor speed of rotation exhibits a much wider variation (70000 to 180000 rpm for the considered turbine). Its control is more challenging due to the combined effects of rotor inertia and extreme operating conditions. This makes the generator's control system a critical component, as it must ensure both fast dynamic response and robustness. One of the most common control methods for electrical machine drives is field-oriented control (FOC), also known as vector control, which improves the performance of PMSM drives. FOC enables the decoupling of torque and flux components, simplifying the control of the motor and allowing for high-performance operation. The strategy is based on a cascade control structure, where the inner current loop regulates the direct and quadrature stator current components, and the outer speed loop adjusts the mechanical speed or torque. Proportional-Integral (PI) controllers are typically adopted in both loops. This structure allows precise speed position regulation and has been extensively validated in industrial applications [129], [130], [131]. For vector-controlled electrical machine drives, precise motor position measurement is crucial. Motor position can be measured using different position sensors, such as encoders or resolvers, and speed sensors to detect the position and speed of the motor, respectively. However, in high-speed applications, these devices suffer from limitations related to size, cost, reliability, and robustness. Moreover, the extremely high rotational speeds considered here further restrict the feasibility of using such sensors. An alternative approach, which has gained significant attention, is sensorless control, where the rotor position and speed are estimated from current and voltage measurements. This approach enhances the robustness and reduces the cost and complexity of the overall system.

9.2.1 Mathematical model of the high-speed PMSM

Before presenting the sensorless estimation strategies, the mathematical model of the high-speed PMSM is introduced. In the $d-q$ rotating reference frame, the motor dynamics are described by the following set of differential equations:

$$\frac{di_{sd}}{dt} = \frac{1}{L_d}\big(- R_s i_{sd} + \rho\omega L_q i_{sq} + v_d\big), \tag{9.1a}$$

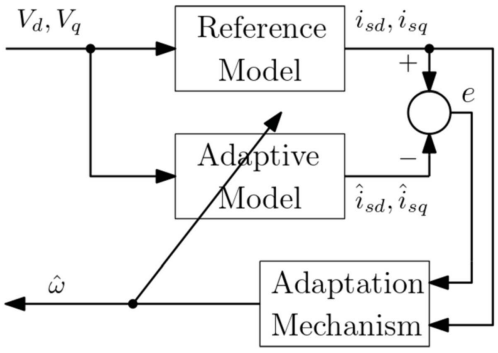

Figure 9.2: Block diagram of MRAS.

$$\frac{di_{sq}}{dt} = \frac{1}{L_q}\big(- R_s i_{sq} - \rho\omega L_q i_{sd} - \sigma\omega K_e + v_q\big), \tag{9.1b}$$

$$\frac{d\omega}{dt} = \frac{1}{J}\left[\frac{3}{2}\big(\rho K_e i_{sq} + \rho(L_d - L_q) i_{sd} i_{sq}\big) - \eta(\omega) - f_v\omega\right], \tag{9.1c}$$

where i_{sd} and i_{sq} are the stator current components, L_d and L_q are the stator inductances, v_d and v_q are the stator voltage components, ρ represents the number of pole pairs, K_e is the flux constant that depends on the magnets, R_s is the stator resistance, J is the moment of inertia, f_v is the viscous friction, and finally, ω indicates the angular velocity of the rotor. The model neglects magnetic saturation, eddy currents, and hysteresis losses, while assuming sinusoidal electromotive force generation [132], [133]. This mathematical model serves as the basis of the development and validation of the proposed sensorless control algorithms.

9.3 Sensorless control strategies

In high-speed PMSM applications, sensorless control offers a significant advantage by enhancing the overall reliability of the drive system. The extremely high rotational speed, vibrations, and high temperatures make traditional position sensors, such as encoders or resolvers, susceptible to damage. Sensorless control thus provides a practical solution, reducing the mechanical complexity of the system and operating in hostile environments at high speed by reducing the maintenance requirements. Among the several sensorless control techniques available in the literature for PMSM drives [133], [134], [135], [136], this thesis focuses on two principal approaches: the MRAS observer and the EKF estimator. These methods were selected because they represent the main principal approaches in the literature used for deterministic and stochastic sensorless control, respectively. The MRAS observer operates in a deterministic framework, where stochastic effects are not explicitly considered, whereas the EXF explicitly accounts for process and measurement noise in a stochastic framework. This allows for a comparative analysis of their performance under high-speed operating conditions.

9.3.1 MRAS observer

The MRAS observer is one of the most widely used sensorless control techniques due to its simplicity, ease of implementation, and robust estimation of motor speed [137], [138], [139], [140], [141]. The observer, as shown in Fig. 9.2, consists of three main elements:

- a reference model;
- an adaptive model;
- an adaptation mechanism.

Both the reference and adaptive models estimate the stator currents along the d-q axis; however, the reference model does not require knowledge of the speed to estimate the currents. The adaptation mechanism adjusts the estimated speed to minimize the difference between the outputs of the adaptive and reference models. In this configuration, the physical PMSM represents the reference model, and the currents are measured. To derive the adaptive model, it is necessary to consider equations (9.1a)-(9.1b). In particular, it can be represented by the following model:

$$\begin{bmatrix} \dot{\hat{i}}_{sd} \\ \dot{\hat{i}}_{sq} \end{bmatrix} = \begin{bmatrix} -\frac{R_s}{L_d} & \rho\hat{\omega}\frac{L_q}{L_d} \\ -\rho\hat{\omega}\frac{L_q}{L_d} & -\frac{R_s}{L_q} \end{bmatrix} \begin{bmatrix} \hat{i}_{sd} \\ \hat{i}_{sq} \end{bmatrix} + \begin{bmatrix} \frac{1}{L_d} & 0 \\ 0 & \frac{1}{L_q} \end{bmatrix} \begin{bmatrix} V_d \\ V_q \end{bmatrix} + \begin{bmatrix} 0 \\ -1 \end{bmatrix} \frac{\rho\hat{\omega}K_e}{L_q}, \tag{9.2}$$

where $\hat{i}_{sd}$, $\hat{i}_{sq}$, and $\hat{\omega}$ represent the estimated values of i_{sd}, i_{sq}, and ω, respectively. The adaptive model calculates the same variables as the reference model using the rotor speed value provided by the adaptation mechanism, which is designed to generate the value of the estimated speed used to minimize the stator current errors. To ensure the convergence to zero of the estimation error, the adaptation mechanism is constituted by a PI controller. Moreover, the error considered as input for the PI is represented by the angular difference between the measured and the estimated stator-current space vectors. Therefore, the equation for the estimated speed can be written as follows:

$$\hat{\omega} = \left(K_p + \frac{K_i}{s}\right)\left[\frac{L_q}{L_d} i_{sd}\hat{i}_{sq} - \frac{L_d}{L_q} i_{sq}\hat{i}_{sd} - \frac{K_e}{L_d}(i_{sq} - \hat{i}_{sq})\right]. \tag{9.3}$$

This choice of the adaptation mechanism ensures the stability of the observer, as demonstrated using Popov's theory in [142], where the convergence to zero of the following error dynamics is shown:

$$\dot{e} = Ae - \lambda, \tag{9.4}$$

where $e = [e_{sd} \;\; e_{sq}]^\top = [(i_{sd} - \hat{i}_{sd}) \;\; (i_{sq} - \hat{i}_{sq})]^\top$, $\lambda = J\rho(\omega - \hat{\omega}) \begin{bmatrix} \hat{i}_{sd} & \hat{i}_{sq} \end{bmatrix}^\top$, with $J = \begin{bmatrix} 0 & -1 \\ 1 & 0 \end{bmatrix}$, and finally, A is given by:

$$A = \begin{bmatrix} -\frac{R_s}{L_d} & \rho\omega\frac{L_q}{L_d} \\ -\rho\omega\frac{L_q}{L_d} & -\frac{R_s}{L_q} \end{bmatrix}.$$

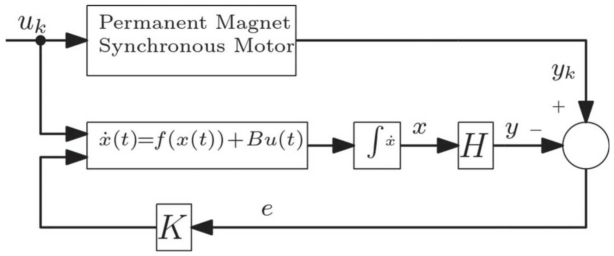

Figure 9.3: Block diagram of EKF.

The MRAS observer is one of the most common methods due to its simplicity, direct stability approach, and low computational effort; furthermore, it is easy to implement in a Digital Signal Processor (DSP). However, the MRAS method cannot get a satisfying performance in low-speed regions, and it strongly depends on the accuracy of the reference model. These problems are irrelevant to the proposed application since the PMSM is operated at high speed, and the machine constitutes the model reference.

9.3.2 EKF estimator

The EKF estimator is widely used for nonlinear stochastic systems. It provides a recursive estimation of the system state based on noisy input-output measurements and knowledge of the stochastic properties of both process and measurement noise. The scheme of the EKF considered in this work is shown in Figure 9.3. In high-speed PMSM applications, the EKF can be employed to estimate rotor speed and position without requiring direct measurement, offering robustness under high-speed and high-disturbance conditions. The first step in EKF design is the formulation of a stochastic model of the PMSM. Starting from the deterministic $d-q$ equations of the motor (9.1), the following stochastic model in continuous time can be obtained:

$$\dot{x}(t) = f(x(t)) + Bu(t) + Qw(t), \tag{9.5}$$

$$y(t) = Hx(t) + Rv(t), \tag{9.6}$$

where $x(t) = \begin{bmatrix} i_{sd} & i_{sq} & \omega \end{bmatrix}^\top$ is the state vector, $u(t) = \begin{bmatrix} V_d & V_q \end{bmatrix}^\top$ is the input vector, and $y(t) = \begin{bmatrix} i_{sd} & i_{sq} \end{bmatrix}^\top$ is the measured output vector. The terms $w(t)$ and $v(t)$ denote a Gaussian zero-mean white process and measurement noise, with covariance matrices Q and R, respectively. The diagonal form of Q and R implies uncorrelated noise components. Finally, $f(x(t))$, B, and H are given by:

$$f(x(t)) = \begin{bmatrix} -\frac{R_s}{L_d} i_{sd} + \rho\omega \frac{L_q}{L_d} i_{sq} \\ -\frac{R_s}{L_q} i_{sq} - \rho\omega \frac{L_d}{L_q} i_{sq} - \rho\omega \frac{K_e}{L_q} \\ \frac{3}{2}\frac{\rho}{J}(K_e i_{sq} + (L_d - L_q) i_{sq} i_{sd}) - \frac{f_v}{J}\omega - \frac{\eta(\omega)}{J} \end{bmatrix}, \; B = \begin{bmatrix} \frac{1}{L_d} & 0 \\ 0 & \frac{1}{L_q} \\ 0 & 0 \end{bmatrix}, \; H = \begin{bmatrix} 1 & 0 & 0 \\ 0 & 1 & 0 \end{bmatrix}.$$

B and H are constant matrices that define the input and output relationships. At the same time, the vector field $f(x(t))$ represents the nonlinear system dynamics and is

time-varying because it depends on the state. To design the EKF, the nonlinear model (9.5) can be discretized by applying Euler's method as follows:

$$x_{k+1} = x_k + T_s f(x_k) + T_s B u_k + T_s Q w_k, \tag{9.7}$$

$$y_k = H x_k + R v_k, \tag{9.8}$$

where T_s is the sampling time. The EKF algorithm proceeds recursively with two main steps:

- the *measurement update* phase;
- the *time update* phases.

During the k-th *measurement update*, the a-posteriori estimates of the state $\hat{x}_{k|k}$ and the covariance matrix of the estimation error $P_{k|k}$ are updated according to the measured outputs and the predicted state as follows:

$$\hat{x}_{k|k} = \hat{x}_{k|k-1} + K_k(y_k - H\hat{x}_{k|k-1}), \tag{9.9}$$

$$P_{k|k} = P_{k|k-1} - K_k H P_{k|k-1}, \tag{9.10}$$

where $x_{k|k-1}$ is the predictive estimate of the state at the instant $k-1$, and K_k is the gain of the filter given by:

$$K_k = P_{k|k-1} H^\top \left(H P_{k|k-1} H^\top + R\right)^{-1}. \tag{9.11}$$

The filter gain K_k is automatically computed to minimize the estimation error covariance, ensuring optimal state estimation. Using $\hat{x}_{k|k}$ and $P_{k|k}$, the prediction of the state is computed in the *time update* phase as follows:

$$\hat{x}_{k+1|k} = f_k(\hat{x}_{k|k}) + B u_k, \tag{9.12}$$

$$P_{k+1|k} = F_k P_{k|k} F_k^T + T_s Q, \tag{9.13}$$

where F_k is the jacobian of the vector field $f(x(t))$ and is given by:

$$F_k = \left.\frac{\partial f_k(x_k)}{\partial x}\right|_{x=\hat{x}_{k|k}} = \begin{bmatrix} -\frac{R_s}{L_d} & \rho\omega_{k|k}\frac{L_q}{L_d} & \rho\frac{L_q}{L_d} i_{sq\,k|k} \\ -\rho\omega_{k|k}\frac{L_d}{L_q} & -\frac{R_s}{L_q} & -\rho(\frac{K_e}{L_q} + \frac{L_d}{L_q} i_{sd\,k|k}) \\ \frac{3}{2}\frac{\rho}{J}(L_d - L_q) i_{sq\,k|k} & \frac{3}{2}\frac{\rho}{J} K_e & -\frac{1}{J}(f_v - \left.\frac{\partial \eta}{\partial \omega}\right|_{k|k}) \end{bmatrix}. \tag{9.14}$$

The initial conditions of the filter, including $\hat{x}_{0|0}$ and $P_{0|0}$, as well as the choice of covariance matrices Q and R, play a crucial role in performance. In this work, the filter was initialized at the instant $k = 0$, with $\hat{x}_{0|0} = x_0 = [0 \;\; 0 \;\; 0]^\top$ and $P_{0|0} = P_0 = \alpha I_4$, where α is a constant with a sufficiently high value. Covariance matrices Q and R were experimentally tuned to ensure that the estimated stator currents closely track the measured values, providing accurate rotor speed estimation for sensorless control of the high-speed PMSM. From a hybrid systems standpoint, the comparison between MRAS and EKF-based sensorless strategies can be interpreted as an analysis of different

Table 9.1: Motor parameters.

Parameter	Value
Power P	$10kW$
Direct (Quadrature) axis inductance $L_d(L_q)$	$55\mu H$
Stator resistance R_s	0.012Ω
Permanent magnets flux K_e	$0.0141Wb$
Pole-pair number ρ	1
Inertia momentum of the rotor-turbine system J	$133.2\mu Kgm^2$

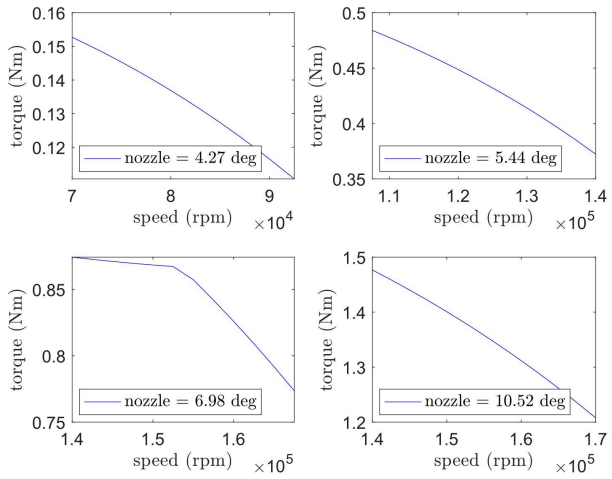

Figure 9.4: Torque-speed characteristics of the considered turbine.

Table 9.2

Blade angle [°]	Turbine inlet pressure [bar]	Turbine inlet temperature [K]	Rotor speed of rotation [rpm]
4.27	1.705	1006	$70000 - 92500$
5.44	2.702	1061	$107500 - 140000$
6.98	3.712	1102	$140000 - 167500$
10.52	3.938	1115	$140000 - 170000$

Table 9.3: IAE performance indexes

Blade position angle [°]	Speed tracking error	Estimation error with EKF	Estimation error with MRAS
4.27	105.8	0.6	65.5
5.44	128.8	1.3	179
6.98	116.6	2.3	246.4
10.52	129.9	3.9	282.2

$$\text{Speed tracking error: } \int_0^T \Big|\omega_{ref}(t) - \omega(t)\Big| dt$$

$$\text{Estimation tracking error: } \int_0^T \Big|\omega(t) - \hat{\omega}(t)\Big| dt$$

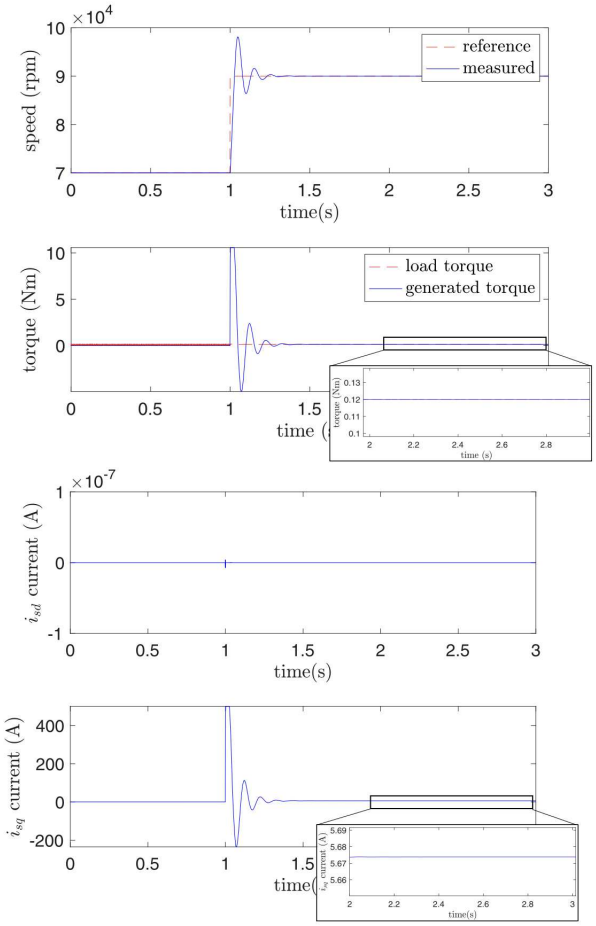

Figure 9.5: Motor speed ω and torque generated by the motor, and stator current along *d-q* axis, for the nozzle angle equal to 4.27 during a step variation of the reference speed from 70 to 92.5 krpm.

observer dynamics associated with distinct operating regimes. The estimation process can be viewed as a switched system, where performance and robustness depend on the underlying observer structure and its interaction with the plant dynamics. The robustness analysis carried out in this chapter aligns with the switched-system concepts introduced in Chapter 3, where different estimation dynamics correspond to different subsystems whose properties must be assessed under parameter variations and uncertainties.

9.4 Experiments

In this section, the proposed sensorless estimation strategies are validated through numerical simulations. The objective is to evaluate their performance in the specific application of exhaust gas energy recovery, where the PMSM operates at very high speeds and under variable turbine operating conditions. The experimental study has been designed with the following goals:

- to verify the effectiveness of the MRAS observer and EKF estimator in reproducing the rotor speed;

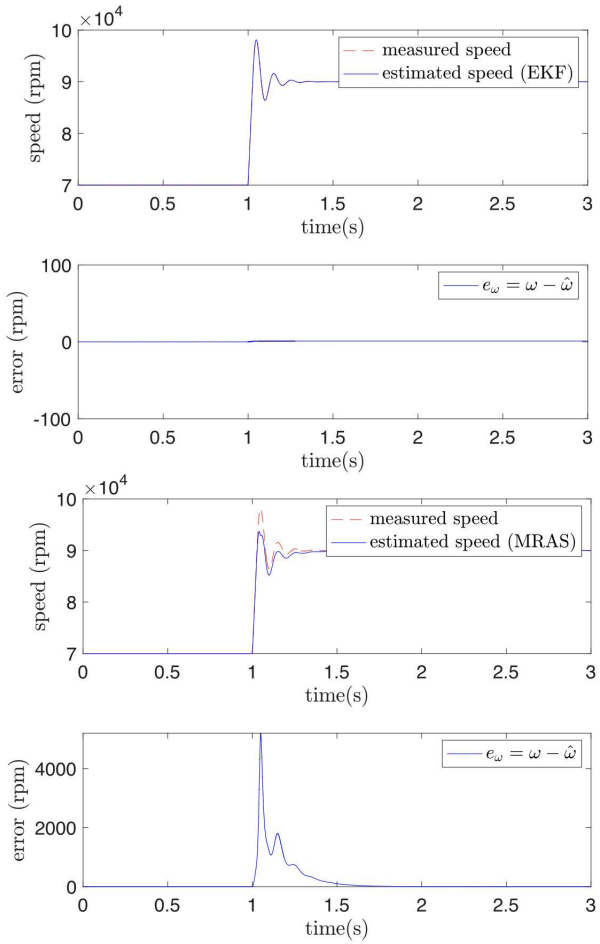

Figure 9.6: Reference and estimated speed as well as estimation error using EKF, and MRAS, corresponding to the test of Fig. 9.5.

- to highlight their strengths and limitations in terms of dynamic response, steady-state accuracy, and robustness;
- to investigate the impact of the parameter variations and measurement noise;
- to assess the computational requirements of both approaches.

All these characteristics make it possible to define the best estimator to apply for exhaust gas energy recovery in ICE.

9.4.1 Simulation setup

The proposed MRAS observer and EKF estimator were implemented and tested in MATLAB/Simulink to evaluate their performance in high-speed PMSM applications for exhaust gas energy recovery. The simulation platform included the complete drive system, including the PMSM model, the turbine, the FOC scheme, and the two sensorless estimators. The nominal parameters of the implemented PMSM are given in Table 9.1. Different turbine operating points and speed transients have been tested to reproduce realistic working conditions The system was tested under four turbine operating conditions

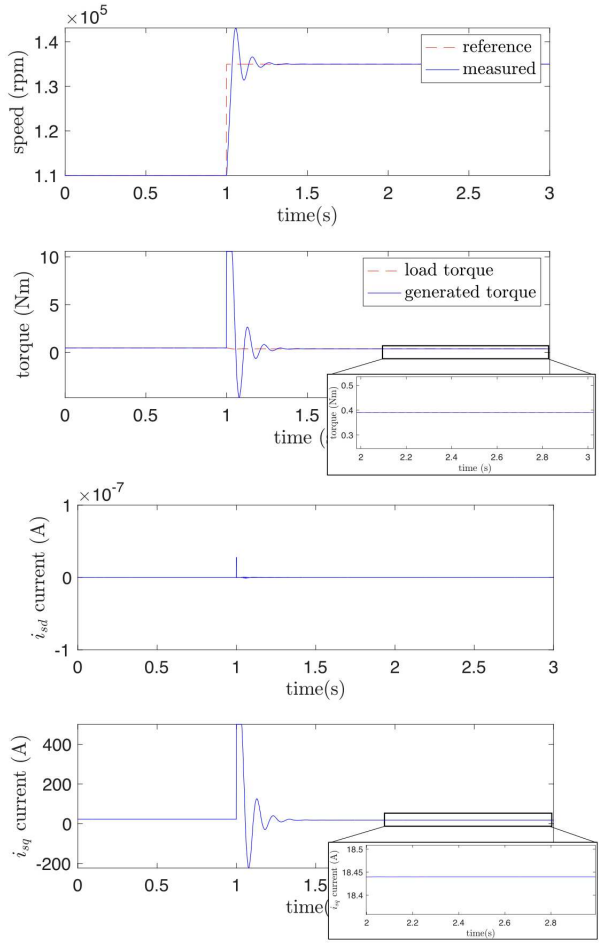

Figure 9.7: Motor speed ω and torque generated by the motor, and stator current along *d-q* axis, for the nozzle angle equal to 5.44 during a step variation of the reference speed of the motor from 110 to 135 krpm.

corresponding to nozzle angles of 4.27, 5.44, 6.98, and 10.52 degrees. Fig. 9.4 shows the turbine's torque-speed characteristics for the nozzle angles. These waveforms represent the function $\eta(\omega)$ in equation (9.1c), and they were obtained considering, for each nozzle blade position, constant pressure and temperature at the turbine inlet. The turbine outlet pressure was supposed to be 1.05 bar independently of the operating conditions (see Table 9.2). The PI controllers of the FOC are tuned with the following parameters: the proportional and integral constants of the inner loop PI controllers are selected equal to 100 and 6000, respectively, while the parameters of the speed PI controller are equal to 0.2 (proportional constant) and 25 (integral constant). The sampling frequency for both estimators was initially set to $5MHz$ and gradually reduced to determine the minimum sampling frequency for each estimator. For the MRAS observer, $K_p = 20$ and $K_i = 200$ are chosen for the PI-based adaptation mechanism. Both the EKF estimator and the MRAS observer were simulated under the same environment and conditions, with zero-mean white noise affecting the inputs. The EKF implementation required careful parametrization of the covariance matrices of the observation noise R, process

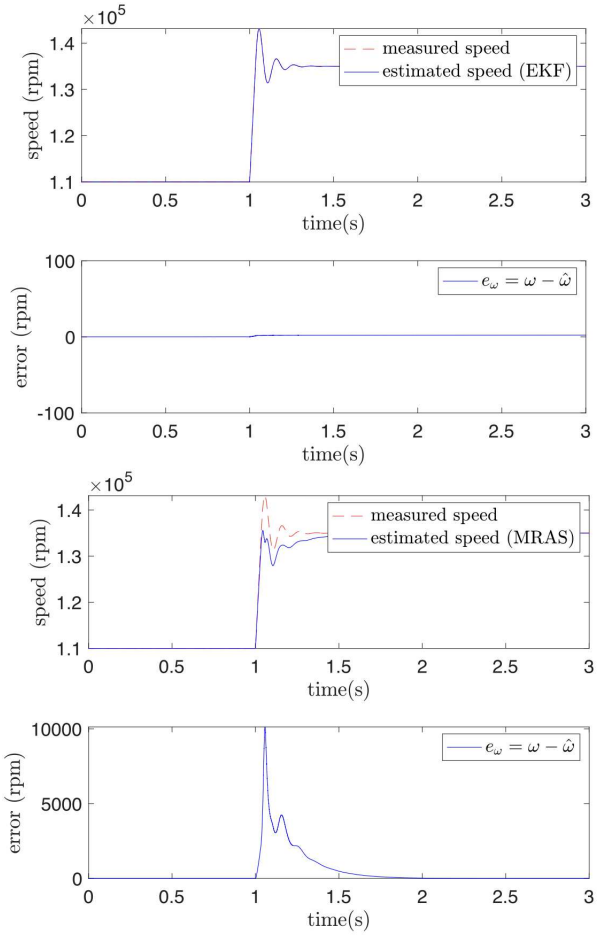

Figure 9.8: Reference and estimated speed as well as estimation error using EKF, and MRAS, corresponding to the test of Fig. 9.7.

noise Q, and the initial estimation error covariance matrix P_0. In the literature, the values of the matrices Q and R are often computed through a trial-and-error procedure [142], aiming to minimize the estimation error. This procedure was also used in this case. Specifically, $P_0 = \text{diag}\{2, 2, 0.05, 1\}$, $R = \text{diag}\{4, 4\}$, and $Q = \text{diag}\{40^3, 40^3, 40^4\}$ were found to provide satisfactory performance for this application.

9.4.2 Experimental results

The performance of both estimators was analyzed during step variations of the motor reference speed for each nozzle angle. Fig. 9.5 shows the motor speed and the stator currents, i_{sd}, i_{sq}, for the nozzle angle equal to 4.27 during a step variation of the reference speed of the motor from 70 to 92.5 krpm. Fig. 9.6 shows the estimated speed as long as the estimation error using EKF (upper plot) and MRAS (bottom plot). Both estimators successfully tracked the motor speed, but the EKF exhibited superior transient performance with near-zero error due to its automatically optimized gain, while the MRAS bandwidth was limited by its adaptation mechanism. This is confirmed by the integral absolute error (IAE) indexes reported in Table 9.3. Figures 9.7 and 9.8 show

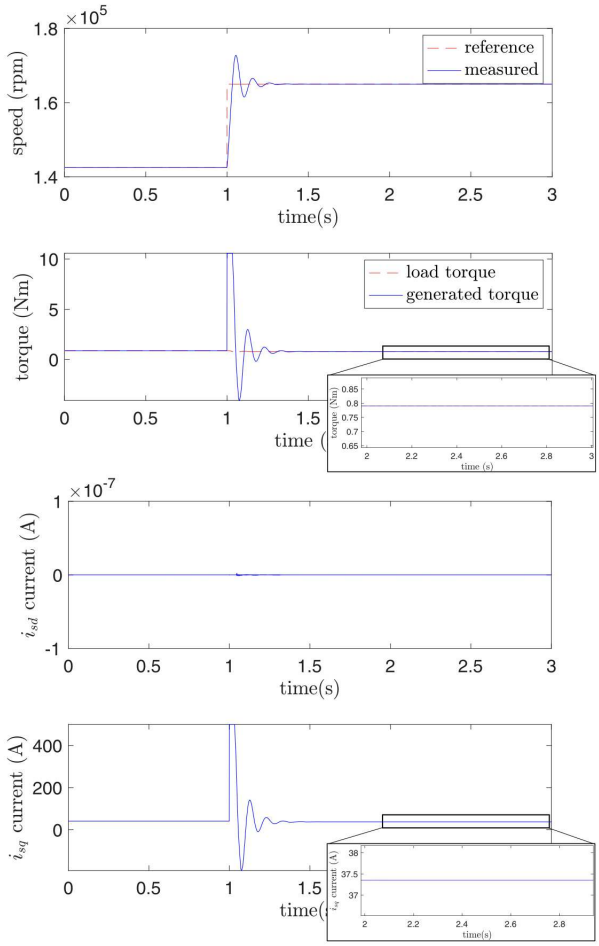

Figure 9.9: Motor speed ω and torque generated by the motor, and stator current along *d-q* axis, for the nozzle angle equal to 6.98 during a step variation of the reference speed of the motor from 143 to 168 krpm.

identical waveforms, but for a nozzle angle of 5.44 and a step variation of the reference speed of the motor from 107.5 to 140 krpm. In Figures 9.9 and 9.10, the nozzle angle is set equal to 6.98, and a step variation of the reference speed of the motor from 140 to 167.5 krpm is considered. Finally, the last test is shown in Figures 9.11 and 9.12 where the nozzle angle is set equal to 10.52 and the step variation of the reference speed of the motor is from 140 to 170 krpm. In all cases, both EKF and MRAS were capable of following the speed reference, although estimation errors increased with higher nozzle angles. Table 9.3 indicates that this error increment is, in percentage terms, almost the same for the two estimators, while the absolute value is significantly higher in MRAS than in EKF. This means that very high speeds are critical for MRAS, while in the EKF, it does not represent a problem.

9.4.3 Robustness and sensitivity analysis

To evaluate the robustness of the proposed estimators against parameter variations, simulations were carried out by detuning the parameters of EKF and MRAS. Specifically,

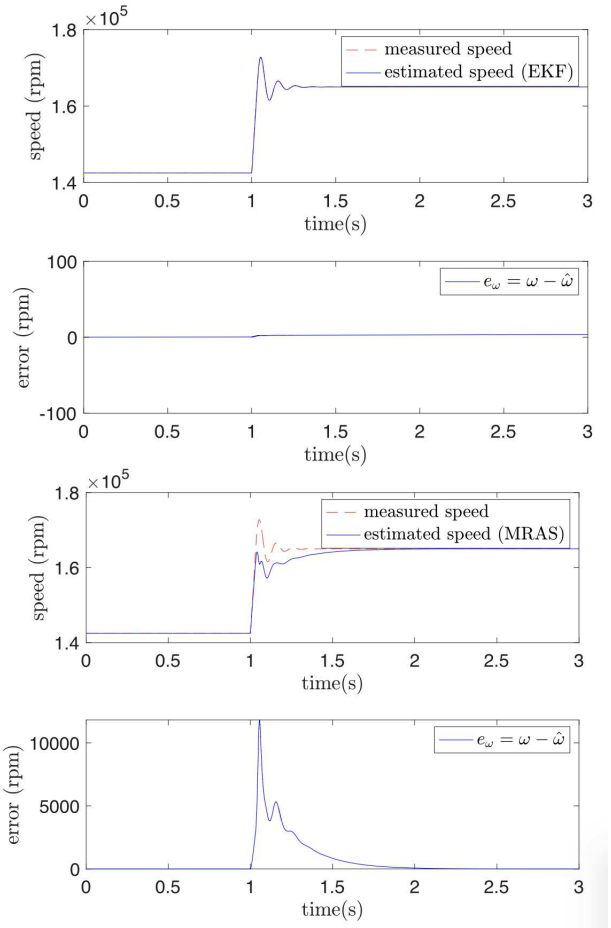

Figure 9.10: Reference and estimated speed as well as estimation error using EKF, and MRAS, corresponding to the test of Fig. 9.9.

the stator resistance R_s and the moment of inertia J are varied within ±20%. Indeed, the stator resistance could vary with the temperature, and the inertia could vary with the gas density. These tests were conducted under the third turbine operating condition, corresponding to a nozzle angle of 6.98 degrees. Figures 9.13 and 9.14 show the results of these simulations. Fig. 9.13 corresponds to a 20% decrement of R_s and J, while Fig. 9.14 shows a 20% increase. The results demonstrate that both estimators maintain effective speed estimation even under parameter variations, confirming the robustness of both methods. Comparing the two estimators, the EKF exhibits better transient performance due to its ability to automatically optimize the gain, whereas the MRAS bandwidth is limited by the PI-based adaptation mechanism. On the other hand, the MRAS presents almost zero steady-state error, while the EKF shows a small steady-state error of approximately 3%. These observations indicate that MRAS is more robust than EKF with respect to parameter variations, although EKF excels during transient response.

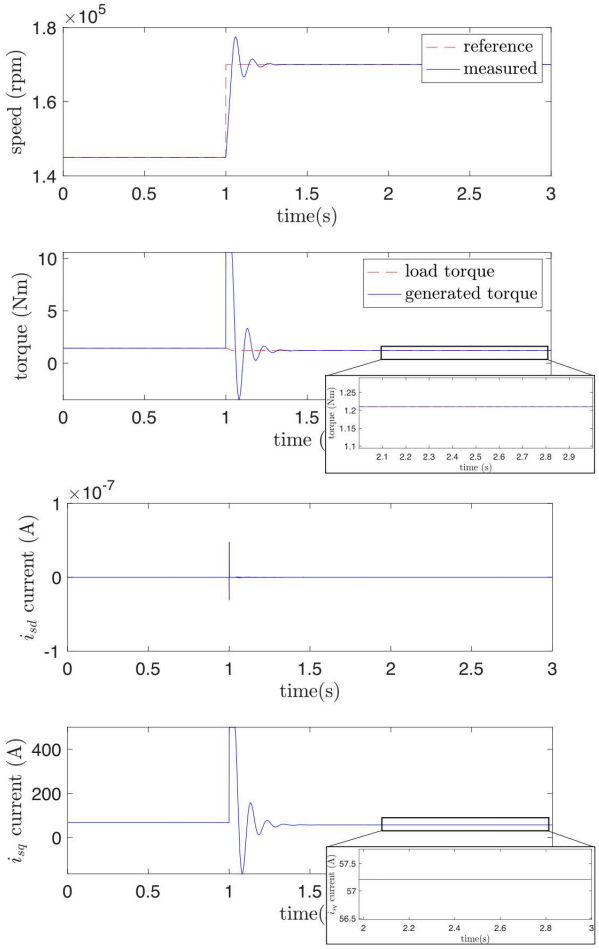

Figure 9.11: Motor speed ω and torque generated by the motor, and stator current along d-q axis, for the nozzle angle equal to 10.52 during a step variation of the reference speed of the motor from 145 to 170 krpm.

9.4.4 Computational load

The computational requirements of both estimators were analyzed by progressively reducing the sampling frequency from the initial $5MHz$ to determine the minimum frequency allowing correct operation. For the MRAS observer, the minimum acceptable sampling frequency was found to be $5MHz$; lower frequencies resulted in insufficient dynamics during step changes in the motor speed. In contrast, the EKF remained stable even at a minimum sampling frequency of $20kHz$, significantly lower than for MRAS. However, the computational load for each step is much more significant in the EKF than in MRAS since the MRAS's structure is simple and requires few calculations. In contrast, the EKF requires heavy calculations that embed matrix products and inverses. This means that even if the minimum sampling frequency achievable with EKF is lower than MRAS, they are almost equivalent from the computational load point of view.

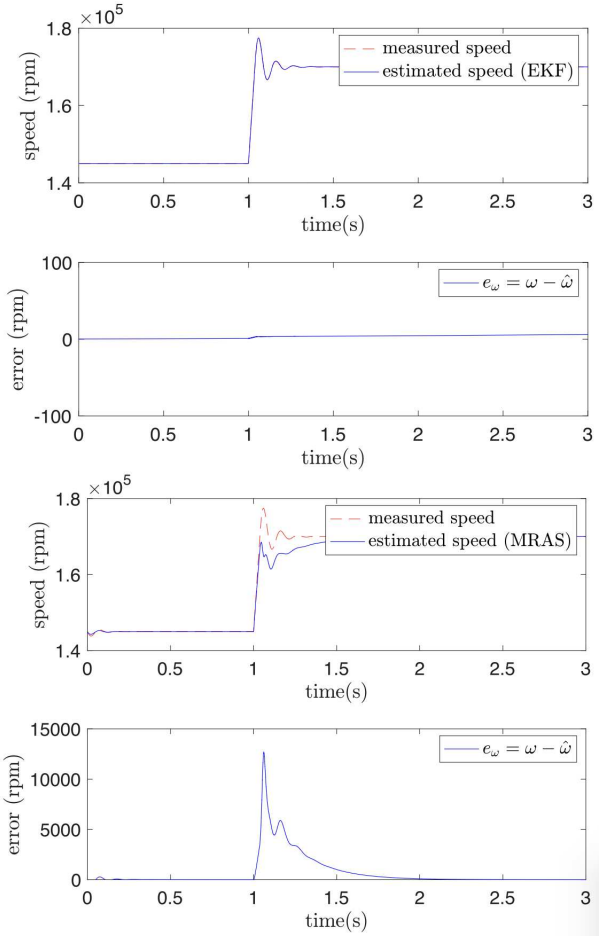

Figure 9.12: Reference and estimated speed as well as estimation error using EKF, and MRAS, corresponding to the test of Fig. 9.11.

9.5 Summary

This chapter has presented the design, implementation, and simulation-based validation of two sensorless speed estimator strategies for a high-speed PMSM employed in exhaust gas energy recovery applications. The proposed approaches, based on an MRAS observer and EKF estimator, have been analyzed in terms of dynamic response, steady-state accuracy, robustness to parameter variations, and computational load. A complete simulation platform was developed in MATLAB/Simulink, including the PMSM model, the turbine system, the FOC scheme, and the two estimators. Numerical results demonstrate that both estimators are capable of accurately reproducing the rotor speed across different turbine operating conditions. The EKF exhibits superior transient performance due to its automatically optimized gain, while MRAS provides excellent steady-state accuracy and robustness against parameter variations. Sensitivity analyses confirm that both methods maintain effective operation under significant variations of stator resistance and rotor inertia. Regarding computational requirements, EKF requires more intensive calculations but can operate at lower sampling frequencies, whereas MRAS requires a higher sampling frequency but simpler computations. Overall, the simulation results indicate that both

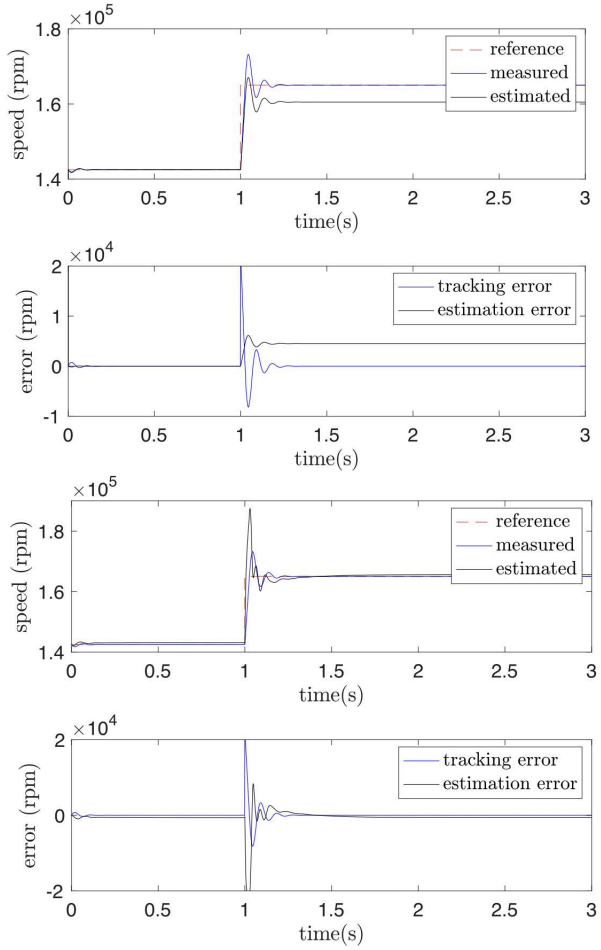

Figure 9.13: EKF and MRAS responses when R_s and J are decreased by 20%, for the third operating condition.

EKF and MRAS are suitable for sensorless speed estimation in high-speed PMSM drives, with the EKF being preferable for fast transient tracking and MRAS offering robustness and minimal steady-state error. This chapter confirms that the proposed estimation strategies can be successfully applied in the context of exhaust energy recovery, providing reliable and efficient rotor speed estimation under realistic operating conditions.

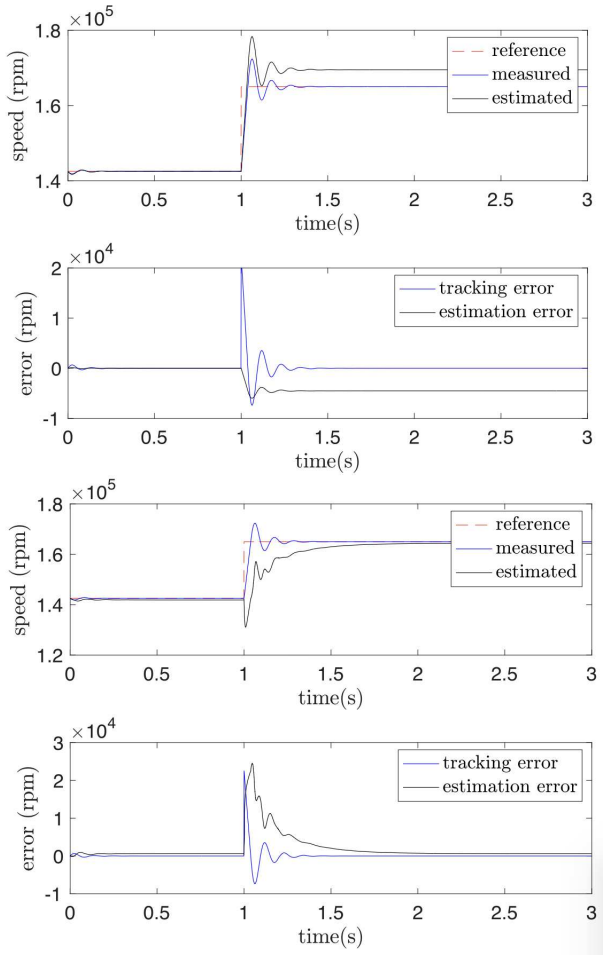

Figure 9.14: EKF and MRAS responses when R_s and J are increased by 20%, for the third operating condition.

Conclusions

Chapter 10

Conclusions and future perspectives

10.1 Conclusions

This thesis focused on the study, modeling, and control of hybrid dynamical systems and switched systems, with specific applications in the field of power electronics and electric drives. The introduction of hybrid and robust control frameworks in these domains is motivated by:

- their ability to capture the intrinsic mixed continuous-discrete nature of power converters and electrical machines;
- the possibility of improving classical continuous-time controllers in terms of robustness, efficiency, and adaptability.

The main conclusions related to the contributions of this dissertation are summarized below.

10.1.1 Theoretical foundations of hybrid and switched systems

In Part I, the theoretical framework of hybrid and switched systems was introduced, and their modeling, solutions, and stability properties were analyzed. Lyapunov-based methods were emphasized for stability, providing a solid foundation for the subsequent control strategies. The study of stability under arbitrary and constrained switching highlighted the importance of tailored switching laws to guarantee robustness and performance. This section establishes the mathematical and conceptual tools required for the practical designs developed later in the thesis.

10.1.2 Applications in power electronics

Part II focused on hybrid control strategies for DC-DC and multi-input converters. In Chapter 4, min-type hybrid controllers were designed for boost converters, with their performance analyzed through mathematical modeling, simulation, and experiments. The hybrid control with hysteresis and minimum dwell-time implementation demonstrated improved robustness and efficiency compared to conventional controllers. Chapter 5 extended these ideas to multi-input converters by introducing a dynamic input allocation strategy. The hybrid min-type control law enabled flexible equilibrium selection and robust stability guarantees. Both simulation and experimental validation confirmed the effectiveness of the proposed strategies. Chapter 6 presented an advanced nonlinear robust control scheme for a DC/AC inverter, combining a disturbance observer, SMC,

and ADRC. This strategy significantly enhanced robustness against model uncertainties and disturbances, with validation through both simulations and experiments.

10.1.3 Applications in electric drives

In Part III, the proposed control strategies were applied to electric drives. Chapter 7 introduced adaptive robust nonlinear controllers for induction motors, demonstrating their ability to ensure stability and robustness under parameter uncertainties and external disturbances. Unknown input observers enabled accurate disturbance estimation and compensation. Chapter 8 addressed dual three-phase induction motors, designing a dynamic input allocation scheme to reduce harmonic losses. Experimental validation confirmed improvements in efficiency and current quality. Chapter 9 studied sensorless control of high-speed PMSM for energy recovery applications. Different observer-based strategies (MRAS, EKF) were compared, with analyses focusing on robustness and computational complexity.

The above case studies demonstrate the practical potential of hybrid control strategies. The overall contributions of this thesis can be summarized as follows:

- establishment of a systematic link between the theoretical hybrid system framework and practical applications in power electronics and drives;
- design of novel hybrid and robust control laws, validated through simulations and experimental prototypes;
- demonstration of improved robustness, efficiency, and adaptability compared to traditional control methods;
- extension of hybrid approaches to multi-input systems and sensorless motor drives, opening new perspectives for future control architectures.

10.2 Future perspectives

Although this thesis presents significant contributions, several directions remain open for further research:

- Hybrid control design: min-type and hysteresis-based hybrid control strategies could be extended to more complex topologies (e.g., multi-level converters, modular power electronics architectures);
- Predictive and data-driven methods: integration of hybrid control with MPC or learning-based methods could enhance adaptability in real-time applications;
- Scalability and networks: future work may explore the extension of hybrid approaches to interconnected systems such as microgrids, distributed energy resources, or coordinated multi-motor drives;

- Sensorless and fault-tolerant strategies: the development of advanced observer-based and fault-tolerant hybrid controllers will be crucial for safety-critical applications, especially in electric mobility and renewable energy systems;
- Experimental validation: while this work provides experimental evidence, large-scale and industrial-level testing is necessary to fully assess the practical feasibility of the proposed approaches.

10.3 Final comments

Most control problems in power electronics and electric drives are traditionally studied using either continuous-time or discrete-time approaches. The hybrid systems framework, enhanced with robust and adaptive techniques, demonstrates a powerful alternative capable of addressing the unique challenges of these systems. Although contributions are presented across different case studies, the results highlight the versatility and effectiveness of hybrid control methods. This work indicates that hybrid dynamical systems are not only a theoretical tool but also a practical and valuable approach for the design of next-generation control strategies in energy conversion and electric drive applications.

References

[1] Goebel, R., Sanfelice, R. G., and Teel, A. R., "Hybrid dynamical systems," *IEEE control systems magazine*, vol. 29, no. 2, pp. 28–93, 2009.

[2] Liberzon, D., *Switching in systems and control*. Springer, 2003, vol. 190.

[3] Goebel, R., Sanfelice, R., and Teel, A., *Hybrid dynamical systems: Modeling, stability, and robustness. 41 william street*, 2012.

[4] Lygeros, J., Johansson, K. H., Simic, S. N., Zhang, J., and Sastry, S. S., "Dynamical properties of hybrid automata," *IEEE Transactions on automatic control*, vol. 48, no. 1, pp. 2–17, 2003.

[5] Branicky, M. S., "Multiple lyapunov functions and other analysis tools for switched and hybrid systems," *IEEE Transactions on automatic control*, vol. 43, no. 4, pp. 475–482, 2002.

[6] Leine, R. I. and Nijmeijer, H., *Dynamics and bifurcations of non-smooth mechanical systems*. Springer Science & Business Media, 2013, vol. 18.

[7] Van Der Schaft, A. J. and Schumacher, H., *An introduction to hybrid dynamical systems*. springer, 2007, vol. 251.

[8] Nešić, D. and Teel, A. R., "Input-to-state stability of networked control systems," *Automatica*, vol. 40, no. 12, pp. 2121–2128, 2004.

[9] Sastry, S., *Nonlinear systems: analysis, stability, and control*. Springer Science & Business Media, 2013, vol. 10.

[10] Lunze, J. and Lamnabhi-Lagarrigue, F., *Handbook of hybrid systems control: theory, tools, applications*. Cambridge University Press, 2009.

[11] Liberzon, D. and Morse, A. S., "Basic problems in stability and design of switched systems," *IEEE control systems magazine*, vol. 19, no. 5, pp. 59–70, 2002.

[12] Åström, K. J. and Wittenmark, B., *Computer-controlled systems: theory and design*. Courier Corporation, 2013.

[13] Hespanha, J. P., "Uniform stability of switched linear systems: Extensions of lasalle's invariance principle," *IEEE transactions on Automatic Control*, vol. 49, no. 4, pp. 470–482, 2004.

[14] Filippov, A. F., "Differential equations with discontinuous right-hand side," *Matematicheskii sbornik*, vol. 93, no. 1, pp. 99–128, 1960.

[15] Clarke, F. H., Ledyaev, Y. S., Stern, R. J., and Wolenski, P. R., *Nonsmooth analysis and control theory*. Springer Science & Business Media, 2008, vol. 178.

[16] Johansson, M. K.-J., *Piecewise linear control systems: a computational approach*. Springer, 2003, vol. 284.

[17] Shorten, R., Wirth, F., Mason, O., Wulff, K., and King, C., "Stability criteria for switched and hybrid systems," *SIAM review*, vol. 49, no. 4, pp. 545–592, 2007.

[18] Hespanha, J. P. and Morse, A. S., "Stability of switched systems with average dwell-time," in *Proceedings of the 38th IEEE conference on decision and control (Cat. No. 99CH36304)*, IEEE, vol. 3, 1999, pp. 2655–2660.

[19] Lan, Y.-H., Gu, H.-B., Chen, C.-X., Zhou, Y., and Luo, Y.-P., "An indirect lyapunov approach to the observer-based robust control for fractional-order complex dynamic networks," *Neurocomputing*, vol. 136, pp. 235–242, 2014.

[20] Sontag, E. D. and Wang, Y., "On characterizations of the input-to-state stability property," *Systems & Control Letters*, vol. 24, no. 5, pp. 351–359, 1995.

[21] Morse, A., "Supervisory control of families of linear set-point controllers," in *Proceedings of 32nd IEEE Conference on Decision and Control*, IEEE, 1993, pp. 1055–1060.

[22] DeCarlo, R. A., Branicky, M. S., Pettersson, S., and Lennartson, B., "Perspectives and results on the stability and stabilizability of hybrid systems," *Proceedings of the IEEE*, vol. 88, no. 7, pp. 1069–1082, 2002.

[23] Mohan, N., Undeland, T. M., and Robbins, W. P., *Power electronics: converters, applications, and design*. John wiley & sons, 2003.

[24] Erickson, R. W. and Maksimovic, D., *Fundamentals of power electronics*. Springer Science & Business Media, 2007.

[25] Khalil, H. K. and Grizzle, J. W., *Nonlinear systems*. Prentice hall Upper Saddle River, NJ, 2002, vol. 3.

[26] Sferlazza, A., Albea-Sanchez, C., Martinez-Salamero, L., Garcia, G., and Alonso, C., "Min-type control strategy of a dc–dc synchronous boost converter," *IEEE Transactions on Industrial Electronics*, vol. 67, no. 4, pp. 3167–3179, 2019.

[27] Redl, R. and Sokal, N. O., "Current-mode control, five different types, used with the three basic classes of power converters: Small-signal ac and large-signal dc characterization, stability requirements, and implementation of practical circuits," in *1985 IEEE Power Electronics Specialists Conference*, IEEE, 1985, pp. 771–785.

[28] Qiu, Y., Chen, X., and Liu, H., "Digital average current-mode control using current estimation and capacitor charge balance principle for dc–dc converters operating in dcm," *IEEE Transactions on Power Electronics*, vol. 25, no. 6, pp. 1537–1545, 2010.

[29] Vidal-Idiarte, E., Marcos-Pastor, A., Garcia, G., Cid-Pastor, A., and Martinez-Salamero, L., "Discrete-time sliding-mode-based digital pulse width modulation control of a boost converter," *IET Power Electronics*, vol. 8, no. 5, pp. 708–714, 2015.

[30] Deaecto, G. S., Geromel, J. C., Garcia, F. S., and Pomilio, J. A., "Switched affine systems control design with application to dc–dc converters," *IET control theory & applications*, vol. 4, no. 7, pp. 1201–1210, 2010.

[31] Theunisse, T. A., Chai, J., Sanfelice, R. G., and Heemels, W. M. H., "Robust global stabilization of the dc-dc boost converter via hybrid control," *IEEE Transactions on Circuits and Systems I: Regular Papers*, vol. 62, no. 4, pp. 1052–1061, 2017.

[32] Martínez-Salamero, L., García, G., Orellana, M., Lahore, C., and Estibals, B., "Start-up control and voltage regulation in a boost converter under sliding-mode operation," *IEEE Transactions on industrial electronics*, vol. 60, no. 10, pp. 4637–4649, 2012.

[33] Martinez-Salamero, L., Cid-Pastor, A., El Aroudi, A., Giral, R., Calvente, J., and Ruiz-Magaz, G., "Sliding-mode control of dc-dc switching converters," *IFAC Proceedings Volumes*, vol. 44, no. 1, pp. 1910–1916, 2011.

[34] Bosque-Moncusi, J. M., Valderrama-Blavi, H., Flores-Bahamonde, F., Vidal-Idiarte, E., and Martínez-Salamero, L., "Using low-cost microcontrollers to implement variable hysteresis-width comparators for switching power converters," *IET Power Electronics*, vol. 11, no. 5, pp. 787–795, 2018.

[35] Albea, C., Garcia, G., and Zaccarian, L., "Hybrid dynamic modeling and control of switched affine systems: Application to dc-dc converters," in *2015 54th IEEE Conference on Decision and Control (CDC)*, IEEE, 2015, pp. 2264–2269.

[36] Sanchez, C. A., Garcia, G., Hadjeras, S., Heemels, W. M. H., and Zaccarian, L., "Practical stabilization of switched affine systems with dwell-time guarantees," *IEEE Transactions on Automatic Control*, vol. 64, no. 11, pp. 4811–4817, 2019.

[37] Sortomme, E. and El-Sharkawi, M., "Optimal power flow for a system of microgrids with controllable loads and battery storage," in *2009 IEEE/PES Power Systems Conference and Exposition*, IEEE, 2009, pp. 1–5.

[38] Farhadi, M. and Mohammed, O., "Energy storage technologies for high-power applications," *IEEE Transactions on Industry Applications*, vol. 52, no. 3, pp. 1953–1961, 2015.

[39] Justo, J. J., Mwasilu, F., Lee, J., and Jung, J.-W., "Ac-microgrids versus dc-microgrids with distributed energy resources: A review," *Renewable and sustainable energy reviews*, vol. 24, pp. 387–405, 2013.

[40] Fontes, G., Turpin, C., Astier, S., and Meynard, T. A., "Interactions between fuel cells and power converters: Influence of current harmonics on a fuel cell stack," *IEEE Transactions on Power Electronics*, vol. 22, no. 2, pp. 670–678, 2007.

[41] Aman, S., Simmhan, Y., and Prasanna, V. K., "Energy management systems: State of the art and emerging trends," *IEEE communications Magazine*, vol. 51, no. 1, pp. 114–119, 2013.

[42] Chaouachi, A., Kamel, R. M., Andoulsi, R., and Nagasaka, K., "Multiobjective intelligent energy management for a microgrid," *IEEE transactions on Industrial Electronics*, vol. 60, no. 4, pp. 1688–1699, 2012.

[43] Li, Z., Onar, O., Khaligh, A., and Schaltz, E., "Design and control of a multiple input dc/dc converter for battery/ultra-capacitor based electric vehicle power system," in *2009 Twenty-Fourth Annual IEEE Applied Power Electronics Conference and Exposition*, IEEE, 2009, pp. 591–596.

[44] Di Napoli, A., Crescimbini, F., Capponi, F. G., and Solero, L., "Control strategy for multiple input dc-dc power converters devoted to hybrid vehicle propulsion systems," in *Industrial electronics, 2002. isie 2002. proceedings of the 2002 ieee international symposium on*, IEEE, vol. 3, 2002, pp. 1036–1041.

[45] Chen, Y.-M., Liu, Y.-C., and Wu, F.-Y., "Multi-input dc/dc converter based on the multiwinding transformer for renewable energy applications," *IEEE transactions on industry applications*, vol. 38, no. 4, pp. 1096–1104, 2002.

[46] Zaccarian, L., "On dynamic control allocation for input-redundant control systems," in *2007 46th IEEE Conference on Decision and Control*, IEEE, 2007, pp. 1192–1197.

[47] Zaccarian, L., "Dynamic allocation for input redundant control systems," *Automatica*, vol. 45, no. 6, pp. 1431–1438, 2009.

[48] Sira-Ramirez, H., "Flatness and trajectory tracking in sliding mode based regulation of dc-to-ac conversion schemes," in *Proceedings of the 38th IEEE Conference on Decision and Control (Cat. No. 99CH36304)*, IEEE, vol. 5, 1999, pp. 4268–4273.

[49] Caceres, R. and Barbi, I., "A boost dc-ac converter: Operation, analysis, control and experimentation," in *Proceedings of IECON'95-21st Annual Conference on IEEE Industrial Electronics*, IEEE, vol. 1, 1995, pp. 546–551.

[50] Sanchis, P., Ursæa, A., Gubía, E., and Marroyo, L., "Boost dc-ac inverter: A new control strategy," *IEEE Transactions on power electronics*, vol. 20, no. 2, pp. 343–353, 2005.

[51] Jha, K., Mishra, S., and Joshi, A., "High-quality sine wave generation using a differential boost inverter at higher operating frequency," *IEEE Transactions on Industry Applications*, vol. 51, no. 1, pp. 373–384, 2014.

[52] Caceres, R. O. and Barbi, I., "A boost dc-ac converter: Analysis, design, and experimentation," *IEEE transactions on power electronics*, vol. 14, no. 1, pp. 134–141, 2002.

[53] Cortes, D., Vázquez, N., and Alvarez-Gallegos, J., "Dynamical sliding-mode control of the boost inverter," *IEEE Transactions on Industrial Electronics*, vol. 56, no. 9, pp. 3467–3476, 2008.

[54] Lopez-Caiza, D., Flores-Bahamonde, F., Kouro, S., Santana, V., Müller, N., and Chub, A., "Sliding mode based control of dual boost inverter for grid connection," *Energies*, vol. 12, no. 22, p. 4241, 2019.

[55] Qi, Q., Ghaderi, D., and Guerrero, J. M., "Sliding mode controller-based switched-capacitor-based high dc gain and low voltage stress dc-dc boost converter for photovoltaic applications," *International Journal of Electrical Power & Energy Systems*, vol. 125, p. 106 496, 2021.

[56] Deo, R. N., Shrivastava, A., and Chatterjee, K., "Implementation of sliding mode backstepping controller for boost converter in real-time for led application," *Expert Systems*, vol. 40, no. 6, e13095, 2023.

[57] Mohammadhassani, F. and Narm, H. G., "Dynamic sliding mode control of single-stage boost inverter with parametric uncertainties and delay," *IET Power Electronics*, vol. 14, no. 12, pp. 2127–2138, 2021.

[58] Musona, R. and Serban, I., "Differential single-phase inverters with active power decoupling: A survey," *IEEE Access*, vol. 11, pp. 53 654–53 670, 2023.

[59] Seo, S.-W. and Choi, H. H., "Digital implementation of fractional order pid-type controller for boost dc–dc converter," *IEEE Access*, vol. 7, pp. 142 652–142 662, 2019.

[60] Pereira, L. F. d. S., Batista, E., Brito, M. A. de, and Godoy, R. B., "A robustness analysis of a fuzzy fractional order pid controller based on genetic algorithm for a dc-dc boost converter," *Electronics*, vol. 11, no. 12, p. 1894, 2022.

[61] Caceres, R. O. and Barbi, I., "A boost dc-ac converter: Analysis, design, and experimentation," *IEEE transactions on power electronics*, vol. 14, no. 1, pp. 134–141, 1999.

[62] Cortes, D., Vázquez, N., and Alvarez-Gallegos, J., "Dynamical sliding-mode control of the boost inverter," *IEEE Transactions on Industrial Electronics*, vol. 56, no. 9, pp. 3467–3476, 2009.

[63] Flores-Bahamonde, F., Valderrama-Blavi, H., Bosque-Moncusi, J. M., García, G., and Martínez-Salamero, L., "Using the sliding-mode control approach for analysis and design of the boost inverter," *IET Power Electronics*, vol. 9, no. 8, pp. 1625–1634, 2016.

[64] Ahmad, S. and Ali, A., "Active disturbance rejection control of dc–dc boost converter: A review with modifications for improved performance," *IET Power Electronics*, vol. 12, no. 8, pp. 2095–2107, 2019.

[65] Zhuo, S., Gaillard, A., Guo, L., Xu, L., Paire, D., and Gao, F., "Active disturbance rejection voltage control of a floating interleaved dc–dc boost converter with switch fault consideration," *IEEE Transactions on Power Electronics*, vol. 34, no. 12, pp. 12 396–12 406, 2019.

[66] Zhou, X., Liu, Q., Ma, Y., and Xie, B., "Dc-link voltage research of photovoltaic grid-connected inverter using improved active disturbance rejection control," *IEEE Access*, vol. 9, pp. 9884–9894, 2021.

[67] Zhuo, S., Gaillard, A., Xu, L., Bai, H., Paire, D., and Gao, F., "Enhanced robust control of a dc–dc converter for fuel cell application based on high-order extended state observer," *IEEE Transactions on Transportation Electrification*, vol. 6, no. 1, pp. 278–287, 2020.

[68] Middlebrook, R. D. and Cuk, S., "A general unified approach to modelling switching-converter power stages," in *1976 IEEE power electronics specialists conference*, IEEE, 1976, pp. 18–34.

[69] Tan, S.-C., Lai, Y., and Tse, C. K., "Implementation of pulse-width-modulation based sliding mode controller for boost converters," *IEEE Power Electronics Letters*, vol. 3, no. 4, pp. 130–135, 2005.

[70] Gehan, O. et al., "A nonlinear state feedback for dc/dc boost converters," *Journal of Dynamic Systems, Measurement, and Control*, vol. 139, no. 1, 2017.

[71] Shtessel, Y. B., Zinober, A. S., and Shkolnikov, I. A., "Sliding mode control of boost and buck-boost power converters using method of stable system centre," *Automatica*, vol. 39, no. 6, pp. 1061–1067, 2003.

[72] Slotine, J.-J. E., Li, W., et al., *Applied nonlinear control*. Prentice hall Englewood Cliffs, NJ, 1991, vol. 199.

[73] Vas, P., *Sensorless vector and direct torque control*. Oxford university press Oxford, UK, 1998.

[74] Cirrincione, M., Pucci, M., and Vitale, G., *Power converters and AC electrical drives with linear neural networks*. CRC Press, 2017.

[75] Marino, R., Tomei, P., and Verrelli, C. M., *Induction motor control design*. Springer, 2010.

[76] Accetta, A., Cirrincione, M., Pucci, M., and Sferlazza, A., "Feedback linearization based nonlinear control of synrm drives accounting for self-and cross-saturation," *IEEE Transactions on Industry Applications*, vol. 58, no. 3, pp. 3637–3651, 2022.

[77] De Luca, A. and Ulivi, G., "Design of an exact nonlinear controller for induction motors," *Automatic Control, IEEE Transactions on*, vol. 34, no. 12, pp. 1304–1307, 1989.

[78] Kim, D.-I., HA, I.-J., and KO, M.-S., "Control of induction motors via feedback linearization with input-output decoupling," *International Journal of Control*, vol. 51, no. 4, pp. 863–883, 1990.

[79] Accetta, A. et al., "Robust control for high performance induction motor drives based on partial state-feedback linearization," *IEEE Transactions on Industry Applications*, vol. 55, no. 1, pp. 490–503, 2018.

[80] Accetta, A., Alonge, F., Cirrincione, M., Pucci, M., and Sferlazza, A., "Feedback linearizing control of induction motor considering magnetic saturation effects," *IEEE Transactions on Industry Applications*, vol. 52, no. 6, pp. 4843–4854, 2016.

[81] Alonge, F., Cirrincione, M., Pucci, M., and Sferlazza, A., "Input-output feedback linearization control with on-line MRAS based inductor resistance estimation of linear induction motors including the dynamic end-effects," *Industry Applications, IEEE Transactions on*, vol. 52, no. 1, pp. 254–266, 2016.

[82] Marino, R., Peresada, S., and Valigi, P., "Adaptive input-output linearizing control of induction motors," *Automatic Control, IEEE Transactions on*, vol. 38, no. 2, pp. 208–221, 1993.

[83] Alonge, F., Cirrincione, M., D'Ippolito, F., Pucci, M., and Sferlazza, A., "Adaptive feedback linearizing control of linear induction motor considering the end-effects," *Control Engineering Practice*, vol. 55, pp. 116–126, 2016.

[84] Gao, Z., Huang, Y., and Han, J., "An alternative paradigm for control system design," in *Decision and Control, 2001. Proceedings of the 40th IEEE Conference on*, IEEE, vol. 5, 2001, pp. 4578–4585.

[85] Han, J., "From PID to active disturbance rejection control," *Industrial Electronics, IEEE transactions on*, vol. 56, no. 3, pp. 900–906, 2009.

[86] Huang, Y. and Xue, W., "Active disturbance rejection control: Methodology and theoretical analysis," *ISA transactions*, vol. 53, no. 4, pp. 963–976, 2014.

[87] Guo, B.-Z. and Zhao, Z.-l., "On the convergence of an extended state observer for nonlinear systems with uncertainty," *Systems & Control Letters*, vol. 60, no. 6, pp. 420–430, 2011.

[88] Zhou, X., Cui, H., Ma, Y., and Gao, Z., "The research on energy conservation controller for asynchronous motor based on adrc," in *2017 29th Chinese Control And Decision Conference (CCDC)*, IEEE, 2017, pp. 4010–4014.

[89] Liu, C., Luo, G., Duan, X., Chen, Z., Zhang, Z., and Qiu, C., "Adaptive ladrc-based disturbance rejection method for electromechanical servo system," *IEEE Transactions on Industry Applications*, vol. 56, no. 1, pp. 876–889, 2019.

[90] Qu, L., Qiao, W., and Qu, L., "An enhanced linear active disturbance rejection rotor position sensorless control for permanent magnet synchronous motors," *IEEE Transactions on Power Electronics*, vol. 35, no. 6, pp. 6175–6184, 2019.

[91] Lin, P., Wu, Z., Liu, K.-Z., and Sun, X.-M., "A class of linear–nonlinear switching active disturbance rejection speed and current controllers for pmsm," *IEEE Transactions on Power Electronics*, vol. 36, no. 12, pp. 14 366–14 382, 2021.

[92] Tian, M., Wang, B., Yu, Y., Dong, Q., and Xu, D., "Discrete-time repetitive control-based adrc for current loop disturbances suppression of pmsm drives," *IEEE Transactions on Industrial Informatics*, vol. 18, no. 5, pp. 3138–3149, 2021.

[93] Zhang, Z., Chen, Y., Feng, X., Xie, S., and Zhao, C., "Linear active disturbance rejection speed control with variable gain load torque sliding mode observer for ipmsms," *Journal of Power Electronics*, vol. 22, no. 8, pp. 1290–1301, 2022.

[94] Alonge, F., Cirrincione, M., D'Ippolito, F., Pucci, M., and Sferlazza, A., "Robust active disturbance rejection control of induction motor systems based on additional sliding-mode component," *IEEE Transactions on Industrial Electronics*, vol. 64, no. 7, pp. 5608–5621, 2017.

[95] Marino, R., Peresada, S., and Valigi, P., "Adaptive input-output linearizing control of induction motors," *IEEE Transactions on Automatic control*, vol. 38, no. 2, pp. 208–221, 2002.

[96] De Luca, A. and Ulivi, G., "Design of an exact nonlinear controller for induction motors," *IEEE Transactions on Automatic Control*, vol. 34, no. 12, pp. 1304–1307, 2002.

[97] KIM, D.-I., HA, I.-J., and KO, M.-S., "Control of induction motors via feedback linearization with input-output decoupling," *International Journal of Control*, vol. 51, no. 4, pp. 863–883, 1990.

[98] Accetta, A., Di Piazza, M. C., Luna, M., and Pucci, M., "Electrical losses minimization of linear induction motors considering the dynamic end-effects," *IEEE Transactions on Industry Applications*, vol. 55, no. 2, pp. 1561–1573, 2018.

[99] Bojoi, R., Caponet, M. C., Grieco, G., Lazzari, M., Tenconi, A., and Profumo, F., "Computation and measurements of the dc link current in six-phase voltage source pwm inverters for ac motor drives," in *Proceedings of the Power Conversion Conference-Osaka 2002 (Cat. No. 02TH8579)*, IEEE, vol. 3, 2002, pp. 953–958.

[100] Pant GK Singh, V., "Analysis of a multiphase induction machine under fault condition in a phase-redundant ac drive system," *Electric Machines &Power Systems*, vol. 28, no. 6, pp. 577–590, 2000.

[101] Jahns, T. M., "Improved reliability in solid-state ac drives by means of multiple independent phase drive units," *IEEE Transactions on Industry Applications*, no. 3, pp. 321–331, 1980.

[102] Ferraris, P. and Lazzari, M., "Phase numbers and their related effects on the characteristics of inverter fed induction motor, drives," in *1983 Annual Meeting Industry Applications Society*, IEEE, 1983, pp. 494–502.

[103] Bojoi, R., Farina, F., Profumo, F., and Tenconi, A., "Dual-three phase induction machine drives control—a survey," *IEEJ Transactions on Industry Applications*, vol. 126, no. 4, pp. 420–429, 2006.

[104] Fortescue, C. L., "Method of symmetrical co-ordinates applied to the solution of polyphase networks," *Transactions of the American Institute of Electrical Engineers*, vol. 37, no. 2, pp. 1027–1140, 1918.

[105] Nelson, R. and Krause, P., "Induction machine analysis for arbitrary displacement between multiple winding sets," *IEEE Transactions on Power Apparatus and Systems*, no. 3, pp. 841–848, 2007.

[106] Ward, E. and Härer, H., "Preliminary investigation of an invertor-fed 5-phase induction motor," in *Proceedings of the Institution of Electrical Engineers*, IET, vol. 116, 1969, pp. 980–984.

[107] Abbas, M. A., Christen, R., and Jahns, T. M., "Six-phase voltage source inverter driven induction motor," *IEEE Transactions on industry applications*, no. 5, pp. 1251–1259, 1984.

[108] Lipo, T., "A dq model for six phase induction machines," in *Conf. Rec. ICEM'80*, 1980.

[109] Zhao, Y. and Lipo, T. A., "Space vector pwm control of dual three-phase induction machine using vector space decomposition," *IEEE Transactions on industry applications*, vol. 31, no. 5, pp. 1100–1109, 1995.

[110] Hu, Y., Zhu, Z.-Q., and Odavic, M., "Comparison of two-individual current control and vector space decomposition control for dual three-phase pmsm," *IEEE Transactions on Industry Applications*, vol. 53, no. 5, pp. 4483–4492, 2017.

[111] Pucci, M., "State-space space-vector model of the induction motor including magnetic saturation and iron losses," *IEEE Transactions on Industry Applications*, vol. 55, no. 4, pp. 3453–3468, 2019.

[112] Bojoi, R., Lazzari, M., Profumo, F., and Tenconi, A., "Digital field-oriented control for dual three-phase induction motor drives," *IEEE Transactions on Industry Applications*, vol. 39, no. 3, pp. 752–760, 2003.

[113] Bojoi, R., Farina, F., Griva, G., Profumo, F., and Tenconi, A., "Direct torque control for dual three-phase induction motor drives," *IEEE Transactions on Industry Applications*, vol. 41, no. 6, pp. 1627–1636, 2005.

[114] Levi, E., Bojoi, R., Profumo, F., Toliyat, H., and Williamson, S., "Multiphase induction motor drives–a technology status review," *IET Electric Power Applications*, vol. 1, no. 4, pp. 489–516, 2007.

[115] Cirrincione, M., Pucci, M., and Vitale, G., *Power converters and AC electrical drives with linear neural networks*. CRC Press, 2017.

[116] Aghaali, H. and Ångström, H.-E., "A review of turbocompounding as a waste heat recovery system for internal combustion engines," *Renewable and sustainable energy reviews*, vol. 49, pp. 813–824, 2015.

[117] Alshammari, M., Alshammari, F., and Pesyridis, A., "Electric boosting and energy recovery systems for engine downsizing," *Energies*, vol. 12, no. 24, p. 4636, 2019.

[118] Pasini, G. et al., "Evaluation of an electric turbo compound system for si engines: A numerical approach," *Applied Energy*, vol. 162, pp. 527–540, 2016.

[119] Arsie, I., Cricchio, A., Pianese, C., Ricciardi, V., and De Cesare, M., "Evaluation of co2 reduction in si engines with electric turbo-compound by dynamic powertrain modelling," *IFAC-PapersOnLine*, vol. 48, no. 15, pp. 93–100, 2015.

[120] Millo, F., Mallamo, F., Pautasso, E., and Mego, G. G., "The potential of electric exhaust gas turbocharging for hd diesel engines," SAE Technical paper, Tech. Rep., 2006.

[121] Hopmann, U. and Algrain, M. C., "Diesel engine electric turbo compound technology," SAE Technical Paper, Tech. Rep., 2003.

[122] Mohd Noor, A., Che Puteh, R., Rajoo, S., Basheer, U. M., Md Sah, M. H., and Shaikh Salleh, S. H., "Simulation study on electric turbo-compound (etc) for thermal energy recovery in turbocharged internal combustion engine," in *Applied Mechanics and Materials*, vol. 799, 2015, pp. 895–901.

[123] Kant, M., Romagnoli, A., Mamat, A. M., and Martinez-Botas, R. F., "Heavy-duty engine electric turbocompounding," *Proceedings of the Institution of Mechanical Engineers, Part D: Journal of Automobile Engineering*, vol. 229, no. 4, pp. 457–472, 2015.

[124] Cipollone, R., Di Battista, D., and Gualtieri, A., "Turbo compound systems to recover energy in ice," *Int. J. Eng. Innov. Technol*, vol. 3, no. 6, 2013.

[125] Zhuge, W., Huang, L., Wei, W., Zhang, Y., and He, Y., "Optimization of an electric turbo compounding system for gasoline engine exhaust energy recovery," Tech. Rep., 2011.

[126] Pipitone, E., Caltabellotta, S., Sferlazza, A., and Cirrincione, M., "Hybrid propulsion efficiency increment through exhaust energy recovery - part 1: Radial turbine modelling and design," *Energies*, vol. 16, no. 3, p. 1030, 2023.

[127] Pipitone, E., Caltabellotta, S., Sferlazza, A., and Cirrincione, M., "Hybrid propulsion efficiency increment through exhaust energy recovery - part 2: Numerical simulation results," *Energies*, vol. 16, no. 5, p. 2232, 2023.

[128] Gerada, D., Huang, X., Zhang, C., Zhang, H., Zhang, X., and Gerada, C., "Electrical machines for automotive electrically assisted turbocharging," *IEEE Trans. on Mechatronics*, vol. 23, no. 5, pp. 2054–2065, 2018.

[129] Consoli, A., Scarcella, G., and Testa, A., "Slip-frequency detection for indirect field-oriented control drives," *IEEE Trans. on Industry Applications*, vol. 40, no. 1, pp. 194–201, 2004.

[130] Qian, W., Panda, S. K., and Xu, J.-X., "Torque ripple minimization in pm synchronous motors using iterative learning control," *IEEE Trans. on power electronics*, vol. 19, no. 2, pp. 272–279, 2004.

[131] Wang, B., Chen, X., Yu, Y., Wang, G., and Xu, D., "Robust predictive current control with online disturbance estimation for induction machine drives," *IEEE Trans. on Power Electronics*, vol. 32, no. 6, pp. 4663–4674, 2016.

[132] Kulkarni, S. and Thosar, A., "Mathematical modeling and simulation of permanent magnet synchronous machine," *International Journal of Electronics and Electrical Engineering*, vol. 1, no. 2, pp. 66–71, 2013.

[133] Morimoto, S., Kawamoto, K., Sanada, M., and Takeda, Y., "Sensorless control strategy for salient-pole pmsm based on extended emf in rotating reference frame," in *IEEE Industry Applications Conference*, IEEE, vol. 4, 2001, pp. 2637–2644.

[134] Liang, D., Li, J., Qu, R., and Kong, W., "Adaptive second-order sliding-mode observer for pmsm sensorless control considering vsi nonlinearity," *IEEE Trans. on Power Electronics*, vol. 33, no. 10, pp. 8994–9004, 2017.

[135] Qiao, Z., Shi, T., Wang, Y., Yan, Y., Xia, C., and He, X., "New sliding-mode observer for position sensorless control of permanent-magnet synchronous motor," *IEEE Trans. on Industrial electronics*, vol. 60, no. 2, pp. 710–719, 2012.

[136] Wang, Z., Lu, K., and Blaabjerg, F., "A simple startup strategy based on current regulation for back-emf-based sensorless control of pmsm," *IEEE Trans. on Power Electronics*, vol. 27, no. 8, pp. 3817–3825, 2012.

[137] Alonge, F., Cirrincione, M., Pucci, M., and Sferlazza, A., "Input–output feedback linearization control with on-line mras-based inductor resistance estimation of linear induction motors including the dynamic end effects," *IEEE Trans. on Industry Applications*, vol. 52, no. 1, pp. 254–266, 2015.

[138] Cirrincione, M., Pucci, M., Sferlazza, A., and Vitale, G., "Neural based mras sensorless techniques for high performance linear induction motor drives," in *IECON - Annual Conference on IEEE Industrial Electronics Society*, IEEE, 2010, pp. 918–926.

[139] Kojabadi, H. M. and Ghribi, M., "Mras-based adaptive speed estimator in pmsm drives," in *IEEE International Workshop on Advanced Motion Control*, IEEE, 2006, pp. 569–572.

[140] Kivanc, O. C. and Ozturk, S. B., "Sensorless pmsm drive based on stator feedforward voltage estimation improved with mras multiparameter estimation," *IEEE Trans. on Mechatronics*, vol. 23, no. 3, pp. 1326–1337, 2018.

[141] Kim, Y. S., Kim, S. K., and Kwon, Y. A., "Mras based sensorless control of permanent magnet synchronous motor," in *SICE - Annual Conference*, IEEE, vol. 2, 2003, pp. 1632–1637.

[142] Rasvan, V., "Popov theories and qualitative behavior of dynamic and control systems," *European journal of control*, vol. 8, no. 3, pp. 190–199, 2002.